# Effects of the space environment on the performance of SMILE SXI CCDs

Thesis submitted for the degree of

Doctor of Philosophy

at the Open University

by

**Thomas Buggey**

Centre for Electronic Imaging

Faculty of Science Technology Engineering and Mathematics

The Open University

November 2021

# Effects of the space environment on the performance of SMILE SXI CCDs

Thomas Buggey

## Abstract

This thesis investigates the effects of the hazardous space environment on the performance of SMILE SXI CCDs, split between the roles of radiation and micrometeoroid damage. The radiation damage work focuses on developing an analytical technique to guide experimental CCD charge transfer optimisation, which is often a significantly time-consuming process. The technique is initially used to inform SXI CCD optimal clocking speeds and subsequently used to predict in-orbit performance benefits of different CCD operation modes. The first key result was the predicted charge transfer performance improvement from implementing tri-level clocking in the SMILE CCDs being less than 7%, which led to the decision to not implement it in the drive electronics. The second key result, related to radiation damage in a cryogenically irradiated CCD280, was the analysis of an unstable defect found to have a half-life of approximately 4 hours. The final key result is that the thermal cycling of SXI in-orbit will not have a noticeable effect on the defect landscape and hence CTI during the 3-year science lifetime.

The micrometeoroid work focuses on development of a framework to quantify the effects of micrometeoroid impacts in CCD-based soft X-ray space telescopes. The work is tailored specifically for SMILE SXI but can be used in future CCD-based soft X-ray space missions, or any mission that will use silicon micropore optics. The key result of the analysis was the prediction that between 20 and 100 micrometeoroids of a least $1\times10^{-6}$ m diameter will strike the CCDs of SMILE SXI over 3 years. Additional analysis was carried out using crater damage equations to estimate the number of pixels affected by the number of micrometeoroid impacts stated above. Finally, a bespoke experimental setup was built and tested by the author, in preparation for a micrometeoroid experiment testing campaign.

Declaration

I hereby declare that no part of this thesis has been previously submitted to this or any other university as part of the requirement for a higher degree. The work described herein was conducted solely by the undersigned except for those colleagues and other workers acknowledged in the text.

Thomas Buggey

November 2021

**Dedication**

This thesis is dedicated to Hattie, Mum, Dad, Grandad, Tony, Jill, Mr Kitty and Miss Rab, and one small addition to the family very soon…

A**cknowledgements**

I would not of got this far without help from a significant number of people. Firstly, my physics teacher at A-level, Mr Crawley, who inspired me to pursue physics, and if not for him, I would of pursued a different career entirely. Next, my parents, who always supported me no matter what I did. If it wasn't for my Mum I probably never would of submitted my UCAS application! Finally, and most importantly, to Hattie. Thank you for all your support over the last 8 years and helping me get this far.

During my PhD I had a great supervisory team, so thank you to Matt, Dave and Andrew who taught me all that I know and helped me get through the process. Also thank you to all the PhD students in the CEI, Chris, Anton, Saad, Alice, Matt, James, Daniel-Dee, Harry, Dom, Dave, Edgar, Lawrence and Daniel, who provided comic relief over the 3 year period!

To everyone else at the CEI, past and present who I met, Ross, Xiao, Ben, Jesper, Chiaki, Steve, George, Ollie, Michael, Neil, Konstantin, Julian, Nathan, Rob, Sanjaya and anyone else who I missed, thank you for making everything enjoyable and rewarding!

Also thank you to everyone who I interacted with at Te2v, providing me with support and guidance through the PhD.

**List of acronyms and abbreviations**

ESA – European Space Agency

SMILE – Solar Magnetosphere Ionosphere Link Explorer

CAS – Chinese Academy of Sciences

SXI – Soft X-ray Imager

UVI – Ultraviolet Imager

LIA – Light Ion Analyser

MAG – Magnetometer

UV – Ultraviolet

CCD – Charge-Coupled Device

TRL – Technology Readiness Level

CTI – Charge Transfer Inefficiency

CTE – Charge Transfer Efficiency

ATM – Active Trap Model

CME – Coronal Mass Ejection

SWCX – Solar Wind Charge Exchange

CMOS – Complementary Metal Oxide Semiconductor

RSM – Radiation Shutter Mechanism

FEE – Front End Electronics

PLATO – Planetary Transits and Oscillations of stars

FF – Full Frame

FT – Frame Transfer

QE – Quantum Efficiency

SAA – South Atlantic Anomaly

SRH – Shockley Read Hall

sMPO – Silicon Micropore Optics

RT – Room Temperature

OU – Open University

EOL – End of Life

NIEL – Non-Ionising Energy Loss

BLC – Bi-Level Clocking

TLC – Tri-Level Clocking

TR – Transmission Rate

SW – Solar Wind

# Table of Contents

# 1. Introduction

The joint European Space Agency (ESA) and Chinese Academy of Sciences (CAS) mission SMILE is an S-class space telescope due to launch into a highly elliptical orbit around the Earth in 2024. The SMILE spacecraft will study space weather in close vicinity to the Earth, by investigating the interaction between the solar wind and the Earth's magnetosphere on a global scale. Previous space missions such as Cluster, THEMIS, Swarm and Magnetospheric Multi-Scale have investigated micro-aspects of the Earth-Sun interaction (ESA, 2018), but none to date have observed the full chain of events that drive the Earth-Sun connection. SMILE will fill this niche. Figure 1.1 shows a cartoon of SMILE in-orbit around the Earth, with the Sun, SMILE spacecraft and Earth highlighted.

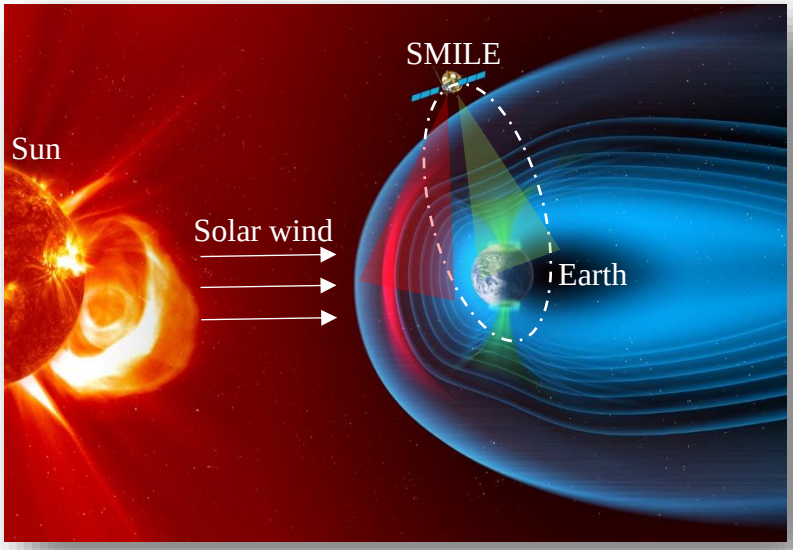


**Figure 1.1**: Cartoon of the SMILE mission concept (ESA, 2018) with SXI and UVI observations highlighted in red and green respectively, along with the elliptical orbit in white. Note that the field of view of the instruments and orbital path is not exact, and merely shown for illustrative purposes.

The science goals of SMILE are defined by three primary questions (chapter 2 will add sufficient background information to add context to these science goals):

1. What are the fundamental modes of the dayside solar wind/magnetosphere interaction?

2. What defines the substorm cycle?
3. How do coronal mass ejection-driven storms arise and what is their relationship to substorms?

To answer these questions, SMILE contains a suite of four instruments, with development split equally between ESA and CAS. The two in-situ instruments are currently being developed by CAS and focus on measuring properties of the solar wind and the strength of the local magnetic field. The light ion analyser (LIA) will measure the velocity and density of the solar wind, providing an early indication of solar activity before the Earth-Sun interaction occurs. The magnetometer (MAG) provides three-axis measurements of the local magnetic field, showing explicitly how the magnetosphere interacts with the solar wind. The remaining two instruments are imagers, developed by ESA, focusing on observations of UV and soft X-rays. The ultra-violet imager (UVI) will monitor the Earth's northern aurora (green regions in Figure 1.1), for changes in UV emission. The soft X-ray imager will monitor the quantity of photon emission from the dayside boundary of the Earth's magnetosphere (red arc in Figure 1.1), as well as monitoring soft X-ray emission from two smaller regions at the Earth's poles.

Although monitoring the Earth-Sun interaction from space has many advantages, the environment is harsh, providing a substantial number of challenges to overcome. With regards to the contents of this thesis, the main hazards are radiation and micrometeoroid impact damage, specifically about the detector performance of SXI.

To achieve the instrument performance necessary, the detectors chosen for SMILE SXI were charge-coupled devices (CCDs). CCDs are ubiquitous with space imaging, having been used in a significant number of prominent space missions and thus having a high technology readiness level (TRL). The main drawback of using CCDs, however, is the susceptibility to radiation damage, which can severely limit detector performance if not mitigated against. SMILE SXI is no exception; the CCDs must be optimised to mitigate against radiation damage and maximise science output. If optimisation does not occur, the science performance of the instrument is limited due to charge transfer degradation. Figure 1.2 shows a famous example of the effect of radiation damage on the charge transfers performance of CCDs, specifically in the Hubble Space Telescope.

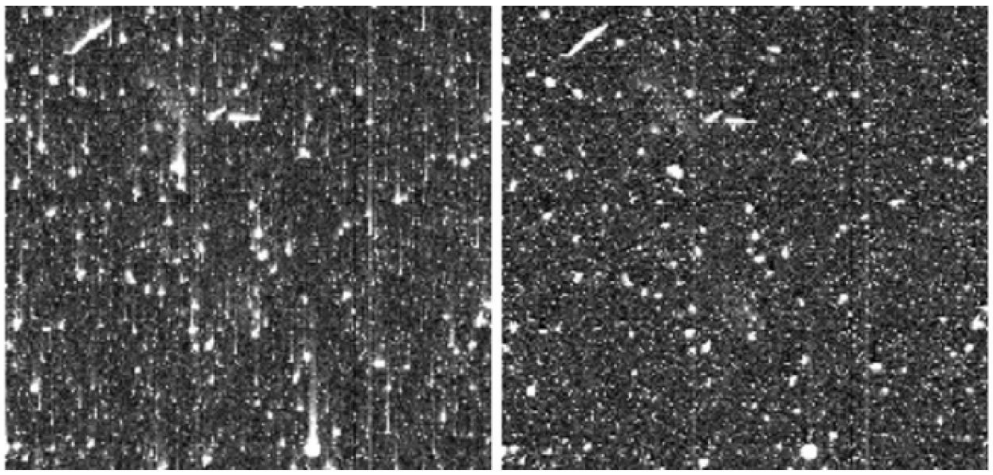

**Figure 1.2**: Charge transfer degradation caused due to deferred charge (Massey et al., 2010). Left – Charge is seen to be "smeared" along the direction of transfer (top to bottom). Right – A corrected image generated by modelling the underlying effects of radiation damage to remove the charge smearing.

The current status quo with regards to CCD charge transfer optimisation is a laboratory-based approach, probing the detector operating parameter space (temperature, charge transfer speeds, charge injection) to minimise charge transfer inefficiency (CTI). CTI is effectively a measure of the charge smearing seen in Figure 1.2 (left) and minimising CTI will ensure that the science output of the detector is maximised. The process of laboratory optimisation is time-consuming and is exacerbated by a wide parameter space. Due to the operating mode of the SMILE SXI CCDs, the parameter space is unfortunately very wide, with three charge transfer speeds to optimise, along with temperature, charge injection and optional clocking modes (e.g. tri-level clocking). While a laboratory-focused approach would work, it would indeed be very time-consuming.

In recent years, knowledge of the radiation damage within a CCD has greatly increased through the use of the trap pumping technique (chapter 5). The trap pumping technique allows the characterisation of radiation damage within a CCD to high precision. The different species of radiation-induced defects within the damaged silicon have been characterised, those of which directly cause poor CTI in irradiated devices. Previous work has utilised this knowledge of radiation-induced defects to focus laboratory CTI optimisation in a basic CCD operating mode. This thesis will build significantly on the previous work (chapters 6 and 7), adapting the

analytical technique to optimise the charge transfer performance of the intricate SMILE SXI CCD readout modes and provide recommendations for laboratory optimisation activities and in-orbit operation modes. The analytical model has been written from scratch and has been written to be as modular as possible, so that future CCD-based space missions can also utilise this powerful technique.

The problem of radiation damage in CCDs has been studied extensively due to the potential detector degradation. However, another threat in space, that of hyper-velocity particulate impacts, has had significantly less attention. The main reason for the lack of focus on hyper-velocity particulate impacts is that key components of the spacecraft are naturally shielded by the body of the spacecraft itself, significantly mitigating the threat. However, open areas to space, such as detector focal planes (and specifically soft X-ray telescopes due to optical geometry), are at risk of detector performance degradation due to particulate impacts. Previous soft X-ray space telescopes have been subject to varying degrees of sporadic detector damage (Figure 1.3), ranging from appearance of hot pixels to entire detectors being rendered unusable due to increased noise (Godet et al., 2009; Koyama et al., 2007; Meidinger et al., 2003).

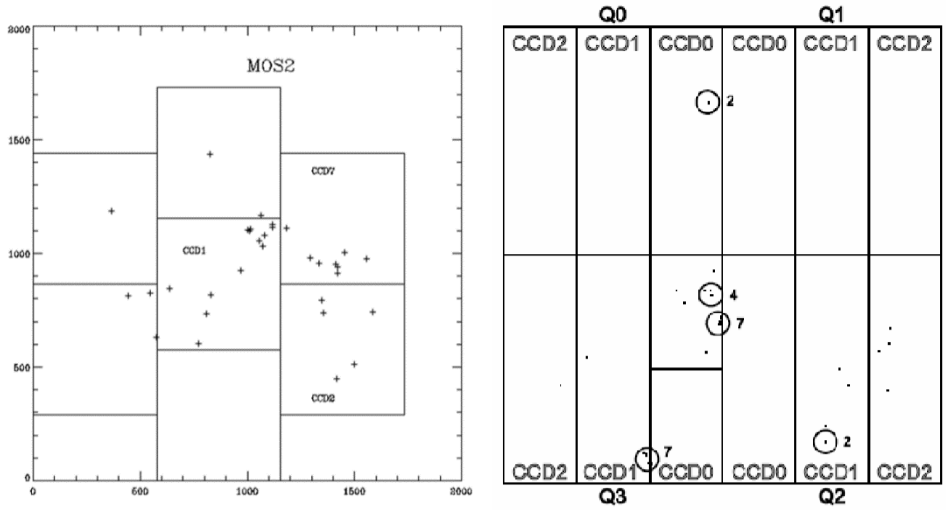


**Figure 1.3**: Location of hot pixels seen in both the MOS CCD array and pn-CCD array in the XMM Newton space telescope (Abbey et al., 2005). Left – Hot pixels seen at the start of orbit 108 in the MOS2 array. Right – Areas of hot pixels seen in orbit 156 (Meidinger et al., 2003).

Although the threat of hyper-velocity particulate impacts to soft X-ray space telescopes is high, no framework currently exists that can assess the risk of these particulate impacts. In this thesis,

an end-to-end framework is developed that will allow the risk of particulate impacts to be assessed, specifically tailored to SMILE SXI. To do this, a combination of current models (chapter 4) and bespoke simulations (chapter 9) developed by the author will be used in addition to approximations where appropriate.

## 1.1. Research output

The results from the work in this thesis are partly contained within the following publications and technical notes.

### 1.1.1. Publications

1. **Buggey, T**. Soman, M. Bush, N. Hall, D. Parsons, S. Randall, G. Hetherington, O. Leese, M., Holland, A. "Developing the Active Trap Model for CCD charge transfer optimisation in large-scale space missions". Accepted to: SPIE Astronomical Telescopes and Instrumentation 14th-18th Dec 2020 Online Forum.
2. **Buggey, T**. Soman, M. Keelan, J. Hall, D. Holland, A. "Monte Carlo simulations of hyper-velocity particulate mechanics within silicon micropore optics". Accepted to: SPIE Astronomical Telescopes and Instrumentation 14th-18th Dec 2020 Online Forum. (Also submitted to JATIS for upgrade – Currently "Decision Pending Editor Approval")
3. **Buggey, T.** Soman, M. Hall, D. J. Parsons, S. Hetherington, A. Holland, A.D. "Short term defect decay in a cryogenically irradiation silicon CCD". In preparation for submission to: RADECs 2022.
4. Parsons, S. Hall, D. Holland, A. Verhoeve, P. Sembay, S. Randall, G. Hetherington, O. Yeoman, D. **Buggey, T.** Soman, S. "Radiation damage testing status of the CCDs for the SMILE SXI", Proc. SPIE 11454, X-Ray, Optical, and Infrared Detectors for Astronomy, IX, 114540Q (13 December 2020); https://doi-org.libezproxy.open.ac.uk/10.1117/12.2560337
5. Parsons, S. **Buggey, T**. Holland, A. Sembay, S. Randall, G. Hetherington, O. Yeoman, D. Hall, D. Verhoeve, P. Soman, M. "Effects of Temperature Anneal Cycling on a Cryogenically Proton Irradiated CCD". Accepted to JINST, https://doi.org/10.1088/1748-0221/16/11/P11005.

### 1.1.2. Technical Notes

1. **Buggey, T**. Soman, M. Keelan, J. "SMILE SXI CCD Micrometeoroid Modelling Report", OPEN_SMILE_CCD_TN_03_1.0. 2018.
2. **Buggey, T**. Soman, M. "SMILE SXI Testing and Calibration Micrometeoroid Test Plan", OPEN_SMILE_MM_TP_01_1.0.2018.
3. Parsons, S. **Buggey, T**. "Room temperature irradiation test report", OPEN_SMILE_TR_01.00, 2018.
4. Parsons, S. **Buggey, T**. "SMILE SXI CCD Testing and Calibration CCD Operational Modes", OPEN_SMILE_CAL_TN_01_1.2.

## 1.2. Thesis Outline

This thesis is comprised of nine chapters including this one, with the first five chapters describing the relevant background information required (the end of chapter 5 has some preliminary results), and the last four chapters containing most of the original and novel work.

Chapter 2 will outline the SMILE mission in more detail, providing adequate detail to add context to the overall mission goals as described in the introduction to this thesis. Each instrument will be described, with most attention paid to SXI (and more specifically the CCDs) as this is the focus of the thesis.

Chapter 3 describes the basic operation of a CCD, in particular the process of charge generation, storage, collection, and digitisation. The CCDs used as part of the SMILE SXI instrument and associated laboratory testing activities are then described in detail.

In chapter 4, the space radiation and hyper-velocity particulate environment near the Earth is described. The effects of ionising and non-ionising radiation on CCDs are discussed, followed by a literature review of the impact of hyper-velocity particulate impacts on space-based soft X-ray telescopes. The chapter concludes with the description of micrometeoroid flux models and damage equations that will be used to subsequent chapters to quantify the damage of hyper-velocity particulate impacts to SMILE SXI.

Chapter 5 outlines the experimental equipment and techniques used during the thesis, in particular the trap pumping methodology and some preliminary results attained that are then used in the following chapter.

Chapter 6 describes the development of the analytical model of charge transfer optimisation (hereon called the Active Trap Model (ATM)) from first principles, with the rationale behind each component of the model explained. The ATM is then used to predict changes in CTI performance in a room-temperature irradiated CCD280. Differences between the model and experimental results are discussed, with subsequent changes (improvements) to the model showing an excellent fit between experimental and model results.

Chapter 7 describes the first cryogenic irradiation of a CCD280 carried out by the OU (and the author). Post-irradiation trap pumping results are presented, with implications for SMILE SXI performance in-orbit discussed.

Chapter 8 describes how the ATM must be developed to simulate the more complicated readout mode of the CCD370 and how this is implemented within the model. The updated ATM is then used to predict optimal readout speeds of the CCD370. As an extension, the ATM is then updated further to predict the performance improvement of using tri-level over bi-level clocking in a CCD370. Implications for the in-orbit readout mode of SMILE SXI are then discussed.

Chapter 9 describes the development of the end-to-end framework for quantifying the damage of hyper-velocity impacts for SMILE SXI CCDs. Results are presented from previous models as well as bespoke particulate tracing simulations. The number of predicted pixels that will be damaged in orbit is then discussed, along with caveats and approximations used through the whole process. The chapter is concluded with several key questions that follow from the work presented here that should be answered by a future comprehensive experimental impact campaign. Experimental equipment built by the author (specifically to answer the key questions) is then described briefly.

# 2. The Solar Magnetosphere Ionosphere Link Explorer

Space weather effects have been observed for many decades by numerous scientists and amateur astronomers. The most famous example of an observed solar storm is the aptly named "Carrington Event" which was named after Richard Carrington, who linked a large geomagnetic storm to a solar flare observed the day previously (Carrington, 1859). Before the 20$^{th}$ century, the study of space weather was limited only to observations, with no theoretical underpinning. It was only when the space-age began that the fundamental mechanisms that underpin space weather could be studied for the first time, leading to a fleet of missions, studying both the behaviour of the Sun and the magnetic environment of the Earth.

Space weather is of interest as it can lead to many effects, some of which can cause major negative disruptions and are triggered by a complex array of systems and processes involving the Sun and the Earth. Examples of the effects of space weather include disruption of power grids, negative effects on aviation and satellites as well as the aurora borealis (northern lights) and aurora australis (southern lights). Many of these effects are indeed negative, and the current fundamental understanding of the triggers of space weather events are not understood. This means that predicting, tracking, and monitoring space weather, much like successfully predicting and tracking that of terrestrial weather, is not yet possible. To compound matters, space weather events are complex, involving many processes occurring simultaneously and over varying timescales, thus making the study of space weather even more difficult. A multitude of previous space missions from different space agencies around the world have studied space weather events and triggers using a mix of in-situ measurements and imagers. However, to date, no single mission has had the capabilities to study space weather events surrounding the Earth in its entirety. One such mission, called the **S**olar **M**agnetosphere **I**onosphere **L**ink **E**xplorer (SMILE) will fill this niche, by studying the global interaction of the solar wind and the Earth's magnetic field, which is necessary to develop the fundamental understanding of magnetospheric physics of the Earth and hence space weather.

This chapter introduces the SMILE mission concept and its goals, complemented by a basic description of the Earth's magnetic field system, known as the magnetosphere, which is necessary to fully understand and appreciate the ambition of SMILE. It is followed by a description of the instruments involved, with explanations of how each instrument will assist

SMILE in achieving its goals of studying the global Earth-Sun interaction. Particular attention is paid to the Soft X-ray Imager (SXI) as this is the focus of the thesis, including descriptions of the Silicon Micro-Pore Optics (sMPO), temperature control systems and silicon-based detectors. The CCDs selected for SMILE will be explained in more detail in chapter 3, preceded by a basic description of CCDs, moving on to more in-depth descriptions of detector architecture and operational modes.

## 2.1. Space weather and the magnetosphere

The main mechanism which drives space weather is the interaction between the solar wind and the Earth's inherent magnetic field, through which energy is transferred. It is this transfer of energy that is the underlying driver behind various space weather events, which can have serious negative consequences for the Earth.

When current flows in a wire, a magnetic field is produced that is proportional to the amount of current flowing. Any external magnetic field can interact with the magnetic field associated with the current flowing and potentially increase the current in the wire. During geomagnetic storms, magnetic field strengths vary depending on the severity of the storm and can produce unexpected and unwanted spikes in current. Large spikes in current can damage electrical components such as transformers, leading to voltage stability issues and hence partial or system wide blackouts. A famous example of such an event was a large geomagnetic storm that occurred due to a coronal mass ejection (CME) on March 9, 1989 ("Geomagnetic Storms Can Threaten Electric Power Grid Earth in Space," 1997). Approximately three and a half days after the CME, the large geomagnetic storm produced caused multiple power blackouts across North America, with Quebec receiving the most severe damage (Boteler, 2019). The entire Quebec power grid was offline for approximately 12 hours, affecting millions of people and leading to a significant economic cost.

### 2.1.1. Effects of space weather

Space weather effects such as geomagnetic storms or radiation storms can disrupt radio communications in the high (HF), super high (SHF) or ultra-high frequencies (UHF), affecting several different industries such as commercial airline communications, government agencies and satellite communications. During a geomagnetic storm, the density of charged particles in

the ionosphere can increase significantly, affecting the transmission path of HF radio waves. In severe cases, HF radio waves can be blocked completely, meaning that no signals are transmitted and causing major disruptions for the industries affected. The underlying mechanism that disrupts the propagation of radio waves in the HF, SHF and UHF bands is due to attenuation and scintillation of signal in the ionosphere (Guo et al., 2019).

Communications in global positioning systems (GPS) are also affected for identical reasons to that of radio communications as described above. In particularly noisy solar conditions, errors of 10s of metres are seen, and cannot be sufficiently corrected by analytical models. Many industries utilise GPS such as farming, construction, geological exploration, and surveying on top of the navigation and geo-tagging applications that are more frequently used in every-day life.

Satellites positioned at low-Earth-orbit (LEO, ~2000 km) or lower, will experience some form of drag due to the presence of air molecules. Although the density of air is significantly lower than on the surface of the Earth, it is still sufficient to have a noticeable impact. Solar activity also affects the drag force, meaning that for satellites to maintain their orbits, the activity of the Sun must be closely monitored. At a solar minimum, satellites in LEO must boost their orbits a set number of times per year, largely dependent on the orbital altitude (Oliveira and Zesta, 2019). However, at a solar maximum, the density of particles in LEO is increased, leading to larger drag forces, and requiring orbits to be maintained more frequently. Along with the additional effort required to maintain orbits more frequently, an additional knock-on effect from uncertainty in position is encountered. The ever-increasing quantity of man-made space debris means that the location of a satellites orbit must be known very precisely to avoid potentially devastating orbital collisions.

### 2.1.2. Magnetosphere structure

The magnetic field of the Earth is generated by electrically conducting convection currents flowing in the liquid outer core of the Earth (Weiss, 2002). Extreme heat generated by processes within the inner core maintains the convection currents flowing in the outer core and in turn leads to the generation of a large and stable magnetic field.

The basic layout of this magnetic field is like that of a bar magnet, a magnetic dipole with field lines diverging and converging at the south and north poles respectively. This entire volume is

known as the magnetosphere and is comprised of many distinct and dynamic features. Excellent summaries of the magnetosphere's found in the Solar System are available within the literature (Schubert and Soderlund, 2011, (Blanc et al., 2002), describing the complexities of these systems. For this thesis however, the focus will be on the magnetosphere of the Earth, as this is SMILE's entire focus.

For the case of the Earth, the magnetosphere is severely distorted by the solar wind, leading to the characteristic shape seen in Figure 2.1. Many distinct features are seen such as areas known as the bow shock, magnetosheath, magnetopause, magnetotail and polar cusps. All the above features, among many others, are dynamic in nature, changing over varying time scales due to solar activity. In the following section, a description of each part of the Earth's magnetosphere relevant to SMILE will be given.

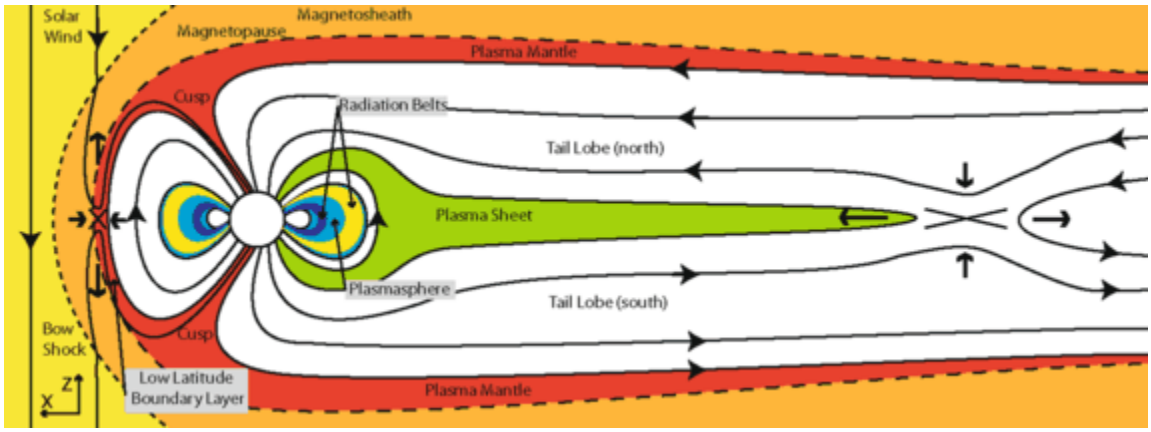


**Figure 2.1**: A schematic of the Earth's magnetosphere (Eastwood et al., 2015). In this depiction, the Sun is on the left-hand side of the page, with solar wind flowing towards the dayside of the Earth.

#### 2.1.2.1. Bow Shock

Although the bow shock is, strictly speaking, not within the Earth's magnetosphere, it plays an important role in creating the distinct shape which is exhibited by the Earth's magnetosphere. The bow shock is the area in which the velocity of the solar wind drastically drops as it decelerates from supersonic to subsonic velocities. Deceleration occurs due to the obstruction of the Earth, impeding the flow of the solar wind from the Sun. The location of the bow shock is significantly far from the planet, approximately 90,000 km, but the thickness of the bow

shock itself is incredibly thin by astronomical terms, approximately 17 km as measured by the ESA mission Cluster (Lobzin et al., 2007).

The bow shock is important as it significantly changes the conditions of the incoming plasma, from highly linear solar wind to shocked and turbulent. It is this disrupted plasma that interacts with the magnetosphere, driving a myriad of subsequent processes and causing the effects of space weather as seen on the Earth. Although SMILE will not study the behaviour of the bow shock explicitly, understanding the importance of the role of the bow shock with respect to subsequent events is crucial.

#### 2.1.2.2. Magnetosheath

The magnetosheath is the region between the bow shock and the magnetopause and is considered a transitionary zone where turbulent plasma interacts with the magnetic field of the Earth. In contrast to the highly organised magnetic field close to the Earth, the magnetic environment within the magnetosheath is irregular and turbulent due to the deceleration of the solar wind at the bow shock. The magnetosheath plays a key role in space weather as it is the interface between the high density of charged particles within the interstellar medium and the low density of charged particles within the magnetosphere.

#### 2.1.2.3. Magnetopause

The magnetopause is the interface which clearly defines the boundary between the Earth's magnetic field and the magnetic field which is carried by the solar wind (known as the interplanetary magnetic field (IMF)). The location of the magnetopause is dynamic and is closely linked to solar activity, namely the speed and density of the solar wind (Dessler, 1968). The stream of particles contained in the solar wind carries momentum, with each particle imparting a small amount of pressure on the magnetopause. The magnetopause moves as pressure is exerted from the solar wind, until equilibrium is reached between the two layers.

Although the magnetopause is considered the boundary between two sets of magnetic fields, it is not a perfect shield, and can be considered "open" or "closed" depending on the surrounding plasma conditions. The following implication is that in a scenario where the magnetopause is "open", there can be a net flow of mass and hence energy from the magnetosheath into the magnetosphere. Many processes are associated with the "opening" and "closing" of the dayside

of the magnetopause, including the Dungey cycle (Dungey, 1961) which describes the constant process of magnetic reconnection on both the dayside and nightside of the Earth. Again, excellent summaries are found within the literature (Eastwood et al., 2015), describing the mechanisms which control the structure and dynamics of the Earth's magnetosphere in significant detail, much of which is beyond the scope of this instrumentation-related thesis.

Studying this boundary is of key importance with respect to space weather, as this is the location where the main trigger (energy in the form of charged particles), enters the magnetosphere and causes subsequent effects. However, studying the magnetopause has been difficult until recently, when a mechanism known as charge exchange was found to produce a significant number of soft X-rays. This emission of photons could indeed be exploited to image specific parts of the magnetosphere and study in detail the interaction between the SW and the Earth's magnetic field.

#### 2.1.2.4. Imaging the magnetopause – Charge exchange

Evidence for the process of charge exchange was first seen by the Röntgen X-ray satellite in 1996 (Lisse et al., 1996), when a surprisingly high number of X-rays and extreme UV photons were seen emanating from comet C/Hyakutake. The underlying mechanism behind the emission was later revealed to be from the interaction between the ions located in the solar wind and the neutral atoms located in the tail of the comet (Cravens, 1997). The process is not strictly tied to comets, indeed any object which contains neutral atoms which then interact with ions will produce photon emission dependent upon the energy of the electron transition. To date, this process has been used to study objects such as supernova remnants (Katsuda et al., 2012), starburst galaxies (Ranalli et al., 2008) and the interaction between planetary and stellar winds (Tremblin and Chiang, 2013).

More specifically, the process of *solar wind* charge exchange (SWCX) is an interaction between ions in the solar wind (green circle in Figure 2.2) with neutral atoms (yellow circle in Figure 2.2) in a planetary body's exosphere (the outermost volume of an object, where the atmosphere terminates and merges with interplanetary space). In the interaction (Figure 2.2 left), a minimum of one electron (black circle in Figure 2.2) is transferred from the neutral atom to the incident ion via a quantum mechanical process (Shindo and Kawai, 1986), promoting the incident ion to an excited state (Figure 2.2 centre). Subsequently, the ion relaxes to a lower

energy state through the emission of a photon with characteristic energies (Figure 2.2 right). The energy of the emitted photons depends upon the elements and ionisation state of the atoms involved in the process. Hydrogen and helium ions make up the majority of the ions within the solar wind but other ions such as $C^{6+}$, $N^{6+}$, $O^{7+}$, $O^{8+}$, $Mg^{9+}$ and $Ne^{9+}$ are also present in small quantities and lead to different characteristic photon emission lines (Bochsler, 2007).

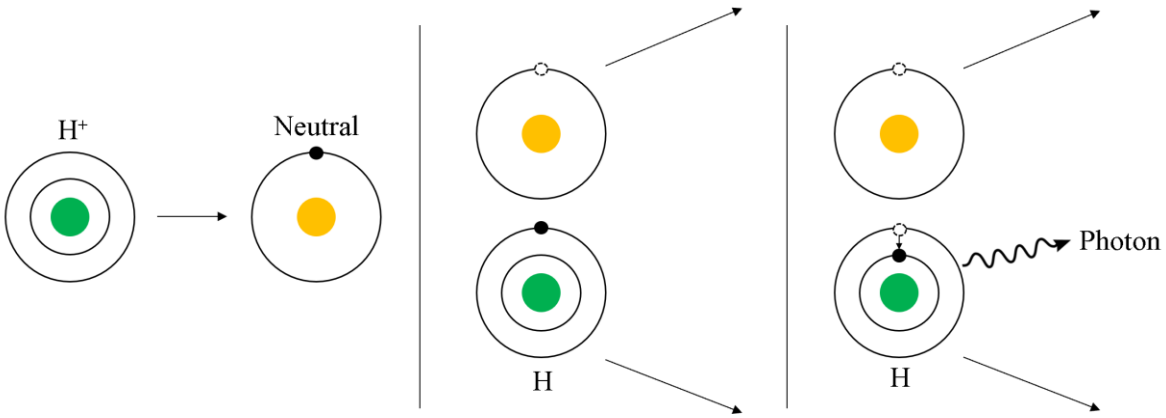


**Figure 2.2**: Example of the SWCX process for a hydrogen ion (from the solar wind) and a neutral atom (from the Earth's exosphere).

For SMILE SXI specifically, the science energy band (0.2 keV – 2 keV) is defined by key emission lines. Within the magnetosphere, photon emission from the lower energy band (approximately 0.2 keV – 0.25 keV) was shown to closely correlate with solar wind fluxes, despite large variations within the solar wind ion composition. As such, studying this soft X-ray energy band is of interest.

Between 0.2 keV – 0.5 keV, many emission lines are present, from many ionisation states and distinct ions. Towards the upper end of the science band (0.5 keV – 2 keV), soft X-ray emission lines are less abundant, but the few emission lines that are present are abundant ($O^{7+}$ (561 eV), $O^{8+}$ (653 eV) and $Ne^{9+}$ (905 eV)).

#### 2.1.2.5. Polar cusps

As explained in section 2.1.2.2, energy can enter the magnetosphere via the dayside of the magnetopause and trigger space weather events. However, another region exists where energy can "leak" into the magnetosphere and trigger identical events, more specifically at the north and south poles of the Earth. These areas are known as the polar cusps, which form due to the

distortion of the magnetic field created by the solar wind (seen in Figure 2.1). During the process of magnetic reconnection, magnetic field lines move around the Earth as dictated by the Dungey Cycle, leaving a region where the magnetic field strength is relatively low. In this region, located at the north and south pole, plasma in the magnetosheath can flow towards the Earth (Reiff et al., 1977, Marklund et al., 1990, Yamauchi and Lundin, 1997), interacting with the neutral atoms in the exosphere, producing emission via SWCX. It is via this process that the behaviour of the polar cusps can also be studied.

Figure 2.3 shows the pattern of emission that occurs via SWCX for different points in the Earth's magnetosphere, as projected into 2D from a typical observing location for SMILE, above the north pole. An arc of emission is seen in the centre of each image, at the points where plasma is entering the dayside magnetopause, as well as two distinct spots at the north and south pole from emission at the cusps.

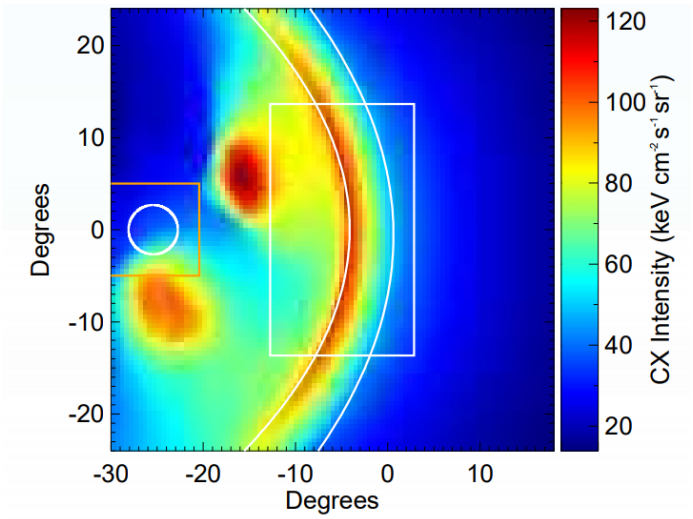


**Figure 2.3**: A single magneto-hydrodynamic (MHD) simulation showing the regions of soft X-ray emission from the Earth's magnetosphere (Raab et al., 2016).

#### 2.1.2.6. Magnetotail

At the dayside of the magnetopause, the magnetopause is compressed due to pressure exerted by the solar wind. At the nightside however, no solar wind pressure exists, but the solar wind still influences the shape of the magnetic field. As the solar wind is deflected around the Earth due to the magnetosphere, the motion of the solar wind from the Earth extrudes the magnetic field (seen by the large tail in Figure 2.1), causing significant distortion, forming what is known

as the magnetotail. The diameter of the tail is between 40 and 60 Earth radii and the length of the tail exceeds 1000 Earth radii (Sibeck and Lin, 2014).

### 2.1.3. Space weather events

In section 2.1.2, the basic layout of the Earth's magnetosphere was described, with focus placed on how the solar wind interacts and then distorts the shape of the magnetosphere. As the Sun continues to influence the magnetosphere of the Earth, specific events can be triggered including geomagnetic storms and substorms, ionospheric disturbances, scintillation of radio signals and the injection of additional particles into the Van Allen radiation belts. As SMILE is the focus of this thesis, the focus will be placed on the events of most interest, most notably the trigger of both geomagnetic storms and substorms.

#### 2.1.3.1. Geomagnetic storms

Geomagnetic storms are, broadly speaking, large disturbances of the Earth's magnetosphere often occurring over periods of days. During periods of intense solar activity, and hence increased solar wind density and velocity, a significant amount of energy is deposited into the Earth's magnetosphere. As a result of the additional energy deposition, major changes are seen in the magnitude of currents, plasma densities and magnetic fields, all of which cause the negative effects described in section 2.1. The frequency of geomagnetic storms are linked to solar activity, with geomagnetic storms occurring more frequently during solar maximum, being driven by coronal mass ejections (CME).

#### 2.1.3.2. Geomagnetic substorms

Substorms are also a disturbance of the magnetosphere, but usually occur over a period of hours as opposed to days when compared to geomagnetic storms. The effects of substorms are again, like that of storms, however the effects are only seen in the polar regions, as most of the energy to trigger a storm is injected into high latitudes close to the polar regions.

## 2.2. SMILE science goals

Given the lack of fundamental understanding behind the triggers of space weather, the SMILE mission will aim to study the dynamic relationship between the Sun and the Earths magnetosphere (Raab et al., 2016), which ultimately lead to space weather events. To achieve

this, SMILE will make observations of both the dayside magnetopause and polar cusps, exploiting the SWCX process. The distinct science goals for SMILE are stated below, with a more thorough explanation of each in section 2.2.1, 2.2.2 and 2.2.3 respectively.

The science goals of SMILE can be broken down into three primary goals:

1. What are the fundamental modes of the dayside SW /magnetosphere interactions, and in particular, what is the manner in which energy and plasma enters the magnetosphere?
2. What defines the substorm cycle, which is thought to be the elemental phenomenon controlling the circulation of energy and plasma internally in the magnetosphere?
3. How do coronal mass ejection (CME) driven storms arise and what is their relationship to substorms?

### 2.2.1. Science goal one

The first goal of SMILE focuses on the locations in which energy and plasma enters the magnetosphere of the Earth. As dayside reconnection occurs as part of the Dungey cycle, plasma flows through the dayside magnetopause and polar cusps, leading to SWCX and hence soft X-ray emission. The rate of plasma flow is dynamic however, with elongated periods of steady reconnection (Frey et al., 2019), contrasted by periods of high rates of reconnection and time-dependent reconnection (Southwood et al., 1988). By tracking the rate and exact location of soft X-ray emission at the dayside magnetopause and polar cusps, it will be possible to see the evolution of each boundary under varying solar wind conditions.

### 2.2.2. Science goal two

The precise trigger of substorms is not understood, with the two main hypotheses being changes in the orientation of the IMF-triggering substorms (Wild et al., 2009, Morley and Freeman, 2007), or the solar wind influencing the shape of the magnetotail and thus triggering substorms (Hubert et al., 2009; Milan, 2004). Not only are the triggers themselves not understood, the magnitude of these triggers is also unknown. SMILE's combination of instruments will allow the study of the solar wind parameters local to the spacecraft, while simultaneously imaging the boundaries in which energy enters the magnetosphere, which is crucial for understanding the trigger of substorms.

### 2.2.3. Science goal three

CMEs are large solar events, where material erupts from the Sun's corona and travels towards Earth at super-magnetosonic speeds (faster than the ambient solar wind, Forbes, 2000). The largest space weather events are associated with CMEs (Richardson et al., 2001), so understanding the roles of CMEs is of utmost importance. However, not all CMEs generate geomagnetic storms, and the exact reason for this is unknown. By tracking the behaviour of the dayside magnetopause, polar cusps and auroral ovals during a large CME, and indeed for many CMEs, it will be possible to find links between solar wind parameters, X-ray/UV emission and the trigger of geomagnetic storms.

## 2.3. SMILE instruments

To achieve these science goals, the payload and orbital selection will be highly tailored to maximise the science return of the mission. SMILE will utilise four instruments, studying properties of the solar wind as well as X-ray and UV emission from the dayside magnetopause and polar cusps. The northern aurora will be studied by the Ultra-Violet Imager (UVI), with the magnetopause and magnetospheric cusps being observed by the Soft X-ray Imager. To compliment these remote instruments, the solar wind density and speed will be measured by the Light Ion Analyser (LIA) and the strength of the magnetic field carried by the solar wind measured by the Magnetometer (MAG). These four instruments will be able to provide the most complete, self-standing image of the interaction between the solar wind and the Earth's magnetosphere to date. Figure 2.4 shows an early model of the SMILE spacecraft, with each of the instruments labelled.

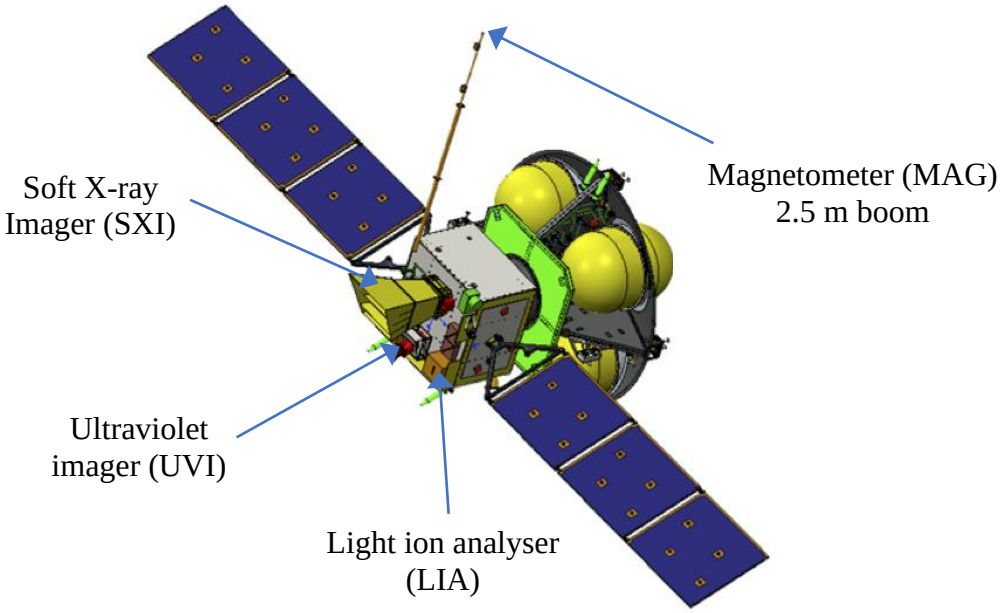


**Figure 2.4**: Model of the SMILE spacecraft (ESA, 2018). SXI, UVI and LIA are located on the body of the spacecraft, whereas the MAG is located on a 2.5m boom to avoid detecting the inherent magnetic field of the spacecraft.

### 2.3.1. SMILE orbital selection

Due to the nature of SMILE's science objectives, views of the entire magnetosphere of the Earth are required, including the outside edge of the magnetosphere while still maintaining adequate spatial resolution of the auroral oval. As a result, a highly elliptical and highly inclined orbit was chosen, to provide a top-down view of the Earth-Sun magnetosphere interaction. A highly elliptical orbit also means that the spacecraft can collect uninterrupted observations for longer periods of time, with ~80% of its orbital period dedicated to science-rich observations. Figure 2.5 shows the orbit of the SMILE spacecraft in red, with apogee at ~19 Earth radii (121,000 km) and perigee at ~0.8 Earth radii (5000 km). Also highlighted are the magnetic field lines originating from the poles of the Earth, which are distorted by the Solar wind (left in Figure 2.5). These magnetic field lines, including the bow shock and magnetopause, show the distance to which the SXI must observe to attain its science goals, which is enabled by the elliptical orbit.

Another reason for the choice of the elliptical orbit is the necessity of telemetry on SMILE. During each orbit, data is gathered from ~80% of the orbit and then stored on-board. The final

20% of each orbit is that which is closest to perigee, where the telemetry rates achievable are at a maximum. During this 20%, science data files are transmitted back to ground stations, with the spacecraft then entering its next orbit, resuming data acquisition. The telemetry phase is also coupled with the spacecraft re-orienting itself such that the solar panels face the Sun, and the spacecraft can fully charge.

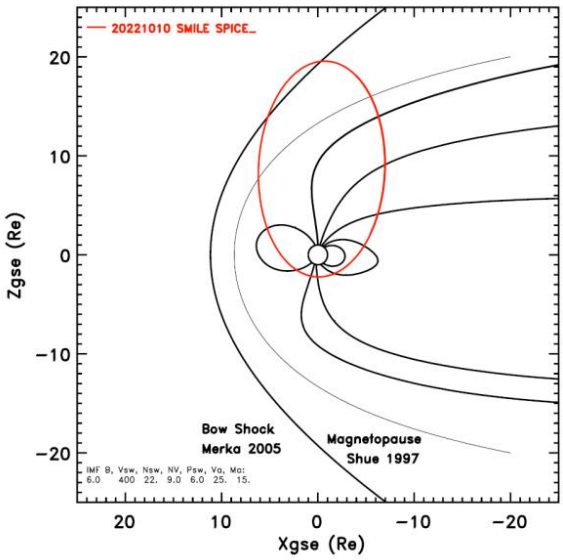


**Figure 2.5**: Schematic of the Earth, magnetic field lines and overlaid SMILE spacecraft orbit in red (ESA, 2018). The Earth is centred in the figure, with the Sun to the left and accompanying Solar wind distorting the magnetic field lines.

In the following sections, each instrument will be outlined, with a focus placed on the SXI instrument and associated focal plane.

### 2.3.2. Light Ion Analyser (LIA)

The LIA is currently being developed by the Chinese National Space Science Centre (CNSSC) in collaboration with the Mullard Space Science Laboratory (MSSL). The LIA will measure the velocity and density distribution of the solar wind in three dimensions.

The LIA is a top-hat style electrostatic analyser that utilises changing voltages applied across nested hemispherical electrodes (ESA, 2018). Charged particles incident upon the nested electrodes will follow a curved path under the influence of the electric field. Only particles within a certain energy range will successfully traverse the curvature of the electrodes without

colliding against the electrodes themselves. The potential is sequentially changed between the electrodes, allowing a range of particle energies to be probed over time. Figure 2.6 below shows a schematic representation of a LIA.

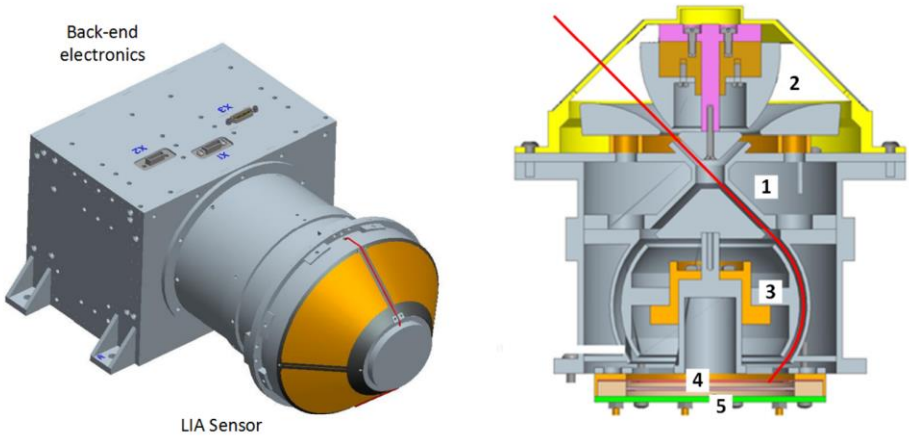


**Figure 2.6**: Left – 3D model of the LIA. Right - Cross section schematic of the 3D model. The red line shows a charged particle trajectory (ESA, 2018).

### 2.3.3. Magnetometer (MAG)

The magnetometer (MAG – shown in Figure 2.7) is currently being developed by the Chinese Academy of Sciences (CAS), Chinese National Space Science Centre and the Austrian Academy of Sciences. MAG will be able to measure both the strength of the magnetic field local to the spacecraft as well as its orientation (ESA, 2018).

The design selected is a fluxgate magnetometer, comprised of three pairs of coils with a magnetic core, each of which can measure magnetic field strength in one dimension. To measure magnetic field strength, an alternating current is first passed through one of the coils within each pair. This causes the magnetic core to oscillate between magnetized and unmagnetized, inducing a current in the second coil. Without an external magnetic field, the input and output current are equal. However, when an external magnetic field is present, the input and output currents differ, which is then measured and used to determine the magnitude of the external magnetic field.

To carry out these measurements, two individual tri-axial sensors will be located on a 2.5 m boom (to reduce the interference from inherent magnetic fields of the spacecraft itself),

approximately 80 cm apart. By comparing the measured fields in these two sensors, the gradient of the magnetic field will also be measured, providing a complete picture of the local magnetic field.

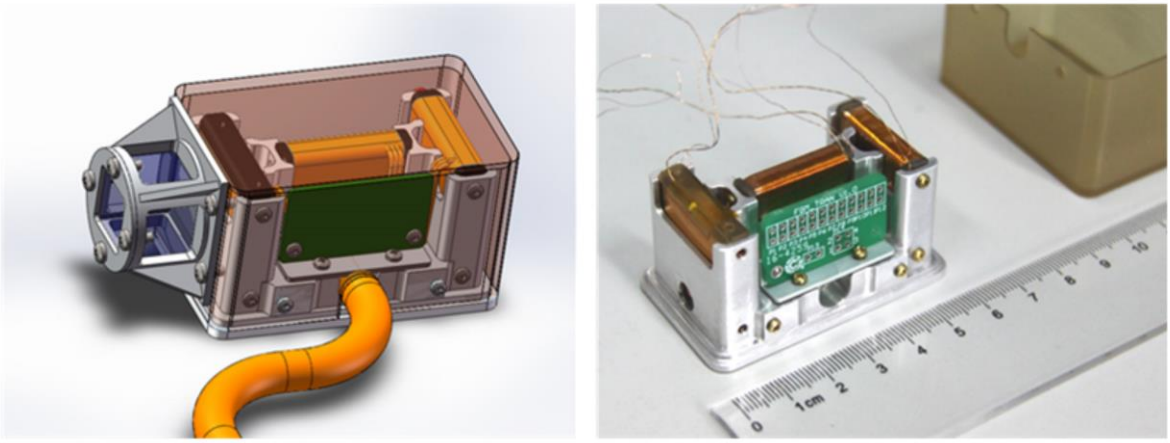

**Figure 2.7**: Left – 3D rendition of the tri-axis fluxgate magnetometer. Right – Usable engineering model (ESA, 2018).

### 2.3.4. Ultraviolet Imager (UVI)

The ultraviolet imager (UVI) is developed by the University of Calgary, with industrial contributions from Honeywell Aerospace and further contributions from both Belgium and Canada. The instrument will observe the Earth's northern aurora (Aurora Borealis) during both dayside and nightside, meaning that observations must be made in direct sunlight. As a result, state-of-the-art filters are currently being developed to obtain UV images while subject to a high level of optical background signal. Figure 2.8 shows the UVI instrument configuration, with a complementary metal-oxide-semiconductor (CMOS) as the detector of choice which will observe in the 155-175 nm waveband (ESA, 2018).

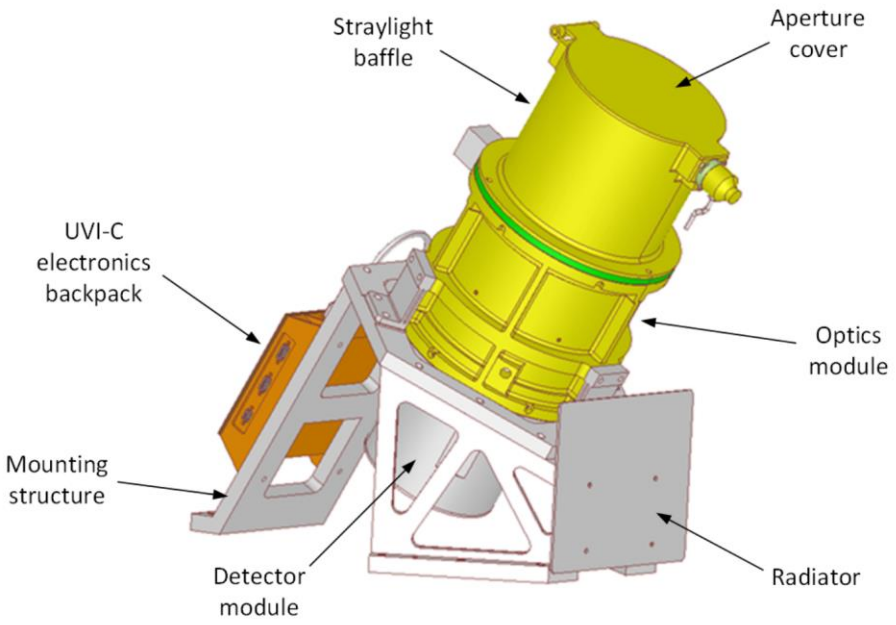


**Figure 2.8**: 3D model of the UVI (ESA, 2018), highlighting the key featured including the straylight baffle and detector and optics module.

### 2.3.5. Soft X-ray Imager (SXI)

The SXI, led by the University of Leicester, is currently under development with contributions from several other institutes in the UK, as well as Austria, Hungary, Spain, the Czech Republic, Norway, and China. SXI, as seen in Figure 2.9, has several different features which are paramount to facilitate the observation of soft X-rays efficiently. SXI will use silicon micropore optics (sMPO) to focus soft X-rays onto the focal plane of the instrument, while a large optical baffle will prevent stray optical light from adding to the background signal level within each image. The focal plane is comprised of two large Teledyne e2v (Te2v) charge coupled devices (CCDs), which are approximately 8 cm × 8 cm per sensor. During the observational period, the temperature of the CCDs will be carefully controlled with the thermal subsystem which utilises a large radiator as well as an active heating feedback loop. Thermal straps will assist in ensuring a strong thermal coupling between the detectors and the radiator. Key components of SXI will be described in the following subsections.

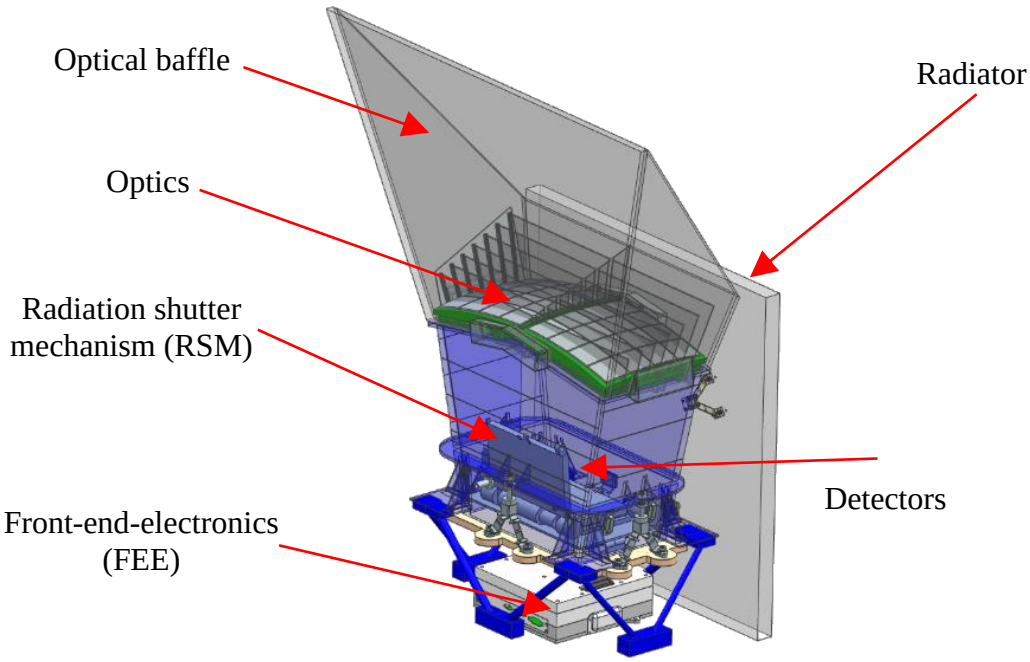


**Figure 2.9**: 3D model of the SXI design with key features highlighted.

#### 2.3.5.1. Optics

SXI will utilise the next generation of soft X-ray optics, which take inspiration from the eyes of lobsters (Bavdaz et al., 2010). Significant effort has been put into the development of this new type of optic, as it offers a wider field of view, while having a lower mass budget compared to that of previous X-ray optics (nested mirrors). The new optics are comprised of many small micropores with highly reflective interiors, allowing narrow-angle deflection of soft X-rays. The optics are often assembled on a slumped surface, such that the pores focus on the focal plane of the instrument. Figure 2.9 shows the sMPO integrated into the 3D model of SXI. For SXI, the entire optical system is comprised of 32 individual modules, in two 4x4 grids, with each grid measuring 4 cm × 4 cm.

Figure 2.10 (left) shows a scanning electron microscope image of a small collection of micropores. The opening of each pore dictates the active area of the optics, which is defined by the area available for photons to enter the entire optical system. Ideally the width of the walls (Figure 2.10 right, red arrow) between each micropore is minimal, to be able to maximise the active area, but manufacturing constraints place minimum limits on the wall widths. For the case of SMILE SXI, the dimensions of the micropores are 40 μm × 40 μm with a wall width

of 5 μm. To assist further in performance, the sMPO are covered with a thin film of aluminium (100 nm) to block optical and UV photons from entering.

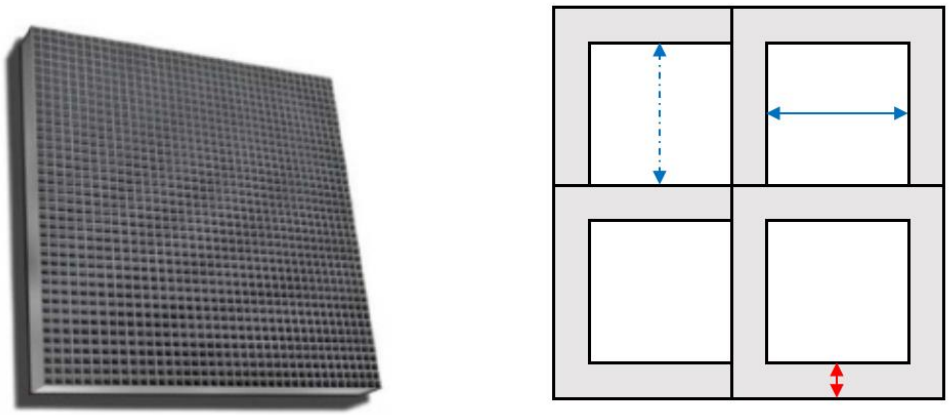

**Figure 2.10**: Left – Grid of individual micropores (Gailhanou et al., 2017). Right – Schematic outlining the pore width (blue arrows) and wall width (red arrow).

#### 2.3.5.2. Radiation shutter mechanism

During passage through the Van Allen radiation belts, and during extreme solar conditions, the radiation shutter mechanism (RSM) will close, protecting the CCDs from receiving a mission-ending dose of radiation. When closed, the instrument cannot observe the magnetosphere and collect science data, so this period is reserved for communications as well as calibration activities. After successfully passing through the Van Allen radiation belts or after the Sun returns to normal activity levels, the RSM can open, allowing science observations to continue.

#### 2.3.5.3. Detectors

Detectors for SMILE SXI (CCD370) have taken significant heritage from the Planetary Transits and Oscillations of stars (PLATO) mission detectors (CCD270, Endicott et al., 2012), to carry over much of the design and qualification work completed under the PLATO programme. This reduces risk, cost, and development time for SMILE. However, as the application is very different between the two missions, the SMILE CCD370 is adapted in several ways to improve soft X-ray detection performance. Additionally, the device is operated in a frame transfer readout mode, with 6:1 on-chip pixel binning. A more comprehensive description of basic CCD operation, along with a thorough description of the operating modes of the CCD370 is given in chapter 3.

Unfortunately, as of the writing of this thesis, CCD370s were not widely available to the consortium, therefore a CCD270 is shown in Figure 2.11, mounted on a vacuum-chamber flange. The area in blue represents the sensitive image area of the device and, in the case of a CCD370, will comprise 6/7$^{ths}$ of the total image area. The remaining 1/7$^{th}$ will be shielded (which is not shown in Figure 2.11), preventing photons from reaching the photo-sensitive silicon.

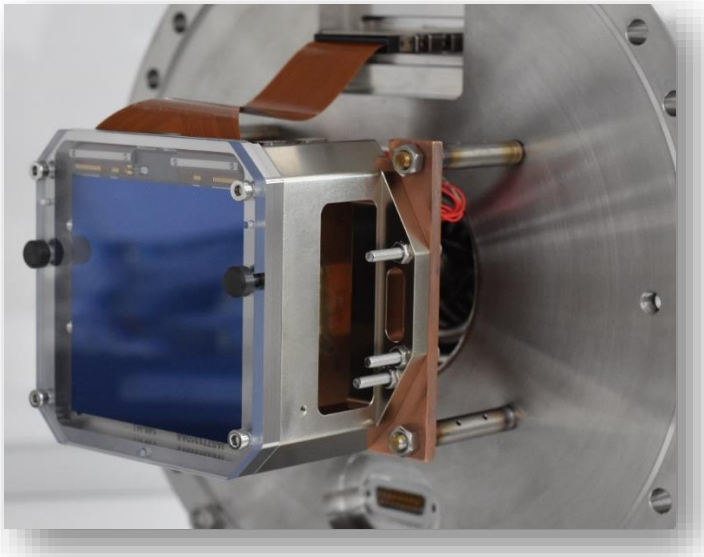

**Figure 2.11**: Image of a CCD270 mounted on a flange as part of a vacuum chamber.

## 2.4. Chapter summary

Space weather surrounding the Earth can have a wide range of potentially devastating effects on human activity. To better understand the triggers behind space weather, the ESA SMILE mission will investigate the Earth-Sun interaction, providing the most complete global understanding of the underlying triggers behind space weather events. A suite of four instruments have been chosen to answer the three broad science goals described in this chapter, including two imagers and two in-situ instruments. SXI will observe soft X-rays (0.2 keV – 2 keV) emitted via the SWCX process through interactions between distinct ions in the solar wind and neutrals in the Earth's exosphere, with most of the soft X-ray photon emission emanating from the dayside magnetopause and polar cusps. To facilitate efficient soft X-ray observations, SXI will utilise state-of-the-art sMPO which are comprised of many millions of

small pores containing highly reflective inner surfaces. To ensure optimal focusing on the detector focal plane, the sMPO are assembled on a slumped surface. The detectors of choice are two Te2v CCD370s which have significant heritage from another upcoming ESA mission (PLATO). Although there is significant heritage, the CCD370s have custom features specific for soft X-ray performance and hence optimised for SMILE SXI science performance. Before the custom features can be described however, the basic operation of a CCD must first be explained.

# 3. The Charge-Coupled Device

Charge-coupled devices (CCDs) were invented in 1969 by Willard S Boyle and George E Smith at Bell Telephone Laboratories (Janesick, 2001) and were initially pitched as a memory device, storing a finite amount of data. It was later discovered that the device could be operated in such a way that it could be used as an imaging device. In the subsequent decades after inception, the idea saw considerable development, with the technology now being widely used in industrial and scientific fields due to its high performance in comparison to other imaging technology. One such use is in the field of space imaging, which has seen many CCDs successfully flown (from many large space agencies), including missions such as XMM-Newton, The Hubble Space Telescope and GAIA (Crowley et al., 2016; Strüder et al., 2001; Windhorst et al., 2011).

This chapter presents an overview of the technology, including a brief description of the device architecture, followed by an explanation of the main stages of CCD operation; charge generation, collection, storage, transfer, and conversion. Once complete, a description of the CCDs specific (and related) to SMILE SXI will be given which have been used as part of the experimental campaigns contained within this thesis.

## 3.1. Device architecture

CCDs are semiconductor-based imaging devices which are used to efficiently observe soft X-ray or optical sources due to the characteristic band gap of silicon. The basic architecture of a three-phase CCD is shown in Figure 3.1. The device is split into two distinct regions, the photo-sensitive image region, where incident photons can efficiently generate electrons, and the orthogonal serial register, which facilitates charge transfer to a single location for charge conversion. The image area is segmented into distinct areas called pixels, using both physical implants within the device as well as applying voltages to distinct regions of each pixel. Pixels are defined in the horizontal direction by vertical implants in the silicon, named channel stops, which prevent charge from drifting in the horizontal direction. In the vertical direction, pixels are defined by the application of voltages to segments of each pixel. Voltages are applied to conductive gates on each pixel, with each pixel containing multiple gates. Figure 3.1 shows an example schematic of a 3-phase CCD, with each pixel defined by both the channel stops and three distinct phases (Iϕ1, Iϕ2 and Iϕ3).

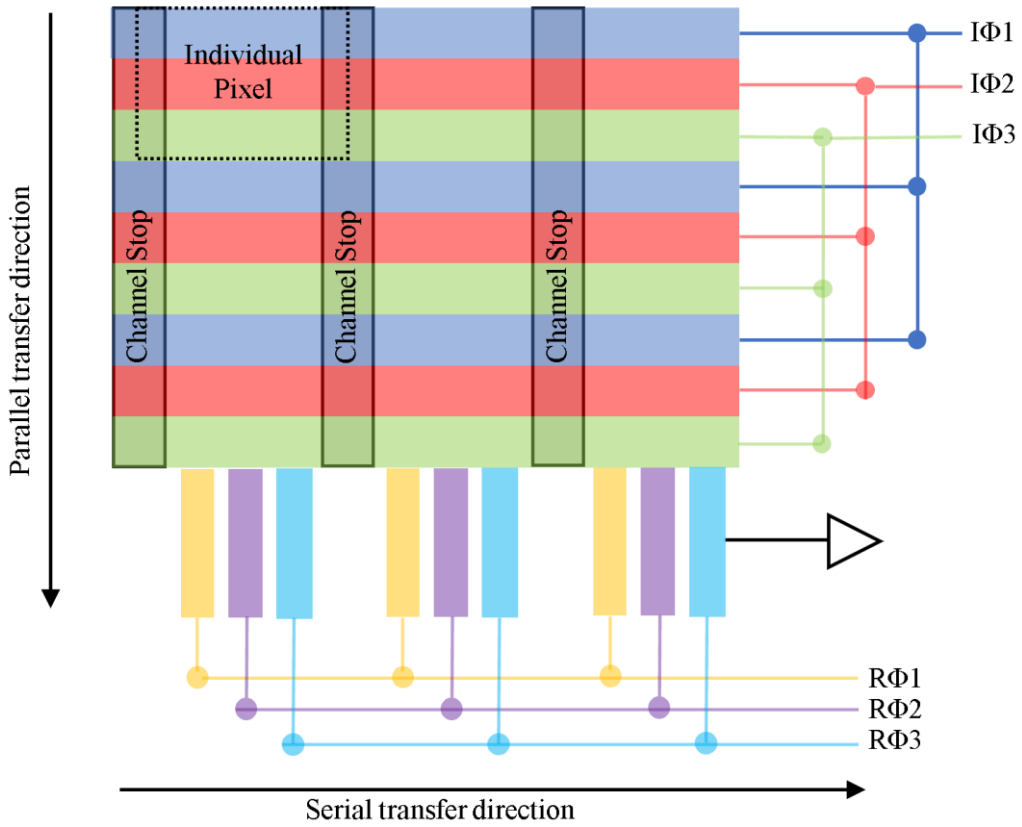


**Figure 3.1**: Schematic of a bird's eye view of a three-phase CCD. Nine individual pixels are shown, arranged in a 3x3 grid with the serial register at the bottom of the figure. CCDs are usually manufactured with many hundreds (and potentially thousands) of rows and columns.

Adjacent to the image area is the serial register, which has a similar architecture to the image area, allowing charge to be stored in distinct elements, with the movement of charge controlled by the application of periodic potentials. The only difference is the direction in which charge is moved. The example of Figure 3.1 has charge moving in the vertical direction within the image area, whereas charge moves in the horizontal direction when in the serial register.

## 3.2. Charge generation

Charge is generated within the pixels of a CCD by the interception of incident photons by the photo-sensitive silicon. The main mechanism (for optical and X-ray photons) through which incident photons are converted to electrons is the photoelectric effect (Einstein, 1905). For an electron to be liberated in the photo-sensitive silicon, the incident photon (carrying energy $E = E_{photon}$) must impart sufficient energy for an electron to successfully transition from the valence

to the conduction band within the silicon. The energy differential between the valence band and conduction band is known as the band gap and is relative to both the material and temperature of the material in question. For silicon, the band gap ($E_g$) is 1.12 eV at 298 K (Sze and Ng, 2006) corresponding to a photon of wavelength ~1100 nm.

If an incident photon has $E_{photon} < E_g$, then insufficient energy is imparted and the electron cannot transition from the valence to conduction band, and no free electrons are generated. The process is known as free carrier absorption (Schroder et al., 1978) and within the context of CCDs, the photon is not detected.

If the incident photon has $E_{photon} > E_g$, then a photoelectron (and associated hole) is generated, known as an electron-hole pair (e-h). The energy surplus ($E_{photon} - E_g$) imparted to the electron dictates the number of e-h pairs formed, with $E_{photon} < 3.1$ eV leading to a single e-h pair, and $E_{photon} > 3.1$ eV leading to multiple e-h pairs generated via subsequent impact ionisation (Janesick, 2001).

### 3.2.1. Quantum efficiency

The number of incident photons that interact within the sensitive silicon and are subsequently detected can be quantified through a metric known as quantum efficiency (QE). The ideal quantum efficiency is 100%, meaning that all incident photons generate at least one electron, and are therefore detected by the CCD. However, fundamental physical processes such as photon reflection and absorption in non-sensitive layers can drastically lower the quantum efficiency of CCDs. Throughout the development of CCDs, manufacturing processes have significantly improved, boosting the quantum efficiency significantly, shown by the two scenarios in Figure 3.2.

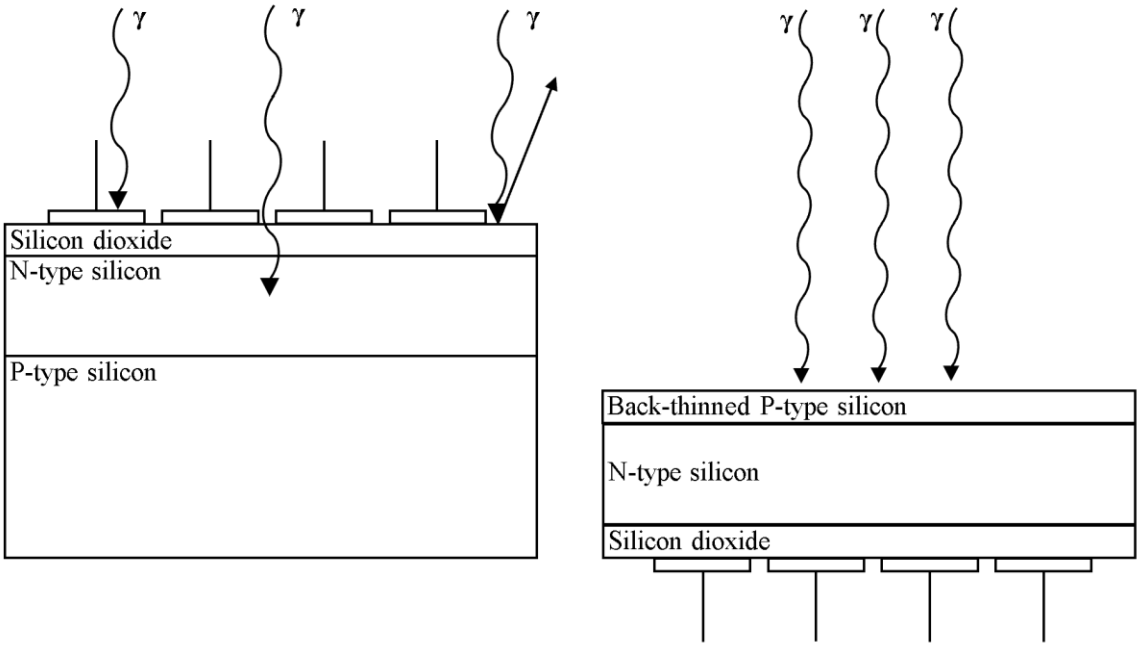


**Figure 3.2**: Left – Frontside illuminated CCD where photons must travel through the gate structure and silicon dioxide layer before reaching the photo-sensitive N-type silicon. Right – Backside illuminated CCD where the P-type substrate has been mechanically and chemically etched away to improve QE, as photons no longer need to travel through the gate structure and silicon dioxide.

Initially, CCDs were frontside illuminated, meaning that the electrode structure and dielectric layer was on the front of the device. As a result, a large proportion of incident photons were either absorbed by the non-photosensitive gate structure and dielectric before reaching the photo-sensitive silicon or were reflected from the silicon surface due to the high refractive index. To remedy the issue, the back illuminated CCD was developed, whereby the device was rotated 180 degrees and the p-type substrate was mechanically and chemically etched away to expose the n-type silicon (Holland et al., 2003, Figure 3.2 – right). Incident photons are no longer absorbed by the gate structure and dielectric, significantly boosting QE. Figure 3.3 shows the comparison of QE between a frontside and backside illuminated CCD, specifically for soft X-ray photons energies.

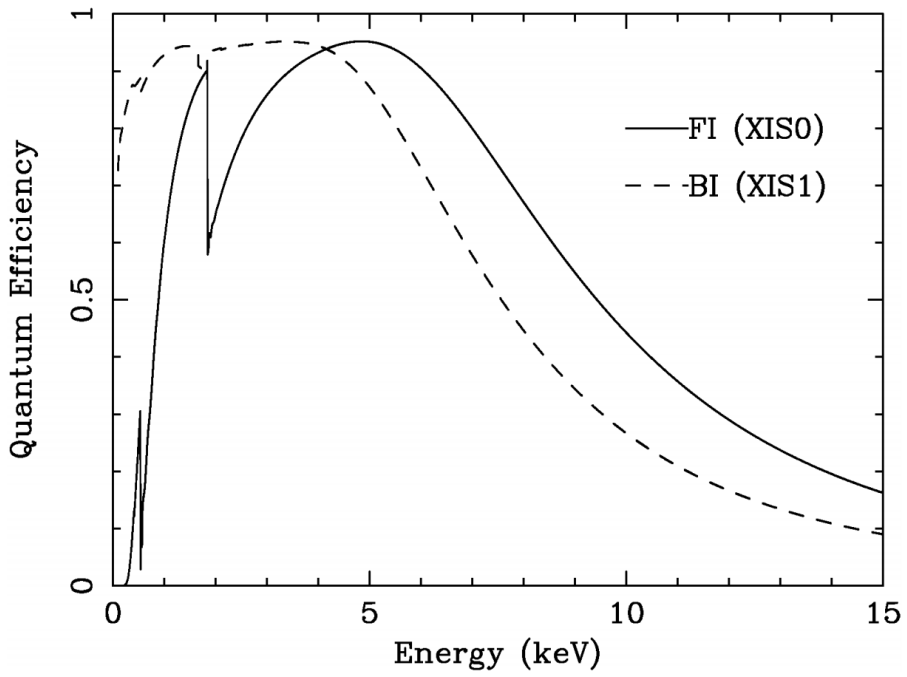


**Figure 3.3**: QE as a function of photon energy (focused on the soft X-ray range) for a frontside illuminated CCD and a backside illuminated CCD (Koyama et al., 2007).

## 3.3. Charge collection and storage

Once photoelectrons are generated, they must be effectively and efficiently collected by each pixel to preserve the generated charge packets. The architecture of each pixel is seen in Figure 3.2, with the n and p-type silicon forming a p-n junction. When the p-n junction is formed, majority charge carriers from each layer (electrons from the n-type and holes from the p-type) diffuse across the interface between the two layers. After some time, an equilibrium state is reached whereby some region of fixed charge space is created, termed the "depletion region". This region is devoid of free charge carriers and any electrons generated in this region will have been generated via incident photons. The depletion region can be extended via a process known as reverse biasing, whereby a positive potential is applied to the n-type silicon (via the conductive gate).

When charge is generated, photoelectrons are accelerated towards the area of highest potential which, in the case of the surface channel CCD, is the silicon silicon-dioxide interface. At this interface a high density of charge traps is located (due to a lattice mismatch between the two layers) which can trap signal electrons, contributing heavily to charge transfer inefficiency. To

remedy this, the potential profile can be altered through the creation of a volume known as a "buried channel" by ion implantation. In the case of N-channel CCDs, the dopant is phosphorous. The buried channel moves the point of highest potential away from the surface. Photogenerated electrons will be held far enough from the silicon silicon-dioxide that they will not interact, avoiding charge trapping and the generation of additional dark current. The potential profiles of both the surface channel and buried channel variant are shown in Figure 3.4.

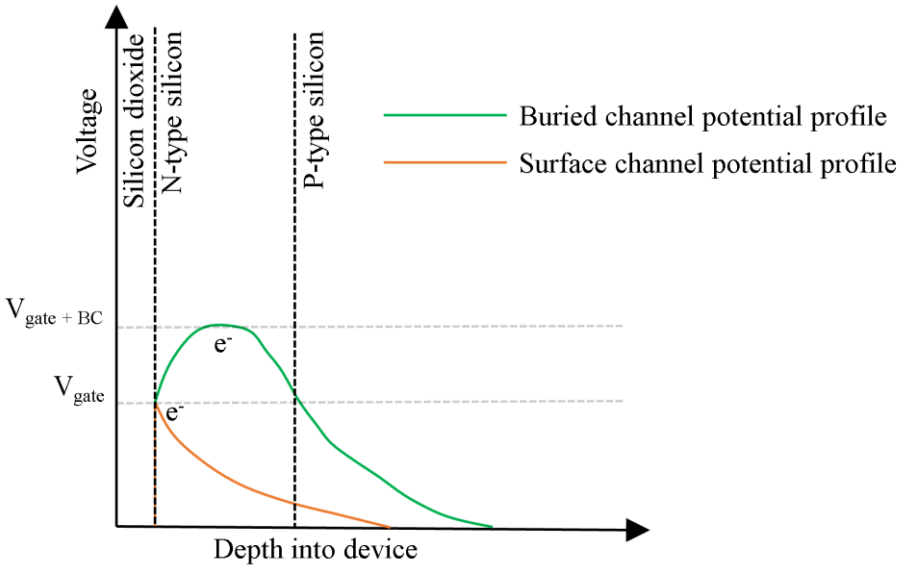


**Figure 3.4**: Potential profiles of both a surface channel CCD (orange) and a buried channel CCD (green). The peak of the potential well is shifted deeper (hence "buried") into the device, moving the charge storage location away from a high density of traps. The peak potential profile is given by the gate voltage ($V_{gate}$) in the case of surface channel CCDs, and the peak potential of the gate and buried channel is shown by $V_{gate+BC}$.

Not only does the buried channel alter the shape of the potential well, improving charge collection efficiency, it also acts as the prime charge storage volume within the device. Although the buried channel provides an efficient location for charge storage, further optimisations are possible via a process known as the supplementary buried channel.

### 3.3.1. Supplementary buried channel

For a significant number of CCD applications, the full well capacity of the device is often significantly larger than the target charge packet size. Hence for small charge packet sizes, storing the charge packet within as small a volume of silicon as possible is ideal, mainly for optimal charge transfer performance. The supplementary buried channel (SBC, also often called a "notch" channel CCD) was developed as a result, once again manipulating potential well profiles to optimise performance. The SBC is created via additional doping within the buried channel. The additional doping creates a deeper potential well, such that small electron packets are confined to a smaller volume of silicon, mitigating the effects of radiation damage within the bulk silicon. SBCs can store charge packets of ~$10^4$ electrons in size and are now commonly used in scientific CCDs, although their use is highly dependent upon the application of the CCD with regards to charge packet size. Large space missions such as XMM-Newton and GAIA have successfully used SBCs to improve the radiation hardness of CCDs (Lumb, 2004; Seabroke et al., 2013).

## 3.4. Charge transfer

Once charge has been successfully generated and collected efficiently within a pixel, the charge packet must now be moved to the output node for charge conversion. Like the charge collection stage, charge transfer is achieved via the use of potential wells generated within each pixel and electrode. Charge packets are first transferred in the parallel direction (direction explicitly shown in Figure 3.1) until reaching the serial register, where they are then transferred in the orthogonal direction towards the output node for charge to voltage conversion.

Efficient charge transfer is achieved via sequential applications of voltages to all bus lines, moving all charge packets within the image area of the device in parallel. Figure 3.5 shows an example scheme that shifts a single charge packet from one pixel to the next, for the case of a four-phase CCD.

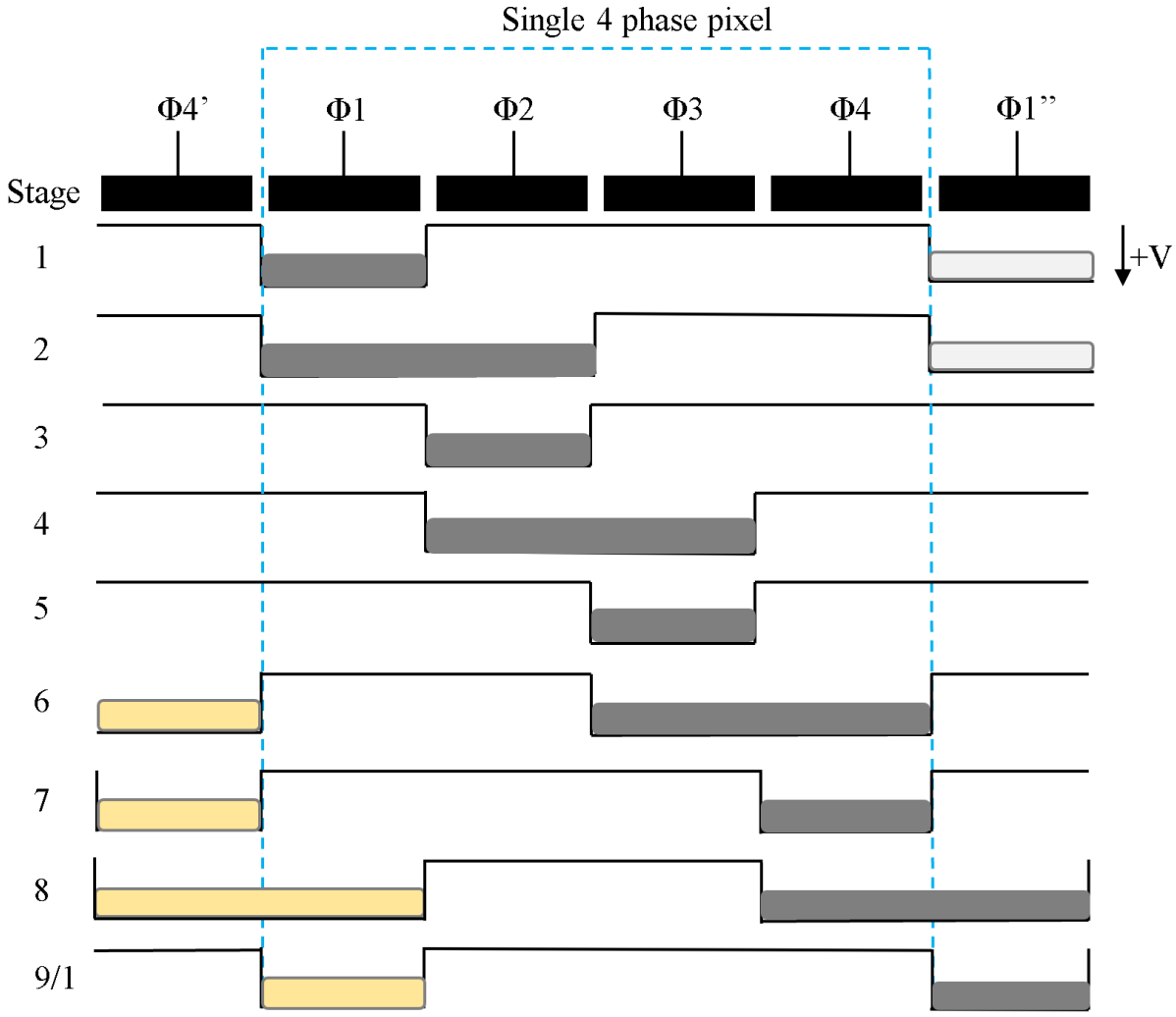


**Figure 3.5**: Charge transfer schematic for a single pixel to pixel charge packet transfer. The potential profile is shown for each stage of the transfer process, with the positive voltage shown by the lower position on the y-axis to highlight the potential wells clearly.

**Stage one:** Charge collection occurs as per the section above, in this case the charge is collected under ϕ1, with the ϕ1 voltage set to high.

**Stage two:** While ϕ1 is still high, ϕ2 is now also switched high, with the potential well (and hence charge packet) spread over two phases. For clarity, the adjacent charge packet is also shown (moving identically) in the adjacent pixel (ϕ1).

**Stage three:** ϕ1 is now switched low, with the charge packet under ϕ1 attracted to the potential well under ϕ2. Charge has now been successfully transferred from ϕ1 to ϕ2.

**Stage four to eight:** The process of stage two to three is repeated with electrodes alternating between one and two electrodes held high, facilitating the movement of charge from one electrode to the next.

Measuring charge transfer performance is key for both manufacturers and downstream users, as charge transfer performance often determines the end point of a device's useful lifetime. Charge transfer efficiency (CTE) provides a measure of how much charge is conserved when a charge packet is moved from electrode to electrode during the readout process. Commonly, CTE and charge transfer inefficiency (CTI) are linked via the equation (Janesick, 2001):

$$CTI = 1 - CTE \qquad \text{Eq 3.1}$$

For modern, scientific CCDs, CTE values are excellent, with values of 0.999999 (or better) reported. For example, a CTE of 0.999999 means that a charge packet of 10,000 electrons will only lose (on average) 20 electrons when transferred across 2000 pixels.

### 3.4.1. Tri-level clocking

The example of charge transfer in Figure 3.5 uses two electrode voltage levels (on or off) and can be described as a bi-level clocking scheme. A third, intermediate, voltage level can also be introduced, known as a tri-level clocking scheme. Previous work (Murray et al., 2013b) has shown that a tri-level clocking scheme can improve CTI when compared to that of a bi-level clocking scheme. Section 8.4 will describe the process of tri-level clocking in more detail.

## 3.5. Charge conversion and digitisation

Once charge has been transferred through the image area, into the serial register and finally to the output node, the signal packet must be converted to a digital signal in order to construct an image. Charge is converted to voltage via use of a voltage amplifier, often outputting values of the order ~µV per electron. The CCD output circuit can be optimised in many ways to reduce noise, however that is beyond the scope of this thesis, so a qualitative description is included

here only for completeness. Many excellent descriptions of the intricacies of CCD charge conversion and digitisation are available in the literature.

## 3.6. Charge-coupled devices for SMILE SXI

Now that CCD operation has been described, the specific devices used as part of the SMILE SXI instrument and testing/characterisation process can be described fully. Although SMILE SXI will utilise two CCD370s, the demanding launch deadline means that different devices will be used for most of the testing and characterisation process, as the CCD370s were not manufactured or delivered as of the writing of this thesis.

SMILE SXI devices have significant heritage from the ESA PLATO mission, drastically reducing the time needed for device development and manufacturing, while also ensuring a high technology readiness level (a measure of a technologies maturity). In terms of the SMILE device characterisation process, PLATO devices were a clear choice to be used as part of the radiation testing before SMILE SXI devices were available. Table 3.1 shows a summary of the devices available for testing as part of the irradiation campaign as well as the flight devices.

Table 3.1: Summary of devices used in the SMILE SXI instrument as well as pre-launch testing activities.

| **Device** | **Mission** | **Baseline readout mode** | **Note** |
|---|---|---|---|
| CCD280 | PLATO | Full frame | Small PLATO device. Used for two device irradiations. |
| CCD270 | PLATO | Full frame | Large PLATO device. Not used for any device irradiations. Used as part of the micrometeoroid experimental campaign. |
| CCD380 | SMILE | Full frame | Small SMILE device, one cryogenic irradiation planned |
| CCD370 | SMILE | Frame transfer | Large SMILE flight device, one cryogenic irradiation planned. |

The CCD280/270 pairing and CCD380/370 pairing are identical apart from the number of pixels within each device, leading to significantly different device size (as shown in Figure 3.6). The main reason for this unusual device manufacturing is due to the large size of the CCD270/370. Each device is processed and cut from a high-purity silicon wafer, ideally with as little waste as possible. The size of CCD270/370 means that only one device can be manufactured from a single wafer, with the remainder of the wafer designated for an identical (but only smaller) CCD280/380 for testing purposes and wafer verification/validation.

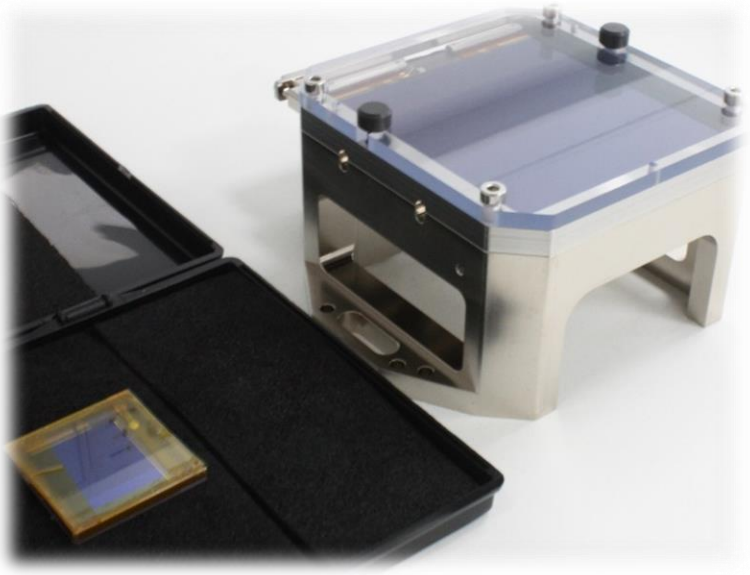

**Figure 3.6**: Side by side comparison of the CCD280 (left) and the CCD270 (right). Each device is protected via a perspex cover over the image and store area which is removed for testing. The CCD270/370 also comes fitted with a handling jig shown, for ease-of-use handling and mounting to thermal benches in test cameras.

### 3.6.1. Differences between the CCD370/380 and the CCD270/280

Although SMILE devices adopt almost all their design from PLATO heritage, key changes were made to the devices that improved both the radiation hardness and signal to noise ratio for small charge packets. The three key changes were: the addition of a supplementary buried channel, a narrower serial channel, and a modified output amplifier (improved purely for SMILE SXI detectors).

### 3.6.2. The CCD370

The CCD370 is a large, back-illuminated CCD comprised of 4510 × 4510 18 µm pitch pixels (a summary of device parameters is shown in Table 3.2). The baseline operating mode of the device is a frame-transfer mode combined with 6×6 on-chip binning. The choice of readout mode was specifically chosen to boost performance. The benefit of 6×6 binning is twofold. Firstly, soft X-rays within the science observation band mainly interact at the field-free back surface. At this location, the generated charge cloud is free to diffuse through the silicon and can often move laterally within the CCD. If this occurs then signal that was generated in a single pixel can be collected in a neighbouring pixel, leading to split X-ray events over multiple pixels. 6×6 binning recombines much of this diffused charge back into a single pixel.

The second reason for 6×6 binning is to mitigate the effect of charge smearing from CTI. Over time, accumulated radiation damage within the silicon will cause defects to capture and emit signal electrons, smearing the lost signal over many rows. Although 6×6 binning cannot completely mitigate the effect of charge smearing, it can significantly help in recombining lost charge back to the original charge packet.

Due to the large numbers of pixels in the CCD370 (and hence potentially long readout times), operation with a frame-transfer mode allows readout of a single frame to occur, while collecting photons for the subsequent frame simultaneously. Although this does help readout times, the frame-transfer mode does come with limitations with charge transfer times between the image and store section. The ratio of the time between transfer from the image to store section and integration time should be maintained at a value of greater than 10:1, to minimise the number of so-called “out of time” events. These events are photoelectrons that have been collected during the image to store charge shift and are thus out of position in relation to their true interaction location within the detector. Maintaining at least a ratio of 10:1 transfer time to integration time helps to mitigate the number of out of time events (Kendziorra et al., 1999).

As a result of both 6×6 on-chip binning and frame-transfer mode, the sensitive area of the device is asymmetrically split between an image and store region, with the image region containing approximately 6/7 of the total rows, and the store region containing the remaining rows. The store section is also covered by a titanium shield (which is attached to the focal

plane), preventing incident photons from interacting within the store section of the device. Figure 3.7 shows a schematic of the layout of a CCD370.

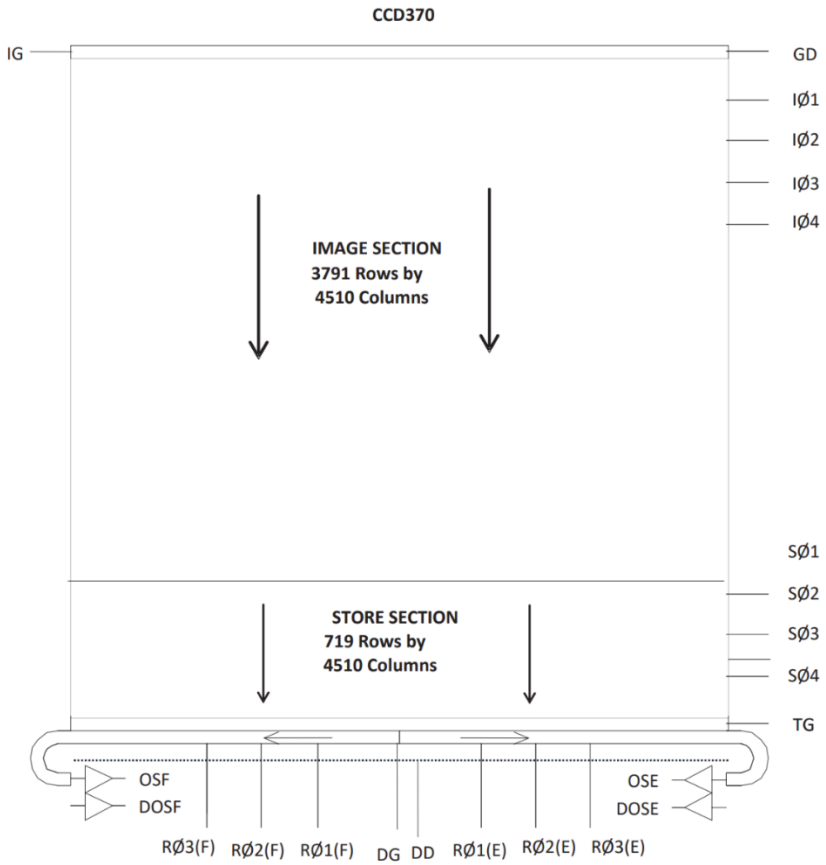


**Figure 3.7**: CCD370 design schematic showing the image and store section areas along with the image and store clocks.

Charge injection has also been baselined for the CCD370s, although the number of injected charge lines are not confirmed. Adding extra charge into the device reduces the CTI of the CCD by filling defects (mainly radiation-induced) with superfluous charge. If the defects are filled, then they cannot capture charge from key science signal packets and thus CTI is reduced. Injecting charge more frequently does reduce CTI further, as defects are filled more often after emptying. However, diminishing returns are reached at some point, as injecting high amounts of signal into multiple rows effectively reduces the image area of the device, which is only exacerbated by also using 6×6 binning. The balance between reducing CTI and minimising the amount of image area lost must be found, and realistically only laboratory testing can achieve this.

Table 3.2: Summary of the CCD370 design parameters

| Property | Units | Value |
|---|---|---|
| Silicon thickness | μm | 16 |
| Pixel size | μm × μm | 18 × 18 |
| Image area size | pixels | 4510 columns × 3791 rows |
| Image area size | mm × mm | 81.18 × 68.24 |
| Store area size | pixels | 4510 columns × 719 rows |
| Store area size | mm × mm | 81.18 × 12.94 |
| Output nodes | - | 2 |
| Serial registers | - | 1 |

## 3.7. CCD requirements

Combining the X-ray lines of interest for SXI (chapter 2), along with an orbital duration of 3 years in a radiation-harsh environment, and thermal constraints on the instrument, a strict set of requirements are placed on SXI. SXI must be able to observe charge packets between ~55$e^-$ (200 eV X-rays) and ~550$e^-$ (2000 eV X-rays) at a temperature of 153K (while considering orbital variations in temperature, see section 7.3.4). Due to the degradation of CTI throughout the 3-year mission due to radiation damage, resolving X-rays at the lowest end of the science band (200 eV) will be the limiting factor, as the loss of electrons due to CTI will affect charge packets with the smallest charge packets most severely. During development, SXI was developed with these issues in mind, most notably the use of 6×6 on-chip binning, frame-transfer mode (section 3.6) and charge-injection, along with the inclusion of a SBC (section 3.3.1) for improved radiation hardness and hence X-ray resolution, particularly at end-of-life. Although these features will help the performance of SXI significantly, the instrument requirements are still challenging, and experimental testing and associated modelling can still most likely yield good performance returns for the instrument.

## 3.8. Chapter summary

The basic operation of the CCD has been described, including the process of charge generation, collection, storage, transfer, and digitisation. A description of CCDs used as part of the SMILE SXI instrument was then given, including a description of the CCD370 readout scheme. Modifications made to the CCD370/380, from the PLATO detector predecessors were also described, including the underlying reasons for including a SBC, narrow serial channel, and improved output amplifier.

Although the modifications mentioned above do improve radiation hardness, radiation damage throughout the SMILE mission will still be a significant problem and will ultimately place a time-limit on the ability for SXI to resolve the lowest energy X-ray photons. To optimise the detectors for SXI, and either extend the duration of the mission or improve the instrument's performance during operations, the nature of the radiation damage in CCDs caused primarily by high energy particles in the space environment will be described in more detail in chapter 4.

# 4. The effects of the space radiation and hyper-velocity particulate environment on charge coupled devices

The previous chapter described the operation of CCDs, from basic architecture to the process of charge generation, storage, transfer, and charge digitisation. In this chapter the effect of the space environment on the performance of CCDs will be described for two distinct sources: displacement damage induced in the silicon lattice at the atomic scale, and then hyper-velocity particulate impacts creating defects at the macroscopic scale. Both sources of damage have the potential to severely degrade detector performance throughout a detectors lifetime and are extremely important for the SMILE SXI's planned operations.

Firstly, the radiation environment of particular interest to this thesis will be described, focusing on the radiation environment surrounding the Earth. Following that, the underlying mechanisms which create sources of radiation damage in silicon CCDs themselves will be described, namely ionisation and displacement damage. Relevant theories which characterise displacement damage will also be described.

Discussion will then turn to the role of micrometeoroids in space, led by a literature review of the previous X-ray astronomy missions that have suffered damage most likely due to sporadic micrometeoroid impacts. Following that, a short review of the particulate impact studies on silicon detectors, showing the edge of current knowledge and the next steps that are needed. Finally, a description of micrometeoroid flux models will follow, that will be used in the subsequent work in this thesis.

## 4.1. Radiation damage in CCDs

The radiation environment in space is comprised of a zoo of highly energetic particles and events, including protons, electrons, and neutrons as well as highly ionising galactic cosmic rays (GCRs). All the aforementioned can cause significant damage to electrical components, reducing performance over time and eventually rendering the component useless. Certain components, including detectors, can be designed to be more "radiation hard", meaning that they can withstand a higher dose of radiation while maintaining performance. Maintaining performance throughout a detectors' lifetime is possible through a variety of techniques, however information regarding the specific radiation environment is key and will vary based

on the location of the space telescope. Due to the orbit of SMILE, focus of discussion here will be placed upon the radiation environment in the close vicinity of the Earth.

### 4.1.1. Near-Earth space environment

The radiation environment throughout space varies significantly, but the fundamental radiation sources are mainly due to GCRs, protons and electrons. Localised areas around planets with magnetic fields can lead to geomagnetically trapped radiation in the form of protons and electrons. In the case of the Earth these localised areas are named the Van Allen radiation belts, named after James Van-Allen's discovery in 1958 (Van Allen, 1959). In total there are three belts, the inner and outer belt which are toroidal in shape, as seen in Figure 4.1, and a third transient belt which was only discovered recently (Ginet et al., 2013). The current shape of the transient belt is not known.

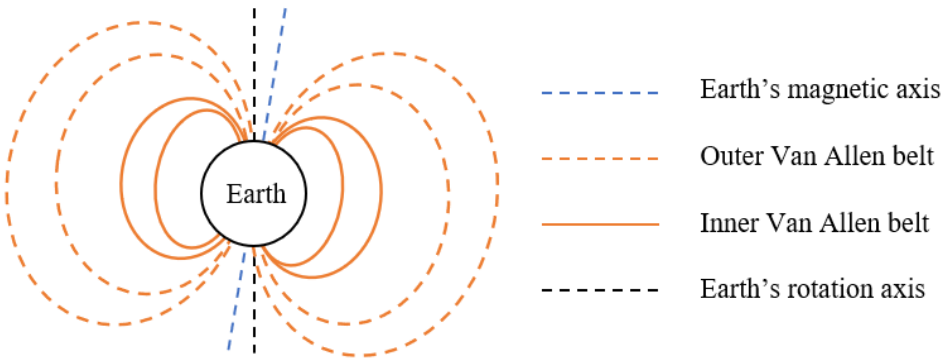


**Figure 4.1**: Schematic of the Earth and associated Van Allen belts. The magnetic axis is offset with respect to the rotation axis (through the centre of the Earth), leading to the inner Van Allen belt extending further towards the surface of the Earth, creating a region known as the South Atlantic Anomaly (SAA).

#### 4.1.1.1. Outer Van-Allen belt

The outer Van Allen belt is dominated by electrons, albeit of a lower energy compared to the inner belt, with energies ranging from 0.1 – 10 MeV (Ginet et al., 2013). The outer belt is significantly wider than the inner belt, starting at approximately 3 Earth radii above the surface of the Earth and extending to approximately 10 Earth radii. As well as being radially larger, the outer belt is also less stable than the inner belt due to the closer proximity to the Sun. This means that solar events cause variations in both the size and composition of the outer belt.

Furthermore, it was recently discovered that a third, transient radiation belt was present and is caused due to large geomagnetic storms (Shprits et al., 2013). After a large coronal mass ejection (CME), the outer belt can potentially split, forming a small pocket which can store charged particles for up to one month.

#### 4.1.1.2. Inner Van-Allen belt

The inner belt, at an altitude of 0.2 to 2 Earth radii (Gusev et al., 2003), contains both protons and electrons. Electrons within the inner belt have energies of approximately 100s of keV and the trapped protons have energies potentially exceeding 100 MeV (Anderson et al., 2018). Due to the magnetic axis being offset with respect to the rotational axis of the Earth, this means that the distance from the closest edge of the inner belt to the Earth is not constant. This leads to a region where the inner belt is ~200 km from the Earth's surface, named the South American Anomaly (SAA) (Figure 4.2).

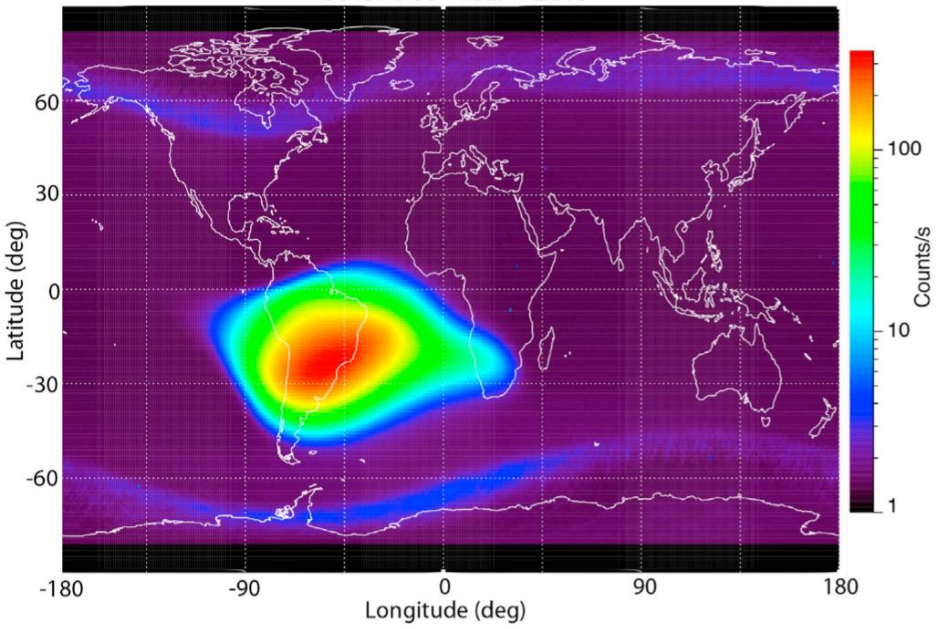


**Figure 4.2**: Map of the Earth with an overlaid colour plot showing the excess electron counts detected at a height of 800 km (Anderson et al., 2018).

#### 4.1.1.3. Solar wind particle flux

Although the near-Earth space radiation environment contains localised, trapped areas of charged particles, a stream of charged particles originating from the Sun, also significantly contributes to the local radiation environment. The solar particle flux is comprised of mainly

protons, electrons, and alpha particles (energies up to 10 keV), with bursts of particle flux superimposed over a steady solar wind background. Transient solar particle flux events are called solar flares and Coronal Mass Ejections (CMEs), and are dominated by highly energetic electrons. The total fluence of these transient events is high relative to the background solar wind flux, and the potential dose accumulated as a result presents a high risk to spacecraft.

The solar wind flux varies over time and is closely tied to the Sun's eleven-year solar cycle, where activity varies between a maximum and minimum. A commonly accepted measure of solar activity is the counting of sunspots over a long period of time (Hathaway, 2015), with Figure 4.3 showing the observed sunspot count over the last 12 years.

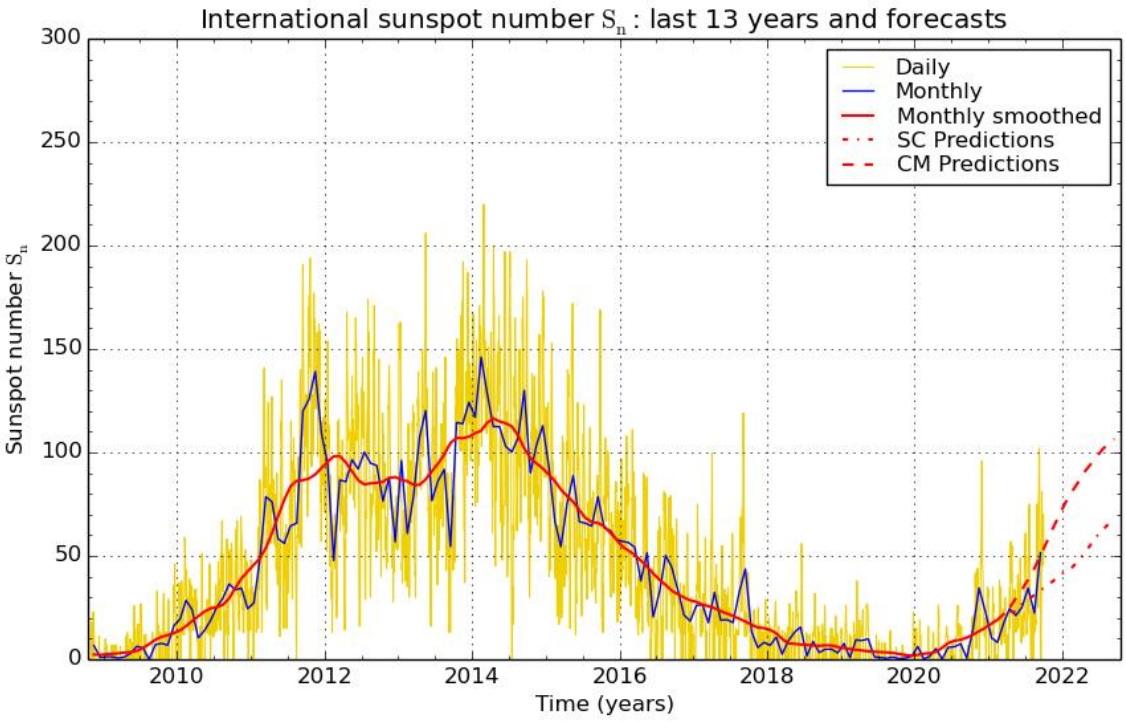


**Figure 4.3**: Number of sunspots seen over the past 12 years, including daily numbers and monthly smoothed values ("SILSO | World Data Center for the production, preservation and dissemination of the international sunspot number," n.d.).

During periods of maximum solar activity, the number of solar flares is also observed to increase, which can also increase the interplanetary proton flux. As a result, the launch date of spacecraft must be carefully chosen to avoid periods of solar maximum, or design changes

must be implemented to mitigate the increased dose that will inevitably be accumulated in-orbit around the Earth.

For the case of the SMILE spacecraft and its highly eccentric orbit, the dominant source of radiation damage will be from protons (both trapped and solar). Although protons will be the dominant source of damage, understanding the exact mechanisms through which these particles interact within the CCDs of SXI is key, and will be described in the following section.

### 4.1.2. Radiation damage mechanisms in CCDs

When an energetic particle interacts with a CCD, energy can be deposited into the device through several processes. Some of these processes are more transient in nature and do not cause permanent damage in a device, and some can cause damage which can hinder the performance of the CCD for the remainder of its lifetime. Radiation damage can be split into two main streams, that of ionising and non-ionising (displacement) damage. The following section will outline the fundamental mechanisms which govern the behaviour of both ionising and non-ionising damage in the context of CCDs. Emphasis will be placed on the role of non-ionising damage as this is fundamental to the later chapters of this thesis. Figure 4.4 provides an overall summary of the effect of both ionising and non-ionising damage and will be described in more detail in the following sections.

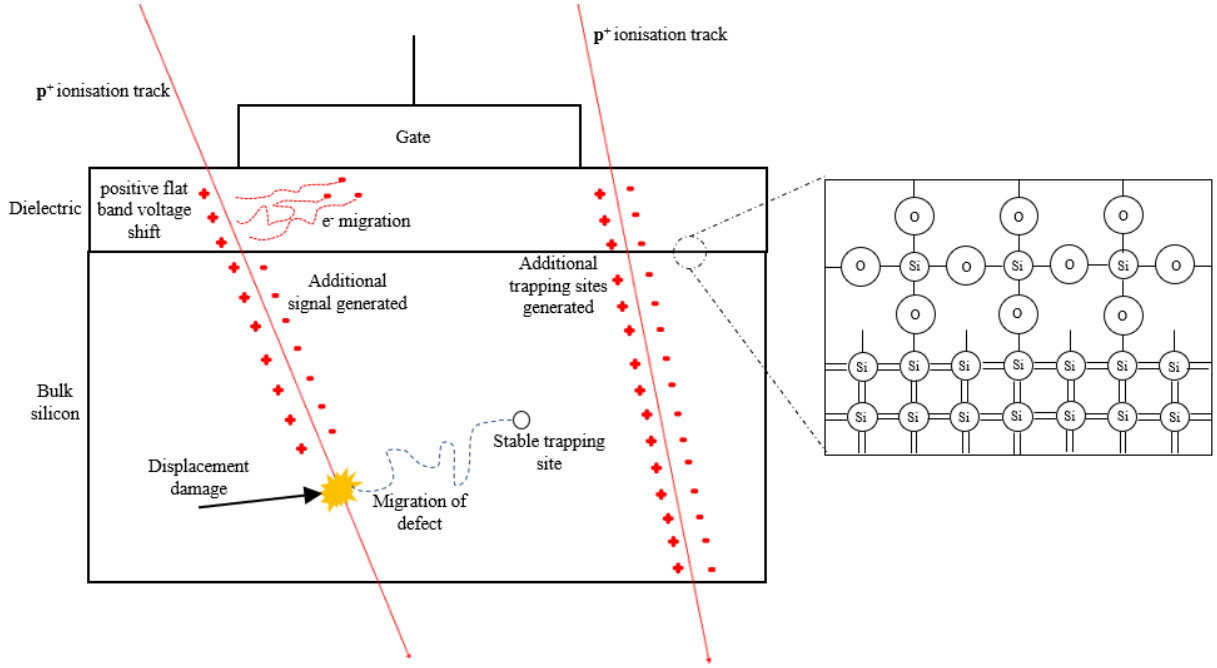


**Figure 4.4**: Summary of the effects of both ionising and displacement damage in CCDs (adapted from the previous works of: Bush, Nathan L., 2018; J. R. Srour et al., 2003). Note that the thickness of the dielectric and conductive gates is not to scale.

#### 4.1.2.1. Ionisation damage

When a proton travels through a CCD, energy is deposited via ionisation, leading to the generation of many electron-hole pairs along its particle track, as seen in Figure 4.4. Depending on the location of the liberated electron-hole pairs, this can lead to permanent effects within the oxide and oxide-silicon interface or transient effects within the silicon.

When electron-hole pairs are generated in the silicon dioxide, electrons move towards the positively charged gate due to both coulombic attraction and increased electron mobility (compared to that of holes in the dielectric, Hopkinson et al., 1996). Over time, the migration of electrons away from charge generation sites, and hence the accumulation of regions of positive charge, causes a flat-band voltage shift. The voltage shift means that a lower voltage is required to achieve the same electric field and hence the same CCD performance. Furthermore, the holes also left at the charge generation sites can form stable trapping sites in both the silicon dioxide and at the interface between the silicon and silicon dioxide (Hopkinson et al., 1996).

When electrons are generated via ionisation within the photosensitive silicon, the electrons either drift through the silicon or are accelerated towards potential wells. Once collected and stored within the potential well, the electrons generated via ionisation are indistinguishable from photoelectrons. The excess charge is then moved during readout, and no detrimental long-term effects are seen.

#### 4.1.2.2. Displacement damage

Displacement damage relies upon the displacement of silicon atoms within the photosensitive silicon of the detector. Once a silicon atom is knocked out of the periodic lattice structure it is known as an "interstitial", not occupying its usual location in the regular crystal lattice structure. After displacement, the silicon atom also leaves behind a vacancy in the silicon crystal lattice. Together, the interstitial silicon atom and vacancy are known as a Frenkel pair. These defects are inherently unstable and therefore can move through the silicon lattice. Fortunately for the performance of CCDs, most Frenkel pairs recombine shortly after creation and do not permanently affect detector performance. However, a small number of Frenkel pairs do not recombine, with the vacancy coupling with either another vacancy, impurity, or dopant atom. This coupling can lead to subsequent stable defects which in turn creates additional energy levels between the valence and conduction bands (J. R. Srour et al., 2003). It is these intermediate energy levels that can act as charge trapping sites and affect the performance of CCDs.

Many stable defects exist within silicon CCDs, arising from impurities introduced during the manufacturing process as well as dopants which are necessary for the performance of the device (such as the introduction of phosphorous for the buried channel within N-channel devices). Historically, Deep Level Transient Spectroscopy (DLTS) has been used to measure both the energy level and cross section of defects, albeit often with large errors (J. R. Srour et al., 2003). Newer techniques, such as the use of "trap pumping" in CCD technology, has allowed defects pertinent to CCD performance to be characterised to much higher degrees of accuracy (Bush, Nathan L., 2018; Hall et al., 2014; Janesick, 2001; Murray et al., 2013a, 2012; Wood, Daniel, 2018). For N-channel CCD performance (as is the focus of this thesis), there are four defects of interest, namely the silicon divacancy, phosphorus vacancy, oxygen vacancy and unknown defect.

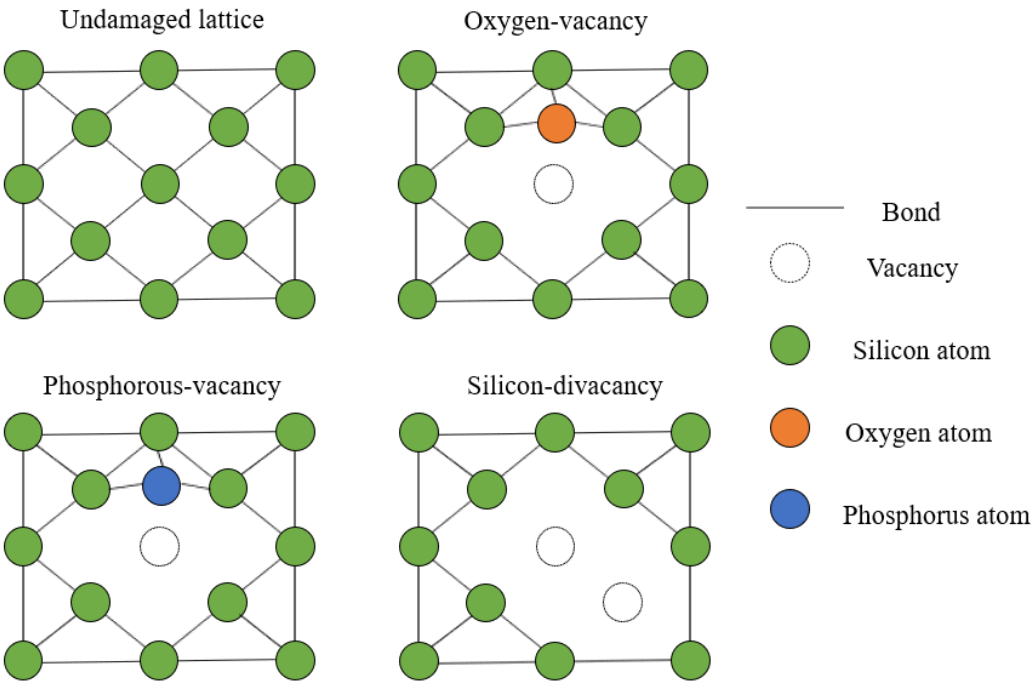


**Figure 4.5**: Lattice configurations of an undamaged silicon lattice (top left), the phosphorous-vacancy (bottom left), silicon-divacancy (bottom right) and the oxygen-vacancy (top right). Note that these are 2D representations of atom locations, and the positions of silicon atoms in 3D are in the face-centred-cubic configuration.

The phosphorous-vacancy (often also called the E-centre, Si-E or PV) is formed from a phosphorous atom coupling with a silicon vacancy to form a stable defect (Figure 4.5 – bottom left). Most recent studies place the energy level of the defect at 0.45 eV (Bush, Nathan L., 2018; Hall et al., 2014; Pichler, 2004) with an effective cross section of $5 \times 10^{-15}$ cm$^2$.

The silicon-divacancy (Figure 4.5 – bottom right) occurs when two silicon vacancies combine to form a single defect. Once formed the divacancy has four charge states (+1, 0, -1, -2), adding three energy levels to the band gap. Two of these energy levels are relevant to N-channel CCDs, namely the singly and doubly ionised acceptor state. Most up-to-date literature values place these traps at 0.345 eV (Bush, Nathan L., 2018; Hall et al., 2014; Pichler, 2004) and 0.225 eV (Bush, Nathan L., 2018; Hall et al., 2014; Pichler, 2004; Wood, Daniel, 2018) below the conduction band with effective cross sections of $5 \times 10^{-16}$ cm$^2$ and $5 \times 10^{-16}$ cm$^2$ respectively.

The oxygen vacancy is formed due to a coupling between a silicon vacancy and an oxygen atom (Figure 4.5 – top right), with the oxygen being introduced into the device during the

manufacturing process. Most recent energy studies place the defect at 0.16 eV below the conduction band (Bush, Nathan L., 2018; Hall et al., 2014; Pichler, 2004), although this defect is particularly difficult to probe with the trap pumping technique due to its shallow energy level and hence fast emission time.

The "unknown" defect was first discovered by Holland (1993) with an approximate energy level of 0.30 eV below the conduction band. More recent studies have placed the defect at 0.34 eV (Bush, Nathan L., 2018; Hall et al., 2014; Pichler, 2004) (with an effective cross section of $1 \times 10^{-14}$ $cm^2$), although the source of the defect is still unclear. Concentration of the defect seem to vary among N-channel CCDs, even between identical devices (devices from the same family, i.e. two CCD270s for example). The source of the defect has never been confirmed; however, the most likely candidates include the boron interstitial (0.37 eV) or the carbon ($C_iP_s$) complex in two different configurations, 0.32 eV and 0.38 eV respectively (Bush, Nathan L., 2018). Due to the varying concentration of the defect between devices, the carbon complex is more likely, as boron is present in all silicon CCDs.

The energy level and cross section of these defects are important; however, the key impact of these defects is their effect on CCD charge transfer performance which is ultimately dictated by Shockley Read Hall (SRH) theory.

#### 4.1.2.3. Shockley Read Hall Theory

Once intermediate energy levels between the valence and conduction band are introduced, then there is potential for these energy levels to negatively affect the charge transfer performance of CCDs significantly. The fundamental mechanism which governs the behaviour of electrons, holes and intermediate band-gap energy levels was described by Shockley, Read and Hall (SRH) in 1951/52 (Hall, 1952; Shockley and Read, 1952).

SRH theory neatly describes the behaviour of electrons and holes with respect to traps in silicon devices. The foundation of the theory is described by two exponential time constants, the capture time constant ($\tau_c$):

$$\tau_c = \frac{1}{\sigma_c n v_{th}} \qquad \text{Eq 4.1}$$

and the emission time constant ($\tau_e$):

$$\tau_e = \frac{1}{X\chi\sigma_e N_c v_{th}} e^{(\frac{E}{kT})} \quad \text{Eq 4.2}$$

where $\sigma_e$ and $\sigma_c$ are the emission and capture cross sections respectively, n is the electron concentration, $v_{th}$ is the thermal velocity of electrons (Eq 4.3), X is the entropy factor that is associated with the change in emission, $\chi$ is an additional factor to account for field enhanced emission, $N_c$ is the density of states in the conduction band (Eq 4.4), E is the energy level of the trap below the conduction band, T is temperature (in Kelvin) and k is Boltzmann's constant.

$$v_{th} = \sqrt{\frac{3kT}{m_c}} \quad \text{Eq 4.3}$$

$$N_c = 2(\frac{2\pi m_{dos} kT}{h^2})^{\frac{3}{2}} \quad \text{Eq 4.4}$$

Where $m_{dos}$ is the effective mass for the electron density of states, $m_c$ is the effective mass of the electron in the conduction band, and h is Planck's constant.

The emission and capture time constants mathematically describe the average time for a single defect to either emit a captured electron or capture a free electron. The process of capture and emission is not a deterministic process and is probabilistic in nature, following an exponential distribution. It follows that the probability density function for capture and emission is:

$$PDF_{c(t)} = \tau_c e^{(\frac{t}{-\tau_c})} \quad \text{Eq 4.5}$$

$$PDF_{e(t)} = \tau_e e^{(\frac{t}{-\tau_e})} \quad \text{Eq 4.6}$$

To calculate the probability that a trap captures or emits an electron, Eq 4.5 and Eq 4.6 can be integrated between times $t_1$ and $t_2$:

$$P_x = \tau_x \int_{t_1}^{t_2} e^{\frac{t}{\tau_x}} dt = e^{(\frac{t_1}{-\tau_x})} - e^{(\frac{t_2}{-\tau_x})} \quad \text{Eq 4.7}$$

where $\tau_x$ can be either the capture or emission time constant. In terms of CCD charge transfer performance (and optimisation), Eq 4.7 is powerful as it can be used to calculate the probability that a single defect can emit (or capture) charge during readout.

### 4.1.3. Temperature-dependent effects

Section 4.1 of this chapter has described the effects on CCDs due to both ionising and non-ionising radiation. Although temperature has not yet been mentioned, the effect of radiation damage on CCDs has some temperature dependence. More specifically, the temperature of the CCD *during* and *after* irradiation can have a subsequent effect on radiation-induced mechanisms in the device.

#### 4.1.3.1. Irradiation temperature

Historically, CCD irradiations for large-scale space mission have been carried out at room-temperature until the last ~5 years. Recent developments within the measurement of defects in irradiated CCDs (Bush, Nathan L., 2018; Hall et al., 2014; Janesick, 2001; Murray et al., 2013a, 2012; Wood, Daniel, 2018), specifically the emission time constant, has led to significant differences in the distribution of said emission time constants. Differences in the emission time constant distribution mean that if irradiation, testing, and optimisation is carried out on a room-temperature irradiated CCD, the in-orbit (cryogenically irradiated) performance may be different than expected. For an accurate irradiation, testing and optimisation campaign, this means that CCDs must be irradiated cryogenically, ideally at the mission operating temperature. An excellent summary of the history of CCD cryogenic irradiations is available in the literature (Bush, Nathan L., 2018).

## 4.2. Hyper-velocity particulate impact damage in CCDs

Within the space environment, micron sized particulates are present with velocities of many km/s. These so-called hyper-velocity particulates present obvious hazards to spacecraft via impact events, and as a result, a significant amount of research is carried out regarding the suitability of spacecraft materials with respect to hyper-velocity particulate impacts. Space-based telescopes are no exception to this and must be designed to withstand such impacts via the selection of suitable materials and appropriate thicknesses.

One issue, however, is the vulnerability of focal planes within space telescopes (specifically soft X-ray telescopes), as they often contain a clear line of sight from the focal plane to the vacuum of space and are thus at greater danger of a hyper-velocity impact event. Previous work has investigated the potential that particulates can scatter off the highly polished mirror surfaces within grazing incidence optics and travel directly towards the focal plane where they can also cause damage (Ambrosi, R. M., et al., 2006; Meidinger et al., 2003; Palmieri, D., 2004). Previous X-ray astronomy missions have experienced sporadic events throughout the observing period of the mission. These events have been attributed to micrometeoroid impacts as it is the only reasonable explanation as to the source of the damage. Future X-ray astronomy missions such as LOFT, eROSITA and ATHENA are also investigating and testing detector performance after hyper-velocity impacts (Perinati et al., 2017).

### 4.2.1. Previous effects on large-scale X-ray space telescopes

In the following section, the damage from suspected micrometeoroid impacts on X-ray telescopes is summarised to provide context and motivation for the work that follows. The damage suffered by X-ray telescopes ranges from the appearance of low numbers of hot pixels, to entire detectors being unusable for scientific purposes.

#### 4.2.1.1. X-ray Multi Mirror Mission (XMM-Newton)

XMM-Newton launched on December 10$^{th}$, 1999 carrying a suite of scientific instruments including three EPIC (European Photon Imaging Cameras) imaging X-ray cameras (Strüder et al., 2001). Two of the cameras contained MOS CCD arrays and the third camera uses p-n CCDs. So far, 65 distinct events have been seen, affecting mainly the MOS detectors. Damage has ranged from bright flashes followed by no new hot pixels to the total loss of both MOS CCD6 and CCD3 due to overall detector noise. Figure 1.3 shows the generation of sporadic hot pixels seen in both the pn-CCD array and MOS cameras in two separate orbits.

#### 4.2.1.2. Suzaku

On the 10$^{th}$ July 2005, the Suzaku X-ray telescope was launched as a collaboration between JAXA and NASA Goddard Space Flight Centre (GSFC) and aimed to observe high energy X-ray sources and beyond. The spacecraft carried four instruments, capable of observing soft X-rays (0.3 keV) to gamma-rays (600 keV). After approximately four years in orbit, the XISO

instrument observed a single micrometeoroid impact. As a result, part of the XISO focal plane was marked as “dead” and was not photosensitive, as seen in Figure 4.6. Areas of increased noise were also detected surrounding the marked-off region.

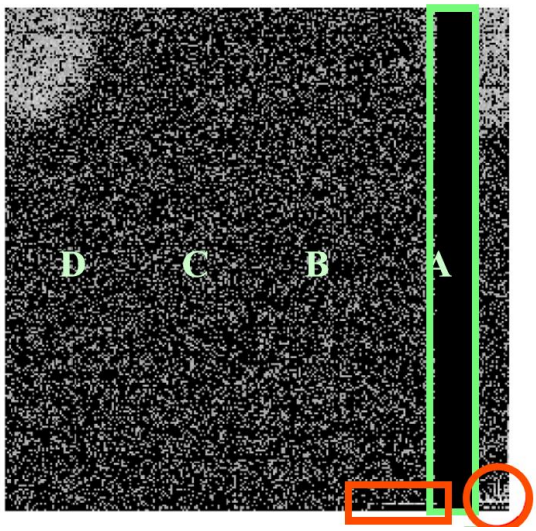


**Figure 4.6**: Example image from the damaged CCD on the XIS instrument from the Suzaku spacecraft (Tsujimoto, 2012). The red areas represent spurious signal that was detected after the columns were damaged.

#### 4.2.1.3. Swift- XRT

The SWIFT Telescope launched on November 20$^{th}$, 2004 and its main aim was to locate and observe new Gamma Ray Bursts (GRBs) using both an X-ray and UV/optical telescope. The X-ray detector was a single e2v CCD-22 having 600x600 pixels behind an optical blocking filter. On the 27$^{th}$ May 2005, SWIFT XRT entered high-count mode, indicating the presence of pixels with above average signal. Subsequent frames showed uneven light illumination along with new bright pixels and hot columns. Although the optical filter was not damaged, the bright pixels and hot columns are no longer usable and have been vetoed as a result (Godet et al., 2009).

### 4.2.2. Previous studies

Evidently, there is a risk to space-based X-ray telescopes from hyper-velocity particulate impacts. However, there is currently no framework to quantify both the risk of hyper-velocity particulate impacts for X-ray telescopes and the extent of the damage to focal planes. To

develop such a framework, background information will be described which can answer the key questions below:

- What is the fundamental nature of the damage to CCDs from hyper-velocity particulate events and what methods can be used to model this damage?
- What are the mechanics of hyper-velocity particulate interactions in soft X-ray optics and how can these mechanics be simulated?
- What are the models which described the flux of micrometeoroids in space, and how can these models be used to calculate the flux incident on a 2D surface?

Micrometeoroid impact studies with respect to CCD performance are sparse, with only one notable study (Meidinger et al., 2003) which aimed to experimentally verify sporadic damage seen in XMM-Newton and will be described in the following section. Other studies (Carpenter et al., 2006) have focused more on the flux rates of micrometeoroids and the information that be extracted from impact rates seen in various X-ray astronomy missions.

#### 4.2.2.1. Experimental verification of XMM-Newton micrometeoroid damage

After sporadic hot pixels were seen in XMM-Newton, an experimental campaign was performed (Meidinger et al., 2003) to verify that the events seen in the detectors in XMM-Newton could indeed be caused by micrometeoroid impacts. The experiment utilised pn-CCDs, identical to those on-board XMM-Newton and used a Van de Graaff generator to accelerate micro-sized dust towards the detectors. To simulate the in-orbit scenario as closely as possible, the accelerated dust was also incident upon grazing incidence optics (with the detector also operated at the in-orbit temperature of 183K). The hypothesis was that particles could potentially scatter off the grazing optics and be focused on the detectors. An example of the experimental setup is seen in Figure 4.7.

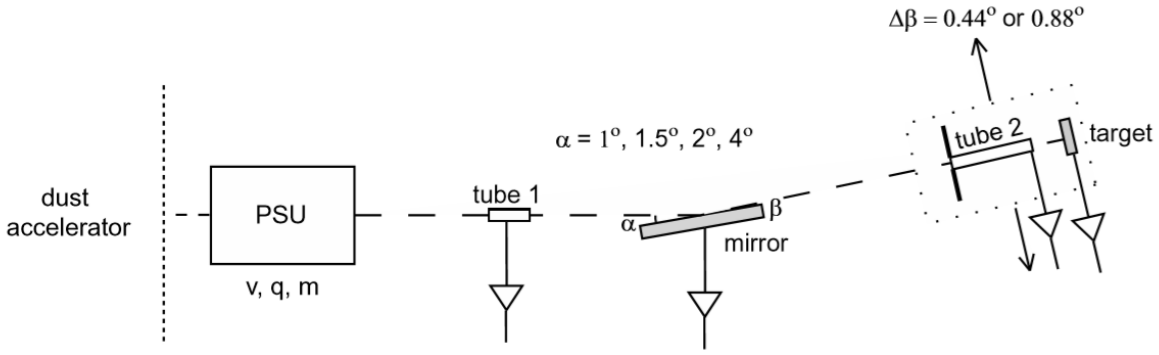


**Figure 4.7**: Experimental setup used to simulate micrometeoroid impacts (Meidinger et al., 2003). Angle of incidence (α) was varied between one and four degrees to further examine the impact and scattering dynamics on polished mirrors.

Figure 4.8 shows the location of hot pixels generated, consistent with those seen during orbits of XMM, and cannot be attributed to heavy-ion impacts. This was strong evidence (for the first time) that hyper-velocity particulate impacts could scatter from polished surfaces and cause increased detector noise in the form of hot pixels. Not only were hot pixels seen, two distinct species of hot pixels were seen which exhibited different behaviour. Figure 4.9 shows the two species of hot pixels seen in the experimental data, with one species showing a single, sharp rise in signal, followed by a constant level of signal. The second species shows a smaller initial rise in signal, proceeded by a stable level of signal for ~750 s. After this time, a steady increase in signal in seen for ~250 s and then a steady state is reached.

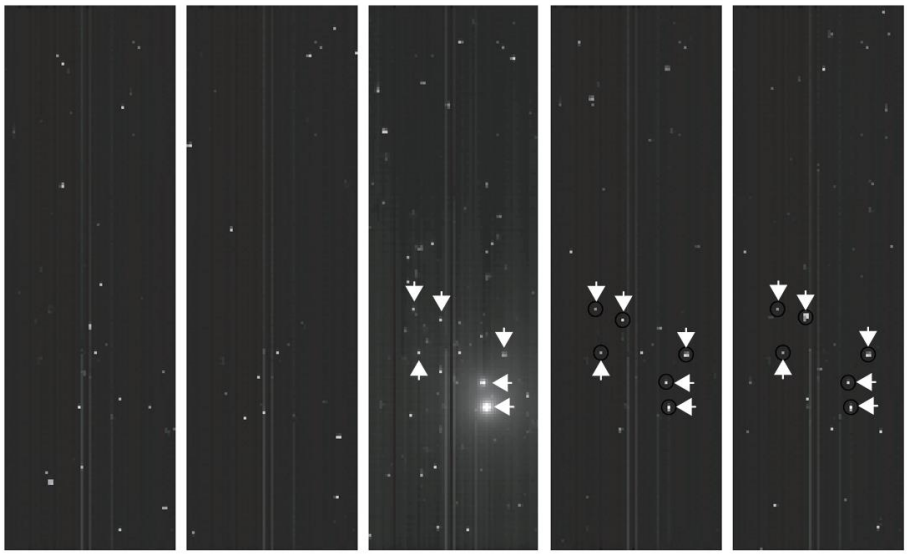

**Figure 4.8**: A selection of five consecutive frames (each frame 44ms) from the experimental campaign. Frame 3 onwards shows the location of hot pixels created due to micrometeoroid impacts (Meidinger et al., 2003). Note that the first frame where hot pixels are seen, are accompanied by a bright flash which is centred around the impact pixel.

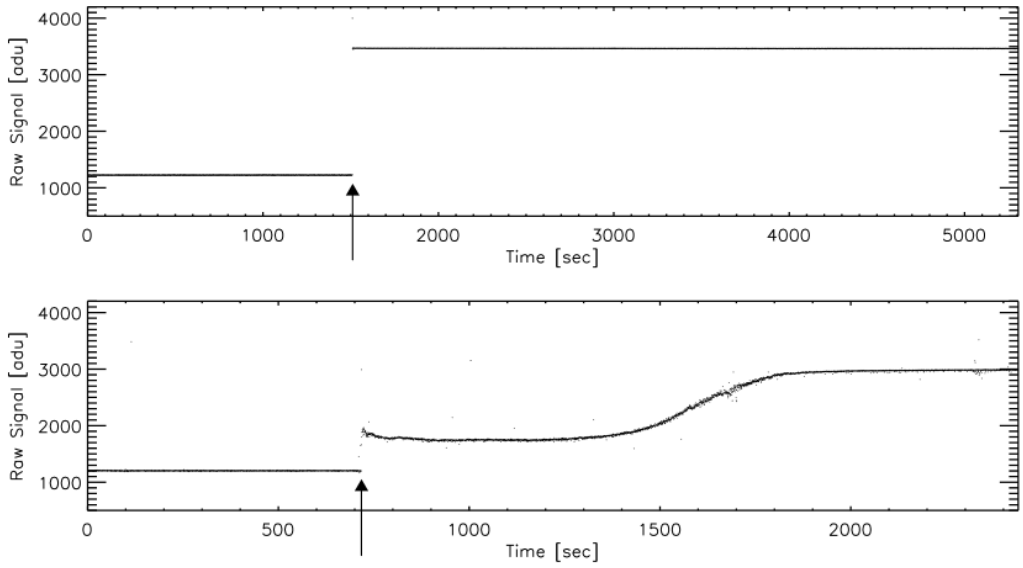


**Figure 4.9**: Two distinct species were seen in the data. Top – Impact at approximately 1500 s followed by a sharp increase and then a steady state. Bottom – A hot pixel which exhibits two levels of signal (Meidinger et al., 2003).

Scattering angle analysis also revealed additional information regarding the incident and exit angles of particulates (with respect to the optics). Particle scattering was observed for incident angles up to four degrees, with the scattering rate relatively constant between zero and four degrees. No incident angles above four degrees were tested.

The exiting angles of particles from the optics revealed that > 50% of scattered particles were almost parallel to the optical plane, meaning that the component of particle velocity normal to the optical plane reduced to zero after an impact with the inner mirror surface.

#### 4.2.2.2. Effects of micrometeoroid impacts in grazing incidence telescopes

As of 2006, both XMM-Newton and SWIFT had seen sporadic micrometeoroid impacts, while Chandra had seen none. This prompted investigation (Carpenter et al., 2006) into the various optical geometries of XMM-Newton, SWIFT and Chandra, to calculate the probabilities of particle impacts over the course of the mission. Figure 4.10 shows the instrument geometry, including detector (CCD) and optical arrangement with associated off-set angles synonymous to Wolter Type 1 optics.

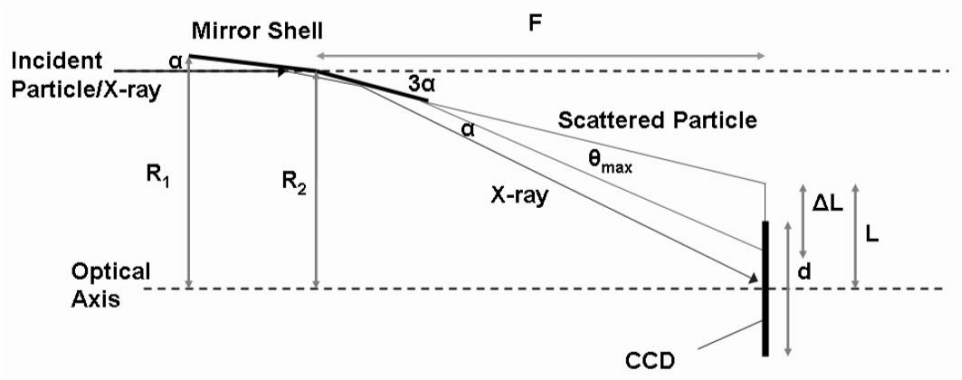


**Figure 4.10**: Schematic of the optical geometry seen in Wolter Type 1 X-ray optics (Carpenter et al., 2006). Shown here is a single shell, however X-ray telescopes are generally constructed of many concentric shells, increasing the field of view (FoV) of the instrument.

The main conclusions of the paper were that care must be taken when building the next generation of X-ray telescopes, due to large FoVs which increases the area available to micrometeoroids. For Chandra in particular, the lower effective optical collecting area (relative to XMM-Newton and SWIFT) was the main reason for the lack of sporadic micrometeoroid impacts. As each soft X-ray space telescope has a bespoke optical system, designed specifically

for the science goals of the mission, each telescope must be assessed independently for particulate impact risks.

Furthermore, the authors outline the main sources of uncertainty, most notably the "poorly defined processes of particle scattering, fragmentation and ejecta release from grazing incidence impacts on smooth X-ray mirrors". They also mention that CCD failure modes are poorly defined with respect to micrometeoroid damage and how this varies with particle size and velocity distribution.

### 4.2.3. Modelling micrometeoroid quantities

To generate a framework for quantifying the risk of X-ray space telescopes to hyper-velocity particulate impacts, specific quantities such as the micrometeoroid flux, velocity distributions, densities and damage equations must be defined.

#### 4.2.3.1. Micrometeoroid fluxes – The Grün Model

The Grün model (Grün et al., 1985) underpins the micrometeoroid impact work carried out in this thesis and describes the total average micrometeoroid flux in terms of an integral flux. The total flux contains a sporadic component, due to the Earth's passage through the Solar System, encountering streams of particles travelling in similar heliocentric orbits. The sporadic component is in addition to a steady background component, originating from large meteors decaying in size over time.

The integral flux is the number of particles with mass m or larger per $m^2$ per year impacting a randomly orientated flat plate under a viewing angle of $2\pi$. The integral flux, defined at 1 AU from the sun is given by:

$$F_{met,0}(m) = 3.15576 \times 10^7 \, [F_1(m) + F_2(m) + F_3(m)] \qquad \text{Eq 4.8}$$

where

$$F_1(m) = (2.2 \times 10^3 \, m^{0.306} + 15)^{-4.38} \qquad \text{for } m > 10^{-9} \text{ g}$$

$$F_2(m) = 1.3 \times 10^{-9} \, (m + 10^{11} m^2 + 10^{27} m^4)^{-0.36} \qquad \text{for } 10^{-14} \text{ g} < m < 10^{-9} \text{ g}$$

$$F_3(m)=1.3x10^{-16}\ (m+\ 10^6 m^2)^{-0.85} \qquad \text{for } m < 10^{-14}g$$

where m is the mass of the particle in grams and the factors $F_1$, $F_2$ and $F_3$ were derived from empirical fits to experimental data that was gathered in-situ from orbiting satellites (HEOS 2) around the Earth (Grün, E. and Zook, H. A., 1979).

The flux given by Eq 4.8 is an unshielded flux, meaning that it does not consider large gravitational bodies such as the Earth (the environment in which SMILE will be situated). Two opposing factors, namely the gravitational enhancement factor and Earth shielding factor, can alter the flux calculated in Eq 4.8.

#### 4.2.3.2. Gravitational enhancement factor

The flux impinging on a randomly orientated plate will be modified according to its proximity to the Earth. The gravitational attraction of the Earth means that the micrometeoroid density increases at lower altitudes. The gravitational enhancement factor, $G_e$, is defined in Eq 4.9 (ESA-ESTEC, 2008).

$$G_e\,(r) = 1+ \frac{R_e}{r} \qquad \text{Eq 4.9}$$

where $R_e$ is the radius of the Earth in km and r is the radius of the orbit in km.

#### 4.2.3.3. Earth shielding factor

The geometrical shape of the Earth also plays a role in reducing the micrometeoroid flux as proximity to the Earth increases. This value, known as the Earth Shielding Factor, $S_f$, is dependent upon the altitude and orientation of the spacecraft (ESA-ESTEC, 2008). $S_f$ is defined as:

$$S_f = \frac{(1+\cos\alpha)}{2} \qquad \text{Eq 4.10}$$

where α is:

$$\sin\alpha = \frac{(R_e+100)}{(R_e+r)} \qquad \text{Eq 4.11}$$

Eq 4.9 and Eq 4.10 mean that for spacecraft orbiting the Earth (like SMILE), the micrometeoroid flux incident on the spacecraft will be a function of orbital radius, and the orbit of SMILE must be considered when calculating fluxes using the Grün model. This naturally leads to the corrected Grün flux ($F_c$):

$$F_c = F_{met,0} \times G_e \times S_f \qquad \text{Eq 4.12}$$

#### 4.2.3.4. Flux enhancement from spacecraft motion

Spacecraft orbital velocity further modifies the flux received and varies with respect to the side of the spacecraft relative to the ram direction. Calculation of this additional factor is tailored specifically for the spacecraft and associated orbit in question and will be calculated for SMILE specifically in chapter 9.

#### 4.2.3.5. Micrometeoroid velocity distributions

To fully calculate the momentum of particulates incident on the SMILE spacecraft (which is ultimately needed to assess the damage of particulate impacts), the velocity of micrometeoroids is also required. Unlike the ubiquitous Grün flux model, to calculate micrometeoroid velocities, there are three popular models known as the Cour-Palais distribution (Cour-Palais, B. G., 1969), NASA90 distribution (ESA-ESTEC, 2008) and the Taylor distribution (ESA-ESTEC, 2008). Although all are used, the most used is the NASA 90 distribution, with Table 4.1 describing the velocity distributions.

**Table 4.1**: The velocity distribution of micrometeoroids for the NASA90 distribution model.

| **Velocity Distribution (number per km/s)** | **Velocity (v) Range (km/s)** |
|---|---|
| 0.122 | $11.1 < v < 16.3$ |
| $3.328 \times 10^{5}\ v^{-5.34}$ | $16.3 < v < 55$ |
| $1.695 \times 10^{-4}$ | $55 < v < 72.2$ |

For the micrometeoroid work contained in this thesis (chapter 9), the mean micrometeoroid velocity from Table 4.1 (15 km/s) will be used exclusively.

#### 4.2.3.6. Micrometeoroid densities

The mass density of micrometeoroids has a significant amount of uncertainty, with values varying between 0.15 g/cm$^3$ to 8 g/cm$^3$ (ESA-ESTEC, 2008). Typically, an average value is assumed which is equal to 2.5 g/cm$^3$. For reference, the density of silicon is 2.33 g/cm$^3$.

### 4.2.4. Damage equations

Section 4.2.3 described the necessary flux models, velocity distributions, and density values to calculate the momentum of micrometeoroids that will be incident upon the SMILE spacecraft. These key values can be used, along with so called "damage equations" to assess the impact of hyper-velocity particulate impacts on materials. The equations were empirically derived from a substantial amount of experimental data. Due to the complex physics involved, historically, the empirical approach was relied upon as computation power prevented the execution of complex simulations (such as hydrocode models , Palmieri, D., 2004), equivalent to the use of GEANT4 for the interaction of high energy particles in materials. In recent times, hydrocode simulations have become more accurate due to increased computing power. The empirical equations are still useful however, as they are quick to implement and require considerably less computing power than the hydrocode models.

The damage equations are split into different groups depending on the application required. For example, there are equations which calculate the ballistic limit of a single wall, providing the point in which the incident structure fails. For the applications required in this thesis, the equation governing the crater sized caused by particles incident on a surface (of a CCD focal plane for example) are of most interest, aptly named the crater size equation.

#### 4.2.4.1. Crater size equations

The crater size equation (Eq 4.13), describes the diameter of a crater ($D_c$) caused by an incident particle impacting a semi-infinite surface. The parameters, including empirical constants, are summarised in Table 4.2.

$$D_c = K_1 K_c d_p^{\lambda} \rho_p^{\beta} v_p^{\gamma} \cos^{x}(\alpha) \rho_t^{\kappa} \qquad \text{Eq 4.13}$$

**Table 4.2**: Summary of the variables and empirical constants initially described in Eq 4.13.

| Symbol | Units | Description | Value |
|---|---|---|---|
| $K_1$ | N/A | Intrinsic property of material | Varies with chosen model |
| $K_c$ | N/A | Brittleness of target material (10 maximum, 1 minimum) | 1 - 10 |
| d | cm | Particle diameter | $10^{-6}$ to $10^{-1}$ |
| ρ | g / $cm^3$ | Density of target and particulate ($\rho_t$ and $\rho_p$) | 2.33 (silicon target)<br>2.5 (micrometeoroid) |
| v | km / s | Velocity of particulate | 15 |
| α | Degrees | Angle between particulate and normal to the target | 0 |
| λ, β, γ, x, κ, | N/A | Empirical constants | Varies with chosen model |
| S | cm | Spacing | N/A |
| D | cm | Crater or hole diameter | N/A |

Although Eq 4.13 provides the general form of the equation, there are however different empirical sub-models (Cour-Palais, B. G., 1969; Fechtig, H. et al., n.d.; Gault, 1973; McHugh, A. H. and Richardson, A. J., 1974) (specifically for brittle targets, such as silicon) which yield slightly different results due to small variations in the empirical constants (shown in Table 4.2). To be able to quantify the damage to SMILE SXI CCDs from hyper-velocity particulate impacts, Eq 4.13 can be used to estimate the size of crater caused by a particulate impact in a scenario where a micrometeoroid strikes a silicon CCD.

The crater size equation should, strictly speaking, only be used in a semi-infinite target where the target is significantly thicker than the particulate diameter. For the case of a micrometeoroid impact on a CCD, a particulate with one-micron diameter is significantly smaller than the thickness of the silicon (10s of microns), meaning the application of Eq 4.13 is valid (for particulates of this size).

## 4.3. Chapter summary

Within this chapter, the interaction mechanics of high energy protons in CCD technology have been described, with a focus on displacement damage and the subsequent defects induced in N-channel CCDs. The defects induced are important, as their interaction with signal electrons significantly degrades the CTI of a CCD. To be able to optimise the CCD performance in an informed manner, knowledge of the emission time constants of radiation-induced defects is necessary. Experimental techniques have been developed in recent years, which allow extraction of the emission time constant for all the relevant defects to N-channel CCD technology. This technique will be harnessed in chapter 5 and 7 of this thesis to extract the distribution of emission time constants from a room-temperature and cryogenically irradiated CCD, respectively. These results will then be used in chapter 6 and 7, in combination with appropriate analytical modelling, to predict CTI performance of different CCD operation modes, with the end goal of guiding experimental CTI testing and informing in-flight CCD operation modes of SMILE SXI.

The second half of the chapter focused on the role of micrometeoroids in space, in relation to X-ray telescopes, highlighting the damage that can be caused because of hyper-velocity particulate impacts. To be able to quantify the damage for future telescopes (such as SMILE SXI), knowledge of micrometeoroid flux models, such as the Grün model was first described. The Grün model (and associated orbital parameters for SMILE), will allow the total number of micrometeoroids incident upon the sMPO to be calculated. Hyper-velocity particulate mechanics in soft X-ray optics were next described, with the key result describing the scattering mechanism that occurs as particulates interact with the highly polished inner surfaces of nested mirror optics. Knowledge of this mechanism is important, as currently there is no method to calculate or simulate how many particulates can traverse soft X-ray optics (either nested mirrors or sMPO). Knowing that this mechanism exists will allow simulations to be created from first principles, to calculate the number of particles that can traverse sMPO (chapter 9, section 9.3.2). Finally, damage equations describing the size of craters produced by incident particulates on a surface were stated (Eq 4.13). Once the total number of particulates successfully traversing the sMPO of SXI are estimated, Eq 4.13 can be used to estimate the size of craters produced and hence the total damage to the focal plane of SMILE SXI (section 9.4).

# 5. SMILE SXI room-temperature irradiation campaign, associated equipment and experimental methodology

From the previous chapter, it is clear that the radiation environment around the Earth will create stable defects within SXI's CCDs, degrading the charge transfer performance and limiting the science lifetime of the instrument. To fully understand the performance degradation however, devices must be tested pre-flight to assess the extent of the performance degradation and determine if the devices can meet the required specifications to fulfil the science requirements of the mission. As such, an extensive irradiation campaign was planned (and is still being carried out), spanning multiple irradiations utilising both PLATO and SMILE CCDs, operated under a range of operating parameters.

This chapter will outline the room-temperature section of the irradiation campaign (the first irradiation), focusing on the experimental techniques used which are most applicable to the content of this thesis, most notably trap pumping, and the relevant experimental equipment needed. The technique will be described from first principles, giving a step-by-step explanation of the rationale behind each stage in the data collection and subsequent analysis. The chapter will conclude by presenting trap pumping results from the room-temperature irradiated CCD280, which will subsequently be used in later chapters to develop methods to optimise charge transfer performance of CCDs.

## 5.1. Irradiation campaign outline

The overall irradiation campaign is shown in Table 5.1, with four distinct irradiations planned over a period of ~3 years. Over time, the irradiations and associated detector choice move towards, and finally converges in as mission-like a scenario as possible in a laboratory setting, the irradiation of a CCD370 under cryogenic conditions. At the time of writing, two irradiations have been carried out, both using a CCD280 but under different temperatures, a room-temperature and cryogenic irradiation. Although both are relevant, and provide useful data, this chapter will focus on the first CCD280 room-temperature irradiation and the associated trap-pumping results.

**Table 5.1**: SMILE SXI OU irradiation plan and associated detector choices and irradiation temperatures (Parsons, S., 2019). The single room-temperature irradiation is highlighted in red, with the subsequent cryogenic irradiations shown in blue. Note that the time for dose delivery is significantly quicker than would be seen in-orbit but is unavoidable due to practicalities of beamline irradiations. Significant amounts of previous work from multiple missions have seen a good correlation between laboratory testing and in-orbit radiation damaged data, so it is assumed that the dose deposit time is not a key factor in mission-like testing on the ground.

| Device type | Irradiation steps | Irradiation temperature (K) | Dose | Date of irradiation | Dose deposit time | Comment |
|---|---|---|---|---|---|---|
| CCD280 | 1 | RT (~293) | EOL ($3.43 \times 10^9$ p/cm$^2$) | 10/09/2018 | ~60 seconds | Establish procedures and compare results with ESTEC |
| CCD280 | 1 | 153 | ½ EOL ($1.62 \times 10^9$ p/cm$^2$) | 22/01/2020 | ~60 seconds | Comparable temperature to in-orbit but only PLATO detectors still. |
| | 2 | 153 | EOL ($1.62 \times 10^9$ p/cm$^2$) | 31/01/2020 | ~60 seconds | |
| CCD380 | 1 | 153 | ½ EOL | TBD | TBD | In-orbit temperature and SMILE device |
| | 2 | 153 | EOL | TBD | TBD | |
| CCD370 | 1 | 153 | ½ EOL | TBD | TBD | Should be comparable to cryogenic CCD380 but FT operating mode |
| | 2 | 153 | EOL | TBD | TBD | |

The room-temperature irradiation of a CCD280, which includes writing a comprehensive test plan (pre- and post-irradiation), assembly and testing of equipment, actual irradiation of the device as well as post-irradiation data analysis, is a substantial task, and was carried out by

multiple people. The authors individual contribution was assisting in preliminary assembly of the equipment, transporting experimental equipment to the beamline, performing the irradiation, transporting equipment back to the OU, and post-irradiation data analysis. The majority of the work carried out by the author was the carefully chosen trap pumping plan (post-irradiation, section 5.4 and 5.5) and the subsequent analysis that followed.

### 5.1.1. Irradiation facility

The first irradiation facility used for the room-temperature CCD280 irradiation was the Birmingham proton facility in the UK, offering proton energies between 2.7 MeV and 40 MeV. The beam was operated at an energy of 28 MeV, delivering an EOL equivalent dose of $3.43 \times 10^9$ p/cm$^2$ (10 MeV equivalent), using the NIEL formula to scale the dose and beam energy as necessary.

## 5.2. Experimental equipment

Before equipment can be transported to the beamline, it must be assembled and tested thoroughly to ensure the system can collect the wide range of data required for a full device characterisation. Figure 5.1 shows the equipment bench setup in the laboratory, with several key features labelled. This section will describe the most relevant pieces of equipment and the purpose that they fulfil.

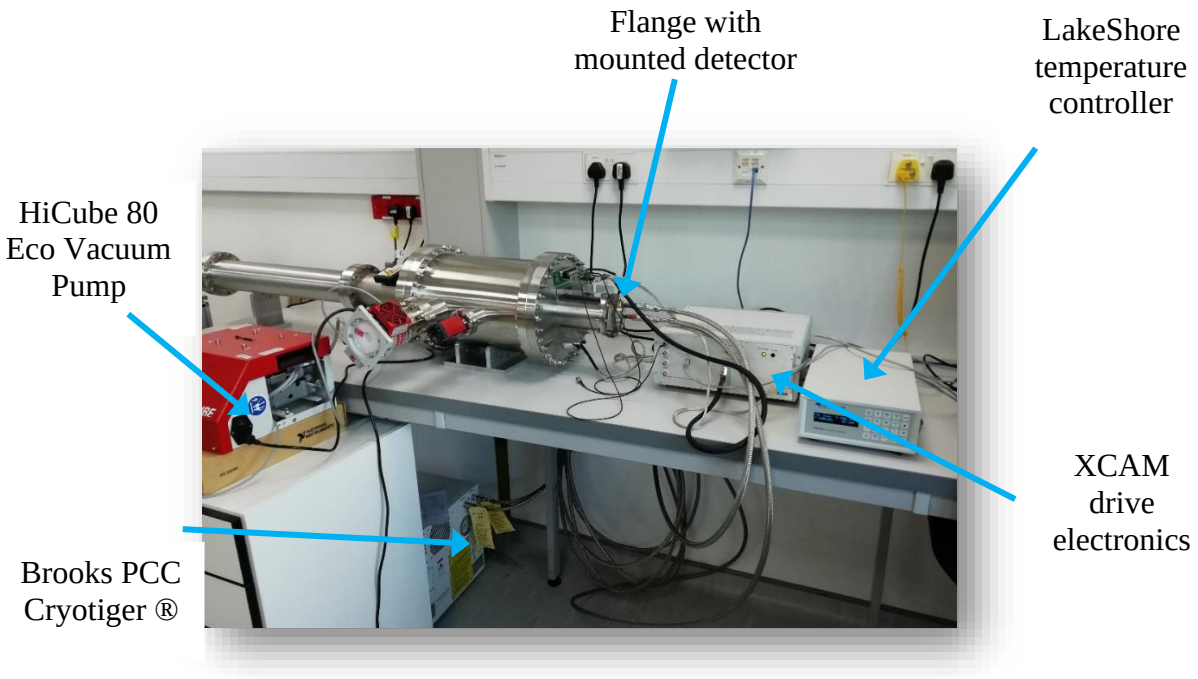


**Figure 5.1**: Experimental bench setup including vacuum pump, thermal control system, XCAM drive electronics and a computer (not visible) which controls the entire system.

### 5.2.1. Vacuum setup

The chamber pressure is controlled via a Pfeiffer HiCube 80 Eco pumping station comprised of both a backing and turbopump, capable of reaching ultra-low vacuum pressures of $\sim 1 \times 10^{-9}$ mbar (or lower).

### 5.2.2. Thermal solution

Although the first CCD280 irradiation was at room-temperature, experimental measurements such as X-ray CTI, dark current and many others must be collected at a range of cryogenic temperatures. This necessitated the use of a thermal control system including a Brooks Polycold Compact Cooler (PCC) Cryotiger and a LakeShore PID temperature controller. The Brooks PCC Cryotiger provide constant cooling power, with fine control determined by the LakeShore PID temperature controller in combination with resistor heaters.

The PCC Cryotiger outputs constant cooling power and can reach theoretical temperatures (for the PT-30 gas blend) of approximately 100 K. However, thermal connections within the

mechanical design of the chamber will limit the lowest temperature possible. Although the Brooks PCC Cryotiger can reach a suitably low temperature, it cannot actively control the temperature of the cold end and thermally coupled device, which is necessary for many experimental CCD measurements. An additional component is required, in this case a LakeShore PID temperature controller.

The basic concept of the LakeShore PID temperature controller relies upon passing a designated amount of current through a single (or multiple) heater strips to heat the CCD cold bench sufficiently to reach the desired temperature. To precisely stabilise at the set temperature, a proportional-integral-derivative (PID) controller is used to control and modulate the amount of current flowing through the heater strips, ensuring that the target temperature is stable.

### 5.2.3. Device integration within the chamber

Within the chamber, the CCD280 is mounted onto a copper cold bench (seen in Figure 5.2), with the copper cold bench connected to the cold end of the Cryotiger via malleable copper thermal straps. The copper cold bench is connected to the vacuum flange via four hollow legs, designed specifically to minimise thermal conductivity between the cryogenically cooled cold bench and the room temperature end flange.

The CCD280 is held securely by a clamp pushing the reverse side of the CCD package onto the copper cold bench. To maximise thermal conductivity, indium foil (highly malleable) is used as an interface between the CCD and copper cold bench.

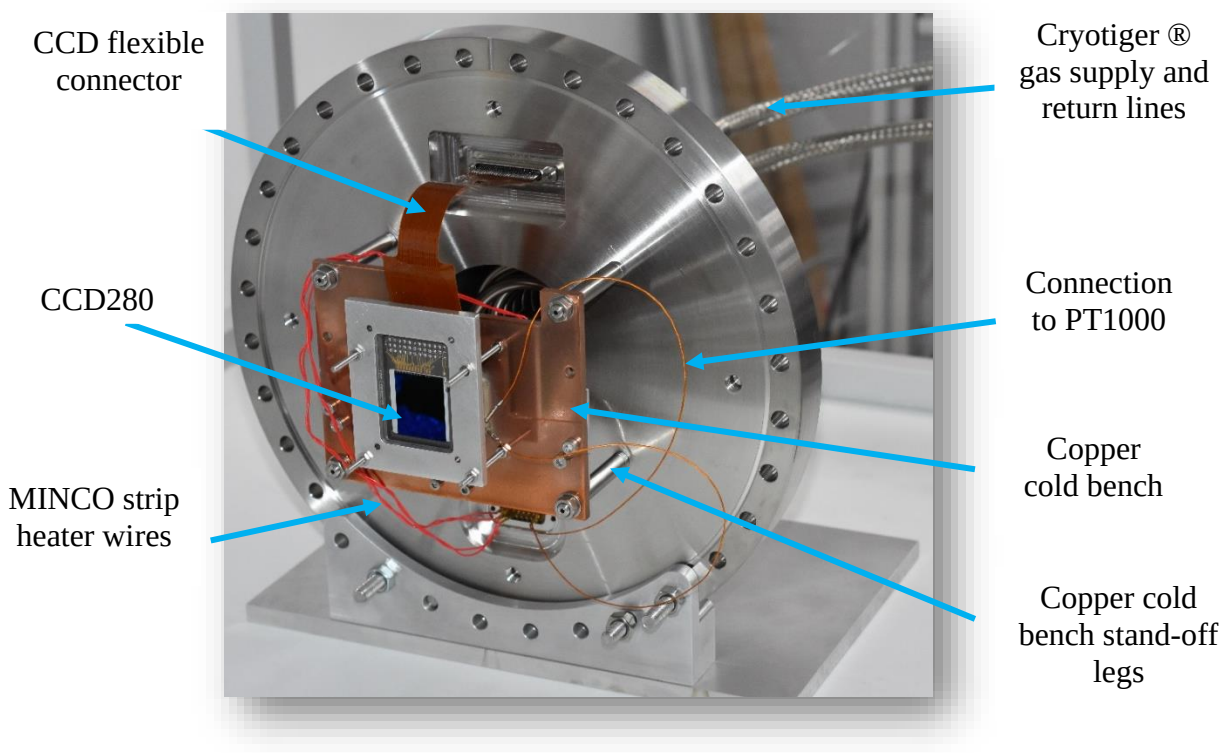


**Figure 5.2**: End flange with mounted cold bench and CCD280. Additional key components are also highlighted for clarity

### 5.2.4. Shielding

During irradiations, shielding is often used to order to protect certain regions of the device from both displacement damage and ionising effects. The shielded region of the device is often used as a control region during irradiation and subsequent data collection. Figure 5.3 shows a schematic of the CCD280, with the bottom right corner of the device covered by stainless steel shielding. Shielding can be moved into position via manual push pull mechanisms, controlled from the outside of the chamber, or in the case of the room temperature CCD280 irradiation, is mounted directly onto the clamp in front of the detector package. Figure 5.3 shows a schematic of the CCD280, with overlaid shielded region in grey, covering ~1/4 of the image area of the device and half of the serial register. This orientation of shielding allows intricacies within the data analysis, such as the analysis of X-ray CTI. By analysing X-rays in different regions of the sensitive area, and hence different numbers of transfers through either unirradiated or irradiated pixels, the exact amount of charge degradation due to parallel or serial CTI can be calculated.

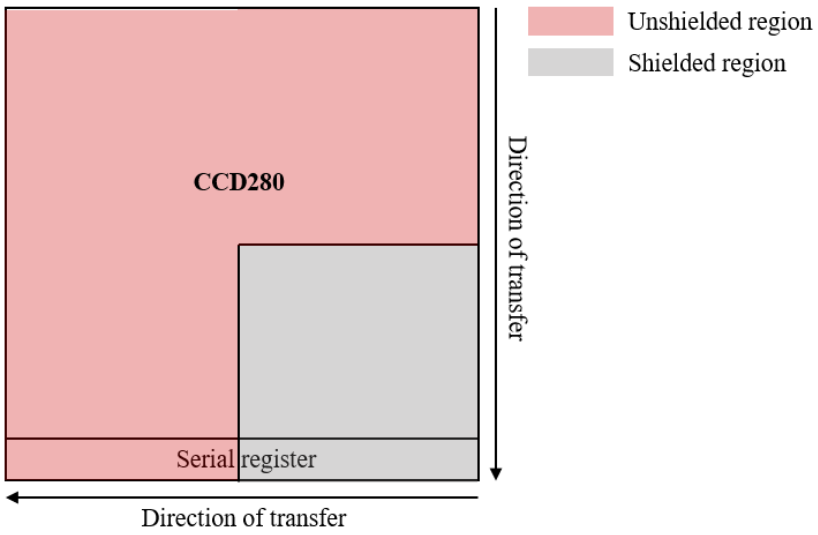


**Figure 5.3**: Schematic of the CCD280 device and associated region of the device which is protected by stainless steel shielding (10mm thickness).

### 5.2.5. Transport trolley and beamline setup

Once the experimental setup was tested in the laboratory (as seen in Figure 5.1) and the device was characterised pre-irradiation, the equipment had to be moved onto a portable trolley for transportation to the irradiation facility. Figure 5.4 shows the portable trolley and all associated experimental equipment. The trolley is specifically designed and setup to be moved into the beamline room and connected directly onto the proton beamline via the large gate valve labelled in Figure 5.4.

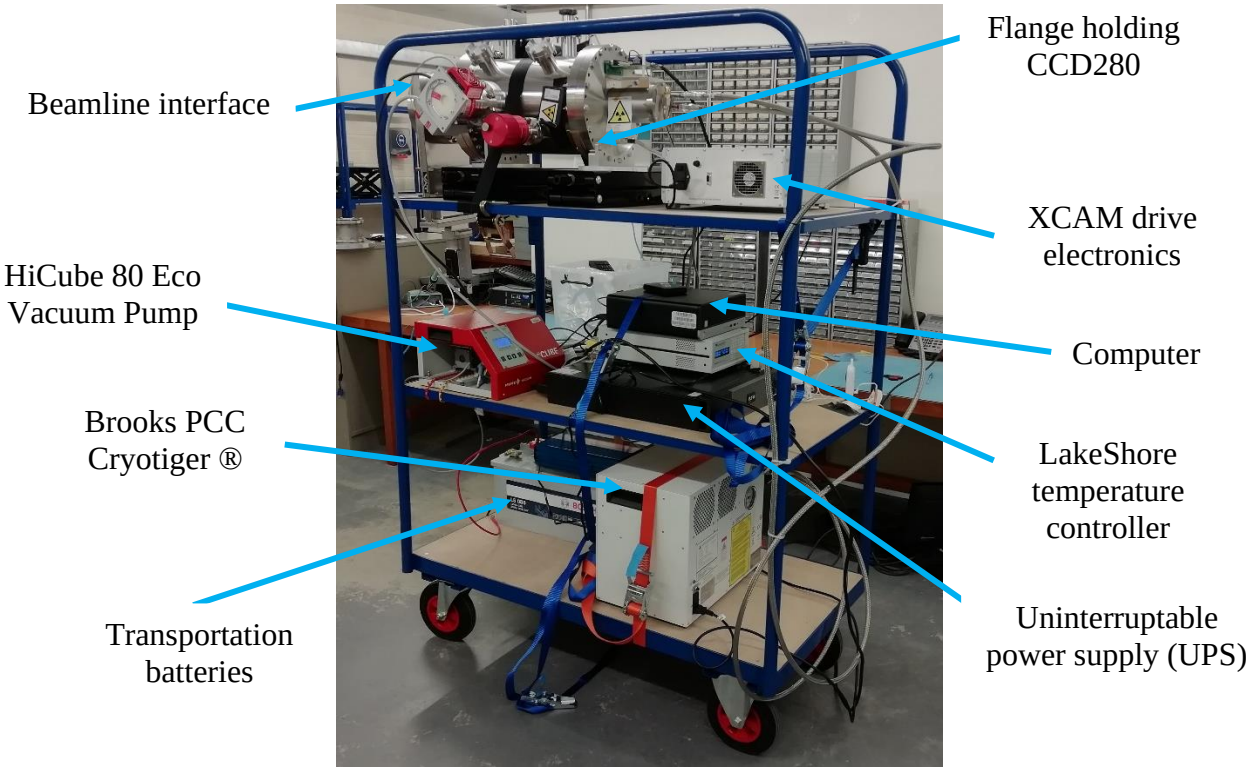


**Figure 5.4**: Identical experimental equipment as seen in Figure 5.1, arranged onto a portable trolley that was transported to proton beamlines for device irradiations.

## 5.3. Experimental methodology

Several characterisation tests were carried out, both pre- and post-irradiation, to assess the performance of the CCD, including measurements of dark current, EPER, FPR, electrical noise, quantity of bright defects, charge injection uniformity, X-ray CTI and defect identification via the trap pumping technique. All characterisation tests are important as the device needs to meet the required specification to ensure that the device can operate to the required standard. For the purposes of this thesis however, the methodology behind measurements of defect identification through trap pumping will be explained in detail, as this technique underpins a significant amount of work.

### 5.3.1. Defect identification using the trap pumping method

The trap pumping technique is powerful, providing key parameters such as the emission time constant of defects (both intrinsic and radiation-induced), probability of capture, sub-pixel location information as well as the energy level and cross section of the defects within the

device (Hall et al., 2014; Janesick, 2001; Murray et al., 2012). In terms of CCD performance, in particular charge transfer performance, the key parameter is the emission time constant, as this directly affects the amount of charge stolen from charge packets collected by the detector. By utilising the trap pumping technique to accurately determine both the emission time constants of the dominant defects within the device and the quantity of these defects, CCD charge transfer performance can be optimised accordingly.

### 5.3.2. Basic concept

The trap pumping technique relies upon the sequential movement of charge through the device, repeated many times to exploit the capture and emission of the defects present. To facilitate this movement of charge, electrodes within the device are biased in a manner shown in Figure 5.5. Electrodes are pulsed in order from Φ1 to Φ2 to Φ3, with the process then mirrored until Φ1 is the only electrode set to high once again. This four-stage process is known as a single pump cycle and it often repeated up to ~10,000 times per image.

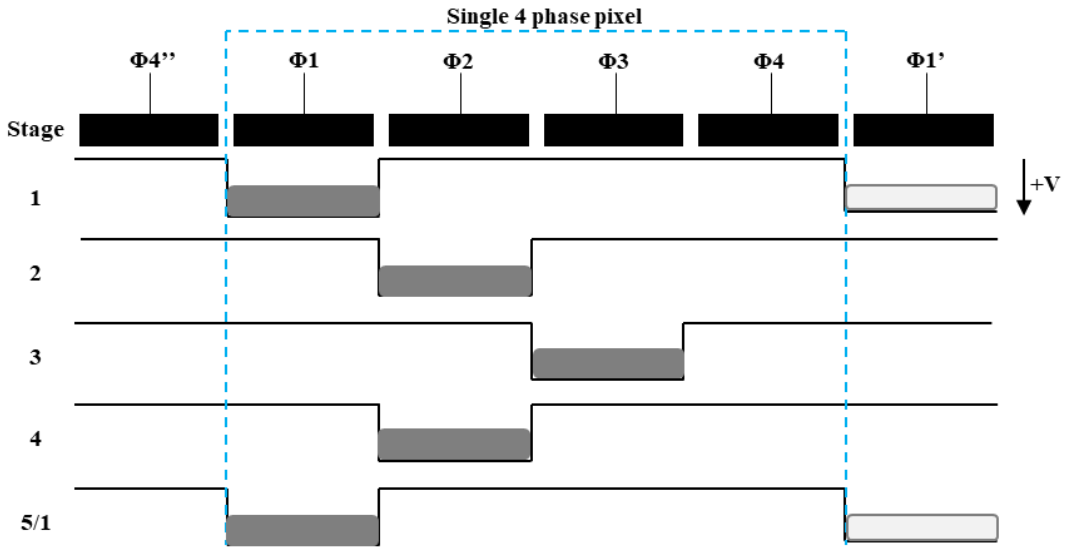


**Figure 5.5**: Voltage profile across a single four-phase pixel for a single trap pumping cycle.

As electrodes are pulsed back and forth many times, charge packets are naturally confined to the potential wells, and move in an identical pattern, as seen in Figure 5.6 . Charge is initially stored under Φ1, with defects under this phase capturing electrons, as seen by the filled red circles in Figure 5.6. After a time $t_{ph}$, charge is moved to Φ2 and the captured charge is now free to emit. The released electron joins the closest charge packet, which is still the source

charge packet, so there is no net movement of charge (indicated by the dashed arrows). Whether the defect is in the left- or right-hand side of Φ1 is irrelevant, both defect locations are still closest to the source charge packet and hence there is still no net movement of charge. The pumping sequence continues, with charge now moved into Φ3. Defects under Φ1 can still be filled by captured electrons (depending on their emission time constant) and will still emit into the closest charge packet. For the case of defects on the right-hand side of Φ1, the closest charge packet is still the source charge packet, so once again no net movement of charge is seen. However, defects located in the left-hand side of Φ1 are now closest to the charge packet in the adjacent pixel, with emitted electrons now joining this non-source charge packet (indicated by the solid black line in Figure 5.6). Overall, this means that an electron has been moved, or "pumped", from the pixel enclosed by the blue dashed line, into an adjacent pixel, from a single pump cycle.

As the number of pump cycles increases, more charge is pumped from one pixel to the next, dependent upon the presence of defects and their associated emission time constant. Although the behaviour of defects under Φ1 is described above, the identical process also happens in Φ3 of this pumping scheme, as charge is captured when the Φ3 electrode is high.

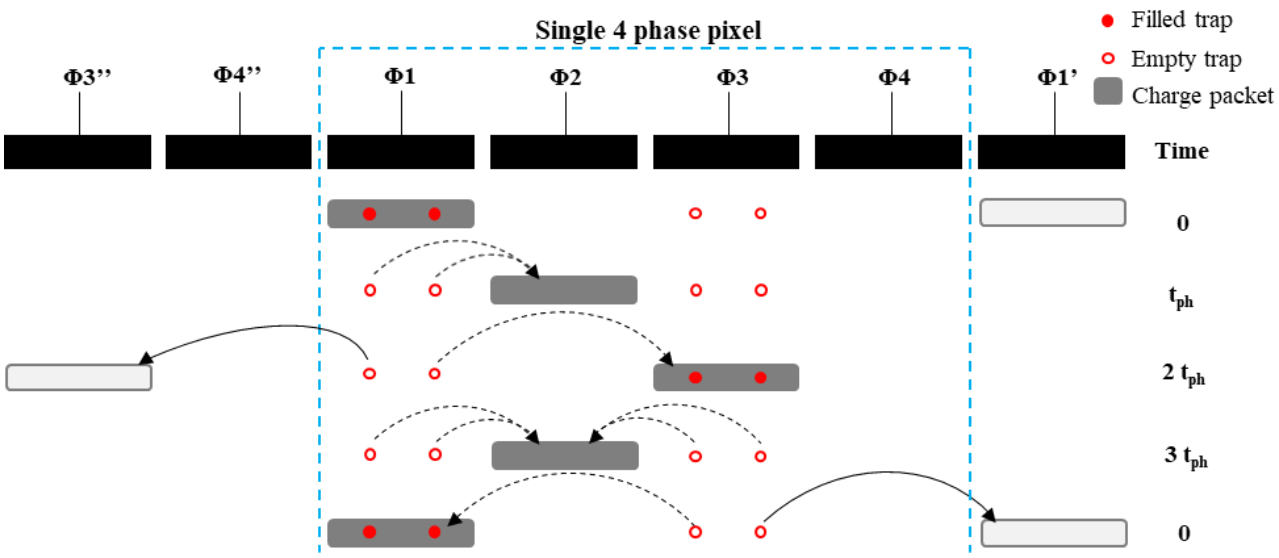


**Figure 5.6**: Defect capture and emission dynamics for a single trap pumping cycle as part of the 1-2-3-2-1 trap pumping scheme. Note that dashed and solid black arrows represent emission into the source and non-source charge packet, respectively.

The pumping scheme described in Figure 5.6 is known as 1-2-3-2-1 and simply refers to the voltage sequence applied to the electrodes. From this scheme, defects located under the left-hand side of Φ1 and the right-hand side of Φ3 are the only defect locations where there is a net movement of charge from one pixel to another (shown explicitly by the black solid lines). To fully probe the entire pixel, three additional pumping schemes are used, identical in manner to Figure 5.6, but the initial electrode set high is different. Table 5.2 shows the four trap pumping modes used (1-2-3-2-1, 2-3-4-3-2-, 3-4-1'-4-3 and 4-1'-2'-1'-4) and which sub-pixel location is probed for the presence of defects.

**Table 5.2**: Four trap pumping schemes used in a four-phase device with the associated sub-pixel locations probed. Also included is the charge dipole orientation, characteristic to each sub-pixel and trap pumping mode pairing. Note that pumping modes with 1' and 2' refers to electrode numbers in the next pixel.

| Trap pumping mode | Electrode probed | Dipole orientation |
|---|---|---|
| 1-2-3-2-1 | Φ1 – Left hand side | High signal/low signal |
| 1-2-3-2-1 | Φ3 – Right hand side | Low signal/high signal |
| 2-3-4-3-2 | Φ2 – Left hand side | High signal/low signal |
| 2-3-4-3-2 | Φ4 – Right hand side | Low signal/high signal |
| 3-4-1'-4-3 | Φ1 – Right hand side | Low signal/high signal |
| 3-4-1'-4-3 | Φ3 – Left hand side | High signal/low signal |
| 4-1'-2'-1'-4 | Φ2 – Right hand side | Low signal/high signal |
| 4-1'-2'-1'-4 | Φ4 – Left hand side | High signal/low signal |

Although not shown explicitly in Figure 5.6, Figure 5.6 shows how the pumped charge generates characteristic patterns within each trap pumping image. Due to the total net movement of charge from the total number of pumping cycles, a significant amount of charge is pumped to and from pixels that contain defects. By analysing the amount of signal pumped by a defect as a function of the pump delay ($t_{ph}$), the key emission time constant of that defect as well as other values such as the probability of capture can be attained.

### 5.3.3. Analysis pipeline

Once separate frames have been collected at a range of pumping delays ($t_{ph}$), the analysis pipeline can begin to extract key values such as the emission time constant and the probability of capture. The analysis pipeline has several stages, each of which will be described in detail below with accompanying figures. The code utilised to analyse the data in this thesis was written from scratch in the MATLAB software package, although previous works have also used the same underlying methodology (Bush, Nathan L., 2018; Wood, Daniel, 2018).

1) Select the region of interest within each frame that had injected charge.

Figure 5.7 shows a trap pumping image (top) and the associated mean column signal (bottom). The area of injected charge is clearly visible across 1250 columns and shows non-uniformity with respect to column number. To remedy this issue, a column-by-column background signal subtraction is performed on only the charge injection region, ignoring the remainder of the low-signal image. Once this is complete, the underlying charge dipoles can be located, and subsequent analysis can continue.

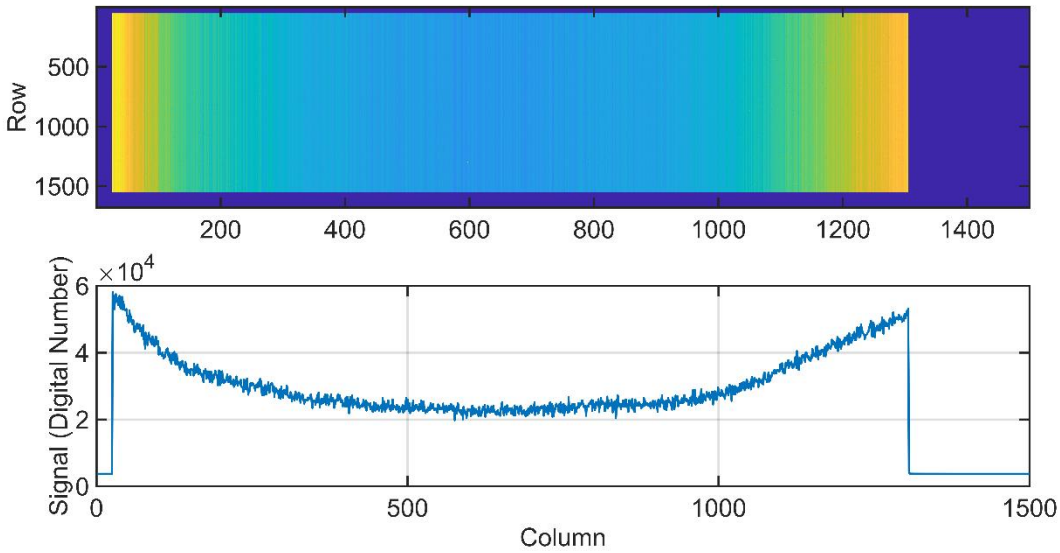


**Figure 5.7**: Example of a raw trap-pumped image (top) with the charge injection region clearly visible. Column signal profile (bottom) showing the charge injection block.

2) Perform a column-by-column signal subtraction to remove the now-useless charge injection signal and reveal the underlying charge dipoles. The subtraction is done by a column basis to fix any issues regarding non-uniformity in the level of charge injection with respect to column number.

Figure 5.8 (left) shows the result of subtracting superfluous background signal, leading to visibility of adjacent pixels (with respect to row number) with significantly higher/lower signal than the background pixels. The pixel location of each charge dipole represents a defect that is moving (or pumping) charge from one pixel to another. Many defects are contained within each image, so the process of finding each defect within each image must be automated. This is achieved via analysing the signal of each column within each image to look for distinct patterns.

3) Charge dipoles are identified by processing each column of pixels individually and selecting pairs of adjacent rows that contain signal either above/below or below/above the upper and lower thresholds. The signal thresholds are determined by taking 3σ sigma above and below the mean column signal.

Figure 5.8 (right) shows an example column signal trace of 500 rows in an example image, with large spikes in signal seen between a background signal level centred at 0. To locate charge dipoles, upper and lower limits are imposed based upon a 3σ above the mean signal level, this is seen by the black solid and dashed lines, respectively. Any pixel which contains signal above/below either threshold is examined, and if either of the adjacent pixels are also above/below the threshold then the pixel is selected as a charge dipole and is analysed further.

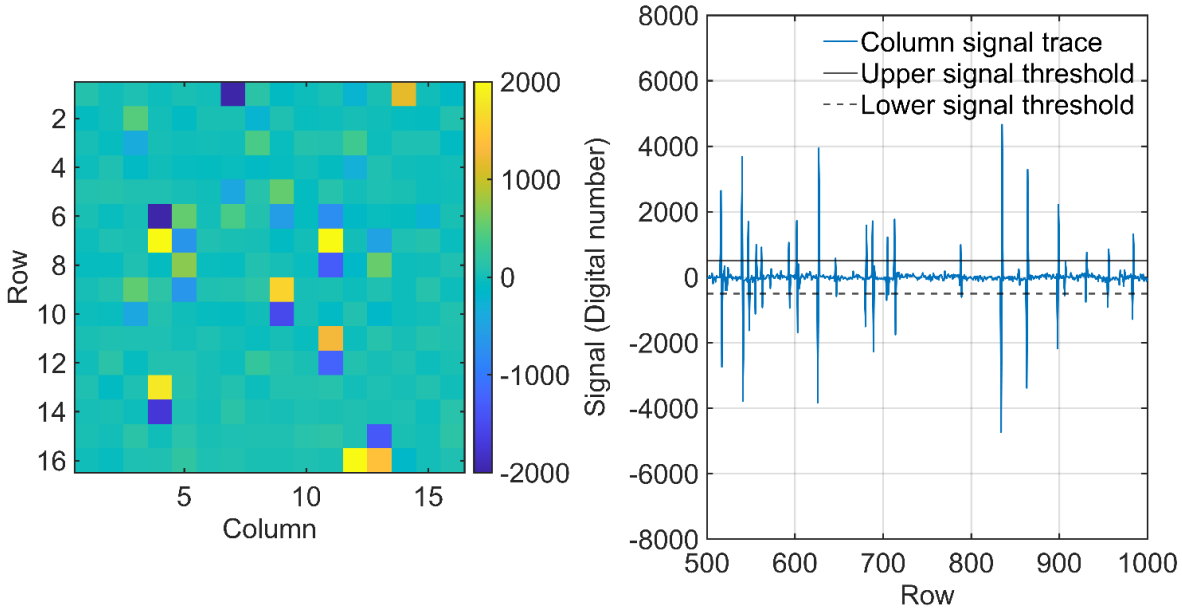


**Figure 5.8**: Charge dipoles that are visible after a background signal subtraction (left). Note that the orientation of the dipoles is not consistent, suggesting that some defects are in different sub-phase locations within each pixel. Right - Changing pixel signal as a function of row number across a single image column, with the upper and lower limit for dipole selection shown.

4) Repeat stages 1-3 for all images.

5) The signal of the brighter pixel within a charge dipole is then plotted as a function of pumping time ($t_{ph}$).

Figure 5.9 shows the characteristic shape of a single defect, whereby a smooth increase in signal is followed by a peak and a subsequent smooth decline. The shape represents the changing pumping efficiency of the trap as the pumping time ($t_{ph}$) is changed. The exact location of the curve peak changes with the inherent emission time constant of the defect in question.

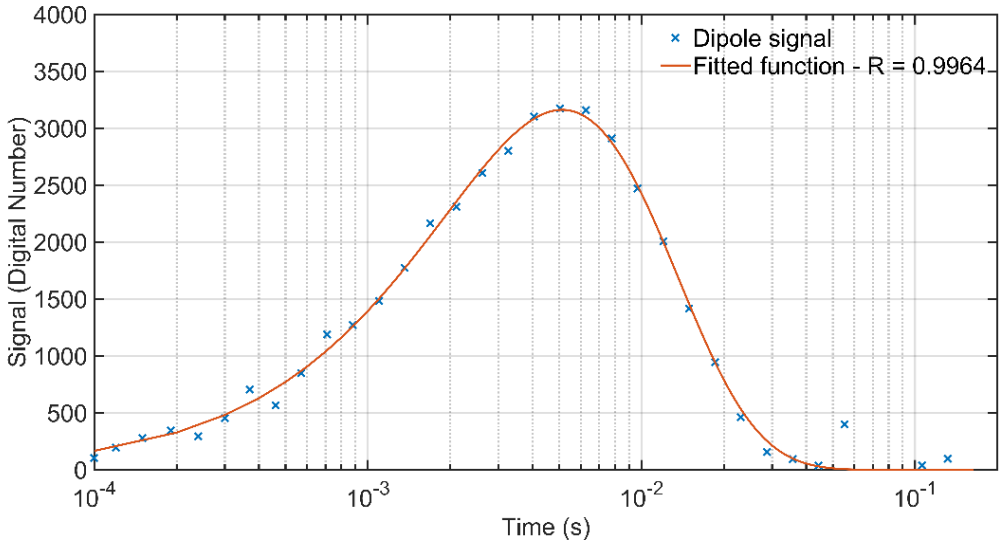


**Figure 5.9**: Dipole intensity curve from a single defect measured at a range of pumping times (blue crosses). Overlaid in red is the fitted function, showing an excellent match to the experimental data points.

6) Once plotted, an appropriate function (Eq *5.2*) is fitted which extracts the emission time constant and probability of capture along with the associated goodness of fit (R value).

To extract the emission time constant, the pumping efficiency of the defects (shown in Figure 5.9) must be described mathematically. The probability that a defect will pump ($P_p$) between the times of $t_1 = t_{ph}$ and $t_2 = 2t_{ph}$ (as shown in Figure 5.6) is (Hall et al., 2014):

$$P_p = \exp\left(\frac{-t_{ph}}{\tau_e}\right) - \exp\left(\frac{-2t_{ph}}{\tau_e}\right) \qquad \text{Eq 5.1}$$

where $\tau_e$ is the emission time constant of the defect which is pumping. Note that Eq 5.1 is specific to a four-phase pumping scheme, specifically 1-2-3-2-1, and the probability of pumping equation will change if a different trap pumping scheme is used. After several pumping cycles, the quantity of charge pumped, or intensity (I) of the charge dipole is given by the equation (Hall et al., 2014):

$$I = NP_p = NP_c(\exp\left(\frac{-t_{ph}}{\tau_e}\right) - \exp(\frac{-2t_{ph}}{\tau_e})) \quad \text{Eq 5.2}$$

where N = number of pump cycles, and $P_c$ = probability of capture of the defect. By fitting Eq 5.2 to the dipole intensity curve in Figure 5.9 (orange curve), both the probability of emission and capture can be extracted for that single defect.

Mathematically, the peak of the curve in Figure 5.9 can be described by the differential:

$$\frac{dI}{dt} = 0 \quad \text{Eq 5.3}$$

Substitution of Eq 5.3 into Eq 5.2, with subsequent rearranging, leads to:

$$\tau_e = \frac{t_{ph(max)}}{\ln(2)} \quad \text{Eq 5.4}$$

Eq 5.4 provides a means of choosing a suitable range of pumping times ($t_{ph}$) that will probe the emission time constant of a specific defect, to attain a curve like the one shown in Figure 5.9.

## 5.4. Room-temperature irradiation trap-pumping results

After the irradiation was performed, the irradiated device was transported back to the Open University and post-irradiation data collection could begin, including the acquisition of trap pumping data. The overall goal of the trap pumping data collection was to probe emission time constant ranges which most concerned N-channel device performance, at a range of suitable temperatures. Once key values such as the emission time constant were acquired, the spread of emission time constants could be used to further inform device performance in future activities.

The author was solely responsible for choosing the experimental parameters to maximise the data taken in the allotted time (approximately 3 weeks). The key values to choose were the exact pumping delays (and associated emission time constant probed) and the range of temperatures used (section 5.4.1) while trap pumping. The number of trap pumping cycles was set to 10,000, as this provided good signal to noise for the defect dipoles, and was commonly used in previous works (Bush, Nathan L., 2018; Hall et al., 2014; Wood, Daniel, 2018).

### 5.4.1. Emission time constants probed

Figure 5.10 shows the four main, radiation-induced, defects than can affect N-channel charge transfer performance and degrade detector performance significantly [(Bush, Nathan L., 2018)]. The key emission time constants regions are situated around the double negative state of the divacancy (yellow line) and the unknown defect (light blue). These regions are also the emission time constants that will most affect parallel CTI in the SMILE CCDs, therefore probing these regions will be prioritised. The key regions can, in theory, be probed at any temperature. However, due to thermal constraints, the detector could only be operated in the temperature range of approximately 165 K – 195 K. Combining the thermal constraints with the main defects to be probed, led to the six trap pumping sweeps performance, as seen by the vertical black lines in Figure 5.10.

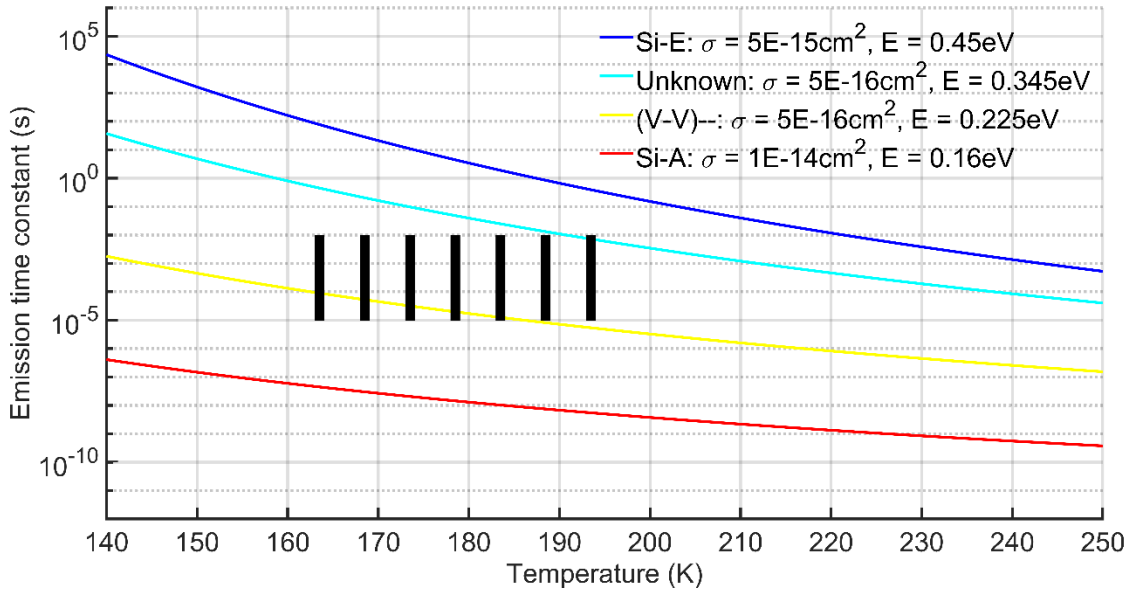


**Figure 5.10**: Trap diagram showing the four most abundant radiation-induced defects relevant to N-channel charge transfer performance (Bush, Nathan L., 2018). Overlaid are the six trap pumping sweeps planned, focusing on the double negative state of the divacancy, the unknown defect, and the emission time constant range between these two defects.

## 5.5. Defect landscapes

By analysing the trap pumping data and binning the calculated emission time constants of identified defects into a single histogram, the overall spread of emission time constants (which were probed) can be examined.

Two distinct species are seen in the four temperatures probed in Figure 5.11, with the locations of the peaks moving in/out of the probed parameter space as temperature is changed. The taller peak towards the quicker emission time constant range (the three peaks in green, red and black sequentially) is attributed to the divacancy as the emission time constant of the peak matches well with literature values (Bush, Nathan L., 2018; Pichler, 2004). The other peak seen is towards the slower end of the emission time constant range, most visible at 193 K, and the peak of the emission time constant matches the unknown defect (Bush, Nathan L., 2018; Pichler, 2004).

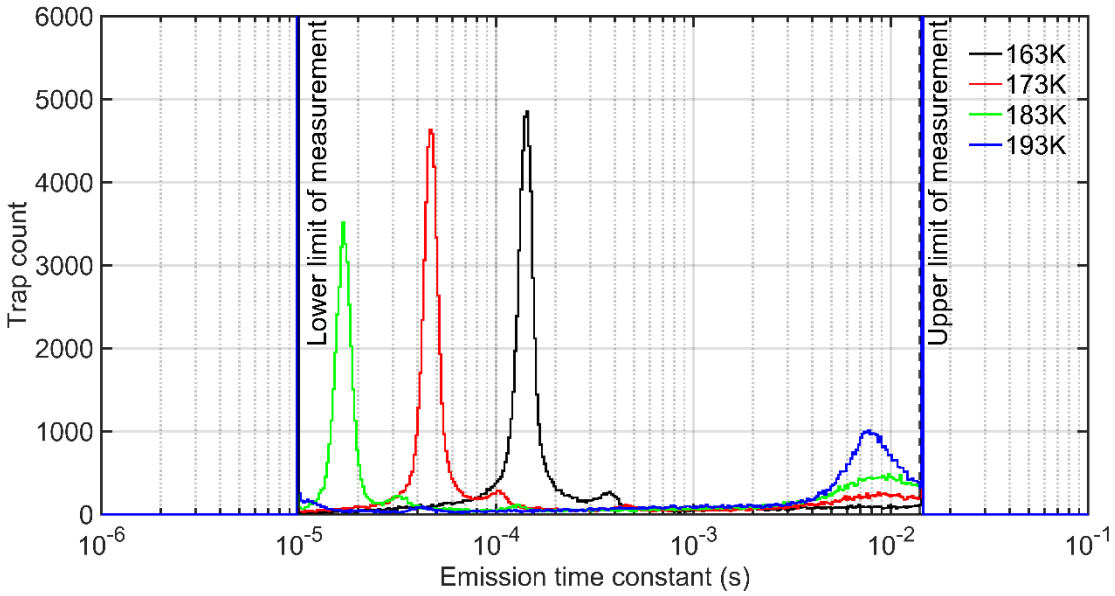


**Figure 5.11**: Trap landscapes directly measured in the CCD280 post-irradiation. The lower and upper limit of measurement are defined by the minimum achievable parallel clocking speed and time allocation for this phase of characterisation, respectively.

Although different parts of the trap landscape are probed at each temperature, the landscapes in Figure 5.11 can be combined to generate wider and more comprehensive landscape (with respect to traps for SMILE CCD operation and performance). This trap landscape can be used

to optimise CCD performance, in particular charge transfer performance, and will be constructed and then utilised in chapter 6.

## 5.6. Chapter summary

This chapter has described the SMILE SXI OU irradiation campaign, focusing on the first room-temperature irradiation and the associated equipment required to complete the irradiation successfully. To carry out the irradiation, a custom vacuum chamber was built and assembled (Figure 5.1) with the CCD280 mounted on the inside of the end-flange (Figure 5.2). To operate the CCD, control the device temperature, and maintain vacuum pressure, an XCAM electronics box, LakeShore temperature controller, Cryotiger and Pfeiffer Hi Cube 80 Eco Vacuum Pump were used (highlighted in Figure 5.1). During the irradiation, the CCD280 was partly protected by a 10mm stainless steel shield, with the shield orientation shown in Figure 5.3. The Birmingham Proton beamline was operated at an energy of 28 MeV, delivering a total fluence of $3.42 \times 10^9$ p/cm$^2$ (10 MeV equivalent).

Once the experimental equipment was described, the main experimental technique used within this thesis was outlined, namely the trap pumping technique. The analysis pipeline was then described, for which the code to complete the analysis was written solely by the author. For the irradiated CCD280, the range of emission time constants probed using the trap pumping technique (and associated temperatures) was determined using previous N-channel CCD defect data (Bush, Nathan L., 2018). The range of temperatures and emission time constants focused on probing the regions that contained both the double negative state of the divacancy and the unknown defect, both of which will contribute heavily to parallel CTI in SMILE SXI CCDs.

Using the trap pumping analysis pipeline, the data was analysed producing trap landscapes containing large peaks in expected locations for both the double negative state of the divacancy and the unknown defect. Only preliminary results were presented however, as the following chapter will utilise this data in combination with an analytical model to predict changes in CTI in the irradiated CCD280.

# 6. Charge transfer optimisation using knowledge of point defects

Many metrics can be used to measure CCD performance, however one of the most important is Charge Transfer Inefficiency (CTI) as it effectively places a limit on the duration of the science-lifetime of the device due to the accumulation of radiation-induced defects in-orbit, degrading the ability of the instrument to identify X-rays and determine their energy. It is therefore imperative that CTI is minimised to prolong the lifetime of the devices and hence maximise the science-return of the mission.

CTI can be minimised by altering the operating parameters of the device including clocking speeds and temperature to reduce the impact of defects contributing to CTI. This means that to fully optimise the device, detailed knowledge of both the total number and distribution of defects is necessary. However, until recently, this was unknown. Recent advances in knowledge of the distribution of defects through the trap pumping technique have led to key results that can be used to optimise CCDs fully. Figure 6.1 shows the emission time constant distribution of both intrinsic and radiation-induced defects in a room-temperature irradiated CCD204 that was attained through the trap pumping technique (black histogram). It is this distribution of defects that affects CCD charge transfer performance and has the potential to heavily degrade performance.

However, due to the way the CCD is operated, not all the defects present within the defect landscape in Figure 6.1 will contribute to charge transfer losses. To calculate which specific defects affect charge transfer performance a minimum and maximum threshold must be defined, with the defects between these limits contributing to CTI and from here on will be called “effective” traps. The precise location of these two thresholds, and hence the effective number of traps, can be determined by the operating parameters of the device such as the image and serial clocking speed as well as the density of X-rays within the device.

Previous work utilised this concept to assist in the optimisation of charge transfer performance of an Electron Multiplying CCD201 for the Nancy Grace Roman Space Telescope (Bush, N et al., 2020; Bush et al., 2018). Bush et al. developed a model (hereon called the Active Trap Model, ATM) to optimise a single phase of readout of the CCD201 for one operating mode (full frame readout) at a range of temperatures. The underlying physics of the model relied

upon calculating the probability that a defect can emit with a minimum and maximum threshold (as stated above), and hence contribute to CTI.

The technique has been developed significantly further in this work to optimise the charge transfer performance of the SMILE SXI CCD370s, with additional features for accuracy and to account for complications in the CCD370 operation. These include the addition of sub-pixel modelling (to calculate the minimum time accurately), the ability to calculate the number of effective traps across a wide parameter space (including temperature, image, store, and serial clock speeds), the inclusion of charge injection, and accurate modelling of the multi-step frame transfer mode with 6×6 on-chip binning. In addition, this technique has also been experimentally verified and improved further (section 6.2).

Without this modelling effort, laboratory testing across the parameter space required would require many months of effort, with the time taken for data collection further extended by experimental necessities such as using a 300 s integration time for some measurements. The power of this analytical technique means that optimal conditions for device operation can be found in approximately 1 s of computation time, compared to many months of laboratory data collection. Furthermore, as this analytical technique will help to save a significant amount of experimental time, this experimental time can be focused on other optimisation efforts which would otherwise be delayed by many months, potentially affecting key instrument development timelines.

Not only does this technique save a considerable amount of experimental time, but it can also predict key results for the CCD370s, before manufacturing and delivery via Teledyne-e2v. This means that when the CCD370s are delivered for testing, the wide parameter space will have already been probed, and optimal parameters will already be known, and experimental testing can focus on verification of these parameters.

This chapter will describe the developed ATM optimisation technique by first outlining the key steps of and the rationale behind each step. Once complete, the ATM will be used to compare X-ray CTI data, attained as part of the SMILE SXI irradiation campaign, to the number of effective traps predicted by the updated model. Once the ATM results have been analysed and fully understood, the model can then be used in subsequent chapters to predict and guide the selection of the optimal operating parameters for the yet-delivered CCD370s. As an extension,

the model will also be adapted to analyse and predict the potential benefits of implementing tri-level clocking for the parallel area readout of the CCD370.

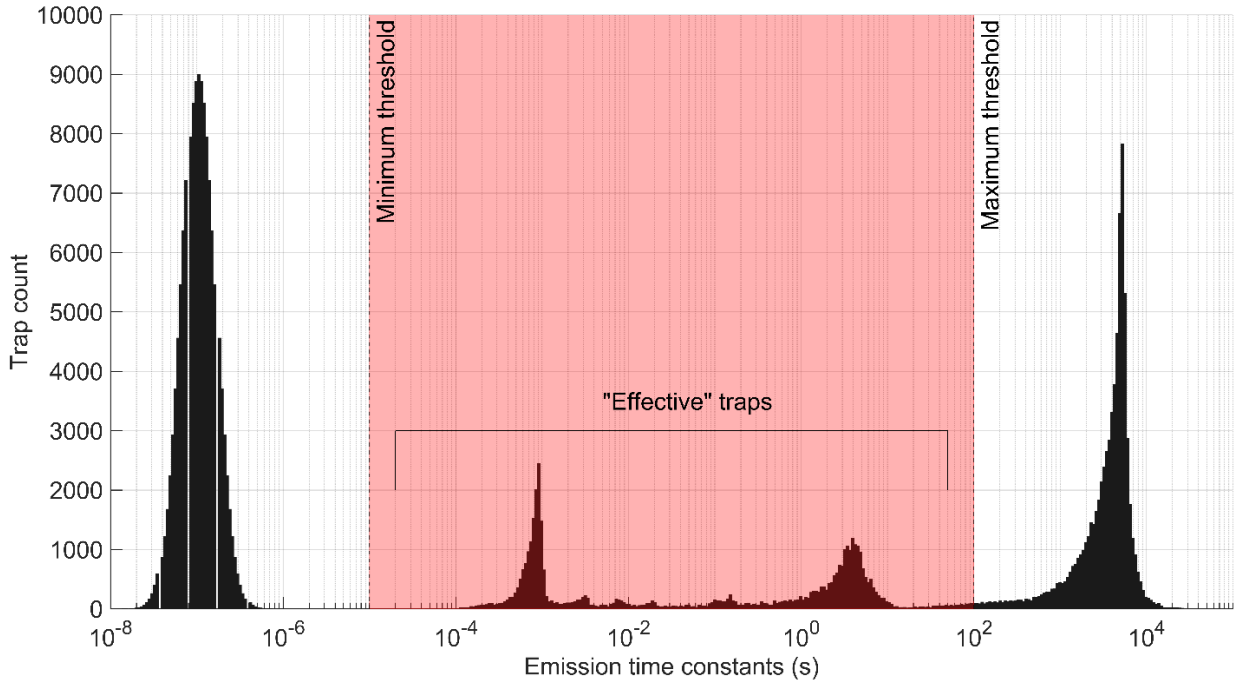


**Figure 6.1**: Trap landscape from a room-temperature irradiated CCD204, generated at 153 K. A range defined by a minimum and maximum threshold is defined, shown in red. Any defects located within this range will contribute to CTI. Note that the CCD204 was used as this was the only dataset available at the time.

The code to implement the ATM was written in the MATLAB language and was written from scratch by the author. The model accepts multiple inputs, and was designed to be modular, allowing different trap landscapes, device readout modes, temperatures and clocking speeds. This means that using the model for future CCD optimisation activities will be straight forward to implement.

## 6.1. Active Trap Model - Basic methodology

The ATM has several steps to estimate the number of effective traps (traps which contribute to CTI, between the minimum and maximum threshold in Figure 6.1) for a given device's operating mode. The method utilises trap landscapes attained previously, trap capture and emission dynamics as well as SRH theory (Hall, 1952; Shockley and Read, 1952) to calculate the probability that a filled trap will emit its captured electron in a given timeframe. Figure 6.2

shows a flowchart representing the stages of the ATM. The following section will describe in detail each stage of the ATM as well as explaining the underlying theory where applicable.

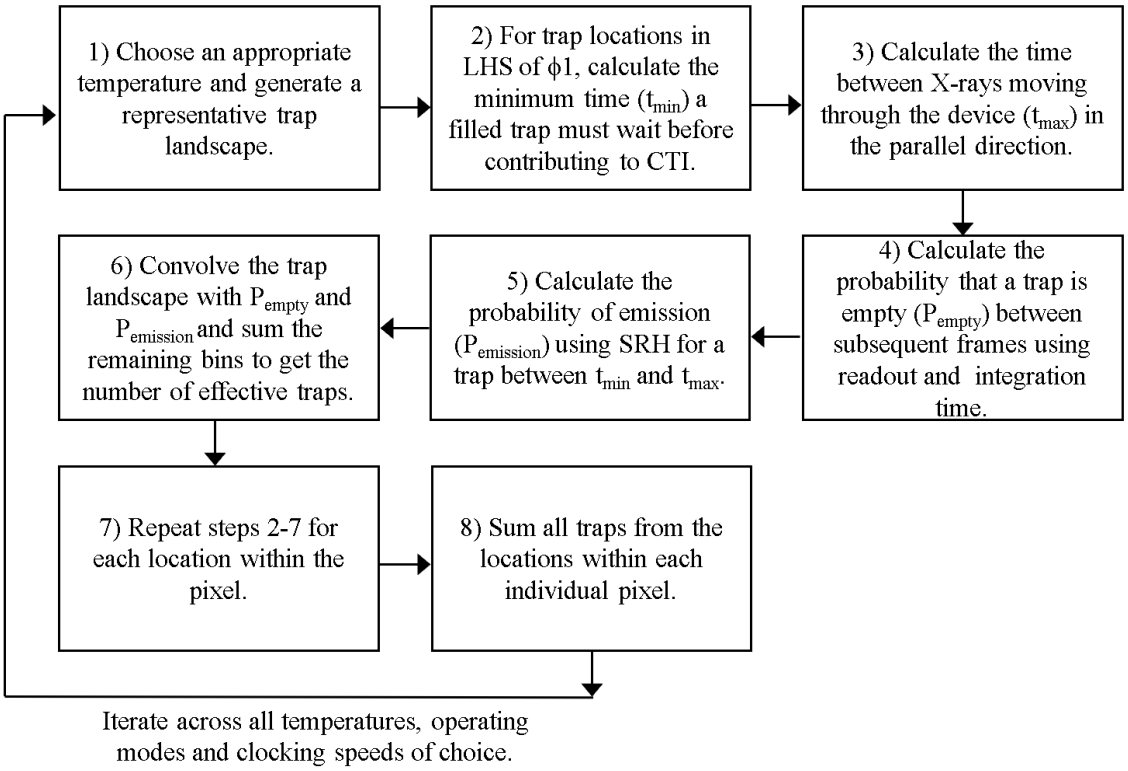


**Figure 6.2**: Flowchart showing the steps of the ATM to estimate the number of effective traps that will degrade CTI in a specific device and readout mode.

### 6.1.1. Generating initial trap landscapes

To correctly estimate the effective number of traps, the most representative initial trap landscape must be used with respect to both irradiation conditions and fluence alongside the operating temperature. Using either a room-temperature (RT) or cryogenically irradiated landscape ensures that the correct distribution of traps are present when comparing the number of effective traps to a CTI value. The correct operating temperature ensures that the emission time constants are in the correct position within the trap landscape. Figure 6.3 shows the same RT landscape generated at three different temperatures. As temperature increases, the entire landscape shifts to a faster emission time constant, while still retaining the same distribution.

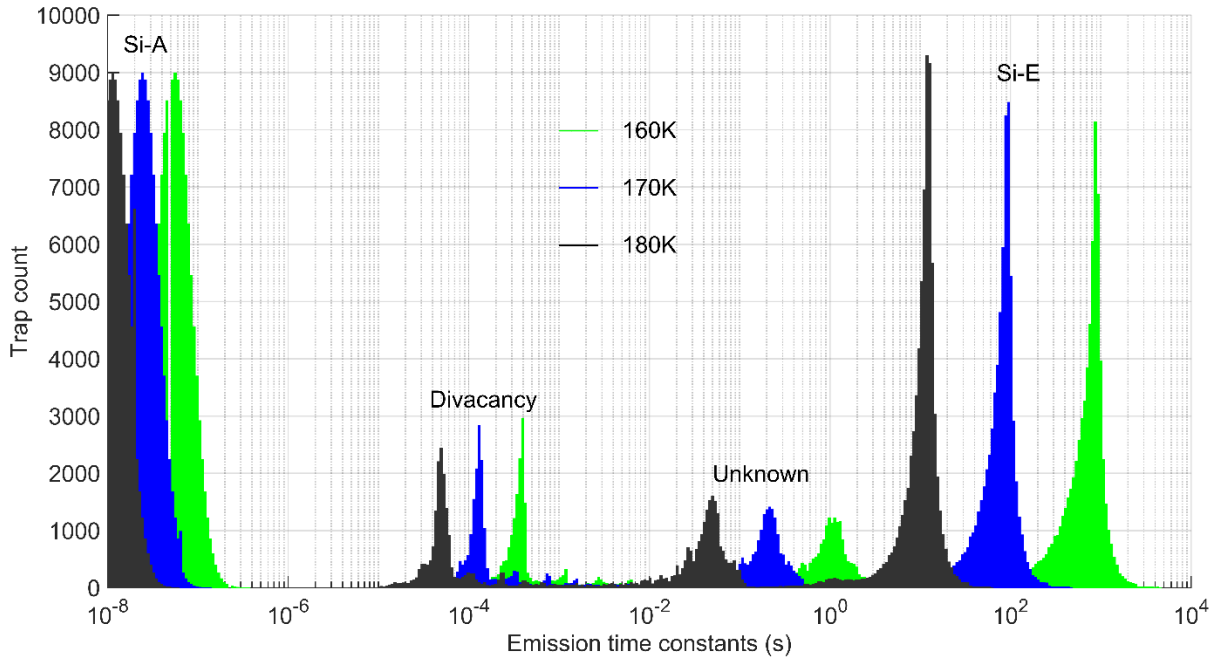


**Figure 6.3**: Generated trap landscapes for a CCD204 at three temperatures, with the main radiation-induced defects highlighted for clarity (Bush, N. et al., 2018).

### 6.1.2. Calculating the lower time threshold for effective traps

The minimum timing defines the trap with the quickest emission time constant that can contribute to CTI and hence be counted as an effective trap. Any traps with a quicker emission time constant than the minimum timing will most likely emit back into the source charge packet and will not contribute to CTI. In terms of device performance, the minimum timing value originates from the timings within the device in question, namely the parallel and serial clocking speeds.

Previous work calculated the minimum timings for traps within each electrode of a single pixel separately but assumed that the trap position within the electrode was irrelevant (Bush, N et al., 2020; Bush et al., 2018). Figure 6.4 (left) shows this whole-electrode approach outlined specifically for a four-phase CCD. Charge is moved sequentially from phase one through to four, with the serial register readout in stage one. The total time for each stage of the transfer process is indicated by the time y-axis. The time $t_{serial}$ is the time taken to readout the serial register, and the time $t_{image}$ is the time taken to shift charge from under a single electrode in the parallel direction. Using this diagram, it is possible to calculate the minimum time that a filled

trap (in different locations in the pixel) must wait before emission can occur into a non-source charge packet and be classified as an effective trap that contributes to CTI.

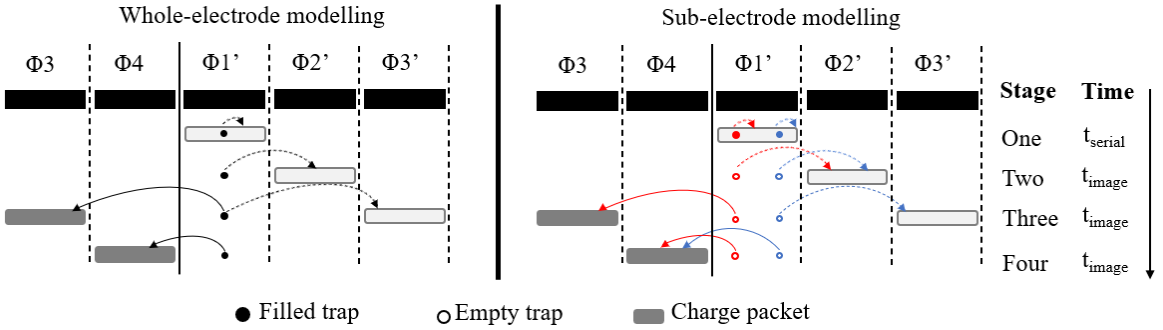


**Figure 6.4**: Trap emission dynamics for a four-phase CCD using the whole-electrode (previous work) or sub-electrode (developed here) modelling approach. Note that the dashed and solid lines represent emission back into the source and non-source charge packet, respectively. Also note that for the whole-electrode modelling, the defect is assumed to be in the centre of the electrode.

Defects present under electrode one fill during stage one of the transfer process. Once charge capture occurs, emission can occur and potentially contribute to CTI. As charge moves to phase two, any emission that occurs will mean that the captured electron re-joins the source charge packet as the source charge packet is still the closest charge packet. When the charge packet moves to electrode three, the whole-electrode approach now faces a complication, as both the succeeding and source charge packet are equidistant from the filled trap. This means that it is not clear whether the time taken for stage three ($t_{image}$) should be included when calculating the lower limit time threshold.

#### 6.1.2.1. Sub-electrode modelling

The issue can be ameliorated by instead considering defects within each half electrode, as seen in Figure 6.4 (right). Analysing the emission of defects under phase one once again, defects under the left-hand-side (LHS) of electrode one emit into the non-source packet and thus the time taken for this stage of transfer is not included in the minimum threshold time. On the other hand, defects on the right-hand-side (RHS) of electrode one are closer to the source charge

packet and thus when emission occurs, emission does not contribute to CTI. This means that the time taken for stage three **is** included in the minimum threshold time.

By repeating the procedure for each half electrode, it is possible to precisely calculate the minimum threshold time. Table 6.1 summarises the minimum threshold times calculated for trap positions in both the whole-electrode and sub-electrode model. Due to the uncertainty of the trap emission dynamics within the whole-electrode model, the whole-electrode model cannot precisely predict the minimum threshold timing. This contrasts with the sub-electrode model, which more precisely calculates the minimum threshold timing.

**Table 6.1**: Minimum threshold timings calculated for both the whole-electrode and sub-electrode modelling. Note that the whole-electrode minimum timing is identical for both trap positions within the electrode as the electrode is not sub-divided into halves.

| **Electrode** | **Trap position within electrode** | **Whole electrode model $t_{minimum}$** | **Sub electrode model $t_{minimum}$** |
|---|---|---|---|
| 1 | Left | $t_{serial} + t_{image}$ *or* $t_{serial} + 2t_{image}$ | $t_{serial} + t_{image}$ |
| 1 | Right | $t_{serial} + t_{image}$ *or* $t_{serial} + 2t_{image}$ | $t_{serial} + 2t_{image}$ |
| 2 | Left | $2_{image}$ *or* $3_{image}$ | $2t_{image}$ |
| 2 | Right | $2t_{image}$ *or* $3t_{image}$ | $3t_{image}$ |
| 3 | Left | $2t_{image}$ *or* $3t_{image}$ | $2t_{image}$ |
| 3 | Right | $2t_{image}$ *or* $3t_{image}$ | $2t_{image} + t_{serial}$ |
| 4 | Left | $3t_{image}$ *or* $3t_{image} + t_{serial}$ | $t_{image} + t_{serial}$ |
| 4 | Right | $3t_{image}$ *or* $3t_{image} + t_{serial}$ | $t_{serial} + 2t_{image}$ |

The main issue with using the approximate whole-electrode model is the difference between $t_{image}$ and $t_{serial}$ timings, with approximate values shown in Figure 6.5. The time to readout the serial register ($t_{serial}$) is significantly longer than the parallel timing ($t_{image}$), meaning that the window (the time between the minimum and maximum threshold) for the effective number of traps is significantly reduced. Any electrode position when the $t_{serial}$ is included in the minimum timing threshold will greatly affect the number of effective traps estimated by the analytical model. This means that the sub-electrode model must be used to accurately calculate the

minimum threshold time, as the whole-electrode model miscalculates the contribution from the image and serial timings respectively.

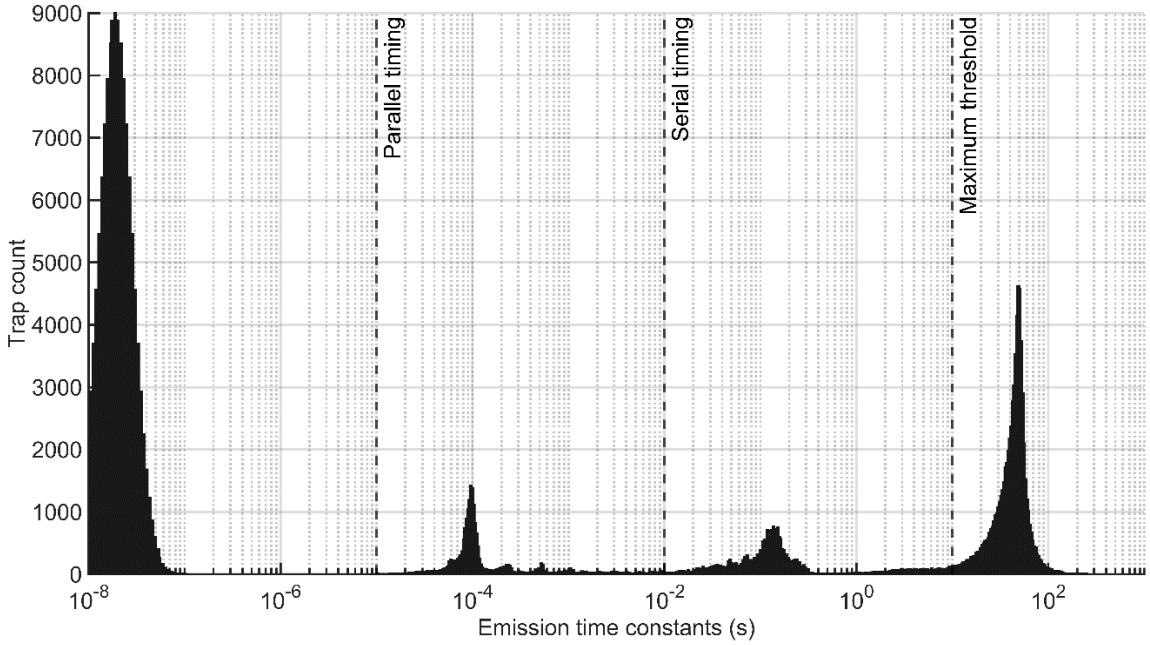


**Figure 6.5**: Trap landscape (CCD204) showing the maximum threshold along with two minimum thresholds, namely the parallel and serial timing. The parallel timing is the time taken to move charge from one electrode to the next ($t_{image}$ in Figure 6.4) and the serial timing is the time taken to empty the serial register ($t_{serial}$ in Figure 6.4).

### 6.1.3. Calculating the time between X-rays

Once the minimum threshold is calculated, the next stage of the ATM is to calculate the maximum threshold. The boundary defines the slowest trap that will be counted as an effective trap and contribute to CTI, any defects that have an emission time constant slower than the upper threshold will not be counted as an effective trap. Physically, this value is defined by the presence of additional charge, either in the form of X-rays often used to measure CTI or supplemental charge injection (often used to reduce CTI). The density of X-rays or number of lines of charge injection has a direct effect on the location of the upper threshold.

As this external charge is moved through the device, it passes over defects, filling them as it moves. If a defect is filled, it cannot capture additional charge and is thus effectively suppressed with respect to degrading CTI. If a higher X-ray density is present, this means that X-rays pass

over defects more frequently, lowering the time between X-rays. As a result, the maximum threshold is lowered, and traps with a faster emission time constant are now suppressed.

### 6.1.4. Probability of empty traps

For a trap to contribute to CTI, it must capture charge from a charge packet and then emit this charge back into the non-source charge packet. This means that the trap must first be *empty*, or charge capture cannot occur, and the trap cannot contribute to CTI. For a fully physical and representative analytical model, this means that the proportion of traps that are empty or full must be calculated.

To be able to calculate the proportion of traps that are empty (and can contribute to CTI) both the readout speed and integration time used must be considered. When X-ray CTI data is collected, many frames are often read out (this is also true for SXI science operating modes) to ensure that an X-ray spectrum can be seen above the detector noise. This means that between frames, traps emit their captured charge and are thus empty to capture charge for the next X-ray CTI frame. Section 6.1.5 will outline how the probability of empty traps is calculated.

### 6.1.5. Calculating probability of emission and the probability of empty traps

Once the minimum and maximum times have been calculated for different locations within each pixel, the probability that a trap will emit within these two timings can be calculated via SRH with Eq 6.1, starting with the general form for emission between times $t_1$ and $t_2$:

$$\text{Probability of emission} = \exp\left(\frac{-t_1}{\tau_e}\right) - \exp\left(\frac{-t_2}{\tau_e}\right) \qquad \text{Eq 6.1}$$

Substituting $t_1 = t_{min}$ and $t_2 = t_{max}$ leads to the expression for the probability that traps of emission time constant $\tau_e$ will emit between the times of $t_{min}$ and $t_{max}$ (Eq 6.2).

$$\text{Probability of emission} = \exp\left(\frac{-t_{min}}{\tau_e}\right) - \exp\left(\frac{-t_{max}}{\tau_e}\right) \qquad \text{Eq 6.2}$$

Similarly, the probability of a trap emptying between frames is given by the equation:

$$\text{Probability of empty traps} = \exp\left(\frac{-0}{\tau_e}\right) - \exp\left(\frac{-t_{r+int}}{\tau_e}\right) \qquad \text{Eq 6.3}$$

where $t_{r+int}$ is the time to read out a single frame plus the integration time. Once calculated, the probability of emission and probability of empty traps can be used in combination with the trap landscape to calculate the total number of effective traps. A graphical representation of the trap landscape and associated probability functions are shown in Figure 6.6.

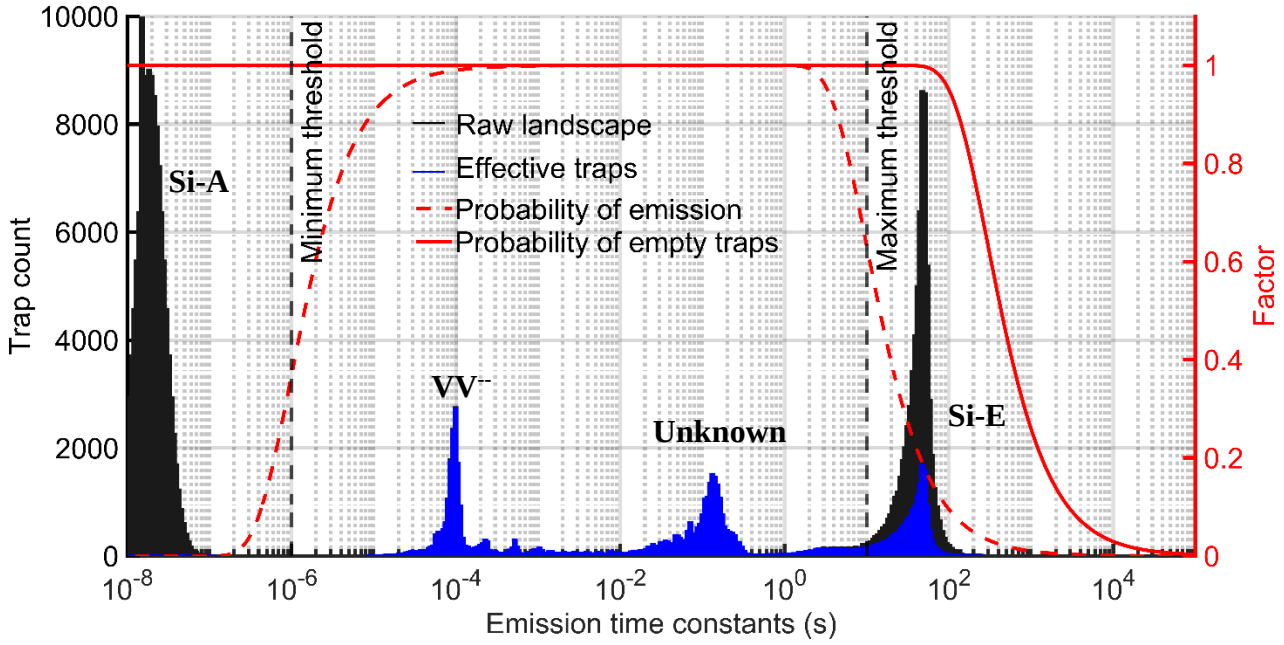


**Figure 6.6**: Raw trap landscape from an irradiated CCD204 in black (Bush, N. et al., 2018). The effective trap landscape is shown in blue which is attained by convolving the raw trap landscape with the two red probability functions. Each of the main radiation induced species is highlighted for clarity. Note that between $10^{-4}$ s and 1s, the black distribution is identical to that of the blue distribution.

The black distribution in Figure 6.6 represents the total defects within an irradiated CCD204 and the left y-axis shows the total trap counts within each bin. The probability of emission and probability of empty traps are represented by the red dashed and solid line respectively and are associated with the right y-axis. A factor of one represents a 100% probability of emission and 100% probability of a trap being empty. Alternatively, a factor of 0 represents a 0% chance of emission and a filled trap.

To calculate the effective number of traps (blue distribution) the raw landscape (black distribution) is convolved with both the probability of emission and probability of empty traps.

In the example of Figure 6.6, the timings used within the ATM affect different parts of the landscape in regard to the number of effective traps. For example, the effective trap contributions from the Si-E are suppressed due to the maximum threshold timing lowering the probability of emission of most of the Si-E defect. This is shown explicitly by the difference in peak height of the Si-E for the raw and effective traps landscape, respectively.

For the area containing the divacancy and unknown defect, the timings used within the device mean that 100% of the defects between approximately $1 \times 10^{-4}$ s and 1 s emit and contribute to the effective number of traps, once again explicitly shown by the identical height of both the raw and effective trap landscape in this region.

## 6.2. Applying the improved model to SMILE SXI CCDs

Using the method outlined in the section above, it is now possible to fully simulate the number of effective traps for a given operating scheme, allowing explicit comparisons between ATM performance and experimental X-ray CTI measurements. As a result, focus will now turn towards replicating trends in X-ray CTI data that were collected as part of the SMILE SXI OU radiation campaign.

The SMILE SXI OU radiation campaign has several stages utilising different devices under different irradiation and operating conditions. This led to a significant amount of data collected from both room-temperature and cryogenic irradiations with a CCD280, including X-ray CTI data with and without charge injection. Due to different landscapes present in both a room-temperature and cryogenic irradiation; this means that a different input landscape must be used as part of the ATM. This provides opportunity to validate the performance of the analytical model with different input parameters before using the model to make predictions about the performance of the CCD370 under cryogenic irradiation conditions.

### 6.2.1. Comparisons to room-temperature irradiation results

The first irradiation as part of the SMILE SXI OU radiation campaign was a CCD280 irradiated at room-temperature at the Birmingham Proton Facility in the UK. The device was irradiated with a fluence of $3.43 \times 10^{9}$ p/cm$^{2}$ (Parsons, S., 2019, p. 280) (10 MeV proton equivalent) and subsequent post-irradiation characterisation tests were carried out including measurements of dark signal, quantity of bright defects, EPER, FPR and X-ray CTI. For the purposes of the

analysis here, the operational parameters of the CCD280 during the collection of X-ray CTI data are of most interest. The operating parameters used are shown in Table 6.2 and will be used as inputs to the analytical model.

To measure X-ray CTI, an Fe55 X-ray source was used due to ease-of-use and availability. Although the energy of each X-ray photon is higher than that seen by SXI in-orbit, the energy dependence of X-ray CTI is weak, therefore the benefits of using the Fe55 source outweigh the extra effect required to setup a system capable of generating different (more mission-like) X-ray photon energies.

**Table 6.2**: Experimental parameters used to collect X-ray CTI data from the CCD280 room-temperature irradiations (Parsons, S., 2019, p. 280). Note that the image line transfer time is the time to transfer charge across four electrodes, whereas $t_{image}$ is equal to the image line transfer time divided by four (for the case of this four-phase device).

| **Parameter** | **Value** |
|---|---|
| Image line transfer time (s) | $58 \times 10^{-6}$ |
| Serial clocking speed (kHz) | 50 |
| Operating temperature (K) | 143 - 188 |
| Input trap landscape (Room temperature or cryogenic) | Room temperature (CCD204) |
| Pixels read per row | 1500 |
| Integration time (s) | 300 |
| X-ray density (per native pixel) | 1/110 |

### 6.2.2. CTI and effective traps as a function of temperature

Using the parameters in Table 6.2 as input to the ATM, the change in CTI and number of effective traps as a function of temperature can be compared, shown by Figure 6.7. Although the number of effective traps can be estimated from the ATM along with the change in traps as a function of temperature, the absolute CTI value caused due to these traps is unknown. This means that for comparisons between experimental CTI and the ATM, the result must be normalised to a specific temperature. Figure 6.7 shows the result normalised to both 143 K

(left) and 188 K (right). A key point to note is that the trap landscape initially used an input to the ATM is from a CCD204, as this trap landscape was all that was available initially. Section 6.2.4 provides additional information as to why the CCD204 landscape was used, and how the model fit was improved by using a CCD280 landscape as measured by the author.

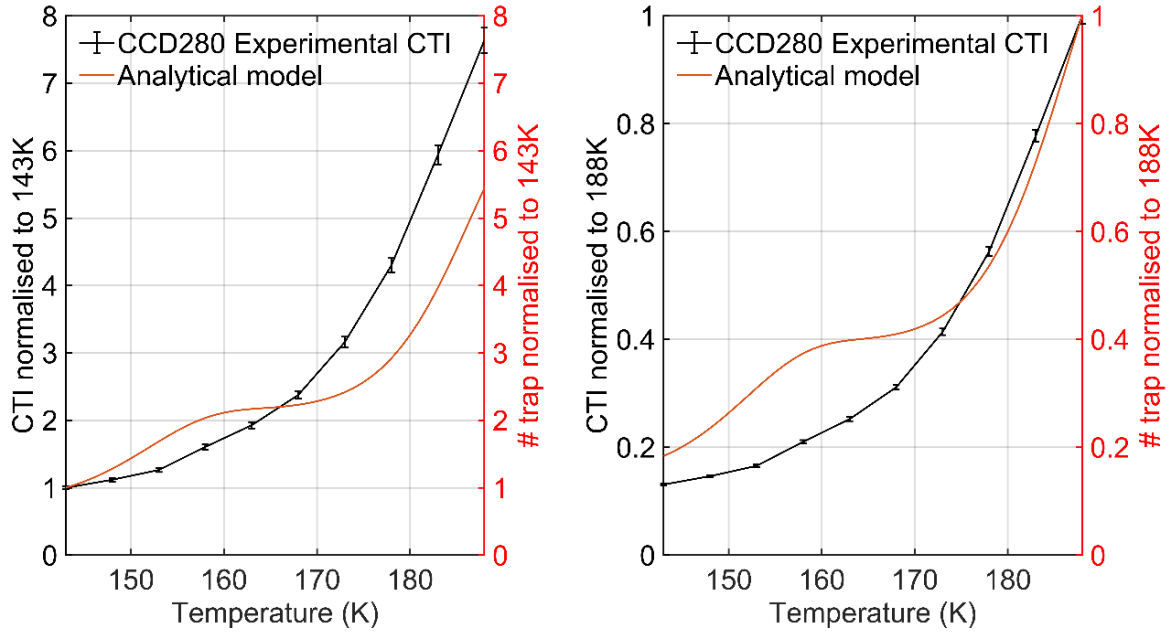


**Figure 6.7**: Comparison between CCD280 X-ray CTI measurements (room-temperature irradiation) and the number of effective traps predicted by the analytical model. Note that the trap landscape used an input to the ATM here is from a CCD204.

The ATM correctly predicts the general trend of increasing CTI as a function of temperature. However, at certain temperature ranges, the model under/over predicts the increase/decrease in the effective number of traps. For example, between 143 K and approximately 160 K the number of effective traps is overestimated, for both normalisation temperatures, albeit of slightly different magnitudes. Conversely, at high temperatures between approximately 175 K and 188 K, the number of defects is underestimated, with a higher underestimate seen in the 143 K normalised figure. In the mid temperature range (approximately 160 K to approximately 175 K) the rate of change of effective traps plateaus, whereas the CTI continues to rise.

The reasons for the discrepancy between the ATM results and the experimental results would most likely result from inputs to the ATM, and not unreliable experimental results. The trends seen in the X-ray CTI data are consistent with previous results (of room-temperature

irradiations), along with the absolute value of CTI being reasonable. This means that incorrect input values used to ATM (in particular the trap landscape) are causing the discrepancy seen in Figure 6.7.

### 6.2.3. Contributions from individual defects

The strength of the ATM is that it can determine precisely which traps are contributing to the number of effective traps and where exactly they are found in the defect landscape. Figure 6.8 shows the effective trap landscape for four temperatures across the range presented in Figure 6.7.

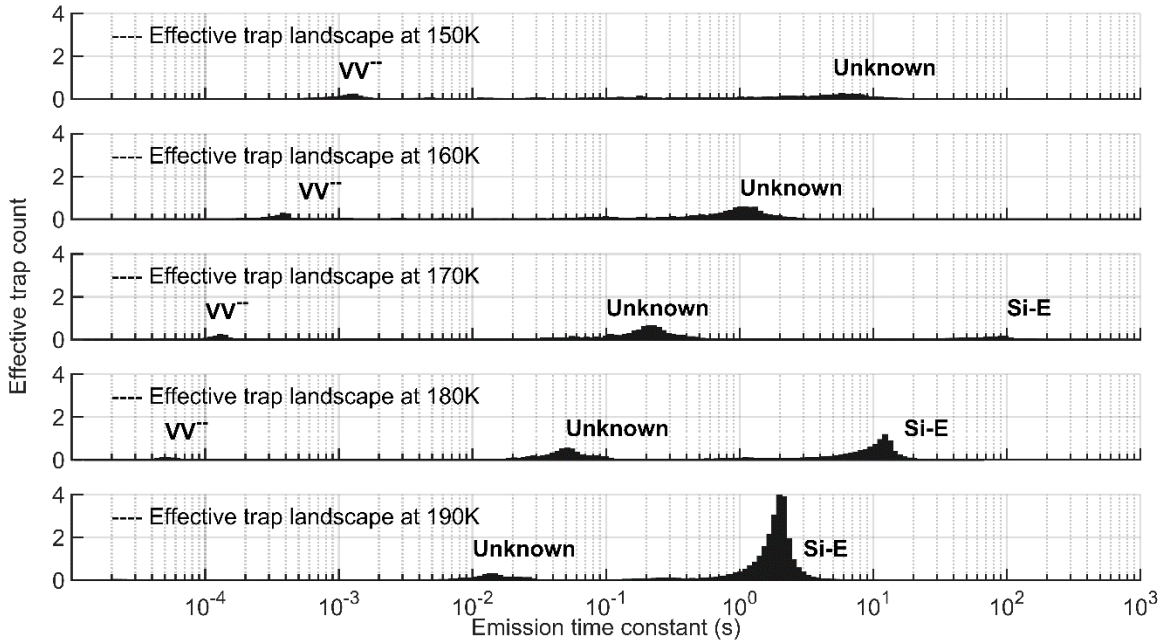


**Figure 6.8**: Effective trap landscapes for five temperatures, showing which parts of the trap landscape dominate the total number of effective traps. The double negative state of the divacancy, unknown and Si-E are highlighted for clarity.

As temperature increases the entire landscape is shifted towards quicker emission time constants, consistent with the fundamental relationship of SRH theory. Due to the shifting landscape however, different defect species are influenced by the probability of emission curves (shown previously in Figure 6.6), meaning that the total contributions from each species changes at each temperature. This is seen qualitatively by the simultaneous decrease of the

divacancy peak and the increase of both the unknown and Si-E trap as a function of increasing temperature.

For a more rigorous and quantitative analysis, the effective trap contributions of each of the main peaks can be compared to the total number of effective traps at each temperature. This will provide the percentage of the total number of effective traps that are contributed by each peak, allowing additional insight into the shape of the curve shown in Figure 6.7. To be able to do this however, limits must be imposed to define the main peak of each defect, with the limits shown in red, blue, and green, representing the peak limits of the divacancy, unknown and Si-E defect respectively (seen in Figure 6.9).

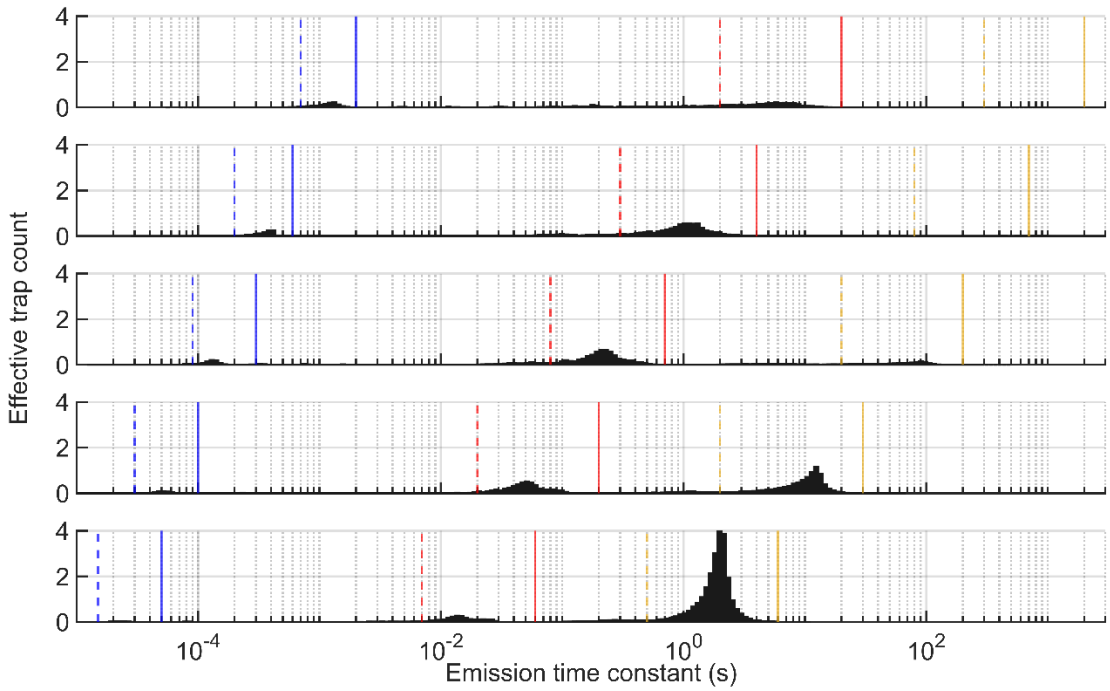


**Figure 6.9**: Identical landscapes to those in Figure 6.8 but with added limits defining the peaks of the divacancy, unknown and Si-E defect. The limits imposed were added manually and do not represent any pertinent physical boundary with the defect behaviour or distribution. It is only used to illustrate which specific peaks dominate the number of effective traps predicted by the analytical model.

Figure 6.10 shows the percentage of total effective traps for the three main defects in the parameter space, the divacancy, unknown, and Si-E. Defects falling into the “other” category are those which do not fall within the main peaks, most notably the area between the divacancy

and unknown as well as between the unknown and Si-E. The five temperatures highlighted in Figure 6.8 have been used, along with an additional temperature at 190 K to emphasise the trend shown.

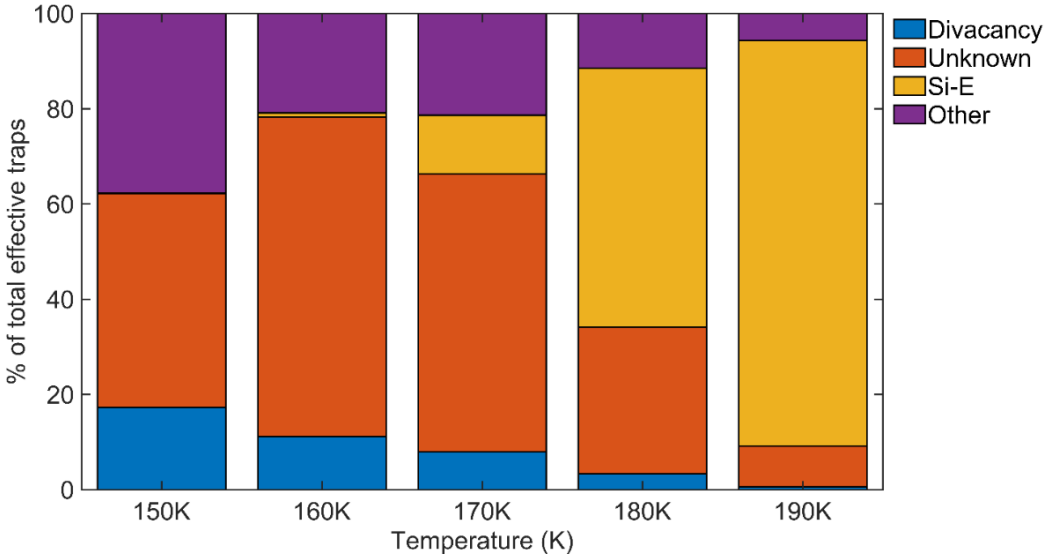


**Figure 6.10**: Stacked bar chart showing the percentage contributions from the main defects in the parameter space.

The general trends in Figure 6.10 show a steady shift from the unknown defect and "other" defects being the main source of effective traps at lower temperatures, to the Si-E being the dominant source of effective traps at high temperatures. Although the divacancy is considered one of the main defects in the parameter space for irradiated N-channel CCDs, due to the abundance of unknown and then Si-E defects, it contributes only a minority of effective traps, even at low temperatures.

The percentage change in contributions from different species of defects can be used to explain the trends seen in the analytical model curve in Figure 6.7 and hence infer reasons for potential differences between the experimental CTI data and ATM output. The over-estimation of defects in the model solution between 143 K and approximately 160 K is from the abundance of unknown defects being the dominant sources of effective traps. The plateau between approximately 160 K and approximately 170 K is due to the Si-E traps still not contributing a significant amount to the total number of effective traps, in combination with the divacancy and unknown defect decreasing in contribution to the total number of effective traps due to the probability of emission curves.

To utilise the ATM described to provide optimal CCD370 operating conditions, the analytical model fit must be improved to increase the validity of the subsequent results. Discussion now turns to towards methods to improve the ATM, focusing on the input trap landscape used in the analytical solution.

### 6.2.4. Improving the analytical model fit

The analytical model curves in Figure 6.7 are representative of the main defects within the parameter space, namely the divacancy and unknown trap at lower temperatures, and mainly the Si-E at higher temperatures. The relative concentration of the main defects will clearly have an impact on the shape of the curve in the ATM and hence the extent to which the CTI data matches the ATM prediction. If the relative concentrations of the three main defects can be measured in the CCD280, this can then be compared to the CCD204 landscape that was used to generate the analytical model solution seen in Figure 6.7. Potential differences in the landscapes can then be used to infer the characteristic shapes seen in Figure 6.7.

The previous chapter briefly described initial trap pumping data from the room-temperature irradiated CCD280 (Figure 6.11) and will be an excellent starting point for the analysis presented in the remainder of this chapter.

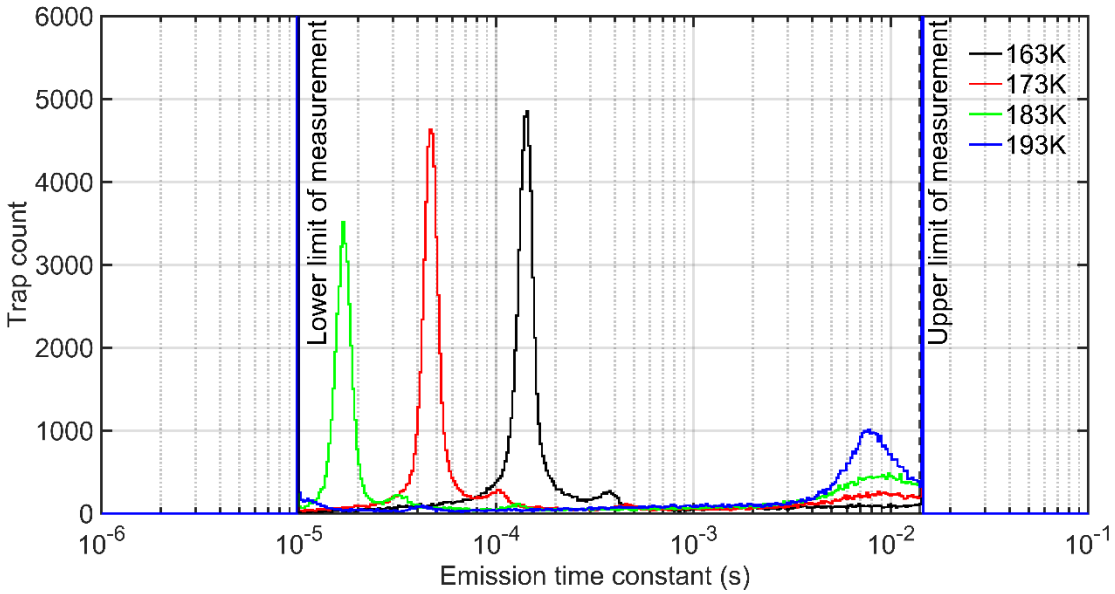


**Figure 6.11**: Trap landscapes directly measured in the CCD280 post-irradiation. The lower and upper limit of measurement are defined by the parallel clock speed and time allocation for this phase of characterisation, respectively.

From these data, it is possible to attain estimates of the relative concentrations of the unknown and divacancy defect. However, due to defects moving in/out of the parameters space, along with analysis quirks, it is initially difficult to compare concentrations of the two defects at each temperature. For example, the peak height of the divacancy changes with temperature, which is unexpected as changing temperature should only change the emission time constant of the defects probed, and not the total number. The reason for this discrepancy is due to the fitting algorithm used in relation to individual dipole intensity curves (example shown in Figure 6.12). At the edge of the parameter space ($10^{-1}$ s for example), the fitting algorithm is attempting to fit functions to incomplete dipole curves, leading to reduced R (goodness of fit) values. This means that when the fitted dipole curves are filtered based on R value, more dipole fits are below the threshold, leading to a lower number of total identified defects. This means that as abundant defects approach the edge of the measured parameter space, the total count of that specific defect reduces, and at a larger rate with increasing proximity to the lower measurement limit. Towards the centre of the parameter space the fitting algorithm can fit to curves with a larger number of points, giving more defects with an increased R value and hence a more physically representative count.

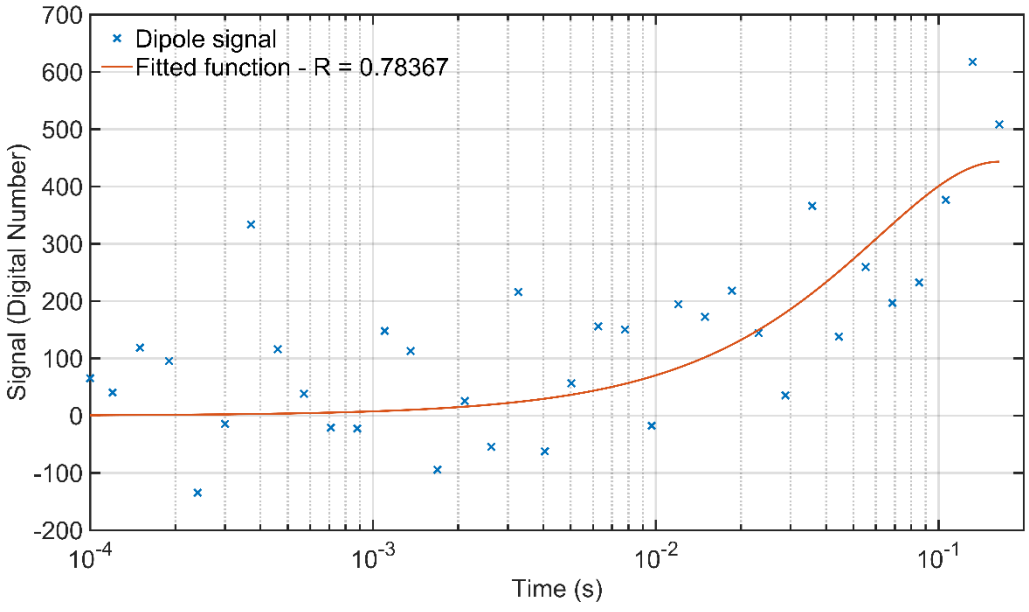


**Figure 6.12**: Example of a poor dipole fit to a pumped trap that has an emission time constant out of the pumped range of times.

Taking this effect into account for Figure 6.11, means that the divacancy peak with the most representative count is most likely the black peak at 163 K, giving a value of ~5000. For the unknown defect, the peak at 193 K (blue line) is the clearest at approximately 939. The author notes however, that the unknown peak at 193 K is very close to the edge of the parameter space, so potentially could be undercounted in an identical manner to that of the divacancy as described above. To account for this, the percentage change from the blue to black peak of the divacancy is ~40% higher. Applying the same percentage change to the unknown gives an upper limit of ~1300 (939×1.4). Comparing the ratio of divacancies to unknown defects within the CCD204 and CCD280 lead to the results seen in Table 6.3.

**Table 6.3**: Summary of the divacancy and unknown trap counts (in the main peak) for the CCD204 and CCD280.

| **Device** | **Fluence (10 MeV equivalent)** | **Divacancy trap count** | **Unknown trap count** | **Ratio of divacancy to unknown** |
|---|---|---|---|---|
| CCD204 | $1 \times 10^9$ p/cm$^2$ [3] | 2900 | 1800 | **1.61** |
| CCD280 | $3.34 \times 10^9$ p/cm$^2$ [6] | 5000 | 1300 | **3.85** |

A significant discrepancy is seen between the ratio of the divacancy to unknown when comparing the CCD204 to the CCD280. The CCD280 has more than twice the quantity of divacancy defects compared to unknown defects. It is unclear at this stage if the number of divacancies are overrepresented in the CCD280 or if the number of unknown defects is underrepresented.

Potential reasons for the differences are summarised below:

- Differences in raw materials used and manufacturing processes at Teledyne-e2v and the knock-on effect in terms of the number of unknown defects. The CCD204 is significantly older than the CCD280 and thus the ratio/quantities of intrinsic defects present may be different between the two devices. Due to the uncertainty surrounding

the source of the unknown defect, it is not understood how potential differences in the quantity of intrinsic defects affects the quantity of unknown defects.

- Many studies have looked at the divacancy defect in silicon over many years (Lindley-DeCaire et al., 2019; Wood, Daniel, 2018). The mechanism behind the creation of divacancies is well understood, and as such introduction rates of divacancy defects are also well understood. At this stage, it is more likely that the number of divacancies reported in the CCD280 are reasonable, and the variation in unknown defect quantities is more likely to be causing the discrepancy seen in the results above.
- The landscape from the CCD280 is from a room-temperature irradiation whereas the landscape from the CCD204 is from a cryogenic irradiation followed by a room-temperature anneal. Differences between the landscapes in a room-temperature and cryogenic landscape are well understood, however the differences between a room-temperature irradiation and a cryogenic irradiation (followed by a room-temperature anneal) are not well understood.
- Knowledge of the fluence used in irradiations is important as the number of radiation-induced defects should increase with fluence. Although in this case, different devices are being compared (with different pixel architectures and sizes), it is difficult to disentangle the effect of both differing fluence and device architecture. Nevertheless, fluence should always be considered when comparing levels of radiation-induced defects in devices.

### 6.2.5. Using the CCD280 trap landscape

As a significant discrepancy is seen between the ratios of the divacancy and unknown defect, this means that the comparison in Figure 6.7 between the ATM and CTI data is not a fair comparison. Due to the differences in landscape between the CCD280 and CCD204, it is difficult to say whether the differences between the ATM and CTI data are due to incorrect or inaccurate model assumptions or solely due to discrepancies in the landscape defect distribution.

The landscapes containing the divacancy and unknown (Figure 6.11) can be combined to form a representative landscape, with this landscape then be used as input to the ATM. However, the trap pumping data collected and shown in Figure 6.11 are at different temperatures, as well

as the CTI data in Figure 6.7 being taken at an even wider range of temperatures. To correct this issue, the known literature values for the energy level and cross section of both the divacancy and unknown defect can be used (Bush, Nathan L., 2018), in combination with SRH, to shift the emission time constant of both landscapes. Figure 6.13 shows the original trap pumping data (top) with the combined and temperature corrected data beneath.

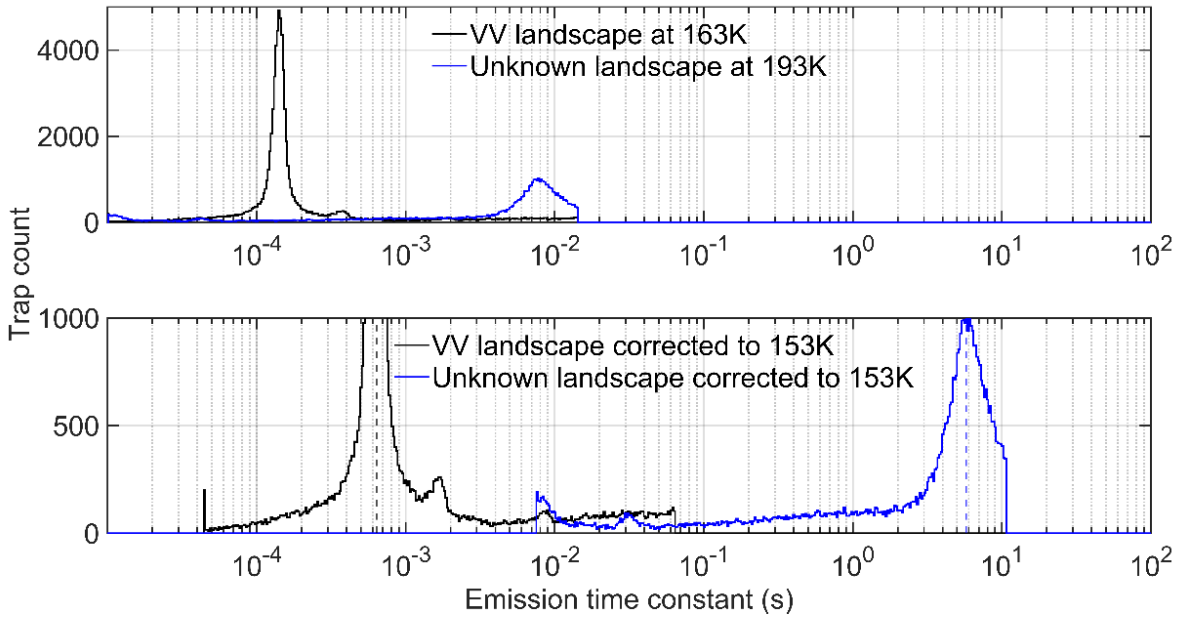


**Figure 6.13**: Original trap pumping data (top) along with the temperature-corrected landscape below. The black and blue dashed line represent the known peak emission time constants of the divacancy and unknown defect respectively.

Figure 6.13 (bottom) shows the distribution of emission time constants for both temperature-corrected landscapes, with the peak of the divacancy and unknown defect aligning with the known literature values (Bush, Nathan L., 2018). However, there is some overlap between the two landscapes, as although different temperatures were used to probe both the divacancy and unknown (163 K and 193 K respectively), some overlap in emission time constant is still present. This is shown most explicitly by the presence of the small peak visible in both the divacancy corrected landscape ($8.5 \times 10^{-3}$ s) and unknown corrected landscape ($3 \times 10^{-2}$ s).

Utilising the known literature values of the divacancy and unknown defect to temperature-correct the landscape does work (as seen by Figure 6.13 (bottom)), however this does not necessarily mean that the remainder of the trap landscape is situated at the correct emission time constant. The reason for this discrepancy is the use of log-spaced bins which is necessary

given the wide range of emission time constants probed. As emission time constants are shifted, emission time constants further away from the corrected peak values are more inaccurate, and the landscape do not align as expected.

To ameliorate the issue, the average of number of defects located between the emission time constant values of $7.5 \times 10^{-3}$ s and $6.3 \times 10^{-2}$ s for both the divacancy and unknown can be used to create a complete landscape. Although this is not a completely physically correct landscape, the distribution of defects between these two points is relatively flat and not dominated by a known abundant defect (such as the divacancy, unknown or Si-E). Furthermore, this approximate defect landscape will be subsequently used as input to the analytical model, to provide an updated curve for Figure 6.7. Figure 6.8 defects in the parameters space, namely the divacancy and unknown at low temperatures showed that the characteristic shape of the ATM curve is dictated by the largest and most abundant. This means that the approximate average defects values used for the range $7.5 \times 10^{-3}$ s and $6.3 \times 10^{-2}$ s are less important, compared to the locations of the main divacancy and unknown peak, which have been temperature-corrected to known literature values (Bush, Nathan L., 2018).

Once average values are calculated, they are used instead of the landscape from either the divacancy or the unknown trap landscape. Figure 6.14 shows the combined CCD280 landscape, with the CCD204 landscape as a reference for comparison.

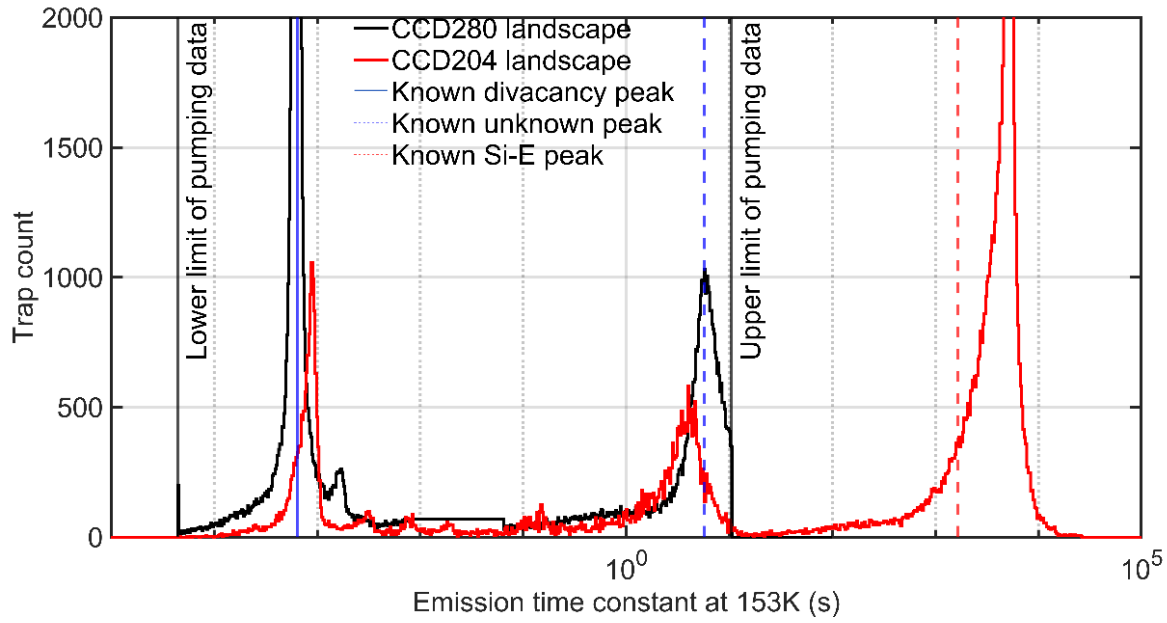


**Figure 6.14**: Comparison defect landscape between the CCD280 and CCD204 with superimposed known peak locations of the divacancy, unknown and Si-E defects. Note that the CCD280 landscape is from combined landscapes from the bottom panel in Figure 6.13.

By design, the peaks of the divacancy and unknown defect in the CCD280 data match the positions in the literature (Bush, Nathan L., 2018). The flat, unphysical, region of defects between the emission time constants of approximately $10^{-2}$ s and $10^{-1}$ s is the location in which the average level of defects between the divacancy and unknown trap pumping data was used. The lower and upper limit of trap pumping data collection is also shown, and as such excludes the Si-E and Si-A as mentioned previously.

The CCD204 landscape is included as a comparison, and shows unexpected trends with respect to the peak location of the divacancy, unknown defect and Si-E. All three defects show some offset between the measured literature values and measured experimental values. The CCD204 data was acquired under a different study and not by the author, so the experimental procedure used to acquire the data makes troubleshooting difficult. However, the temperature sensor used to collect the CCD204 trap pumping data was a platinum resistance thermometer (PRT) PT100, the less accurate version of the PRT1000. This means that a small amount of error may have been introduced, adding a systematic offset to the measurements. However, for the three peaks seen in the CCD204 data (Figure 6.14), the difference between the literature and experimental

value is not consistent, with the Si-E and divacancy peak slower than expected, and the unknown defect quicker than expected, suggesting a non-systematic error.

Another potential reason for the offset seen is the ambient temperature in the laboratory at the time of data acquisition. Due to the exponential nature of the SRH equations, only a small change in ambient lab temperature could produce a noticeable shift in the peak emission time constants of defects. However, the CCD is thermally isolated inside a vacuum (with its own temperature controller), so sources of error from external factors are unlikely. Further investigations into the temperature inconsistencies are difficult, and as such, provide even more reason to use a trap landscape taken during this study by the author, with known experimental conditions and well-understood limitations.

Using the CCD280 landscape as input to the ATM is an improvement in terms of the defects located between the emission time ranges of $10^{-4}$ s and the upper limit of trap pumping data ($10^{-1}$ s). However, as mentioned previously (and seen in Figure 6.14), the abundant Si-E defect is not included within the CCD280 trap pumping data, as the upper limit of probed emission time constant was significantly below the Si-E defect at 153 K. Consequently, using the CCD280 trap landscape in the ATM will not accurately predict the number of defects at higher temperature ranges.

This issue can be fixed, however, as the Si-E is an extensively studied defect, with a known energy level and cross section. Utilising the known energy level and cross section (Bush, Nathan L., 2018), in combination with SRH, it is possible to add the Si-E defect peak into the CCD280 landscape in the form of a gaussian peak with known height, as seen in Figure 6.15.

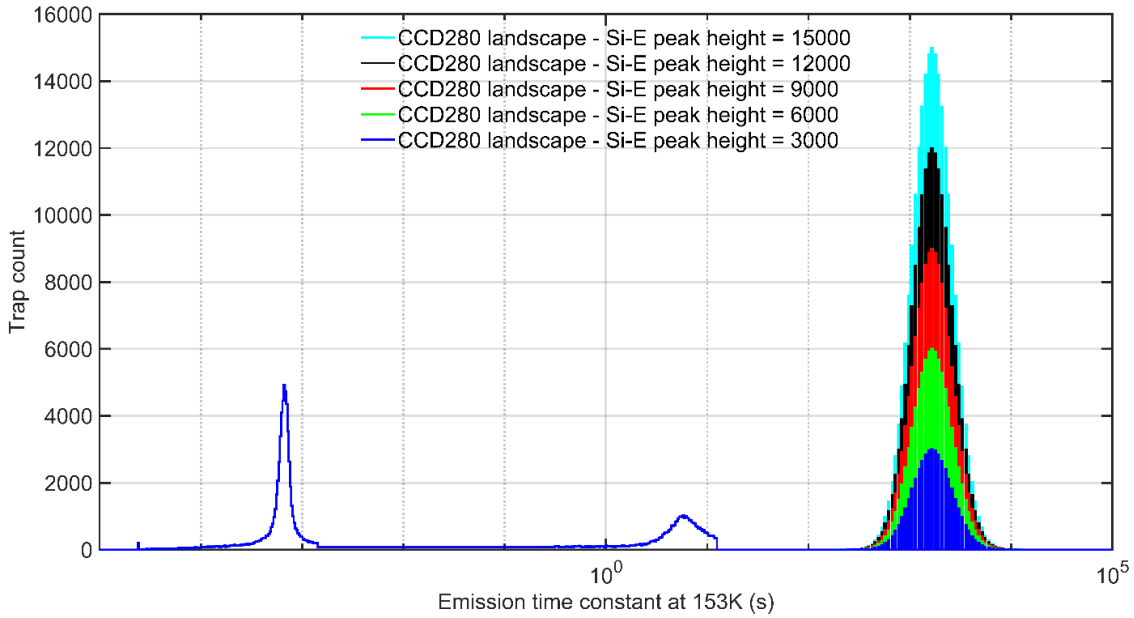


**Figure 6.15**: CCD280 trap landscape with a gaussian shaped Si-E peak added based upon known literature energy level and cross section values (Bush, Nathan L., 2018). Gaussians with differing peak heights are shown here, that will subsequently be used an input to the ATM.

Although the Si-E defect has well known energy and cross section values, the defect abundance (peak height) is less understood. As such, a variety of peak heights are included in Figure 6.15 and will be used an input to the ATM to examine the change in model trends with varying defect density. Figure 6.16 shows the output of the ATM, with the CCD204 results of Figure 6.7 once again included as a reference.

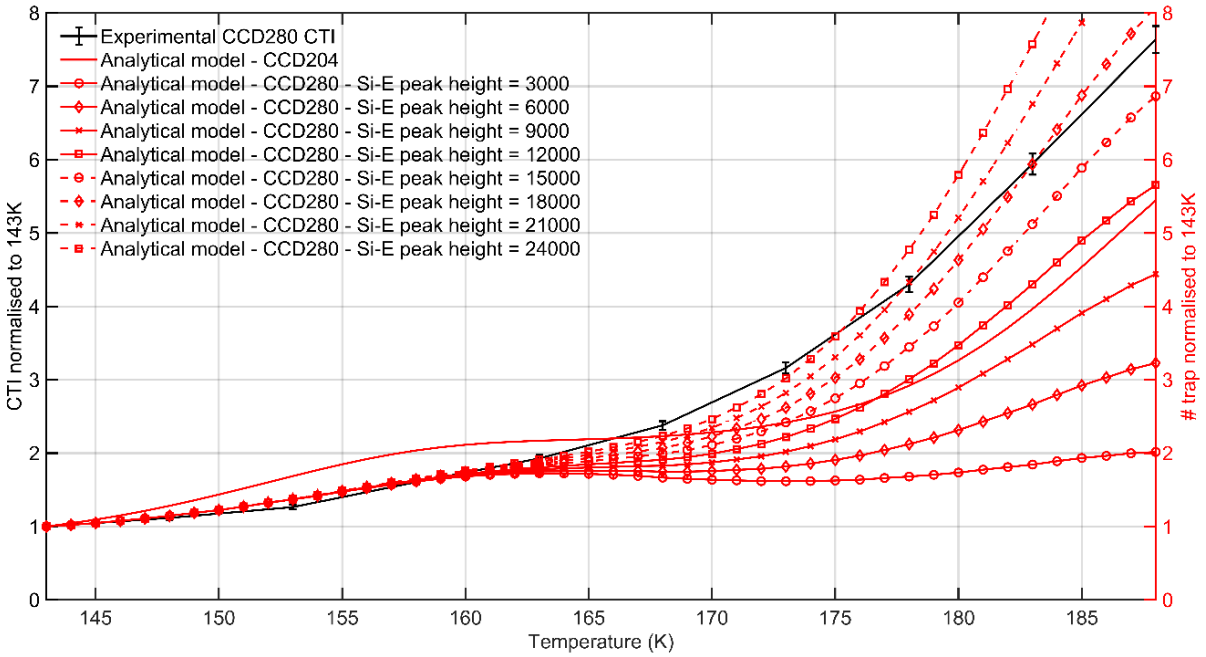


**Figure 6.16**: Comparison between the effective number of traps predicted by the analytical model for both the CCD280 and CCD204 landscape and the experimental CTI data. Note that the data for the CCD204 analytical model is identical to that shown in Figure 6.7 and is only shown again for comparison. Note that no formal fit was made between varying Si-E peak heights and the experimental data, only a range of Si-E peak heights was chosen.

Overall, the CCD280 trap landscape, attained via the trap pumping technique and knowledge of the Si-E defect parameters shows a significantly better fit to the experimental CCD280 data when compared to the CCD204 landscape. At low temperatures (160-165 K and below), the analytical model utilising the constructed CCD280 landscape shows an excellent fit to the CTI data. At these temperatures, as shown previously (Figure 6.8), the rate of increase of effective traps as a function of temperature is overestimated. Using a landscape which is representative of the experimental device (CCD280) leads to a much-improved trend-match when comparing the CCD280 and CCD204. The very slight overestimation of the number of effective traps using the CCD280 data between approximately150 K and 155 K could be attributed to the overestimation of defects in this region when using the averaging approximation seen above, and more explicitly in the CCD280 landscape in Figure 6.14.

At temperatures above 175 K, the number of effective defects varies significantly as a function of Si-E peak height. This is expected, as at this temperature, the dominant defect should be the Si-E, and thus using peak height values such as 3000/6000/9000 (which are likely underestimates), will naturally underestimate the number of effective traps predicted by the ATM. According to the ATM, the estimated peak height of the Si-E is somewhere between 15000 – 18000, as the rate of increase of effective traps as a function temperature is comparable to CTI at these Si-E peak heights.

Between the temperatures of 165 K – 175 K however, the number of effective traps predicted by the model is still slightly underestimated when compared to CTI, mainly due to one factor. Figure 6.15 showed the CCD280 landscape, which was comprised of trap pumping data, combined with theoretical Si-E defect parameters added to the landscape. Between the maximum value of emission time constant that was probed experimentally (approximately 20 s) and the edge of the theoretical Si-E peak that was added, no defects are included in the model. Physically, this is most likely incorrect as the CCD204 data (and other similar data sets) show a small number of defects in this parameter space, which was unable to be probed experimentally. As a result, the analytical model naturally underestimates the number of effective defects in this part of the parameter space, leading to the small discrepancy seen in Figure 6.16.

Furthermore, the Si-E peak, as seen in the CCD204 trap landscape, is not entirely gaussian, and has a slight tail weighted towards faster emission time constants. It is not clear whether the tail of defects is related to the Si-E or another defect species. Adding the Si-E as a gaussian does not include this small number of defects, and it another small underestimate of defects within this area of the trap landscape.

## 6.3. Conclusion

An updated model was initially described which can predict how the effective number of traps changes based on several operating conditions of a CCD. Two main features were added to the initial implementation of the model, which were necessary to produce realistic and accurate results: the sub-electrode modelling, and the calculation of the proportion of empty traps.

The model was then used to compare the change in the effective numbers of traps as a function of temperature to experimental X-ray CTI values that were measured in a CCD280 irradiated

at room temperature. The input parameters used in the ATM were identical to the experimental parameters used in the X-ray CTI measurements, apart from the input trap landscape being that from an irradiated CCD204. The model predicted the general trends seen in the data, but at certain temperature ranges, the model under or overestimated the number of effective traps.

The underlying reason for the discrepancy between the analytical model and experimental data was found to be due to differences between the trap landscapes of the CCD204 and CCD280. Experimental trap pumping data collected and analysed by the author was then used to construct a representative room-temperature irradiated CCD280. The final step was to input the CCD280 trap landscape into the ATM and compare the fit between each ATM output and the experimental CTI. A much-improved fit between the ATM and the experimental CTI data was seen, with small discrepancies explained via assumptions in the analysis. A summary of the result and representative CCD280 trap landscape utilised is shown below (Figure 6.18 and Figure 6.18).

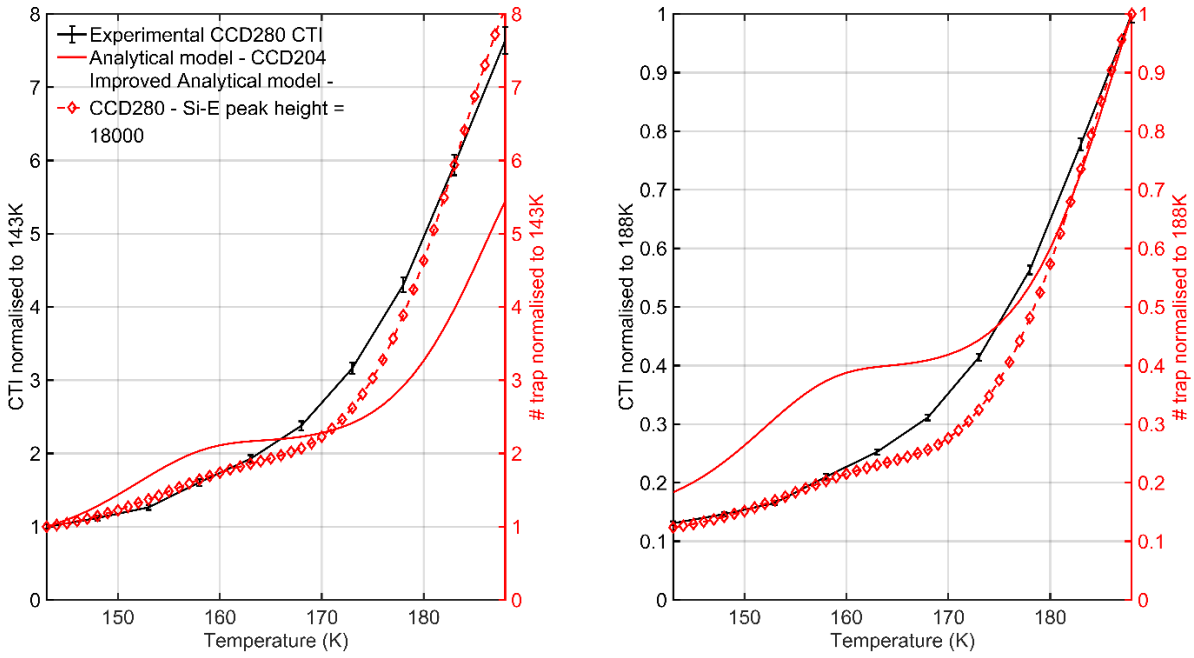


**Figure 6.17**: Comparing the analytical solution using the CCD204 and CCD280 landscape, normalised to both 143K and 188 K.

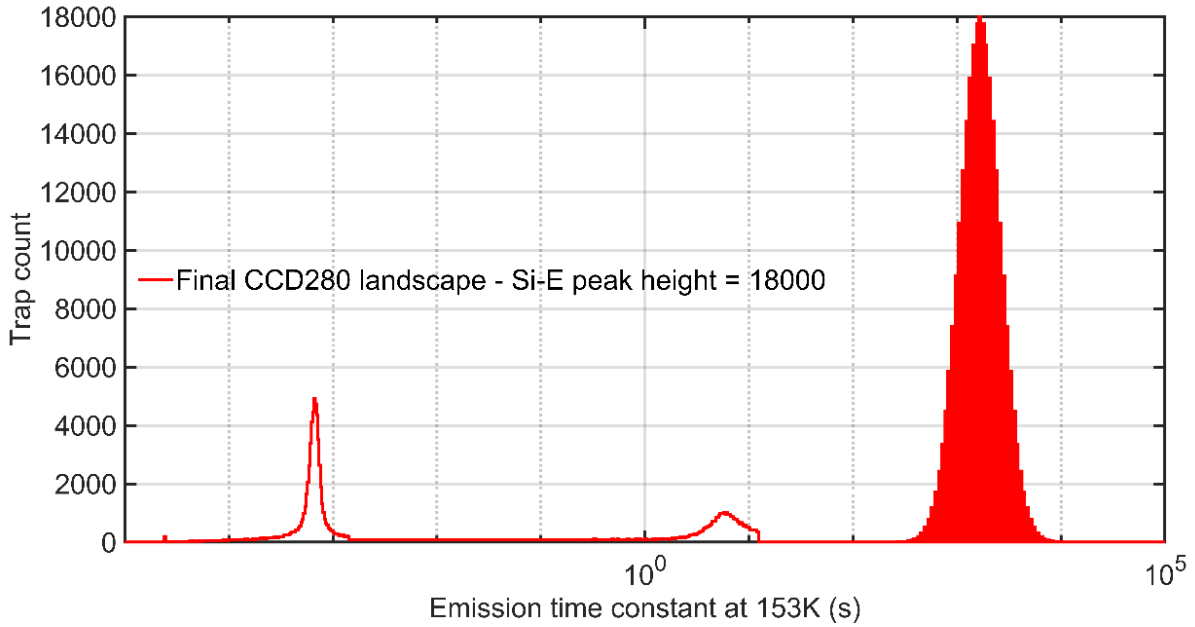


**Figure 6.18**: CCD280 trap landscape used as input to the improved analytical model, with a Si-E peak height of 18000 defects.

Figure 6.17 shows that the ATM can be used to accurately predict changes in X-ray CTI across a range of temperatures and could thus be used to inform laboratory charge transfer optimisation activities across a wider parameter space. For the case of SMILE SXI, the ATM can now be adapted to simulate a FT readout mode, with the ATM results able to guide optimisation activities across temperature and clocking speeds (image, store and serial), potentially saving a considerable amount of time and effort. Chapter 8 will outline the key differences between the CCD280 and CCD370 operating modes and describe how the ATM will implement the more intricate readout mode.

# 7. SMILE SXI cryogenic irradiation campaign, trap pumping results and implications for SMILE SXI CCD performance

The SMILE SXI OU irradiation campaign was briefly described in chapter 5 (and summarised in Table 5.1), with focus placed on the room-temperature irradiation of the CCD280. In this chapter however, focus will be placed on the second irradiation as part of the campaign, the first cryogenic irradiation of a CCD280. The irradiation was carried out in January 2020 at the STERIS facility in Harwell, UK, and was split across two identical irradiations approximately 2 weeks apart.

The CCD280 was characterised before and after each irradiation, with several metrics analysed such as dark current, CTI (EPER, FPR, X-ray) and quantity of bright defects. This chapter, however, will focus on the evolution of defects within the device post-irradiation, once again utilising the trap pumping technique.

Directly after irradiation, a CCD can take many days before the performance stabilises, such that subsequent measurements are representative of actual device performance. In this window between irradiation and stabilisation, the defects created in device from the irradiation can change, leading to changes in values such as CTI. Although the absolute value of CTI during this stage is not particularly relevant (realistically a device would never be irradiated to EOL in the order of seconds/minutes), the behaviour and evolution of defects can provide additional insight into the basic physics at work.

The trap pumping technique can be used in this stabilisation window to probe defects within the device and track the evolution of the defect landscape. The technique, however, does have some limitations associated with the time for data collection relative to the changes in defect evolution/migration. This means that care must be taken when planning what emission time constants to probe, as this can greatly affect the results.

The author was responsible for planning the trap pumping data acquisition (section 7.2) and all the subsequent analysis that followed (section 7.3 and 7.4). The overall goal of the experiment was to probe emission time constant ranges of most interest to SMILE SXI CCD performance, namely the area close to the divacancy, as this region will most likely dictate parallel CTI performance. As an extension, the experiment also aimed to simulate the temperature variations

of the SMILE SXI spacecraft (and CCDs), and how the temperature fluctuations affected the defect landscape present in the CCDs (section 7.4). This was important for the SMILE SXI CCDs, as annealing is known to alter the trap landscape in cryogenically irradiated CCDs, but the exact quantity of annealing as a function of temperature is not well understood.

## 7.1. Equipment and irradiation facilities

The equipment used for the first room-temperature and cryogenic CCD280 irradiation was naturally similar, with the key difference being the inclusion of transportation batteries on the portable trolley (labelled in Figure 5.4). The key difference between the two irradiations is of course the device temperature *during* the irradiation, but more importantly the maintenance of the cryogenic temperature *after* irradiation also. Maintenance of the cryogenic temperature at the irradiation facility post-irradiation is simple, due to the use of external power to the Cryotiger®. However, the high financial cost of irradiation facilities necessitates that the portable trolley be moved back to the OU campus, where the remainder of the post-irradiation characterisation can take place. This means that the portable batteries are required to maintain power to the Cryotiger® and other associated electronics when in transit back to the OU.

The complication of cryogenic irradiations also places constraints on the irradiation facility used, as transport from the facility back to the OU campus is high risk, such that the distance travelled must be minimised. Therefore, thought must be placed into selection of the irradiation facility used for cryogenic irradiations, to sufficiently de-risk the transportation phase.

### 7.1.1. STERIS facility

The cryogenic irradiation was carried out at the STERIS proton irradiation facility in Harwell, UK. Although primarily used as a facility to sterilise medical equipment through proton irradiations, the facility has several features that make it suitable for the purposes required here, including beamline characteristics and geographical location. The key features are summarised below:

- Proton energy (Up to 10 MeV) is suitable for purpose, as the non-ionising energy loss (NIEL) formula can be utilised to scale fluences to the required total dose.
- Beam width (> the width of a CCD370, approximately 8 cm) which covers a CCD370 without the need for potential raster-scanning. Raster scanning adds unwanted

additional mechanical design complications as well as complicating fluences received across the device from multiple irradiations.

- Approximately one-hour drive from the OU Walton Hall Campus. While not as important for the room-temperature irradiations, the subsequent cryogenic irradiations require the device to be irradiated and kept cold. This means transporting all equipment while operational, which carries large risks. Using an irradiation facility only one hour away significantly de-risks this part of the campaign.
- Experience of using this specific beamline many times also re-risks the subsequent cryogenic irradiations.

## 7.2. Pre-irradiation results

Before the cryogenic irradiation campaign begun, a characterisation plan was developed, including time set aside for collection of trap pumping data. The extent of data collection both pre- and post-irradiation was constrained mainly by time, with significantly more restrictions present post-irradiation. Although more time was available pre-irradiation, the device was naturally free of radiation-induced defects and contained only a small number of defects (most likely manufacturing or intrinsic defects). Figure 7.1 shows the trap landscape within the unirradiated CCD280 as measured at 153 K. Between these two limits however, three distinct peaks are seen at approximately $5 \times 10^{-4}$ s, $1.8 \times 10^{-3}$ s and $1 \times 10^{-2}$ s. These peaks are most likely either intrinsic defects arising from impurities added during the manufacturing process or intrinsic defects in the raw silicon, as they are not abundant (when compared to the quantity of radiation-induced defects) and situated at emission time constants similar to that of previous studies of unirradiated devices (Bush, N. et al., 2018).

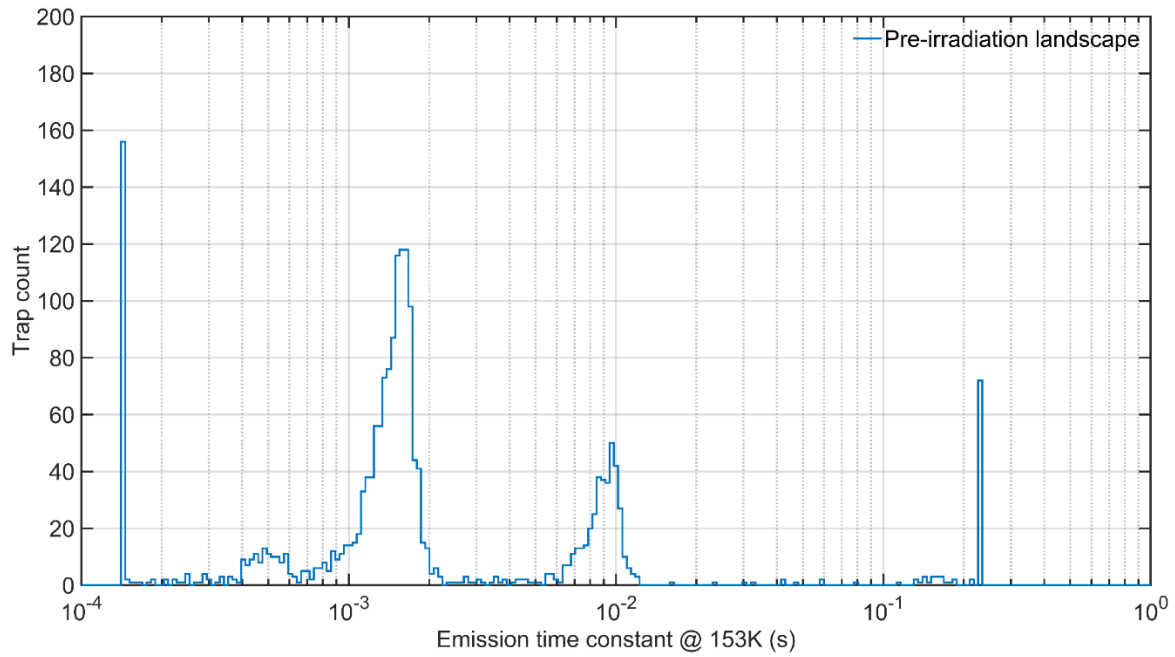


**Figure 7.1**: Pre-irradiated defect landscape of a CCD280. Limits of emission time constant probed are seen at $1.4 \times 10^{-4}$ s and $2.2 \times 10^{-1}$ s by the large pile up of defects where fitting functions have fitted incorrectly to incomplete dipole curves.

To identify these defects with a much higher degree of certainty, the energy level and cross section could be extracted via the pumping of these defects (and appropriate emission time constant ranges) at a range of different temperatures. However, in this case, only one data set was collected at 153 K, limiting the conclusions that can be drawn from the data in Figure 7.1. Although this is a limitation, the focus of the work were investigations into the spread of defects post-irradiation.

A previous study (Skottfelt et al., 2018), specifically for CCDs on the ESA EUCLID mission, performed trap pumping sweeps pre-irradiation identifying two small populations pre-irradiation. The two defect candidates are the boron-interstitial-oxygen-interstitial ($B_iO_i$) and the carbon-interstitial-phosphorous-substitution ($C_iP_s$). At 153 K, the emission time constants of these defects should be approximately $1\times10^{-4}$ s to $5\times10^{-4}$ s and $10^{-3}$ s to $10^{-2}$ s, respectively, with the spread in emission time constant originating from the error on the energy level of each defect. The small peaks seen in Figure 7.1 fall within the emission time constant ranges of both the $B_iO_i$ and $C_iP_s$, with these defects being likely candidates without further investigations.

### 7.2.1. Post-irradiation trap pumping plan

Before the cryogenic CCD280 irradiation took place, a specific and targeted trap pumping plan was constructed to ensure that the most useful data could be collected in a short space of time. The following section will outline the different phases of trap pumping measurements taken after irradiation and the rationale behind each.

To try and maximise the results within the given timeframe of approximately 1 week, the trap pumping measurements is broken down into three distinct phases. Post irradiation, the largest evolution in defects occurs within only a few hours (Bush, N. et al., 2018), meaning that to gather sufficient data points, only a handful of emission time constants can be probed. This is compounded by the fact that longer emission time constants take significantly longer to probe via the trap pumping technique, effectively placing an upper limit on the emission time constant measurable.

#### 7.2.1.1. Phase one

Figure 7.2 (Top) shows the defect landscape at 153 K for a cryogenically irradiated device (CCD201) with six overlaid vertical dashed blue lines, indicating the emission time constants that are to be probed. Each timing has been specifically chosen to explore the evolution of a certain defect/area of the parameter space that is of interest. Moving from left to right on Figure 7.2 (Top), the first timing was chosen for two main reasons. Firstly, this emission time constant is particularly quick and can be collected without affecting the total time for data collection significantly (approximately 30 minutes). Secondly, this area of emission time constant, between the A-centre and divacancy is effectively devoid of defects in a device that has stabilised. This does not mean however, that there are no defects here directly after irradiation,

some migration could occur within the device, and probing this emission time constant could provide additional insight.

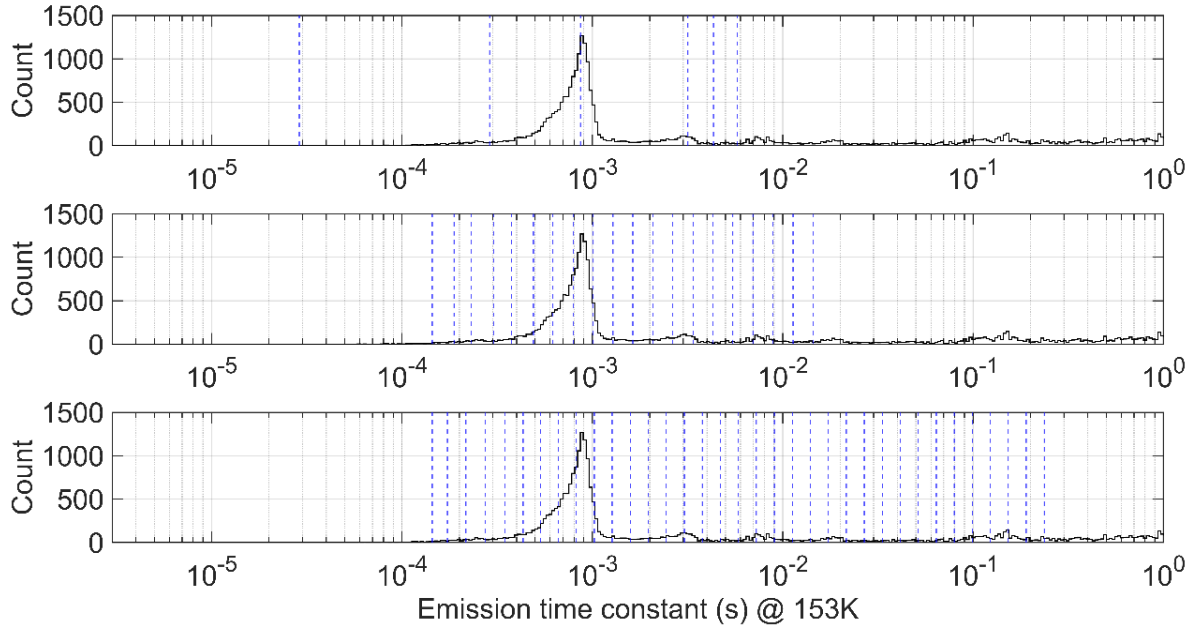


**Figure 7.2**: Emission time constants probed within each phase of the trap pumping campaign (top – phase one, middle – phase two, bottom – phase three), with each distinct emission time constant represented by a dashed blue line. A CCD204 cryogenic trap landscape is shown in the background of each subplot as a reference point as to which defect species is being probed. Note that a representative trap landscape can be created from the sweeps of emission time constants probed in each phase of trap pumping, even in phase one where the emission time constants probed are significantly sparser.

The second and third emission time constant probed are concerned with the evolution of the divacancy, which is of particular interest in a cryogenically irradiated device, as defects can appear to migrate into the "peak" of the divacancy from either side (Lee-Payne, Z. et al., n.d.). The second emission time constant is on the elongated tail of the divacancy whereas the third emission time constant is directly located in the peak. This means that both the evolution of the tail and peak of the divacancy can be studied over time. Furthermore, the divacancy is one of the main traps that can affect parallel CTI, a key performance metric that greatly influences the final science instrument performance. Knowing more about the behaviour of the divacancy in a cryogenically irradiated device will be extremely useful.

The remaining three slowest emission time constants are situated to probe an area which has seen some unexplained results in previous work (Bush, N. et al., 2018). Directly after irradiation, a larger number of defects were seen with emission time constants quicker than that of the divacancy, which rapidly decreased in count until reaching the subsequent background level of defects. These three emission time constants were chosen to potentially replicate the behaviour seen previously and provide further insight into the underlying mechanisms.

In the two hours after irradiation, the six emission time constants shown in Figure 7.2 (Top) can be probed a total of twelve times, providing enough data points to show a trend while still probing the widest range of emission time constants possible. Although more defects do exist with slower emission time constants, probing any slower defect would results in too few repeats of the trap pumping sweep to observe any trends in time during the fast initial anneal after irradiation.

#### 7.2.1.2. Phase two and three

Both phases two and three have significantly more emission time constants probed as these two phases are operated between 2-8 hours and 8-168 hours (7 days) following irradiation, respectively. Consequently, a larger range of times can be probed in combination with a higher resolution of points. The benefit of probing longer emission time constants is that it provides insight into the "continuum" of defects at time constants longer than the divacancy and can provide insight into potential migration of defects from the continuum to the peak of the divacancy.

With the number of emission time constants probed in phases two and three, this allows a large amount of the parameter space to be probed as well as providing six and ten data points for phase two and three, respectively.

## 7.3. Results directly post-irradiation

Once all three phases of the trap pumping data collection were complete after each irradiation, the data could be passed through the processing pipeline. The first stage of analysis was to examine the total defects as a function of time, as this would clearly and directly indicate the time of irradiation and the overall increase of defects due to each proton irradiation.

### 7.3.1. Total defects as a function of time

Although a different range of emission time constants were probed in each phase of the trap pumping analysis (Figure 7.2), to ensure a fair comparison, the defect landscape will be compared for *only* the range of emission time constants dictated by the upper emission time constant limit of phase one, and the lower emission time constant limit of phase two and three.

Figure 7.3 shows the total number of defects as a function of time, relative to the first irradiation. Pre-irradiation, a very low number of defects are seen, which is as expected due to the lack of radiation-induced defects within the silicon. At time t = 0 and t = 215 hours, two large spikes are seen in the number of defects, corresponding to the time of each irradiation.

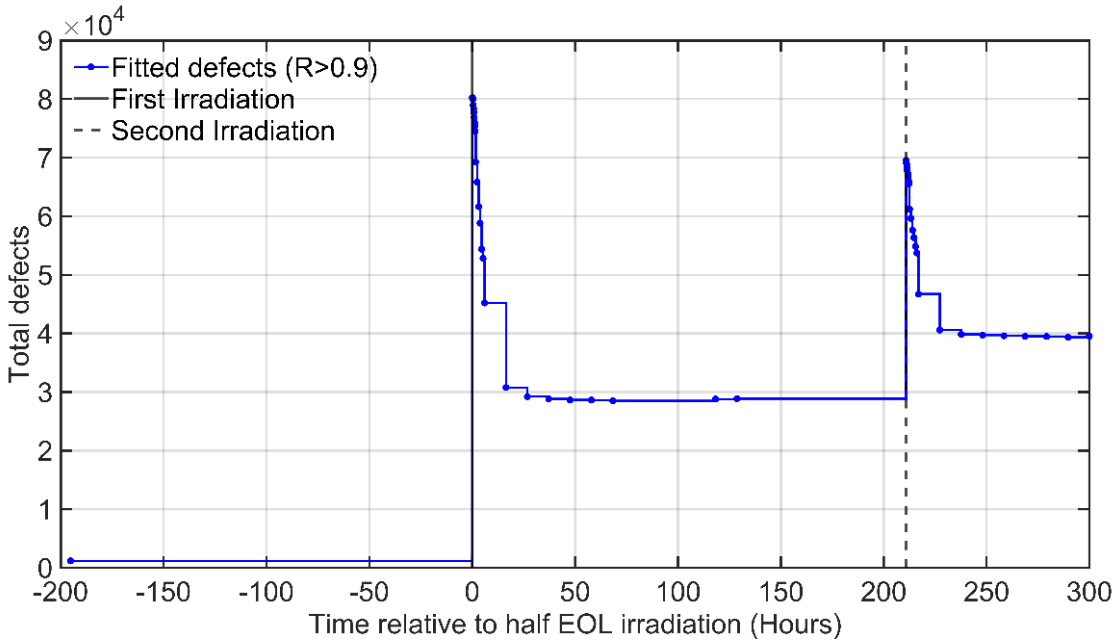


**Figure 7.3**: Total number of defects found as a function of time relative to the first irradiation. Only defects with dipole intensity curve fits with a goodness of fit of 0.9 or above are shown here.

After each irradiation (and each subsequent spike in defects), two main features are seen. Initially, each rapid increase in defects is proceeded by a sharp decline, which eventually stabilises to a constant level. The second feature was both the magnitude of each peak in defects and the stable level that was reached after each irradiation. The second irradiation was quoted as 17.5 % - 20% of EOL (Parsons, S., 2019, p. 280) (with the first irradiation at 50% EOL),

which means that the large increase in defects and subsequent stabilisation should scale accordingly, which is approximately seen in Figure 7.3.

Although a strong decline in the total number of defects is seen after each irradiation, this does not explain what is happening to the distribution of defects in the landscapes specifically, just that the *total* number of defects found within the parameter space is declining. As alluded to previously, the trap pumping technique provides the key emission time constant of each defect found within the parameter space probed. As a result, the total landscape probed can be plotted as a function of time, to examine the large decay in more detail (Figure 7.4).

### 7.3.2. Emission time constant decays

Once the trap landscapes have been generated via binning fitted emission time constants, the spread of emission time constants can be plotted and are shown in Figure 7.4, for both the first irradiation (top) and second irradiation (bottom). Within both trap landscapes, a peak corresponding to the position of the double negative state of the divacancy is seen (Bush, Nathan L., 2018; Wood, Daniel, 2018), as expected. However, to the right of the divacancy (towards slower emission time constants) an abundant population of defects is seen, which rapidly decays until a stable continuum is reached. This unidentified population of defects is seen in the trap landscapes after both irradiations, and decays to the background level somewhere between 7-48 hours post-irradiation.

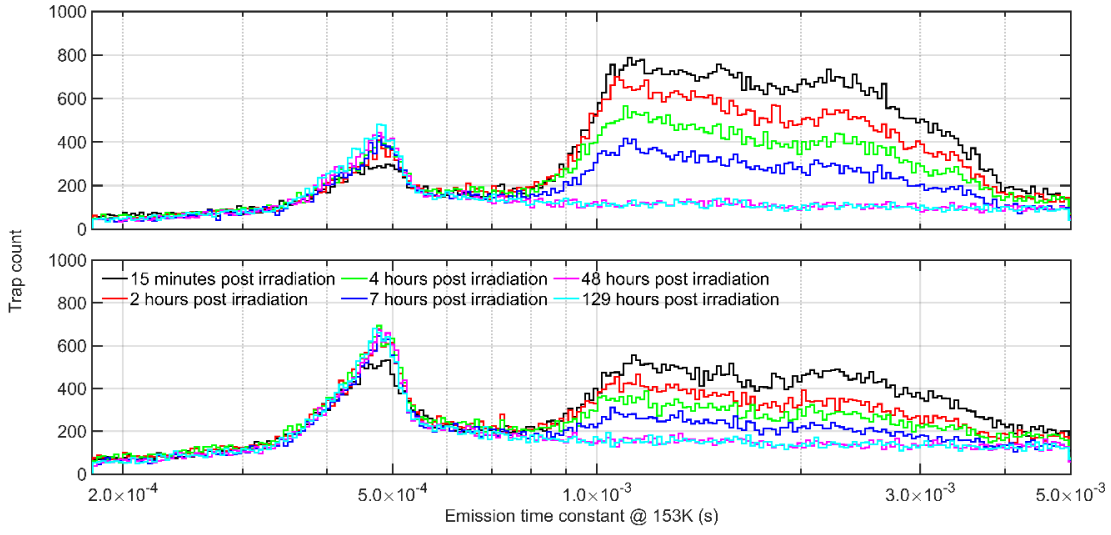


**Figure 7.4**: Trap landscapes plotted as a function of time for both the first irradiation (top) and second irradiation (bottom). The different between the magnitude of the defect counts across

the whole landscape, between each irradiation, is attributed to the inconsistent fluences received in each irradiation.

To investigate the apparent defect decay more quantitatively, ranges of emission time constants can be defined to isolate the unstable defect species. Figure 7.5 shows the landscape from the first irradiation, with limits imposed which define distinct regions in the landscape.

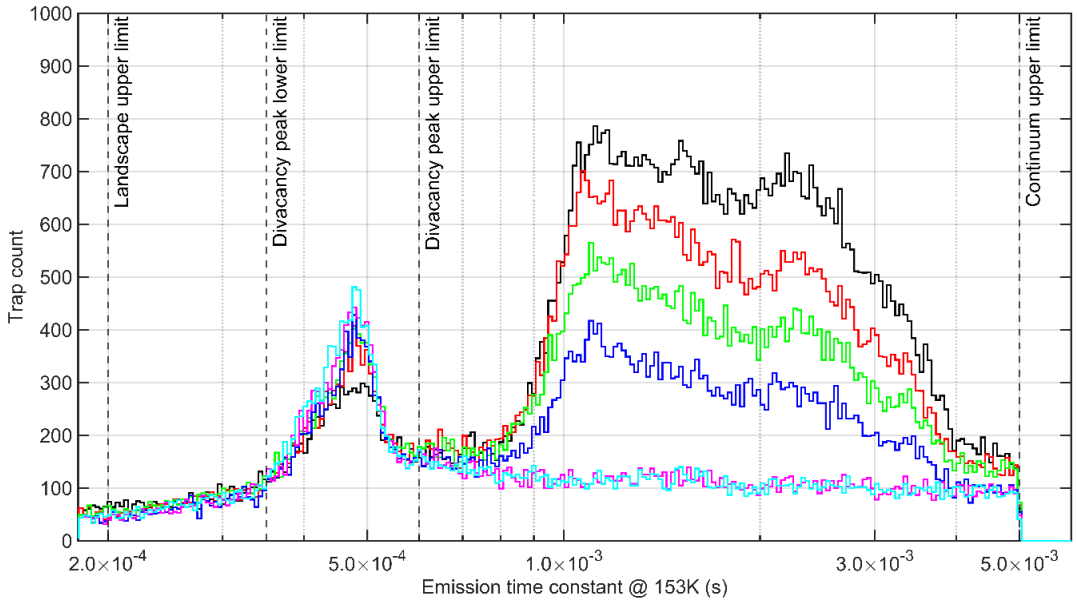


**Figure 7.5**: Trap landscape, identical to that seen in Figure 7.4 (top), with four distinct limits imposed on the emission time constants. Note that the limits do not represent a pertinent physical boundary, but simply an analysis technique used.

By plotting the evolution of the number of defects within certain limits as a function of time (post each irradiation), it is possible to quantitatively examine the change in the number of defects. Figure 7.6 shows the total number of defects within each range of emission time constants as a function of time (post first irradiation).

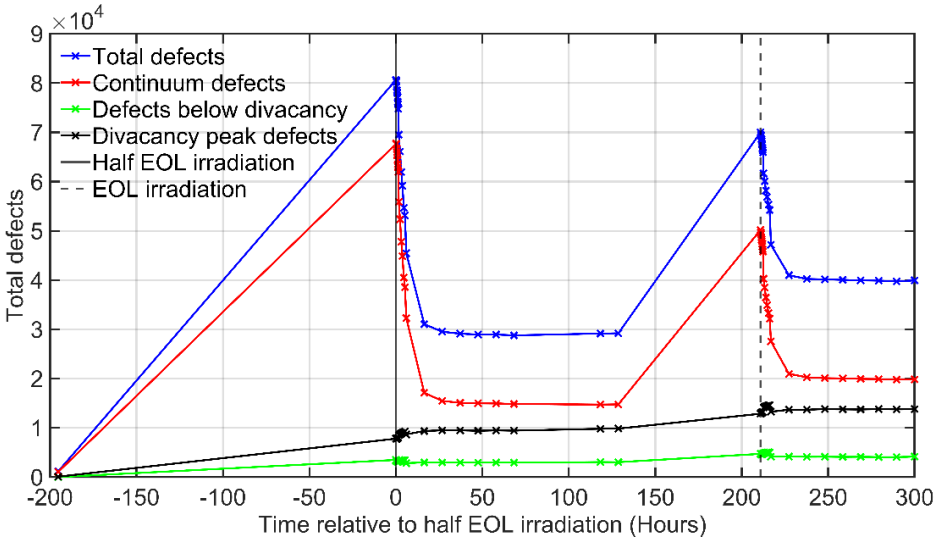


**Figure 7.6**: Relative contributions of defects from different parts of the trap landscape, as defined by the limits imposed in Figure 7.5.

The characteristic spike in defects is once again seen at times correlating to each irradiation, in both the total number of defects and continuum defects. Continuum defects are those defined between the divacancy peak upper limit and continuum upper limit (seen in Figure 7.5). Two other ranges of emission time constants are plotted, defects within the peak of the divacancy and those between the lower end of emission time constants probed and the lower limit of the divacancy peak (black and green line in Figure 7.6 respectively). Both the green and black line show small increases in the number of defects after each irradiation, but no significant decay in the number of defects is seen. This means that the large decay in the total number of defects is primarily from the continuum.

### 7.3.3. Estimating the decay constant

Quantifying the rate of trap decay for the continuum, shown in Figure 7.4 and Figure 7.5, will allow the decay constant to be estimated, which in turn will allow implications for the performance of SMILE SXI to be calculated. Figure 7.7 shows the total number of continuum defects plotted as a function of time (relative to each irradiation). Both curves have been normalised to the stable defect level that was reached after each irradiation, allowing an exponential fit to the data points.

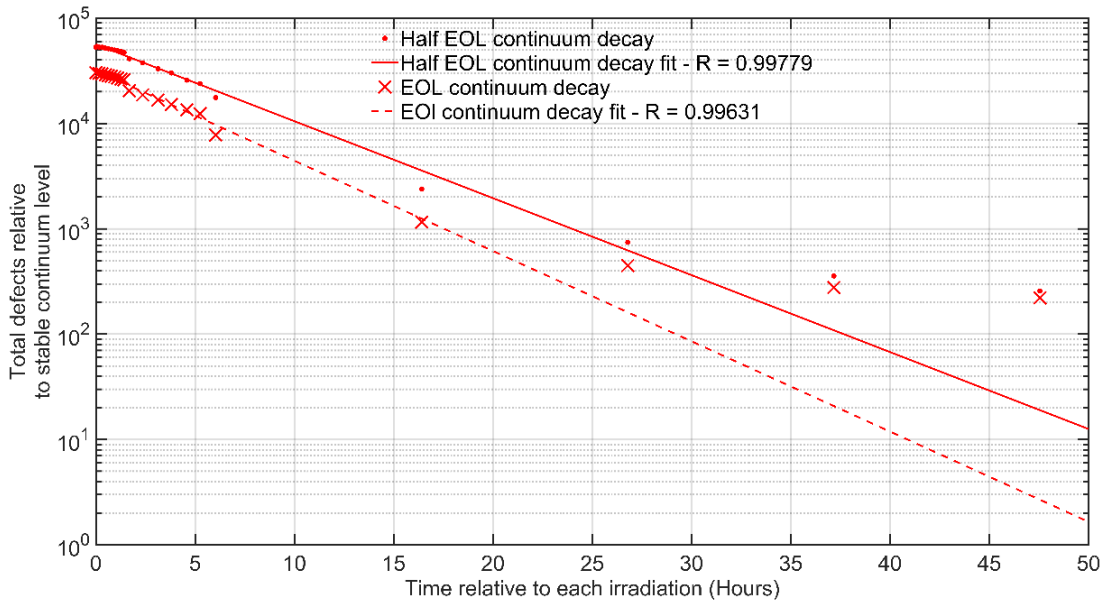


**Figure 7.7**: Rate of defect decay for each irradiation as a function of time relative to each irradiation. Note that the total number of defects has been normalised to the stable number of defects reached after each irradiation, as well as being normalised versus the time of each irradiation.

The half EOL and EOL data points show an offset in the y-axis, the total defects relative to the stable continuum level. The offset is attributed to the different fluences of each irradiation, with the 2$^{nd}$ irradiation (the EOL continuum line) delivering approximately 40% less fluence than the first, also seen more explicitly in Figure 7.3. Although the fluences were most likely different between the two irradiations, fitting an exponential function and extracting the gradient (the decay constant) is independent of the y-axis scale (total defects).

Both exponential fits are shown in Figure 7.7, with the associated R-value of each suggesting an excellent mathematical fit between the data points and the exponential function (R values > 0.996 for both). Looking at Figure 7.7 however, the fit between the data points and function is excellent until approximately 15 hours post-irradiation. Past this point the rate of decrease of continuum defects in both the EOL and half EOL does not follow the same trend, with the rate of decrease slowing.

Potential reasons for the apparent change in trends 15 hours post-irradiation could be due to the normalisation used to fit an exponential function. After each irradiation, the quantity of defects located in the continuum rapidly decay until a stable plateau is reached, seen in Figure

7.3 and Figure 7.6. The normalization level of each irradiation is taken from the minimum value from the plateau, which although does not vary much by eye, small variations potentially arising from the complex defect fitting pipeline can make this minimum value vary slightly.

Although the trends between the data and function fit are not good after 15 hours post-irradiation, the majority of the defect decay occurs in the regime where an excellent fit is seen between the data and the function. This is also compounded by general views of the landscape in Figure 7.4 and Figure 7.5, where most of the decay happens approximately 10 hours post-irradiation. With that being said, implications of the behaviour seen and quantified above can be explored in terms of SMILE SXI performance in-orbit.

Fitting exponentials to the normalized number of defects located in the continuum (defined by the limits in Figure 7.5) provides fitting parameters, including the decay constant, summarized in Table 7.1. The fitted decay constant (and associated half-life) provides an idea as to how quick the large species of defects in the continuum decays and reaches a stable background level.

**Table 7.1**: Summary of the fitted parameters to the continuum decay fit seen in each irradiation.

| Irradiation | R value (3 significant figures) | Fitted decay constant | Half-life (hours) | Half-life error (hours) |
|---|---|---|---|---|
| Half EOL | 0.998 | -0.168 | **4.12** | **±0.643** |
| EOL | 0.996 | -0.197 | **3.51** | **±0.674** |

Converting the EOL and half EOL decay constants into half-lives leads to a half-life of 4.12 and 3.51 hours for each irradiation, respectively. When taking the fitting errors into account (±0.653 and ±0.674 for EOL and half EOL irradiations), both values are within error of each other. Using the half-lives of the unstable defect species calculated in Table 7.1, it is possible to quantify the impact on the performance of SMILE SXI with regards to X-ray spectral resolution.

### 7.3.4. Implications for SMILE SXI performance in-orbit

In terms of SMILE SXI performance, large bursts of solar activity have the potential to deposit a significant amount of dose into SMILE SXIs' CCDs, similar to the proton irradiation described here, although at a lower magnitude. It follows that the unstable defect species that are seen to decay here will most likely also occur in-orbit after large solar events.

It is well understood that radiation-induced defects lead to charge transfer performance losses in CCDs and over the course of a space mission spanning several years, CTI will degrade over time. With new knowledge of this new defect decay and associated decay time constant (Table 7.1), in-orbit CTI decay will not be a linear process. Directly after a large irradiation (like a solar flare), CTI will get significantly worse, and then *improve* as the abundant and unstable defect decays in the subsequent hours post solar flare. Due to the half-life calculated, and SMILE orbital parameters (52 hour orbital period), the defect decay will only be relevant for one orbit at most, after which the defect species will stabilize.

The severity of the effect described above and the implications for SMILE SXI are subject to several caveats:

- The fluence-dependence of this defect decay is unknown, it is seen in both irradiations, but whether this effect occurs for smaller solar events is unclear.
- As CTI is a function of total defects within the device, the severity of this effect is expected to decrease throughout the 3-year SMILE mission as the background concentrations of defects (that also contribute to CTI) is always increasing.
- This unstable defect species is in an emission time constant range whereby the majority, if not all, of the unstable species will contribute to parallel CTI.
- The emission time constant range that affects CTI is significantly wider than the emission time constant range of the unstable defect species seen here. The total number of defects contributing to CTI will most likely be larger than the total number of unstable defects seen in the results here, so the severity of the unstable defect decay is unclear at this stage.

After a large solar event, CCDs in SXI will see dynamic defect behaviour, producing variable (and improved for a time) CTI, impacting the down-stream science output. From the work here, the images taken in the single orbit post-solar flare should be flagged in some way, to alert

down-stream science users that the X-ray resolvability of the detector is dynamic, albeit with a potentially small impact on CTI.

## 7.4. Landscape evolution after annealing cycles

In terms of SXI instrument performance, parameters such as dark current, CTI and noise all have a temperature dependence, meaning that thermal stability of the instrument is important. Ideally, instrument temperature would be very stable, however, factors such as mechanical design limitations and natural temperature variation across orbits, means that some temperature variation is unavoidable in most cases. In the case of SMILE SXI, two extremes of thermal variations across orbits are seen, with thermal simulations shown in Figure 7.8 (ESA, 2018). The "cold" orbit case sees an extremely stable CCD temperature, oscillating slightly around 152K and the "hot" orbit case sees fluctuations between approximately 161 K and approximately 146 K. All orbits of SMILE SXI are expected to fall somewhere between the two extremes.

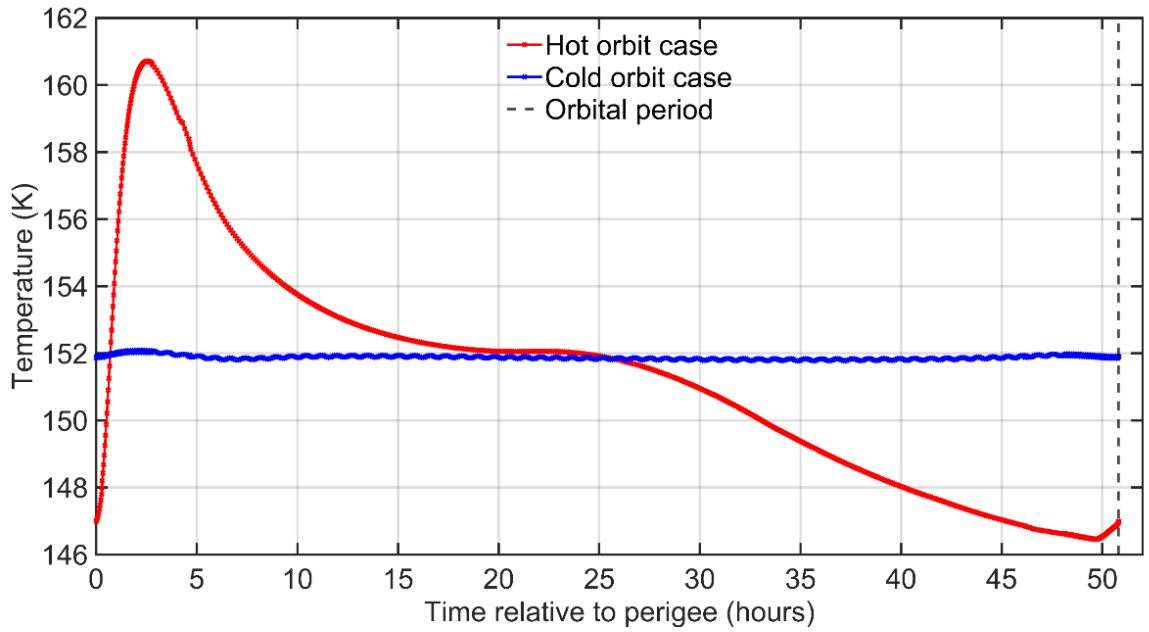


**Figure 7.8**: Temperature fluctuations on the CCD for a single orbit, as a function of time (relative to perigee), for both the "hot" and "cold" orbit cases.

For cryogenically irradiated CCDs (like the CCDs of SMILE SXI in-orbit), it is well understood that warming the device can produce irreversible changes to the emission time constant distribution, which directly affects the CTI and hence overall instrument performance.

It is not well known, however, what the exact relationship is between annealing temperature (for small changes of approximately 10 K) and the extent to which the defect landscape changes. Specifically, for SMILE SXI, a maximum warming of approximately 10 K (seen in Figure 7.8) from operating temperature (153 K) has the potential to irreversibly change the defect landscape, the extent to which is unknown. If optimisation of a cryogenically cooled device is performed in the laboratory (without temperature annealing), and optimal parameters for in-orbit performance are chosen, then the potential temperature annealing due to orbital thermal fluctuations could decrease the effectiveness of optimisation activities. As a result, this means that understanding the annealing behaviour within a SMILE cryogenically irradiated device is key to achieving maximal device performance.

As such, the post-irradiation characterisation plan was amended to contain an annealing phase, to directly address the issue described above. After irradiation, the temperature of the device was dropped to 148 K and 143 K to collect X-ray CTI and trap pumping data (seen in Figure 7.9), to accurately examine the performance changes of the coldest part of the "hot" case orbit. After moving back to 153 K, the device was warmed in 5 K increments, with CTI and trap pumping data collected at each step, and then cooled back to operating temperature (153 K). By measuring the trap landscape at the operational temperature after each 5 K anneal step, any changes induced by the warmer temperature were monitored. The annealing steps extended beyond the warmest temperature in the "hot" orbit case to provide a broader range of annealing data, and to reveal any trends as a function of temperature.

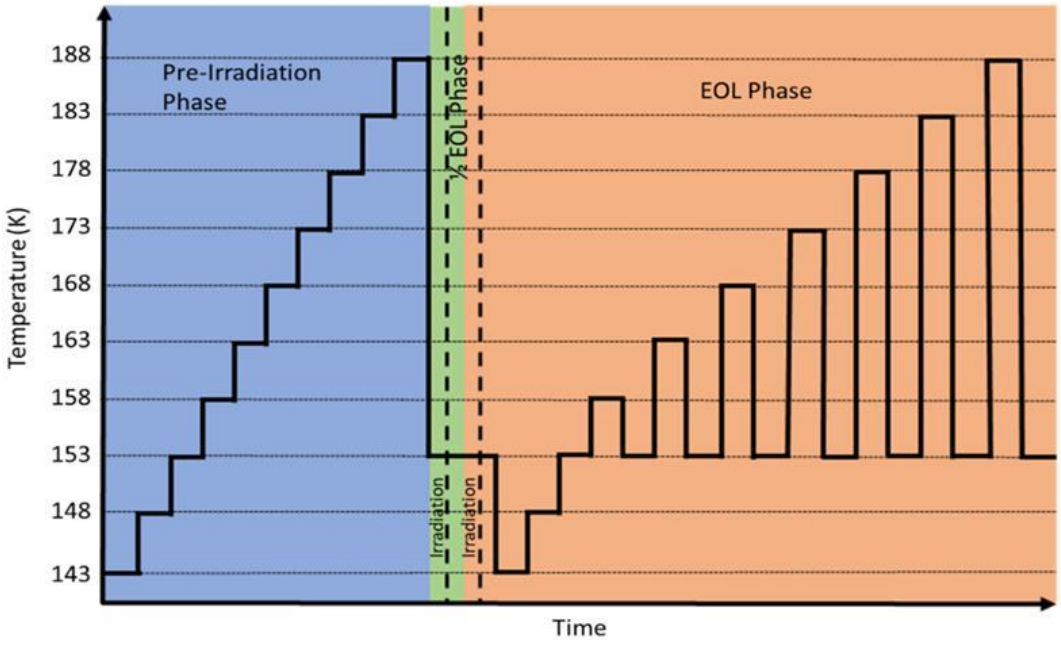


**Figure 7.9**: Pre- and post-irradiation characterisation plan as part of the cryogenic CCD280 irradiation, each anneal step is approximately 3-4 days (for both the 153 K step and the warmer/colder step). (Parsons, S., 2019, p. 280).

### 7.4.1. Emission time constant range probed

Figure 7.10 shows the temperatures and emission time constants probed as part of the annealing cycles, indicated by the black vertical bars. Also included is the hot orbit upper and lower temperature limit, shown by the black solid and dashed lines, respectively. The range of emission time constants probed, in combination with temperature choices (largely dictated by the predicted orbital fluctuations however), will allow the double negative state of the divacancy to be probed at operating temperature (153 K), along with a large part of the continuum. At both locations, annealing is expected at warmer temperatures, so the range of emission time constants chosen should reveal the extent of annealing as a function of temperature.

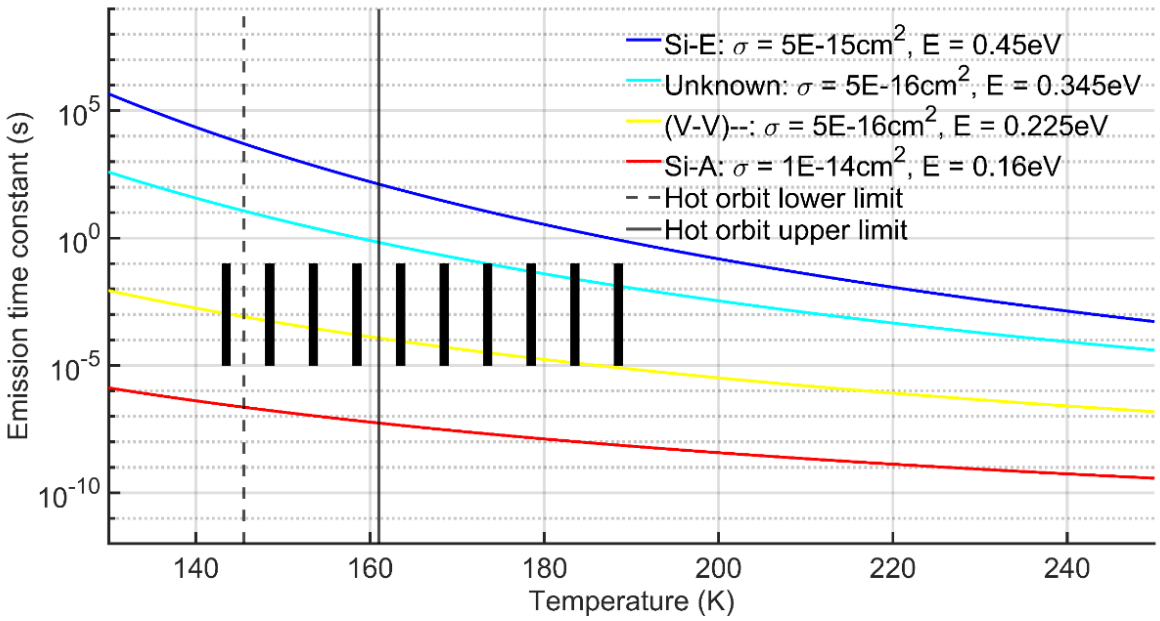


**Figure 7.10**: Trap diagram (Bush, Nathan L., 2018) showing the four main radiation-induced defects in N-channel CCDs, with overlaid ranges of emission time constants probed.

### 7.4.2. Defect distribution evolution measured at operating temperature (153K)

By plotting the defect landscape at 153 K after each subsequent anneal step, the evolution of the defect landscape as a function of annealing temperature can be explicitly seen (Figure 7.11). Generally, the defect landscape is relatively stable as a function of annealing temperature, although some gradual changes are seen in different emission time constant ranges. Within the double negative state of the divacancy state peak, the number of defects gradually increases with anneal temperature, whereas the opposite occurs in the continuum to the right of the divacancy (a gradual decrease). To quantify the defect evolution, limits can once again be imposed on the emission time constant to isolate different areas independently.

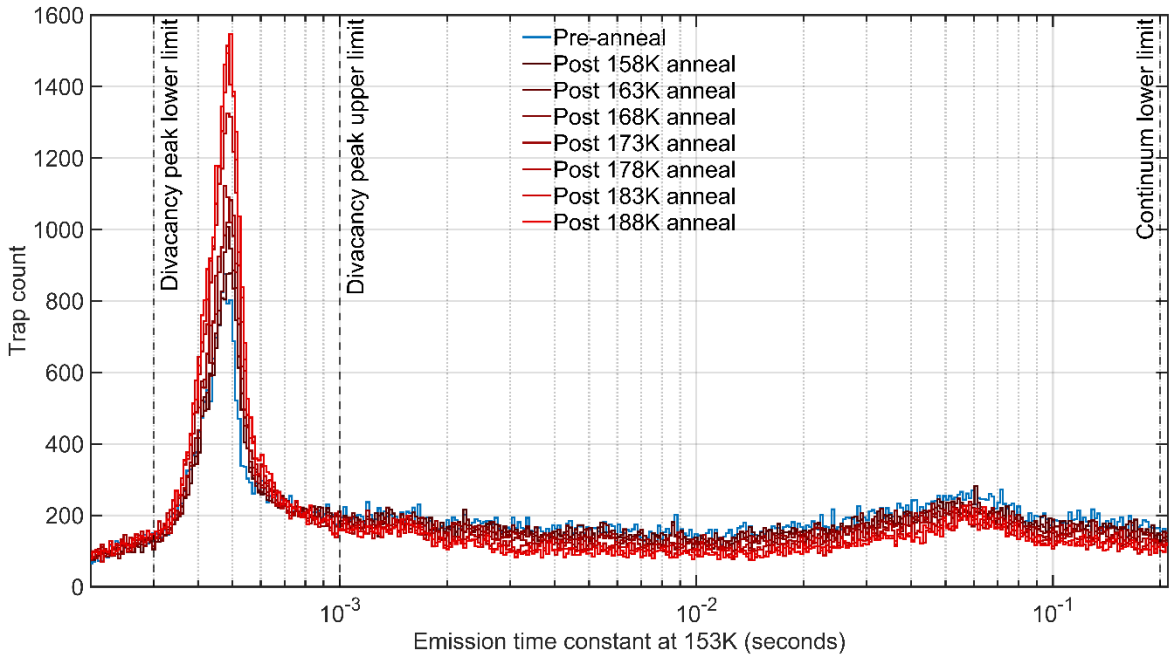


**Figure 7.11**: Trap landscape at 153 K after the annealing steps shown in Figure 7.9. Broadly speaking, as anneal temperature increases, the number of traps decreases in the continuum and increases in the peak of the divacancy.

Three limits are seen in Figure 7.11, two defining the peak of the divacancy, and a third defining the slower end of the continuum of defects. By plotting the quantity of defects between these limits, it is possible to see the change in quantity of defects as a function of annealing temperature and is shown in Figure 7.12.

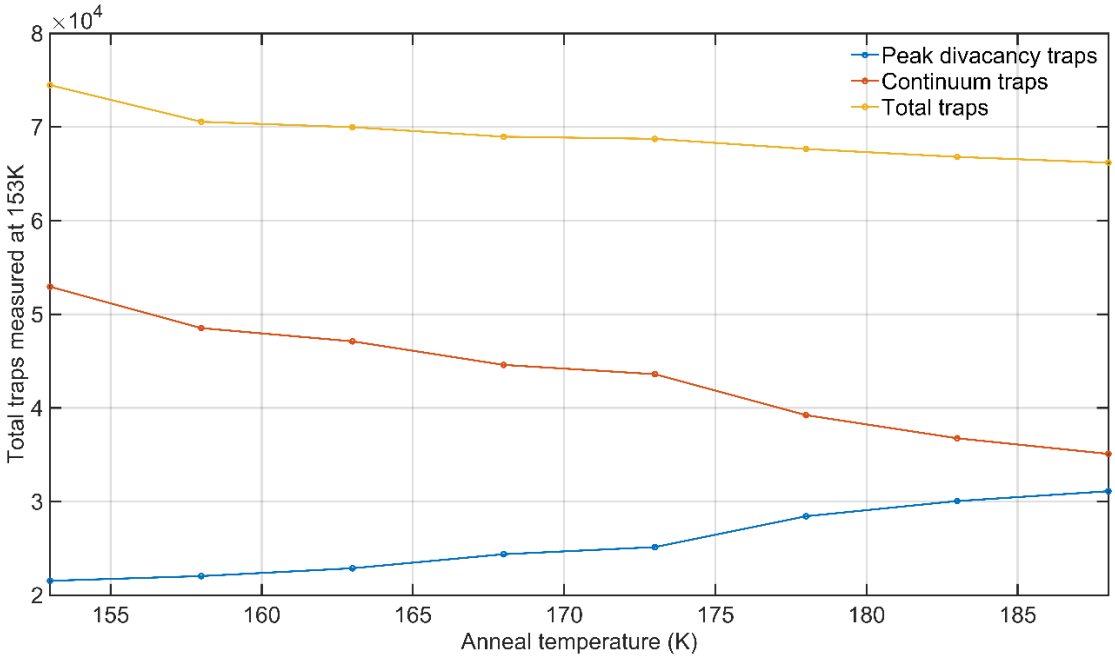


**Figure 7.12**: Quantification of the defects within the parameter space probed as a function of anneal temperature. Note that errors in the total traps measured are plotted but are too small to resolve. The errors are calculated by taking the emission time constant error on each fitted trap and adding the errors in quadrature to calculate an overall error on the summed histogram. The errors are small as the fitted traps shown in the previous histograms are only those with goodness-of-fit values greater than 0.9.

Figure 7.12 shows three distinct lines; the total number of defects between the divacancy peak lower limit and the continuum lower limit (yellow lines); the number of traps in the continuum (red line), between the divacancy peak upper limit and the continuum lower limit, and the peak divacancy traps (blue), between the lower and upper limit of the divacancy, respectively. Overall, the total number of defects within the parameter space is not constant, gradually falling as a function of annealing temperature. Defects located in the continuum and divacancy peak show opposite trends as a function of annealing temperature, with a steady increase and decrease as a function of annealing temperature, respectively. At low annealing temperatures 153 K), the total number of defects are dominated by the continuum, however this is eroded as annealing temperature increases, with an almost equal number of defects in these two populations after the 188 K anneal. The number of divacancy defects located within the peak is slightly overestimated however, as the divacancy peak is situated upon a broad continuum

of approximately 200 defects crossing a wide range of emission time constants, meaning that the true value is slightly lower.

Although Figure 7.12 shows that the quantity of traps within the continuum decreases over time, and the opposite behaviour in the peak of the divacancy, this does not mean that continuum traps are migrating from the continuum to the peak. Another feature of the trap pumping technique is that it can provide pixel location information as to the location of the pumped traps in each frame. If analysed as a function of time, a pixel map can be created, showing dynamic trap behaviour. Although not included here, most pixels containing a continuum trap do not then contain a peak divacancy trap, after the continuum traps have dynamically annealed/changed state. It is unclear at this stage what the underlying mechanisms are. Further work could investigate this behaviour in more detail.

### 7.4.3. Implications for SMILE SXI performance

Figure 7.8 initially showed the orbital variation of temperature for both a "hot" and "cold" orbit case. For the "hot" orbit case, a maximum temperature increase of approximately 10 K in expected above the approximate operational temperature of 153 K. Taking a maximum warming of 10 K above 153 K and applying it to Figure 7.12 suggests that the number of traps decreases by ~ 6% for the worst case heating scenario. Although the number of traps decreases (in the parameter space probed) by 6%, this does not necessarily mean that the number of effective traps (and hence CTI) will also decrease by 6%. There are several caveats to consider.

The trap landscape is broader than the range shown in Figure 7.11, meaning that there are more traps present in the device where the annealing behaviour as a function of temperature is not explicitly shown. Most notably, the area of defects between the unknown and Si-E was not pumped due to lack of time available. Work from the previous chapter showed that traps within the unknown to Si-E range do contribute to CTI (for the specific set of device parameters in the previous chapter) and thus potential annealing within this region would result in a larger decrease in total number of traps as a function of anneal temperature.

Another issue to consider is the potential time dependence of the annealing effects seen in the work above. During the experimental campaign, the annealing was completed in steps consistent with Figure 7.9, cycling periodically between 153 K and the subsequent warmer temperatures. In orbit however, SMILE SXI will be subject to many temperature-variable

orbits, raising the temperature of the CCDs by a few to 10 K many times over the course of the three-year science mission. Without further testing, it is unclear whether subsequent annealing could take place from these repeated cycles, or if an eventual stable defect landscape is reached.

Ongoing work for the ESA EUCLID mission is investigating the long-term changes to the cryogenic trap landscape in an irradiated CCD (operating temperature 153 K). The work so far (Lee-Payne, Z. et al., n.d.) has shown that long term changes in the cryogenic trap landscape, *without* temperature annealing, are similar to the small decrease in defects seen in Figure 7.11. The time scales for the defect decrease seen in the EUCLID CCDs are of the order of months, compared to the shorter time scales shown in Figure 7.11. This suggests that the annealing steps performed on the cryogenically irradiated CCD280 are accelerating the underlying process occurring in the silicon of the device.

## 7.5. Conclusion

Initially, the first cryogenic irradiation of a CCD280 (as part of the OU SMILE SXI irradiation campaign) was described, with the subsequent trap pumping plan post-irradiation outlined. The post-irradiation trap pumping was broken down into three distinct phases, to extract the most amount of information from the data during the time in which the trap landscape within the device was most unstable. An additional annealing experiment was then proposed, aiming to examine changes within the defect landscape that mimics the temperature variations that SMILE SXI will experience in orbit.

During the post-irradiation data analysis, an unstable defect species was identified, supporting other observations seen briefly in a previous recent study (Bush, N. et al., 2018). The analysis of the unstable defect species was taken further, quantifying the rate of defect decay to be a half-life 4.12 hours ±0.643 hours (or 3.51 hours ±0.674 hours) at 153 K. Implications of this defect decay were then discussed in relation to the performance of the CCDs on SMILE SXI in-orbit, in particular the short-term instability in charge transfer performance that could be expected following solar flare events.

From the temperature annealing experiment, changes in the defect distribution were plotted as a function of annealing temperature. Defects located in the “continuum” decreased in count, whereas the number of defects located in the peak of the divacancy increased slightly. Within the emission time constant range probed, a 10K anneal (the worst-case temperature fluctuation

that the CCDs in SMILE SXI are expected to experience in normal operations), reduced the number of defects by approximately 6%. There were caveats to this number however, as the full landscape was not probed, so additional annealing (which would reduce the number of defects by more than 6%) for long emission time constants could not be seen explicitly. Furthermore, the level of annealing seen was following temperatures beyond the range modelled for the SMILE SXI CCD. This could however be offset by multiple anneals at approximately 163K, as SMILE will undergo many of these smaller annealing cycles. Further investigations will be needed to assess the impact of numerous, smaller, annealing cycles.

Future work could investigate the potential variation of the decay time constant with irradiation temperature. For future CCD-based space missions, this is vital as different missions will most likely operate at different temperatures. If the decay constant does vary as a function of irradiation temperature, then the value of the decay constant for the instrument temperature in question must be measured to provide accurate in-orbit trap decay values.

For the temperature annealing experiment, future work could investigate the effects of multiple anneals of the *same* temperature, examining how the rate of annealing changes. For SMILE SXI, this would be useful as the SMILE SXI CCDs will experience multiple temperature fluctuations, each of which could change the distribution of defects (Figure 7.11). This would ensure that the evolution of defects of SMILE SXI CCDs in-orbit (and any CTI effects) would be understood.

# 8. Using the Active Trap Model to predict SMILE SXI CCD370 device performance

In chapter 6, the Active Trap Model was described, modified, and then tested to be able to accurately predict changes in CTI as a function of temperature for a room-temperature irradiated CCD280. One key result attained was that for accurate predictions of changes in CTI, a representative trap landscape must be used which resembles the trap landscape in the experimental CCD. In the case of chapter 6, this meant that a room-temperature irradiated CCD280 trap landscape had to be used to accurately model changes in CTI.

The overarching goal of developing and then using the ATM was to optimise charge transfer performance of the CCD370 for SMILE SXI. To do this however, additional work is required to both adapt the ATM to physically model a frame-transfer (FT) readout mode (with 6x6 binning also) and construct a cryogenic trap landscape from a SMILE-like device. Once the ATM has been sufficiently adapted, and a representative trap landscape generated, the ATM can then be used to predict the optimal clocking speeds for the CCD370s, which can be used to inform and direct experimental verification activities.

As an extension of the optimisation activities described here, the ATM has the potential to explore performance benefits of tri-level-clocking (TLC) for SMILE SXI CCDs. As part of the PLATO mission (and to a lesser extent EUCLID), TLC was baselined for the CCD270s as previous work showed CTI improvements (Peter Verhoeve – Private communication), albeit a small effect. As a result, pre-flight testing was carried out as part of the PLATO experimental campaign to explore the performance benefit that TLC provided on PLATO devices. Although this will be described in more detail in the later sections within this chapter, a broad range of CTI measurements showed a negligible improvement in performance, which opposed the previous work completed (Murray et al., 2013b). In terms of SMILE SXI, this added uncertainty to the decision of including TLC as a requirement in the SMILE CCD drive electronics, as the PLATO and SMILE detectors are similar, and TLC should provide some benefit, although the exact amount is unclear. Pressure to quantify the benefit of TLC was compounded by SMILE's condensed timeline along with significant system redesigns, adding extra risk of delays to the overall launch. A method was required which predicted the improvement in performance due to TLC, specifically in SMILE CCD370s, which was difficult

considering that device delivery had been delayed due to batch yield issues. The analysis described in section 8.4.3 provided the most accurately available analysis on the potential benefits of TLC to the SMILE SXI consortium, allowing an informed decision to be made to remove TLC from the SMILE CCD drive electronics.

## 8.1. Modifying the Active Trap Model for a CCD370 frame-transfer readout mode

Before the ATM can be used to predict the optimal clocking speeds of the CCD370 (and explore the additional benefits of TLC), the model must be adapted to accurately model the differences that arise due to the FT mode and 6×6 on-chip binning, in comparison to a full-frame (FF) readout. To understand the implementation of the CCD370 readout mode in the ATM, it is first useful to understand the main differences between the FF readout of the CCD280 and the FT readout of the CCD370.

### 8.1.1. Differences between full frame and frame transfer mode

The main difference between the FF CCD280 readout and the FT CCD370 readout is the inclusion of an additional clocking stage (controlling storage and movement of charge in the store region) as well as the 6×6 binning from the image region into the store region. In particular, the coupling of the three clock speeds within the CCD370 necessitates modifications to the ATM.

Figure 8.1 shows an example schematic of a FT readout, analogous to that of the CCD370 readout. The example device shows a four column CCD, with an image area comprised of six rows (shown by clear white boxes), a two-row store area (blue boxes), a standard serial register (grey boxes) and output node (triangle). Charge packets are indicated by black circles of varying sizes, corresponding to different size charge packets. In stage one, the CCD is exposed to a light source, collecting equal quantities of charge in each pixel within the image area. The image area is then clocked forward, moving charge from the image area to the store area, with this example showing a binning factor of three, whereby three rows of charge are moved from the image to store area before the store is clocked forward one row.

Stage two of the clocking process happens simultaneously to stage one, with the store area being clocked forward one row when three image rows worth of charge has been deposited into

the first row of the store region. The timing of the store region clocks is coupled with the time taken for the image area to be clocked forward the chosen number of pixel bins (three in this case).

Finally, stage three occurs when the store area is fully loaded with charge from the image area. This stage of the FT readout is identical to that of the FF readout, whereby a single row of charge is transferred into the serial register and subsequently readout. The only difference between this stage of the FT readout and the FF readout is that the charge is being transferred from the store region and not directly from the image area of the device.

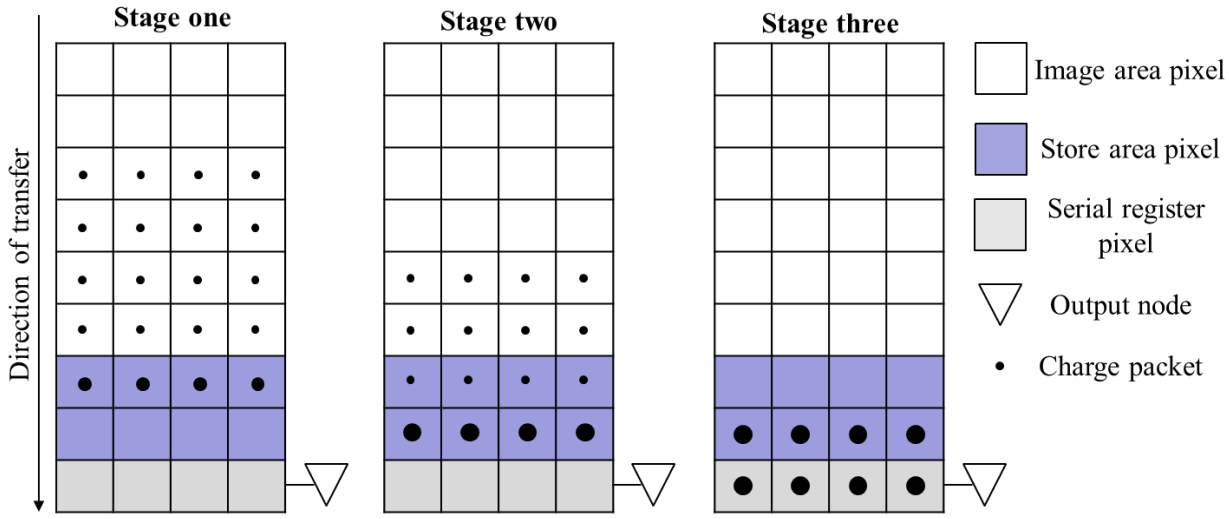


**Figure 8.1**: Schematic of a frame transfer readout, showing the locations of charge packets through three distinct stages of readout. CCD370s will utilise 6x6 binning, but for illustrative purposes a binning factor of 3 is used here.

In terms of the ATM, the additional stages of a frame transfer readout complicate the model as each stage of the FT readout is dependent upon different timings, and hence a different range of emission time constants (and hence different number of effective traps). Table 8.1 summarises the stages of readout for the FF and FT operating modes, highlighting the dominant timing that will set the minimum threshold timing in the ATM. As the dominant timings change for each stage of the frame transfer readout, the ATM will have to be modified to calculate the total number of effective traps for *each* stage of readout.

**Table 8.1**: Summary of the stages of each readout mode for both the full frame and frame transfer and the associated timings which dictate the range of defects which will contribute to CTI. Note that the FF readout mode has only a single stage of readout, consisting of a parallel line shift followed by readout of the serial register.

| Readout mode | Stage | Dominant timings |
|---|---|---|
| Full frame | 1 | Image and serial clocks |
| Frame transfer | 1 | Image clocks |
| Frame transfer | 2 | Store and image clocks |
| Frame transfer | 3 | Store and serial clocks |

#### 8.1.1.1. X-ray position within image area

The necessity of the multi-stage modelling approach for the FT readout leads to another issue regarding the unavoidable distribution of X-rays within the image area of the device. Unlike the FF readout, where the process to readout a frame was simply a single repeated stage (image shift to serial register followed by readout of the serial register), the multi-stage approach of the FT readout mode means that the ratio of stage transfers to readout an X-ray in a particular row is a function of X-ray position in the image area. To highlight this more explicitly, Figure 8.2 once again shows a schematic of a FT readout. As frame readout begins, X-rays in row five (highlighted in red) are moved through the image area until they are finally shifted into the store region. Once shifted into the store region, the X-rays in row five have been through five transfers in stage one (with a summary shown in Table 8.2). Due to the nature of stage one and two happening simultaneously, along with the position of the highlighted X-rays, X-rays within row five are not subject to any transfers in stage two. As stage three of the readout starts, the highlighted X-rays have three stage three transfers before frame readout is complete.

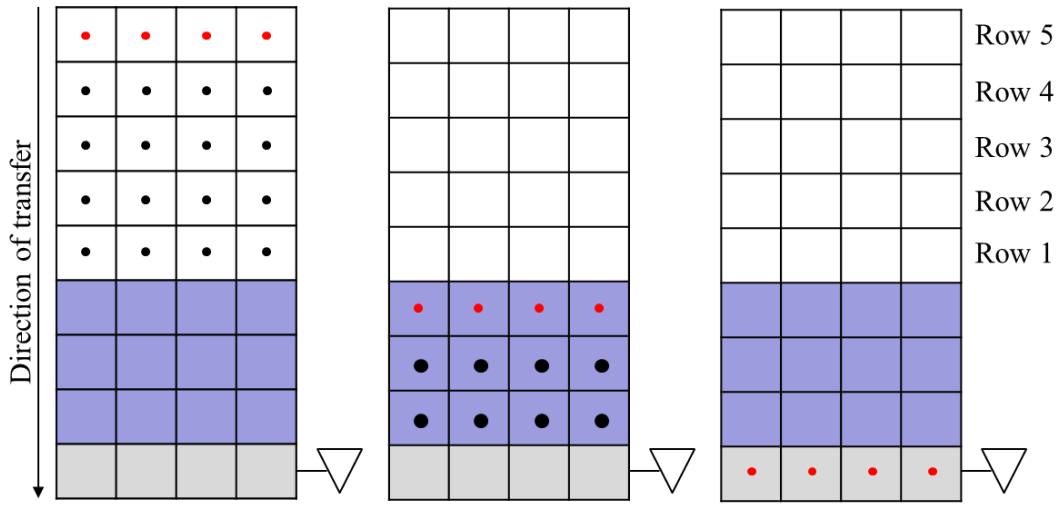


**Figure 8.2**: Schematic of a frame readout mode, highlighting X-rays in row five of the device (red dots).

Row one of Table 8.2 summarises the ratios of stage one/two/three transfers as a function of X-ray position. As X-ray row position changes, the ratio of transfers also changes, which directly affects the total number of defects which will contribute to CTI. In terms of the ATM, this means that the number of effective traps that contributes to CTI must be calculated as a function of X-ray position within the image area of the device.

One approximation used to simulate the CCD370 was in regard to the number of rows assigned to both the store and image section. The image section has 3791 rows, which when divided by 6 (the binning factor), leaving 88 rows spare, which charge will still be clocked through in practice. For simplicity, the simulation ignores these rows, as the total number of traps encountered in 88 rows, compared to the 3791 in the image section and 719 in the store section is negligible.

**Table 8.2**: Summary of the number of transfers required to readout X-rays in a frame as a function of X-ray position.

| X-ray row position | Stage one transfers | Stage two transfer | Stage three transfers |
|---|---|---|---|
| 5 | 5 | 0 | 3 |
| 3 | 3 | 1 | 2 |
| 1 | 1 | 2 | 1 |

### 8.1.2. Updated ATM flowchart methodology

Figure 8.3 shows an updated flowchart of each stage of the ATM for a FT readout mode. The updated flowchart shows the inclusion of both multi-stage readout modes along with the consideration of X-ray position within the image area.

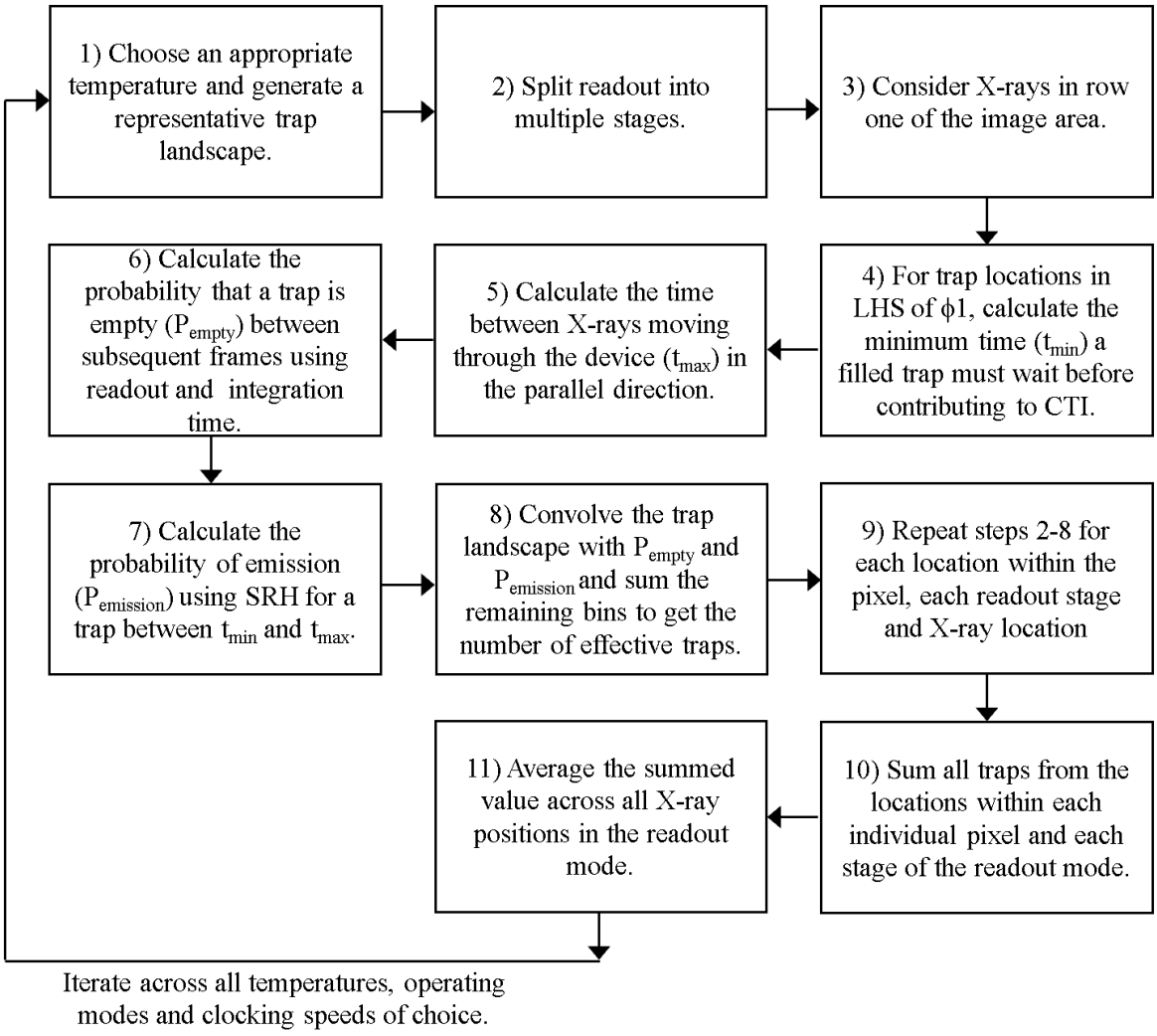


**Figure 8.3**: Updated flowchart of the stages of the ATM for simulating a FT readout mode.

## 8.2. Generating a representative trap landscape

To accurately simulate optimal clocking speeds for the CCD370 using the ATM, a cryogenic trap landscape (like that in-orbit) should be used. As part of the OU SMILE SXI experimental campaign (and undertaken for the preparation of this thesis), a range of trap pumping data was

collected after the irradiation of a CCD280 under cryogenic temperatures (chapter 7 - Figure 7.2).

To build a full trap landscape, containing all the defects of interest, a large amount of time is needed to fully probe the large range of emission time constants. As shown in chapter 6, pumping at different temperatures (and probing a different range of emission time constants) to build parts of the defect landscape can be achieved. These parts of the landscape can later be combined, along with adding known defects (like in Si-E), to generate a full landscape. Due to the nature of the characterisation plan however, complications occur.

The options for generating a full cryogenic landscape are shown in Table 8.3, with the pros and cons for each method highlighted.

**Table 8.3**: Summary of the different options available to generate a cryogenic landscape that will be used as input to the ATM to optimise the clocking of the CCD370s.

| **Method** | **Landscape used** | **Pros** | **Cons** |
|---|---|---|---|
| Combine pre temperature-cycling landscapes | CCD280 cryogenic | Landscape is measured directly in a cryogenic, SMILE-like device, held at 153 K | Narrow landscape (Figure 7.2 bottom), not including the unknown or Si-E. |
| Combine post temperature-cycling landscapes | CCD280 cryogenic (with possible annealing) | Wider emission constants probed (Figure 7.11) including the unknown | Device will include potential annealing effects. Si-E not included. Approximations will need to be used to combine landscapes (as per chapter 6) |
| CCD204 | CCD204 cryogenic landscape | Full cryogenic landscape including all defects (Si-A to Si-E) | Different device to SMILE devices. Some annealing may have occurred during trap pumping data collection |

The first method for generating a representative cryogenic landscape is to utilise the landscapes generated from the range of emission time constants probed, shown in Figure 7.2

(bottom). Within these landscapes, the divacancy will be sufficiently probed, along with a large range of the continuum of defects towards slower emission time constants. However, the unknown or Si-E defect is not sensitive to trap pumping at 153 K (with the pump delays used). This means that these defects would need to be added into the landscape with the same technique as used in chapter 6.

The second method of generating a representative landscape is to use the trap pumping data collected as part of the temperature-cycling part of the experimental campaign, with the emission time constants ranged probed shown in Figure 7.2 (bottom). Compared to method one, this method will be able to generate a landscape with a large emission time constant range (particularly towards slower emission time constants) and will contain the unknown defect. However, to probe these longer emission time constants, warmer temperatures are used (up to 188K) and some annealing can potentially take place as seen in chapter 7. Although the amount of annealing shown in section 7.4.2 is low, only a narrow window of emission time constants was probed, so the effect of annealing on the distribution of emission time constants outside of this range is unknown.

The final method for generating a representative trap landscape is to use previous data from a cryogenically irradiated CCD204. This landscape is complete, including the four main radiation induced defects and all defects between the main species. The main downside is that the landscape is from a different device than the SMILE/PLATO CCD, with a smaller issue being potential temperature annealing occurring during trap pumping data collection of the CCD204.

Considering the reasons stated above, the CCD204 cryogenic landscape was chosen as the input landscape to the ATM, to simulate a CCD370 FT readout and explore the effect of changing the image, store, and serial clocking speeds.

## 8.3. Results – SMILE CCD370 predicted optimal clocking speeds

Now that the ATM has been adapted to simulate a CCD370 FT readout, and the input trap landscape has been chosen, the ATM can now be used to show predicted trends in the number of effective defects (and hence CTI) as a function of different variables (shown in table 8.4). Constant parameters, such as temperature, integration time, X-ray density and the number of serial elements have been assigned values most representative of in-flight values.

The remaining parameters, namely the image, store, and serial clocking speeds, have been varied to investigate changes in charge transfer performance.

**Table 8.4**: Input parameters to the ATM for the simulated CCD370 readout.

| **Parameter** | **Value** |
|---|---|
| Image clocking frequency (kHz) | 10 - 50 |
| Store clocking frequency (kHz) | 10 - 50 |
| Serial clocking frequency (kHz) | 100, 140, 200 |
| Operating temperature (K) | 153 |
| Input trap landscape (Room temperature or cryogenic) | Cryogenic CCD204 |
| Pixels read per row | 2250 |
| Integration time (s) | 10 |
| X-ray density (per native pixel) | 1/3600 |

Before the predicted number of effective traps can be investigated as a function of variable clocking speeds, the number of effective traps as a function of X-ray position can be examined for each stage of the simulated CCD370 readout (shown by Figure 8.4). As the effective trap contributions are simulated for X-rays in different image rows within the CCD370, the relative trap contributions of each stage changes. For example, for X-rays towards the store region (low X-ray position), the number of effective traps is dominated by stage two contributions, as X-rays in this position have a very low number of stage one and three transfers (also shown explicitly by Table 8.2). As X-rays are simulated further from the store region, contributions from stage one and three increase, as X-rays at these positions are subject to more transfers through first the image region, and then through store transfers (including the serial register).

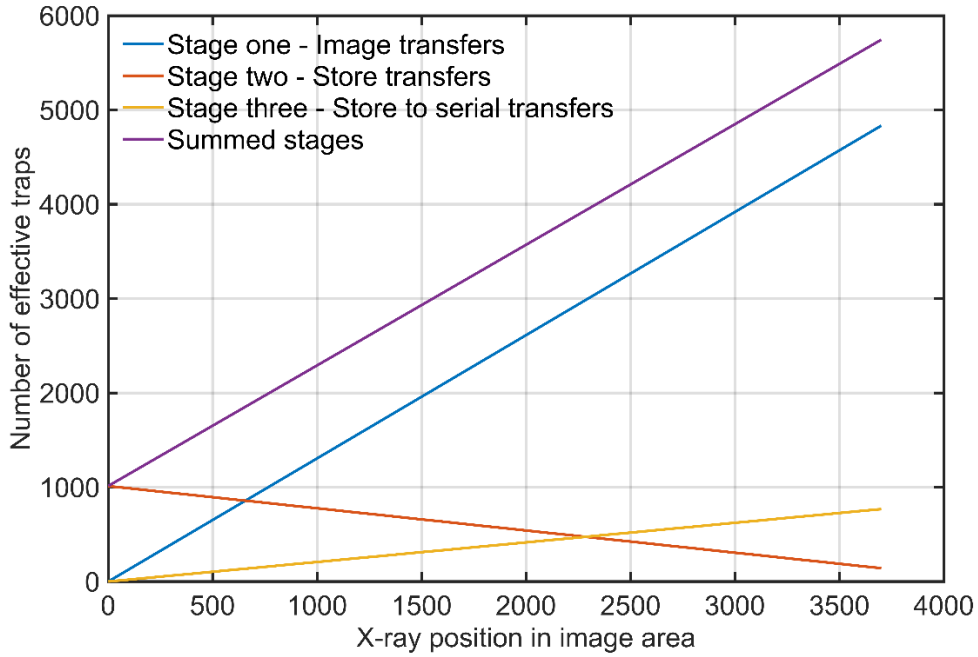


**Figure 8.4**: Number of effective traps predicted by the ATM as a function of X-ray position in the image area of a simulated CCD370, for all three stages of readout.

To generate physical values to guide to targeted optimisation (the end-goal of this modelling), the ATM output must be processed further. Physically, the CTI measured in a device comes from multiple X-rays spread throughout the image area, along with the defects encountered while passing through the image (and store) area and finally the serial register. This means that the output of the ATM should be scaled accordingly, by summing all defects encountered across all three stages of readout for an average X-ray position.

By using the input values summarised in Table 8.4, along with the ATM methodology shown in Figure 8.3, the number of effective traps as a function of the image, store, and serial clocking speeds can be predicted (shown in Figure 8.5). To be able to show the performance trends across a wide variable parameter space, three serial clocking speeds are used and shown in each column of Figure 8.5.

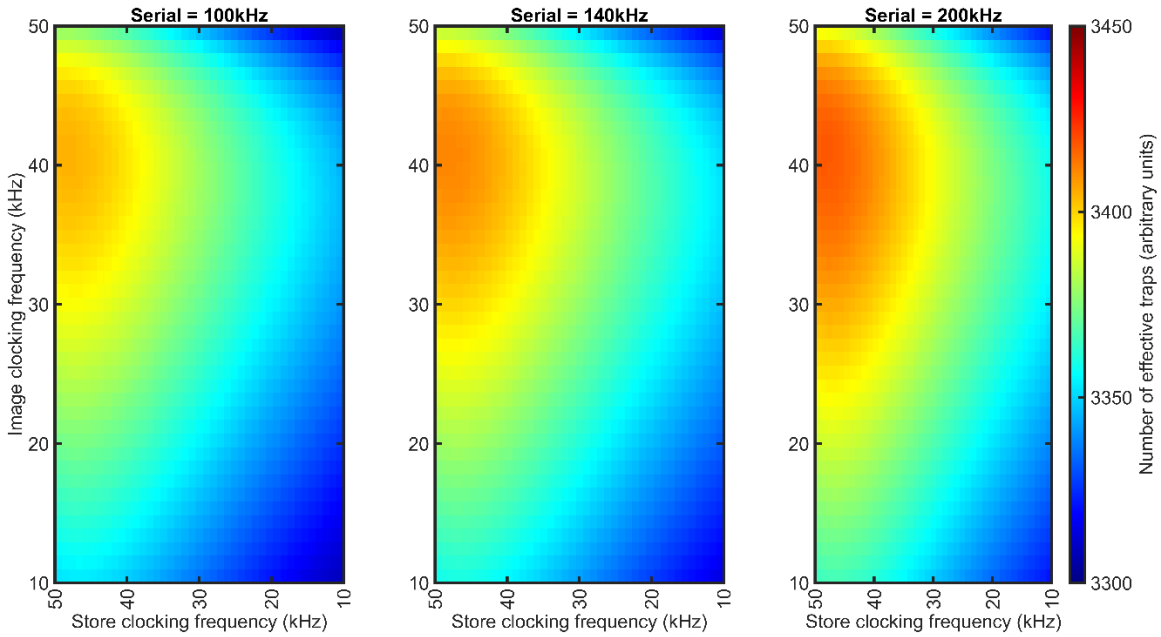


**Figure 8.5**: Output of the ATM as a function of the image, store, and serial clock frequency, with the number of effective traps indicated by the colour scale.

The number of effective traps predicted by the ATM varies with all three image clock frequencies. Generally, a lower serial clocking frequency is favourable, indicated by the shift of the colour scale from red to blue (moving from right to left in Figure 8.5). Across all three serial speeds, a region of higher effective trap density is seen, concentrated at high store clocking frequencies (50 kHz) and higher image clocking frequencies (approximately 30 – 50 kHz). To avoid this region of higher effective trap density, slower store clocking frequencies should be used in combination with image clocking frequencies at the extreme of the ranges (either towards 10 kHz or 50 kHz).

Although the number of effective traps does change with all three image clock frequencies, the changes in the effective number of traps is small (approximately 3% maximum) between extremes in Figure 8.5. However, there is one important caveat to consider, specifically an assumption made for stage two and three (store transfers) of the ATM FT methodology.

Due to the shield (10mm titanium) above the store region of the CCDs in the SMILE SXI instrument design, the level of displacement damage in the store region of the CCD370 should be significantly reduced compared to the image area. This means that as charge packets are transferred through the store region, a lower density of defects will be encountered and the

level of deferred charge in this region will be lower. In the ATM however, the defect landscape generated in stage two (and also stage three) assumed a radiation-induced landscape. This means that the contribution of defects from stage two and three of the ATM are overestimated, and most defects should arise from stage one. The ATM should therefore be amended, to include a lower-density defect landscape for stage two and three contributions. The exact level of reduction is hard to calculate at this stage, as although the 10mm titanium shield does protect the CCDs, protons in space will be incident upon the SMILE spacecraft (and CCDs) from all directions, and a majority will not be intercepted by the shield. The exact reduction in radiation damage will require additional simulations to calculate an accurate dose

As a result of the reduced level of radiation damage in the store region, this should *increase* the benefit of image clock optimisation in stage one of the ATM, as the base level of defects from stage two and three are no longer significantly reduced. When the CCD370 is tested, the performance benefit of changing the image clocks frequencies should be optimised first as a result.

## 8.4. Modelling the performance benefit of tri-level clocking

Previously, in chapter 3, a method known as TLC was briefly described which has been shown to improve CTI (Murray et al., 2013b). TLC utilises an additional voltage level, when compared to traditional bi-level clocking (BLC) schemes. Figure 8.6 shows a schematic of both a BLC and TLC readout scheme for an example four phase device.

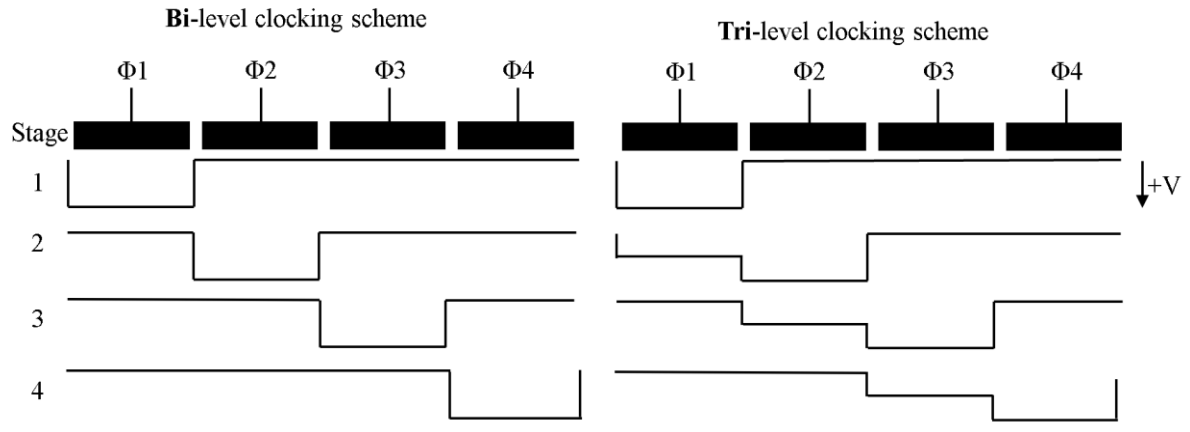


**Figure 8.6**: Simplified voltage profile of a BLC and TLC readout scheme. The intermediate voltage level can be adjusted, similar to the high/low voltage phases.

The additional, intermediate, voltage level is set between the high/low transfer voltage pulse and alters the shape of the potential well within each pixel. By shifting the shape of the potential well, filled defects are encouraged to emit their captured charge back into the source charge packet, thus reducing CTI. Figure 8.7 shows an example of how TLC can alter trap emission dynamics to reduce CTI.

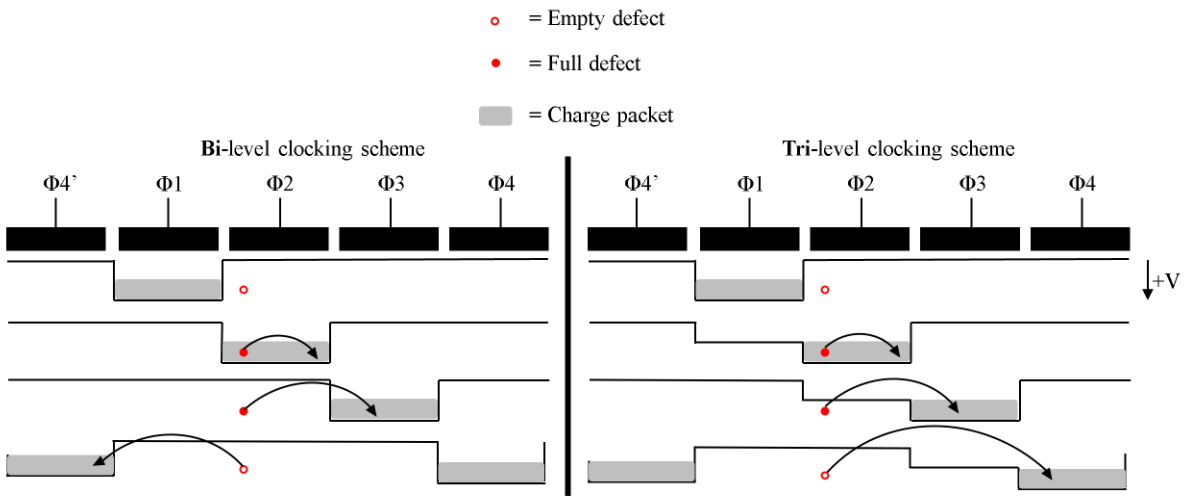


**Figure 8.7**: Trap emission dynamics of both a BLC and TLC scheme. Black arrows indicate the charge packet which the emitted electron will most likely return to. Note that the shape of the potential well physically within the pixel is not a step function, but a smooth curve (Murray et al., 2013b).

In the case of a BLC scheme (Figure 8.7 – left), charge is moved sequentially from $\phi 1$ – $\phi 4$, following the potential wells created by voltages applied to the electrodes. Consider a defect under the left-hand side of $\phi 2$, with this defect filling as charge is transferred under $\phi 2$. Once filled, the defect can emit this charge at any time (with the time governed by the emission time constant of the defect). If the defect emits when the charge is under $\phi 2$ or $\phi 3$, then the captured electron returns to its original charge packet (as this is the closest charge packet), not contributing to CTI. When charge finally moves below $\phi 4$ however, the closest charge packet is not the source charge packet, meaning that if emission occurs, this emitted electron will join the non-source charge packet and cause CTI.

Consider the same scenario using a TLC scheme (Figure 8.7 – right), with another defect in the same position as the BLC case. Under the first three stages of readout, the same emission

dynamics occur, with the captured electron being emitted back into the source charge packet, not contributing to CTI. However, in stage four, although the closest charge packet is the non-source packet, the defect is now encouraged to emit back into the *source* charge packet due to the altered shape of the potential well from the intermediate clock voltage. This individual defect has now effectively been suppressed due to TLC, not contributing to CTI.

Due to CTI performance benefits of TLC (as outlined above), previous pieces of work for CCD space missions such as EUCLID (Murray et al., 2013b) have explored the use of TLC and shown improvements in CTI. SMILE SXI is no different and could potentially benefit from the use of TLC. Initially, TLC was baselined for the PLATO mission as performance benefits were expected before experimental verification. However, surprisingly, a negligible improvement in performance was seen for several operating parameters including irradiation temperature, parallel clocking speed and operating temperature. Even after a room temperature anneal, no additional benefit was seen in PLATO CCDs (Peter Verhoeve – Private communication). Consequently, TLC was removed from the PLATO baseline design, although the exact reason for the negligible improvement in performance was not clear.

Due to the significant heritage of PLATO with respect to the SMILE mission, this created a significant amount of uncertainty with regards to implementing TLC. This uncertainty, combined with the lack of CCD370s (preventing experimental verification as to the performance benefit of TLC), necessitated a different solution to the problem. If the ATM described, tested, and implemented in chapter 7 can be modified to model the improvement of TLC, then a case definitive case can be made to baseline TLC as part of SMILE SXI operating modes.

To be able to model the effects of TLC on trap emission dynamics, TLC must first be implemented correctly, with the new model then validated on the both the EUCLID (Murray et al., 2013b) and PLATO TLC results. Validation is necessary at this stage, as the potential output of the ATM with respect to CCD370 performance cannot be compared to experimental data. Once the implementation of TLC with the ATM is validated, the ATM can then be used to predict performance improvements of TLC for a CCD370 readout mode. The information can then be reported to the SMILE SXI CCD working group, to make an informed decision with regards to baselining TLC as part of the CCD370 readout electronic design.

### 8.4.1. Implementing tri-level clocking within the Active Trap Model

TLC is implemented in the ATM by altering the minimum time threshold (seen in Figure 6.6) for each pixel location simulated in the readout mode. The remainder of the ATM is identical, with the functionality of TLC being switched on/off by changing a single input value. As TLC encourages filled defects to emit back into the source charge packet, this means that the performance benefits are seen in the suppression of *fast* traps. If the implementation of TLC is working correctly, then the effective trap landscapes should show that faster traps are being suppressed, with negligible improvements seen for relatively slower traps.

### 8.4.2. Validating the model

Before the ATM can be used to predict the improvement in TLC for the CCD370s, the results produced from the model must be compared to experimental results. This will help to validate the performance of the model in predicting physical results and trends as well as increasing confidence in the results for application with the SMILE CCD370s. Furthermore, trying to replicate the results in different CCDs, read out with different clocking speeds and temperatures, shows the patterns that the model can produce. When lacking a large base of experimental data (as is the case for the improvements in performance for TLC), seeing trends in the ATM match what is expected physically is invaluable.

#### 8.4.2.1. Comparison to EUCLID results

The first experimental result to be simulated via the ATM was part of the EUCLID mission, in particular the performance of the CCD273s (Murray et al., 2013b). Within the paper, CCD273s were operated in a full frame readout mode, using the parameters seen below in Table 8.5.

**Table 8.5**: Experimental parameters taken from the EULCID TLC paper (Murray et al., 2013b). Note that the image line transfer time was taken directly from the oscilloscope trace in the paper, and the operating temperature as well as X-ray density was provided by David Hall (private communication).

| **Experimental parameter** | **Value** | **Simulated parameter** | **Value** |
|---|---|---|---|
| Image line transfer time (per row) (s) | $400 \times 10^{-6}$ | Image line transfer time (per row) (s) | $400 \times 10^{-6}$ |
| Serial clocking frequency (kHz) | N/A | Serial clocking frequency (kHz) | Varied |
| Operating temperature (K) | 153 | Operating temperature (K) | 153 |
| Initial landscape (Room temperature or cryogenic) | N/A | Initial landscape (Room temperature or cryogenic) | Room temperature (~293 K, CCD204) |
| Pixels read per row | 2048 | Pixels read per row | 2048 |
| Integration time (s) | 300 | Integration time (s) | 300 |
| X-ray density (per raw pixel) | N/A | X-ray density (per raw pixel) | 1/80 |

X-ray CTI measurements were taken using the parameters in Table 8.5, with three different voltage schemes. These three results are shown below in Figure 8.8, with the specific improvements in performance because of TLC highlighted for clarity.

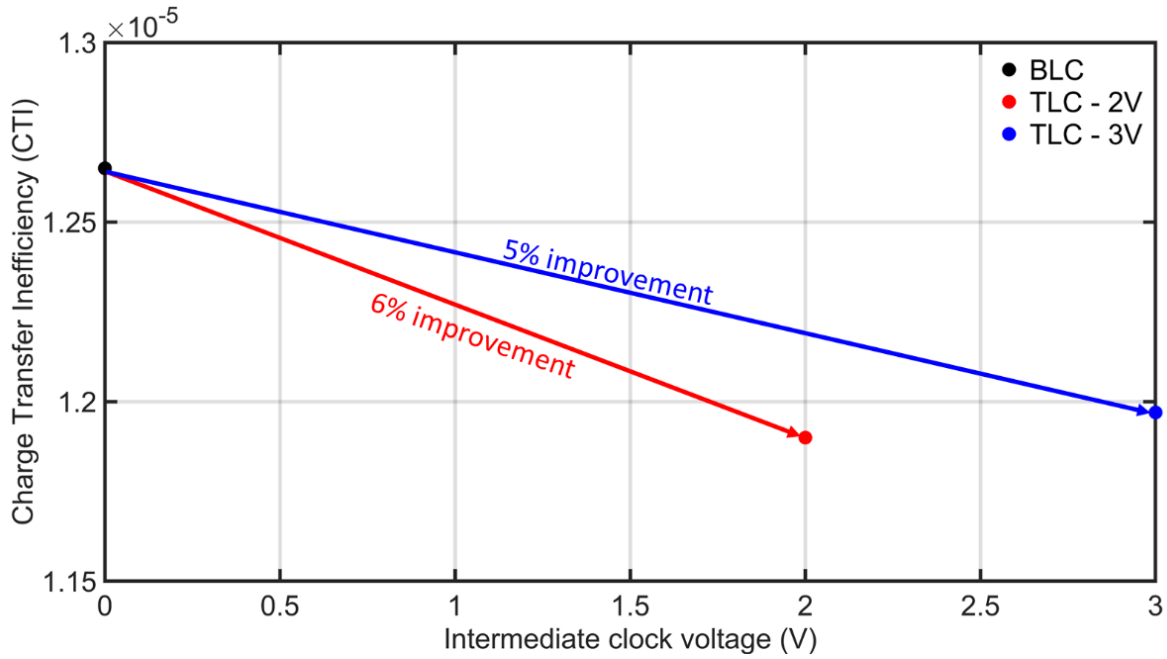


**Figure 8.8**: Recreated CTI as a function of intermediate clock voltage graph (Murray et al., 2013b). Note that no errors bar was included in the results.

Initially, the CCD273 was operated with a BLC scheme, with 0V and 9V used as the electrode off/on voltages, with no intermediate clock voltage. Two additional data sets were then collected using TLC scheme, with the intermediate clock voltage set at 2V and 3V. Comparing CTI between the BLC mode and each TLC mode shows an improvement in performance of between approximately 5-6%.

To be able to simulate the performance of TLC using the ATM, the values in Table 8.5 can be used. However, two key values necessary for the ATM were not available within the paper, namely the serial clocking speed and the X-ray density used for the CTI measurements. The X-ray density was attained from David Hall (private communication) and was 1 X-ray per 80 pixels, a standard value used for X-ray CTI measurements at the time. The serial clocking speed, however, was unknown, and was left as a variable in the ATM. Figure 8.9 shows the comparison between the output from the ATM and the experimental CTI measured.

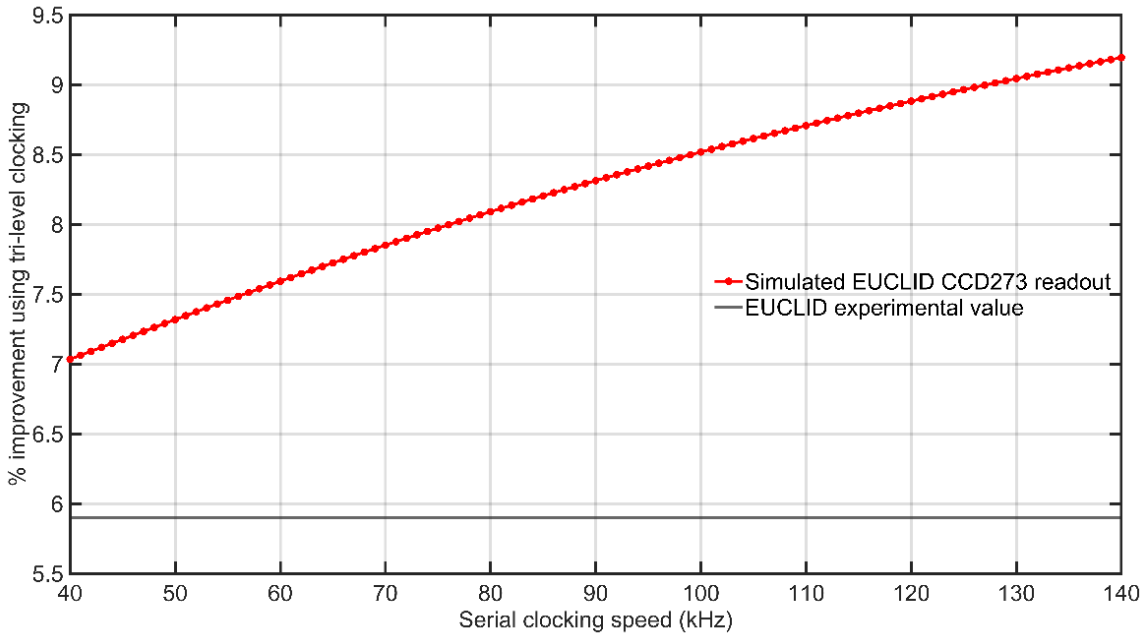


**Figure 8.9**: ATM simulated results vs the EUCLID experimental values (single data point) (Murray et al., 2013b) for a range of serial clocking speeds. Note the y-axis is showing the number of traps predicted by the ATM for both the BLC and TLC operation mode as a function of serial clocking speed. The percentage improvement is simply the ratio of TLC to BLC performance. ATM parameters for the above plot are shown in Table 8.5. Note that a parallel clocking speed equivalent to 2.5 kHz was used.

For the range of serial clocks speeds simulated, the performance benefit of TLC is approximately 7-9%, compared to the experimental value of approximately 6%. As serial clocking speed is increased, the performance benefit of TLC increases gradually. To be able to interpret this overestimate of TLC performance along with the gradual increase in performance as a function of serial clocking speed, the model outputs can be analysed to examine where the specific improvement in performance is originating from.

Figure 8.10 shows the distribution of defects present for three scenarios. The unprocessed landscape is shown in black for reference, with the two subsequent landscapes in green and red showing the effective traps for BLC and TLC, respectively. As expected, the main source of traps contributing to CTI in both the BLC and TLC mode are in the centre of the landscape which does not include the Si-E and Si-A. The improvement in performance by using TLC can be seen by the difference between the red and green landscapes. Most defects that are being

suppressed due to TLC are those with faster emission time constants, most notably within the divacancy peak as well as the two smaller intrinsic peaks to the right of the divacancy.

TLC alters the profile of the potential well, such that defects within a specific location in each pixel can emit their captured charge back into the source charge packet, thus reducing CTI. The defects must emit before the source packet moves sufficiently far away, or else the defect will still emit the captured charge into a different source packet, and still contribute to CTI. This means that TLC should offer more benefit for defects with a shorter emission time constant, as these defects are able to emit before the source charge packet moves into the subsequent pixel. Figure 8.10 shows that it is indeed the faster defects that are encouraged to emit back into source charge packets, thus improving performance due to TLC.

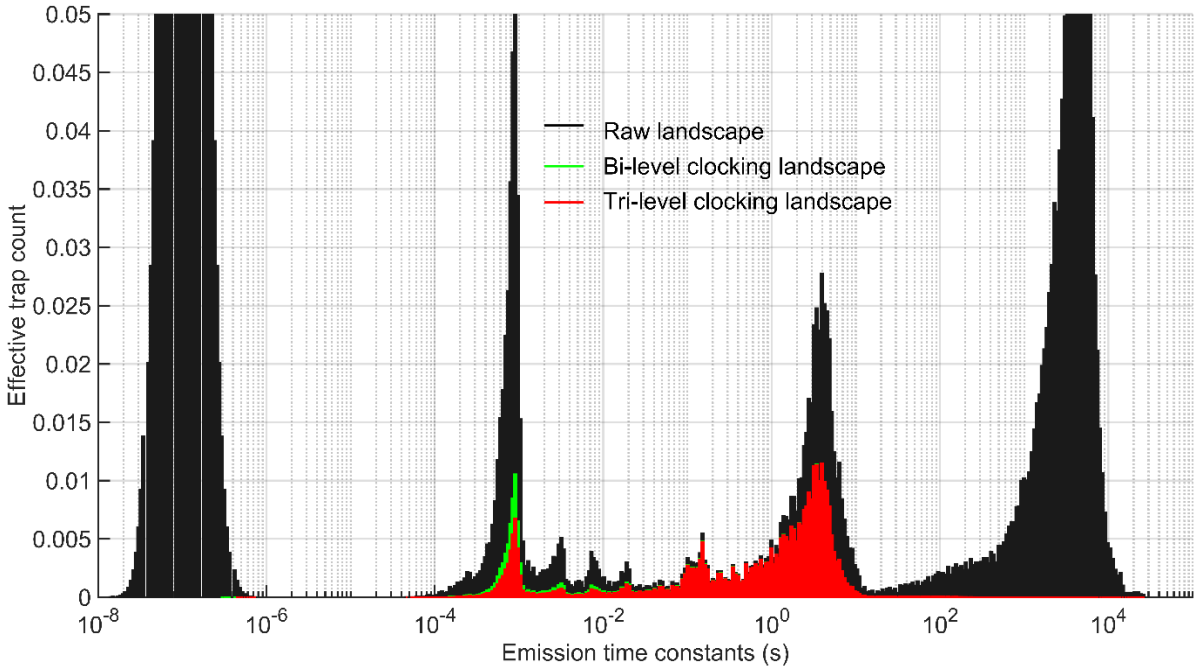


**Figure 8.10**: Three trap landscapes showing the total traps present in an irradiated CCD204 (black) and the effective number of traps present using a bi-level and tri-level clocking scheme in green and red respectively. Note that the effective trap count in the BLC and TLC scheme are identical above $1\times10^{-1}$ s.

The increase in performance for TLC in comparison to BLC as a function of serial clocking speed can be explained by the total number of effective traps for each serial clocking speed. Figure 8.11 shows the effective traps that are present for three serial clocking speeds for both the BLC and TLC schemes, with an identical colour scheme to that seen in Figure 8.10. As

serial clocking speed increases, the benefit of TLC increases, suggesting that TLC is suppressing a larger number of traps when compared to slower serial speeds. In the context of the trap landscape, this means that the difference between the green (BLC) and red (TLC) landscape should increase with serial clocking speed. This is not seen however, as the difference between the red and green landscape is very similar at low emission time constants.

At slower emission time constants however, the number of effective traps contributed from the Si-E in the BLC scheme decreases as serial clocking speed increases. This is due to the faster serial clocking speed reducing the time to readout the entire serial register, thus reducing the time given for slower defects to emit and be counted as an effective trap. As the benefit of TLC is always in relation to the total number of defects in the BLC scheme (*including* the Si-E), the traps suppressed due to TLC are now a larger proportion of the total effective traps and appear to give a larger performance increase.

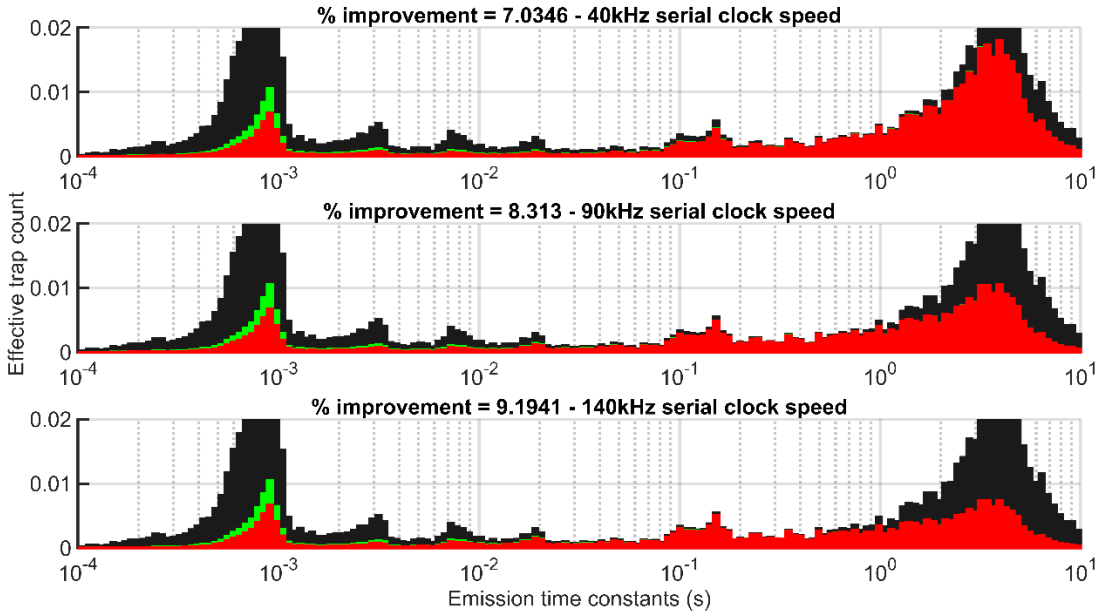


**Figure 8.11**: Effective trap landscapes for three example serial clocking speeds. The raw trap landscape is shown in black, the BLC effective trap landscape in green, and the TLC effective trap landscape in red. Note that the effective trap counts in the BLC and TLC scheme are identical above $1\times10^{-1}$ s.

### 8.4.2.2. Comparison to PLATO results

As part of the PLATO experimental campaign, the benefit of TLC was explored over a range of parameters including parallel clock speed as well as in two separate devices, one irradiated at room temperature, and one irradiated at a cryogenic temperature. The parallel X-ray CTI results are shown in Figure 8.12 (top), with the percentage improvement due to TLC shown in Figure 8.12 (bottom) (Peter Verhoeve – Private Communication). The percentage improvement in CTI for TLC varies between 0% (with a few data points below 0%) and approximately 10%. No strong trend is seen as a function of parallel clock speed, for both the room-temperature and cryogenically irradiate device.

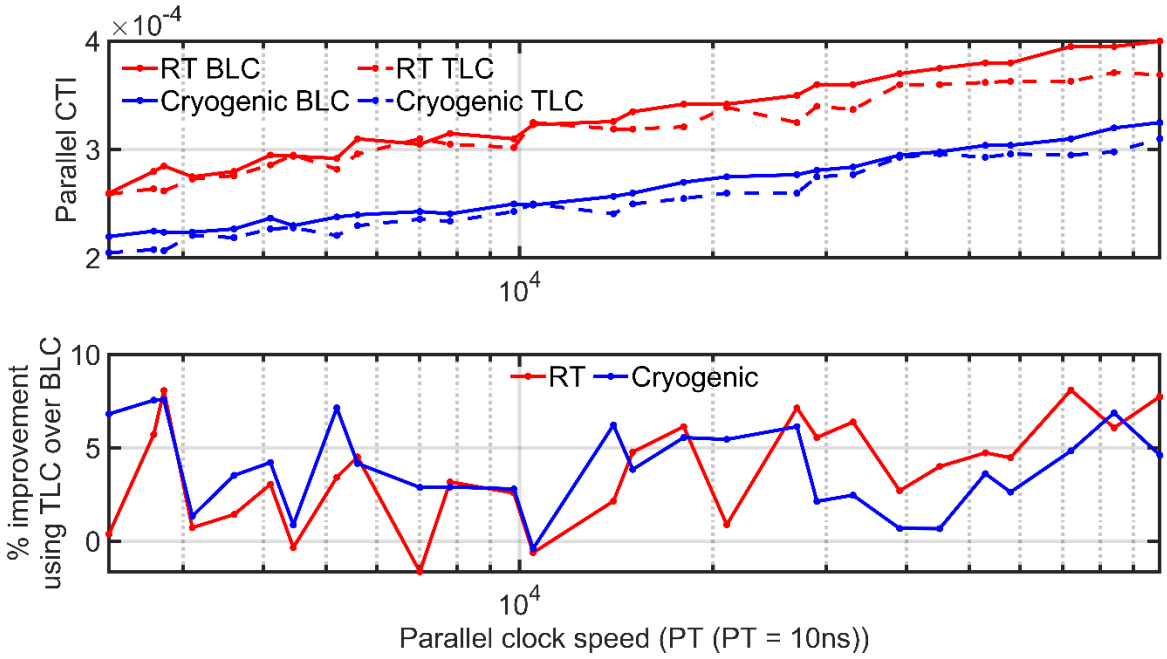


**Figure 8.12**: Parallel X-ray CTI as a function of parallel clock speed for two devices (Peter Verhoeve – Private Communication), and two clocking schemes (top). The percentage improvement as a function of parallel clock speed in shown in the bottom of the figure.

To collect the X-ray CTI data, the experimental parameters that were used are shown in Table 8.6. To simulate the experimental results using the ATM, the simulated parameters are also shown in Table 8.6. Due to the PLATO experiments using two separate devices, irradiated at two different temperatures, different input trap landscapes are required for an accurate comparison. For the room-temperature data, a CCD280 room-temperature landscape is used. However, due to similar reasons as stated in section 8.2, a cryogenic landscape from a CCD204

is used as the CCD204 landscape is a complete landscape, compared to the partial CCD280 cryogenic landscape that was measured by the author.

**Table 8.6**: Experimental parameters for the PLATO data collection.

| Experimental parameter | Value | Simulated parameter | Value |
|---|---|---|---|
| Image line transfer time (s) | Varied | Image line transfer time (s) | Varied |
| Serial clocking frequency (kHz) | 3000 | Serial clocking frequency (kHz) | 3000 |
| Operating temperature (K) | 153 | Operating temperature (K) | 153 |
| Initial landscape (Room temperature or cryogenic) | N/A | Initial landscape (Room temperature or cryogenic) | Room temperature (CCD280) and cryogenic (CCD204) |
| Pixels read per row | 1552 | Pixels read per row | 1552 |
| Integration time (s) | 10 | Integration time (s) | 10 |
| X-ray density (per raw pixel) | 1/155 | X-ray density (per raw pixel) | 1/155 |

The predicted performance improvement due to TLC is shown in Figure 8.13 in the solid red and blue line. For reference, the experimental CTI results are also included, shown by the dashed lines. The ATM predicts very small improvements in performance due to TLC, approximately 1% across the range of parallel clock speeds, with a small divergence between the cryogenic and room-temperature cases at high parallel clock speeds. When compared to the noisy experimental values (which also do not include error bars), the predicted performance improvement due to TLC shows good agreement.

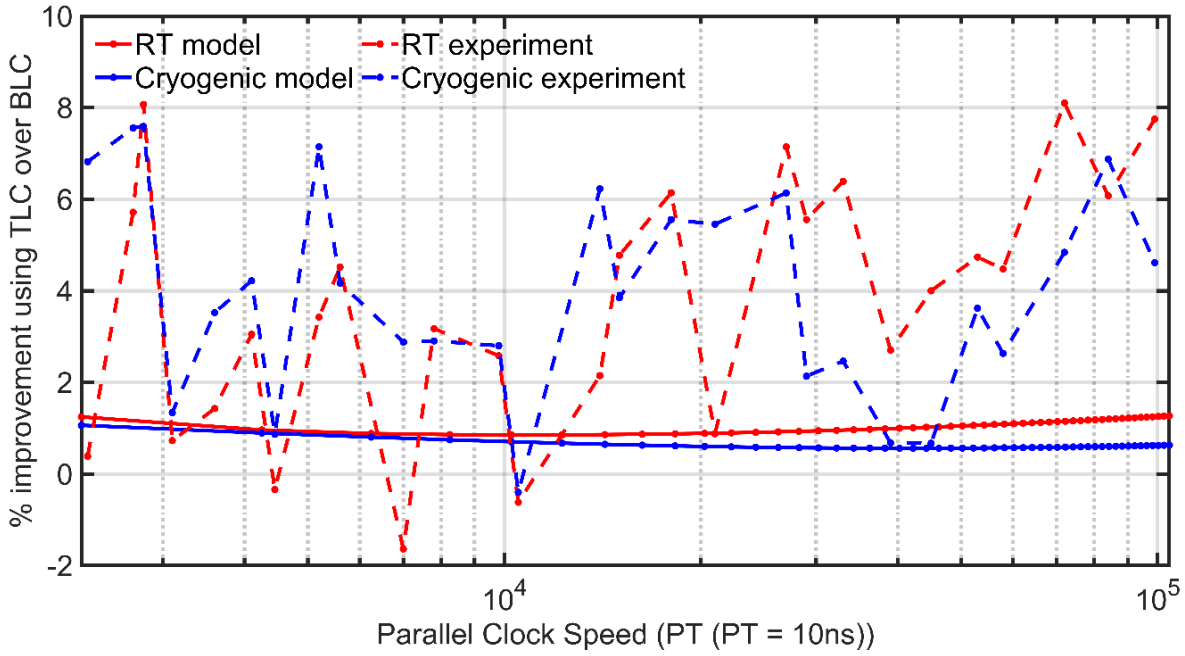


**Figure 8.13**: Comparison of the improvements due to TLC (compared to BLC) for the experimental (dashed lines) and ATM results (solid lines). No discernible trend is seen in the experimental data as a function of parallel clock speed.

### 8.4.3. Predicted performance improvements for SMILE SXI CCD370s

In section 8.4.2.1 and 8.4.2.2 the ATM was used to predict performance improvements due to TLC for two separate devices. The results showed that the ATM could reproduce performance improvements (at least to order of magnitude) seen in experimental X-ray CTI data, indicating that the implementation of TLC within the ATM was working correctly.

Now that the implementation of TLC has been validated (to the few data sets that were available), the ATM can now be used to predict the performance benefit of TLC for a simulated CCD370 readout mode. Table 8.7 shows the input parameters used for the ATM, with operating temperature, X-ray density and integration time chosen to be as mission-like as possible. The cryogenic landscape used was from a CCD204, which is not ideal, but the landscape is still complete compared to the cryogenic CCD280 landscape.

**Table 8.7**: Simulated input parameters to the ATM to predict the performance improvement from TLC.

| Simulated parameters | Value |
|---|---|
| Operating temperature (K) | 153 |
| Input trap landscape | Cryogenic (CCD204) |
| Image clocking frequency (kHz) | 50 |
| Store clocking frequency (kHz) | 50 |
| Serial clocking frequency (kHz) | 140 |
| Integration time (s) | 10 |
| X-ray density (per raw pixel) | 1/3600 |

The ATM was run for both a simulated BLC and TLC readout scheme, with initial results shown in Figure 8.14. The number of effective traps is shown as a function of X-ray position in the x-axis, with stage one, two and three in red, blue, and green, respectively. The effective traps from the BLC and TLC scheme are in solid and dashed lines, respectively.

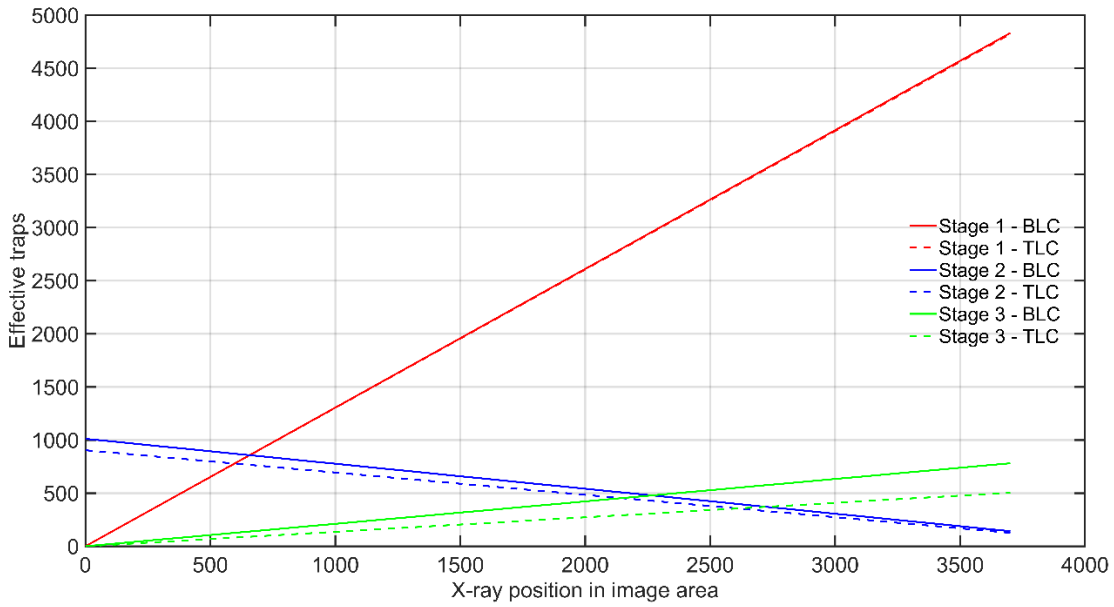


**Figure 8.14**: Predicted number of effective traps as a function of X-ray position for each stage of the simulated CCD370 readout mode for both the BLC and TLC mode.

For each stage, TLC is altering the number of effective traps as a function of X-ray position, albeit with the magnitude of improvement changing for different X-ray positions. The changing magnitude of improvement is once again due to the different ratios of stage one/two/three transfers as a function of X-ray position.

To see the overall performance improvement due to TLC, the defect contributions from each stage can be combined, with ratios of defects compared between BLC and TLC. The overall performance improvement as a function of X-ray position is shown in Figure 8.15.

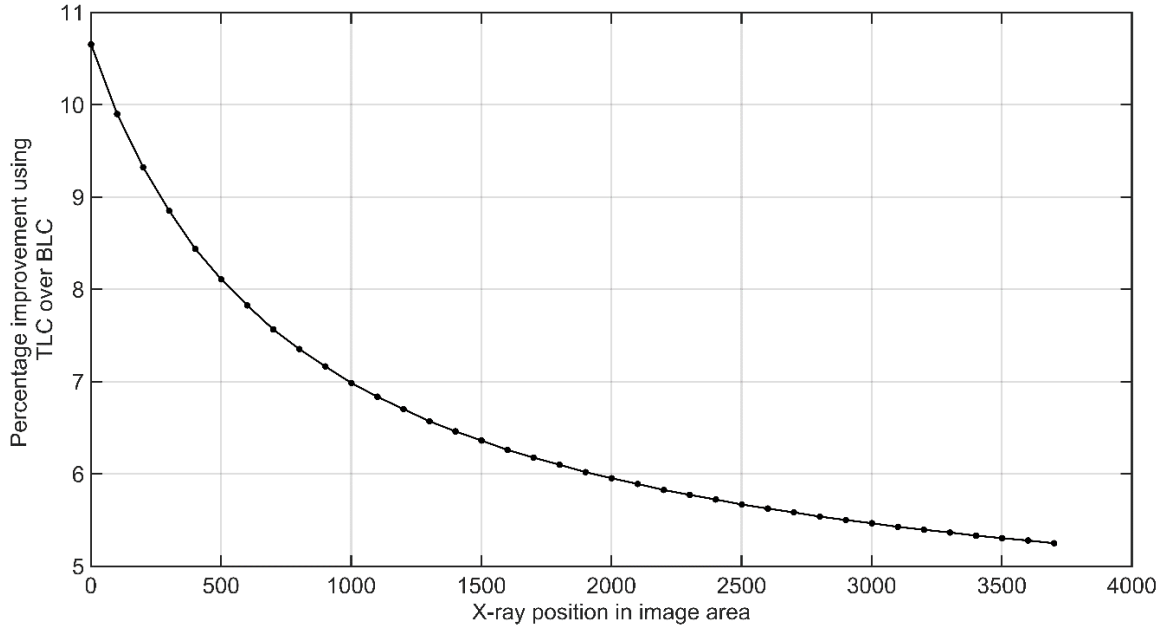


**Figure 8.15**: Output from the ATM, of the predicted performance improvement simulating a BLC versus a TLC readout mode.

The percentage improvement in performance due to TLC decreases as a function of X-ray position. Although, looking at Figure 8.15, the performance improvement of TLC for stage two and three increases as a function of X-ray position, the effective trap contribution of stage one (and lack of TLC benefit) outweighs the performance improvement from stage two and three. For an average X-ray, the predicted performance benefit of TLC by the ATM would be approximately 7-8%. However, the caveats discussed in section 8.3 also applies to this result (as the same base CCD370 simulated clocking mode is used). This means that the defect contributions from stage two and three are overstated in the ATM, meaning that the performance benefit of TLC is also overestimated. The predicted benefit of TLC will most

likely only be due to stage one, where only a very small improvement in performance is seen. Overall, this means that the performance benefit of TLC will be below 7-8%.

#### 8.4.3.1. Implications for SMILE SXI in-flight operating modes

Figure 8.15, along with the ATM TLC validation results (section 8.4.2.1 and 8.4.2.2), were presented to the SMILE SXI CCD working group in 2020. The predicted performance benefit of TLC was assessed versus the risks and costs of implementing TLC in the front end electronics. It was concluded that the predicted performance benefit of TLC did not outweigh the effort required to implement and test the required hardware. As a result, TLC was removed from SMILE SXI in-flight operating modes.

## 8.5. Conclusions

Initially, the differences between a FF and a FT (CCD370) readout was described. The FT readout was split into three stages, an image shift to store region (stage one), a store region shift (stage two) and an additional store region shift (including serial readout of pixel values). An additional complication was then described, arising from the position of X-rays with the image are of the CCD370. The ratio of each number of individual stage transfers is a function of X-ray position within the image area, so this must be taken into account.

The implementation of a CCD370 readout using the ATM was then described, including modelling of multiple stages (stage one, two and three) and the additional input of X-ray position within the image area. To provide estimated, optimal image clocking frequencies, the effective trap contributions from X-rays from individual rows will be calculated separately, with the final estimated effective trap value originating from the average X-ray row. Finally, the effective trap contributions from stage one, two and three, will be summed, as physically, charge packets will be subject to traps from all three stages.

A selection of simulated parameters was then determined using values as close to in-orbit values as possible (values summarised in Table 8.4). The three variables within the ATM were the image, store and serial clocking frequencies. The range of image and store values were determined via similar experimental values, with the maximum achievable image/store clock frequency at approximately 66 kHz (or below). The serial clocking frequency was simulated at

three values, spanning a wide (and experimentally achievable) range, 100 kHz, 140 kHz, and 200 kHz.

Results showed that a *slower* serial clocking frequency should be used (towards 100 kHz). An important caveat was described, involving the reducing of store area defects as a result of the 11 mm titanium store shield. |The ATM overestimates the number of stage two and three defects due to the lack of shielding in the model, which will have subsequent effects for the optimisation of both the image and store clocking frequencies. Once implemented, this reduction in defects should *increase* the effectiveness of optimising the image clock frequencies as the total number of defects present is now reduced (while still maintaining image area defects. The exact magnitude of the effect is unclear at this stage, but due to the potential improve in performance for the image clock frequencies, experimental optimisation of the image clocks should take place first.

The method of TLC was then described, including motivation for investigations into the effectiveness of TLC for SMILE SXI CCDs. The method of implementation of TLC within the ATM was described, with the ATM then used to replicate two previous TLC experimental results. The results from previous work on the EUCLID (Murray et al., 2013b) and PLATO mission (Peter Verhoeve – Private communication) showed that TLC offered small (and often insignificant) benefits to CTI performance, which the ATM then also showed. This helped to validate the implementation of TLC with the ATM and meant that predicting the performance benefits of TLC for SMILE SXI CCD370s could be done with a higher degree of confidence. The ATM showed that TLC provided a performance benefit of approximately 7-8 % (Figure 8.15), with the true value most likely being below this due to the neglect of the store shield in the analysis. The analysis was delivered to the SMILE SXI consortium, with the final (informed) result being the removal of TLC from the SMILE drive electronics.

# 9. Predicting the effects of hyper-velocity particulate impacts on SMILE SXI CCDs

Space-based soft X-ray detectors have been utilised for many decades to observe a myriad of soft X-ray sources including gamma-ray bursts, neutron stars as well as many other hot astronomical objects. Observing from space is essential to avoid atmospheric absorption but also can provide many positives such as uninterrupted views of stellar objects. It does, however, come with downsides such as a harsh environment in the form of radiation and hyper-velocity particulates. The former has been studied extensively, with every component on a space-based X-ray telescope undergoing significant testing and adaptation for radiation hardness. This includes crucial components such as electronic components including detectors and associated materials. Damage due to hypervelocity-particulate impacts has had significantly less research, partly due to the sporadic nature of hyper-velocity particulates, while also partly due to less overall risk as most key components are physically shielded by the spacecraft itself. Areas that are open to space, and thus not shielded, are vulnerable to hypervelocity-particulate impacts, most notably the mission-critical detectors.

Modern advances in X-ray optics, most notably the development of silicon micro-pore optics (sMPO) provide significant advances in field of view (FoV) while offering reduced mass (Bavdaz et al., 2012). However, as sMPO provide direct line of sight from space to the sensitive focal plane, this increases the risk of a potentially fatal hyper-velocity particulate impact. Not only do the sMPO provide line of sight access to the focal plane, the increased FoV leads to a larger photon as well as particulate collecting area, which only increases the risk of a hyper-velocity particle impact.

Future space-based observatories (such as SMILE SXI) which use the new sMPO technology must consider the risk of particulate impacts, which will require new insight into the interaction of particulates with the optics themselves as well as knowing the direct effect of particulate impacts on the detector of choice themselves.

To fully understand the risk and effects to the detectors and optics from particulate impacts many questions require answering such as:

- How many hyper-velocity particulates are expected to be incident on the area during the mission's lifetime?
- What are the mechanisms that control the passage of these particulates through sMPO?
- Once understood, how many particulates can pass through the optics and hence impact the detector for the specific case of SMILE SXI?
- For the impacting particles, how can the damage caused be quantified and translated to a change in detector performance?

To answer these questions, a framework has been developed by the author, bringing together published models and experimental results. An overall description of the simulation package is shown in Figure 9.1 in the form of a block diagram. The development of the simulation package and a study of the results relevant to the SMILE SXI application are presented in this chapter.

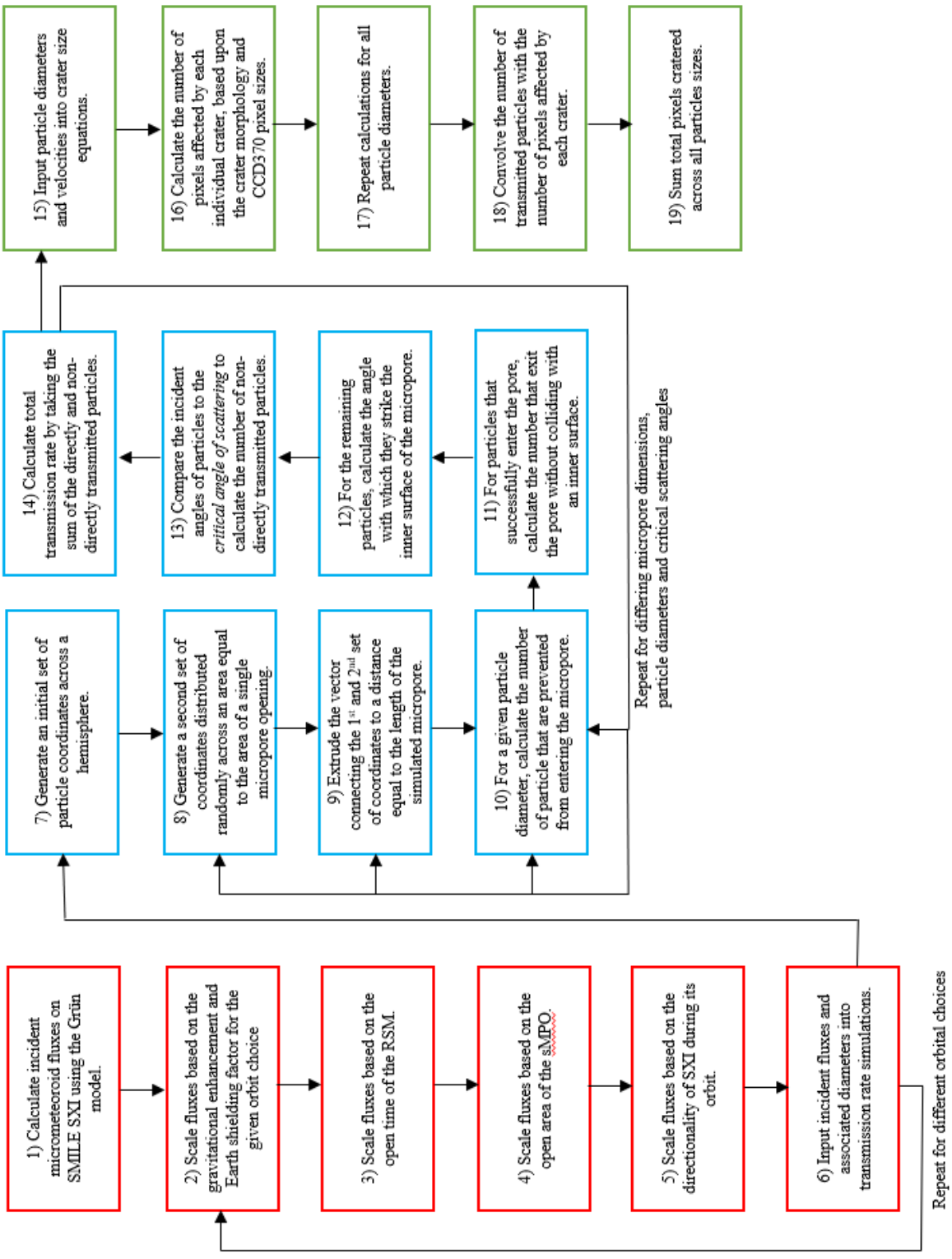


**Figure 9.1**: Block diagram of the simulation package developed, with each colour represent a distinct section. Red – Calculation of the incident particulate flux on the sMPO of SXI. Blue – Calculation of the transmission rate of particulates through the sMPO. Green – Calculation of the size of craters formed by each impact within SXI's focal plane.

## 9.1. Predicted particulate flux incident on the SMILE spacecraft

The total particulate flux incident on the SMILE spacecraft over the course of its 3-year science mission can be calculated using the Grün model (Grün et al., 1985) and ESABASE (SPENVIS, 2019) software for micrometeoroids and space debris respectively using the orbital parameters of the mission, as described in section 4.2. The output is quantified as the number of particulates (including micrometeoroid and space debris) with mass equal to or greater than mass m (as described in Eq 4.8 in chapter 4) which strikes a randomly orientated surface. The predicted flux is dependent upon parameters including the orbital radius, corrections due to gravitational effects associated with the Earth and directional factors that change with orbit and pointing direction.

Although the flux values presented in Figure 9.2 are useful in terms of particulate fluxes on the SMILE spacecraft, investigating fluxes with respect to SXI performance necessitate several modifications, which are summarised below:

- SXI is physically located on one side of the SMILE spacecraft, so a directionality component of flux must be assessed.
- The particulate flux which can potentially damage the detectors is that which is incident upon only the sMPO, and not the whole SMILE spacecraft.
- To reach the focal plane, particulates must then successfully traverse the sMPO.
- The Radiation Shutter Mechanism (RSM) closes for a proportion of each orbit, which effectively shields the detectors of SXI from particulate damage.

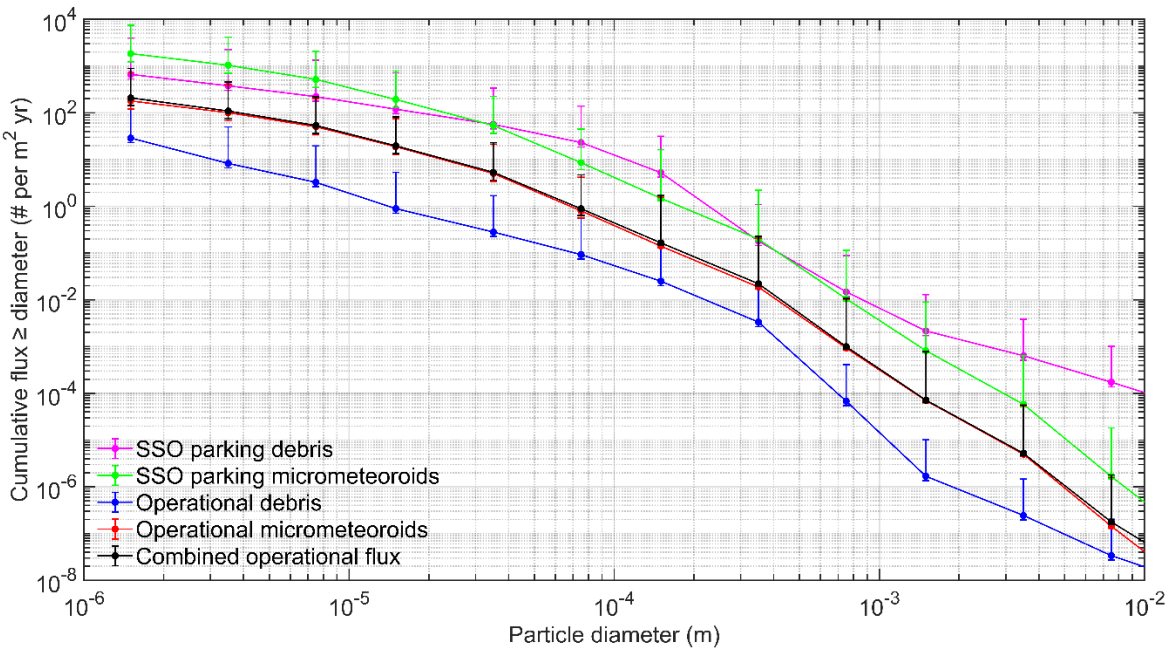


**Figure 9.2**: Replicated micrometeoroid and space debris flux values (Mark Millinger, 2018) with error bars added by the author, which originate from the uncertainties in the diameters and hence masses of both micrometeoroids and orbital debris. Uncertainties in flux arise from uncertainties in flux as a function of particle diameter (Anderson, B. and Smith, Robert., n.d.). Sun-synchronous orbits (SSO) were also included to provide more information, but only the operational (science) orbits were used in the analysis for the work presented in this thesis.

Due to the number of modifications above, flux values will be calculated directly from the Grün model (and not taken directly from Figure 9.2) to provide accurate flux values in relation to those that are incident upon the sMPO. Furthermore, due to the altitude of the RSM closing during each orbit (50000 km), flux values originating from orbital debris will *not* need to be calculated as most space debris is significantly below this altitude where the detectors are shielded by the RSM (ESA-ESTEC, 2008).

## 9.2. Modifying the particulate flux

The Grün model uses orbital parameters to calculate particulate flux estimates. Orbital parameters for three different launch date options are shown in Table 9.1.

**Table 9.1**: Key orbital parameters for the three operational orbit options (Mark Millinger, 2018).

| **Option** | **1** | **2** | **3** |
|---|---|---|---|
| Mission duration (years) | 3 | 3 | 3 |
| Launch date | 22/04/2022 | 22/10/2022 | 22/10/2021 |
| Perigee altitude (km) | 5000 | 5000 | 5000 |
| Apogee altitude (km) | 121000 | 121000 | 121000 |
| Inclination (degrees) | 98.2 | 98.2 | 70 |
| R.A. of ascending node (degrees) | 0 | 165 | 206 |
| Argument of perigee (degrees) | 287.5 | 287.5 | 287.5 |
| True anomaly | 0 | 0 | 0 |

Particulate flux as calculated by the Grün model is a function of orbital altitude, shown explicitly by the dependence of both the gravitational enhancement factor (GEF) and Earth shielding factor (ESF). This means that the SXI science limit altitude of 50000 km effectively places a lower limit on the fluxes received, as any flux incident on the detectors below this altitude is prevented from reaching the focal plane by the RSM. When calculating fluxes using the Grün model, this means that the lower altitude must be set to 50000 km. Due to the change in flux with altitude, the two extremes of altitude (perigee 5000 km and apogee 120000 km) are shown in Figure 9.3, with the true flux received between the two lines in Figure 9.3.

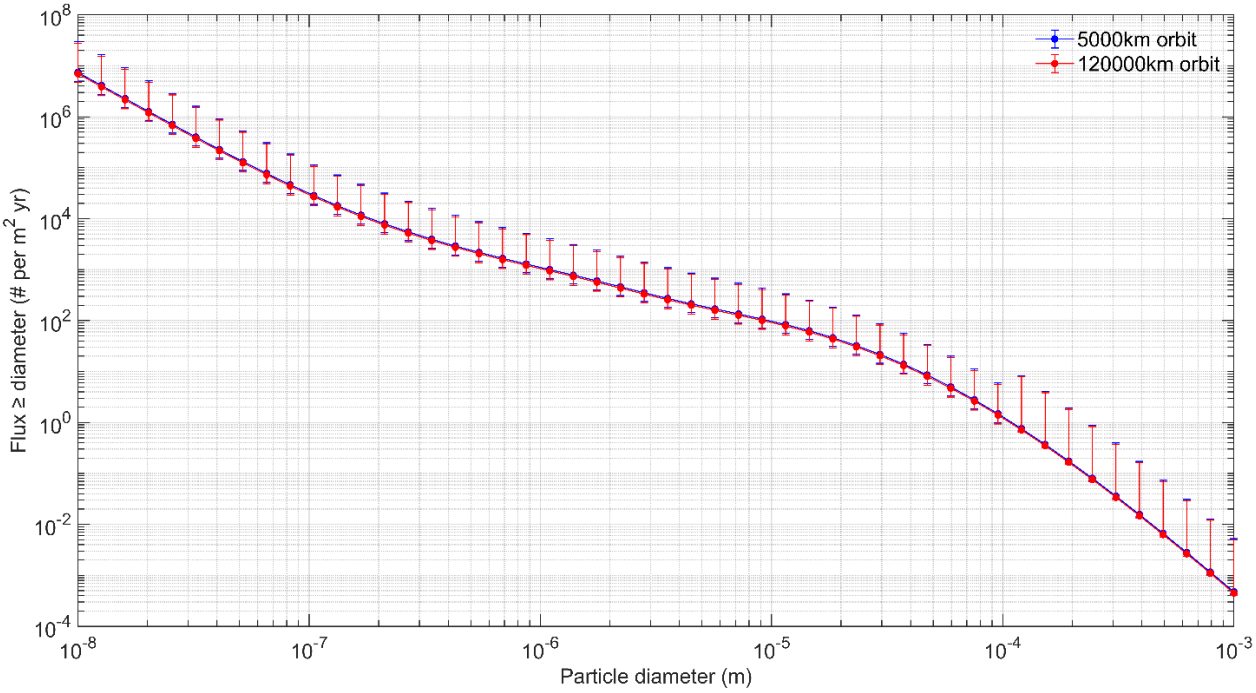


**Figure 9.3**: Particle flux calculated by using the Grün model for two orbital radii, as a function of particle diameter. For both orbits, the curves are nearly identical, showing no difference in flux as a function of particle diameter or orbital altitude.

The difference in flux is minimal, as at these relatively large altitudes with respect to the Earth's diameter, the difference in GEF and ESF are small. Due to the nature of the highly elliptical orbit, SMILE will spend more time closer to its apogee, this means that for subsequent analysis, the flux values from the 120000 km orbit will be used.

### 9.2.1. Radiation Shutter Mechanism

By using the key orbital parameters in Table 9.1, it is possible to plot the variation of altitude with respect to time for each orbital option. Software created by ESA named SPENVIS (**SP**ace **ENV**ironment **I**nformation **S**ystem) (SPENVIS, 2019) is used to plot the orbit of SMILE SXI as seen by Figure 9.4, which shows the periodic nature of 8 total orbits specific to orbital option 1 in Table 9.1. To be able to calculate the total percentage of each orbit that the RSM is open, both the duration of each orbit must be known along with the point at which the RSM opens and closes.

The horizontal black line in Figure 9.4 represents the altitude when the RSM opens and closes (50000 km), with the black dots representing the intersection of the altitude profile and SXI

science limit altitude. The distance between each of these successive black markers is the time in which the RSM is open and closed, respectively.

The next stage of analysis is to calculate the orbital period, which is done by taking the derivative of the altitude with respect to time. By taking the points where the derivative is equal to 0, the perigee and apogee of each orbit is attained. By taking the ratio of the time between the black markers (above 50000 km) and the orbital period calculated using the time between apogees (red markers), the fraction of each orbit that SXI is above 50000 km and vulnerable to particulate impacts is calculated. Taking an average across each orbit in Figure 9.4 provides a value of **83.18%**.

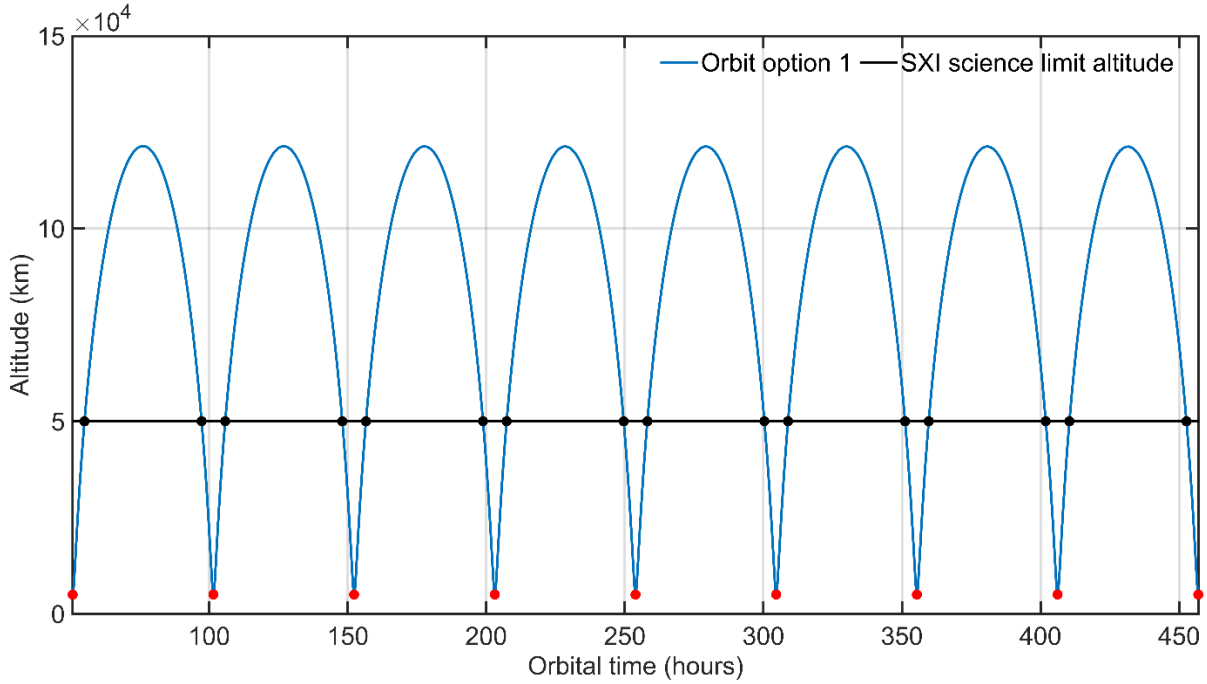


**Figure 9.4**: Altitude profile of SMILE over the course of 8 total orbits of the Earth. The limit at which the RSM opens/closes (black horizontal line) is marked for each orbit. Note that only orbital option 1 is included here, as option 2 and 3 are virtually identical in terms of orbital parameters and hence average percentage of each orbit that the RSM is open.

### 9.2.2. Spacecraft directionality

Another necessary scaling factor originates from the directionality of the SMILE spacecraft with respect to the Earth. Separate directionality scaling factors (DSF) are calculated (Mark Millinger, 2018) for both micrometeoroids and orbital debris as each particle population has a

different spatial distribution. Due to the lack of orbital debris above 50000 km however, the DSF for orbital debris are not needed. Table 9.2 below shows the DSF for three separate spacecraft ratios.

**Table 9.2**: Micrometeoroid directionality values for the SMILE spacecraft (Mark Millinger, 2018).

| Ratio | Value |
|---|---|
| Front/random | ≈ 1.3 |
| Front/rear | ≈ 1.6 |
| Zenith/nadir | ≈ 1.0 |

To be able to use the above ratios to scale the flux for SMILE SXI accordingly, some assumptions must be made regarding the pointing direction of SXI during the portion of its orbit above 50000 km. These assumptions are as follows.

- On SMILE's outbound journey (away from the Earth), it is assumed that the direction of SXI will be purely opposite the RAM direction of the spacecraft, as SXI observes the area of space adjacent to the Earth.
- On the return journey, after apogee, the pointing direction will be purely aligned with the RAM direction of the spacecraft.

Although the actual orientation of SXI with respect to the spacecraft velocity is constantly changing, the use of these assumptions allows the values in Table 9.2 to be used to effectively scale the flux incident on SXI. Taking the average of (1.3 and (1.3/1.6)), equates to a DSF of 1.06, increasing the flux by 6%. It is also assumed that the effect of the ram direction has no bearing on the incident speed of particulates on the detectors of SXI.

### 9.2.3. Optical area flux scaling factor

The total area of the sMPOs are exposed to space, and so can be used in conjunction with the Grün model to calculate total incident fluxes. However, only a fraction of the optics are "open" to both photons and particulates, with the remainder of the area needed for mechanical spacing between each micropore. To be able to calculate the effective open area, the dimensions of the

micropores can be used along with the overall optical area. For the case of SMILE SXI, the dimensions of the micropores are 40 μm × 40 μm with a wall width of 12 μm (Buggey, T. et al., 2018), leading to value of **59%** open area on the optics. Given that the total area of the optics is $\mathbf{5.12 \times 10^{-2}\ m^2}$, the total area available to photons and crucially other hazardous particulates is $\mathbf{3.07 \times 10^{-2}\ m^2}$. Figure 9.5 below shows an example of a micropore module (left) and a schematic highlighting the dimensions for a set of four micropores (right) for clarity. Within the schematic, the grey area shows the spacers between each pore (red arrow) and is equidistant for all micropores. The white area represents the "open" area of the pores, with pore widths and lengths given by the bold blue and dashed lines respectively.

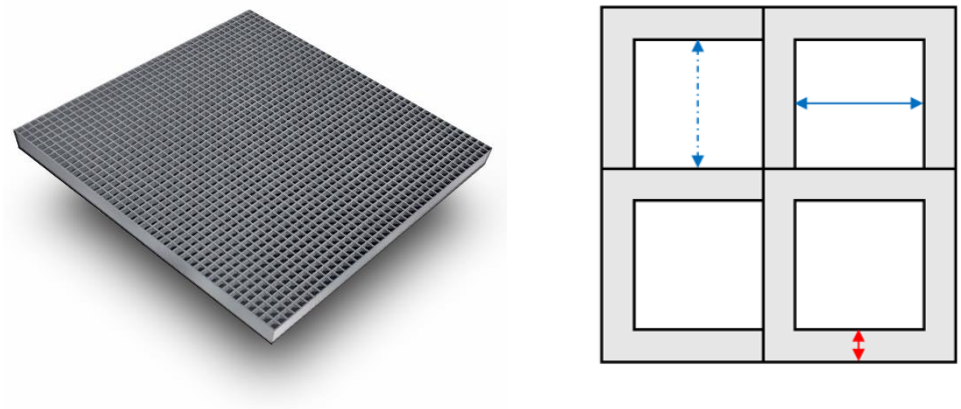

**Figure 9.5**: Left – A grid of micropores arranged as part of a single module ("Micro Pore Optics," n.d.). Right – Schematic of four example micropores.

### 9.2.4. Summary of factors to scale the Grün flux accurately

The total flux shown in Figure 9.2 is the micrometeoroid flux incident upon a randomly tumbling 2D plate. To be able to scale to a value representative of the case of SMILE SXI sMPO, the factors required to compute this calculation are summarised in Table 9.3 below.

**Table 9.3**: Summary of the scaling factors calculated in the previous sections. Note that the GEF and ESF were computed within the Grün model, based solely on orbital radius.

| Scaling factor | Value |
|---|---|
| Gravitational enhancement factor | 1.0531 |
| Earth shielding factor | 0.9993 |
| Ratio of orbit with RSM open | 0.8318 |

| | |
|---|---|
| Optical open area | 0.59 |
| Spacecraft directionality | 1.06 |
| Mission duration (years) | 3 |

By applying the scaling factors to the 120000 km orbit flux in Figure 9.3, it is possible to calculate the total cumulative micrometeoroid flux that is predicted to be incident on the open area of the sMPO of SMILE SXI over the course of its 3-year science lifetime (Figure 9.6). As expected, the flux distribution with respect to diameter is the same as Figure 9.2, however the flux is reduced due to the combined scaling effect factors in Table 9.3. Although the scaling factors reduce the flux, approximately 300 particulates of > 1 µm are predicted to enter the sMPO over the course of the 3-year mission, with that number drastically increasing as smaller diameter micrometeoroids are included.

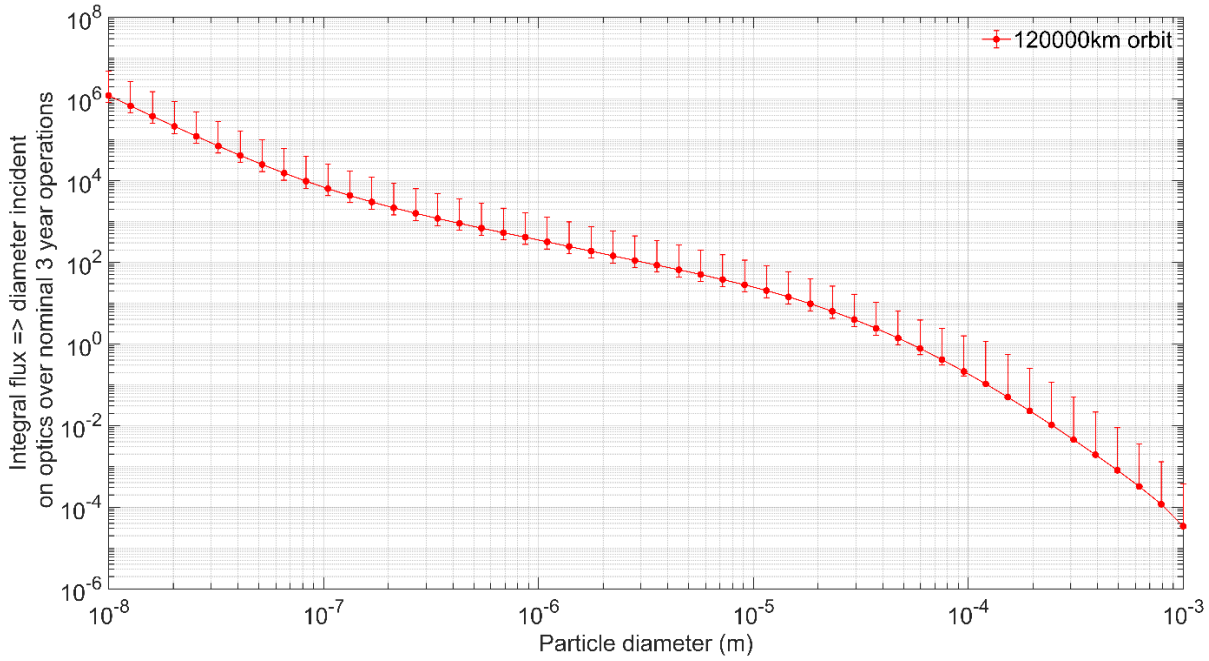


**Figure 9.6**: Using the Grün model, in combination with the specific orbital parameters of SMILE and associated flux scaling factors, the total micrometeoroid flux is shown predicted to enter the sMPO over SXI's science lifetime.

Figure 9.6 shows that a significant number of particulates > $10^{-6}$ m will enter the sMPO which can potentially impact the focal plane of SXI and degrade detector performance. However, one

key value is still unknown which links the total number of particulates entering the optics to the number impacting the focal plane. This value describes the ratio of particulates that enter the sMPO to the number that successfully exit and is key to evaluating the effect of particulate impacts on the SMILE SXI detectors.

## 9.3. Calculating sMPO transmission rates

This value, known from here on as the transmission rate (TR) can be calculated in three ways. Ideally this value can be measured experimentally and can provide strong evidence as to the real TR seen in sMPO. However, this experiment requires a dedicated chamber, detectors, sMPO module, and accelerating mechanism, along with time set aside for testing and experimental implementation. The other two methods are via an analytical or Monte Carlo (MC) approach. The first method that will be utilised is the analytical approach, as analytical solutions can often be implemented quickly and provide reasonable results given the time input, in contrast to the larger amount of time needed to create, implement, and test a bespoke MC solution.

### 9.3.1. Analytical solution

The analytical solution will be centred around the use of solid angle integrals to define an acceptance cone which represents the ratio of particles that can successfully traverse a single micropore. Once the transmission rate of a single pore is found, this value is assumed equal across all pores and hence the whole optical system.

#### 9.3.1.1. Coordinate geometry

A coordinate system is initially defined as seen below in Figure 9.7 (left). $\Theta$ represents an angle measured from the Z axis to the vector (red line) and $\Phi$ represents the azimuth angle which is measured in the XY plane. The length of vector r is also defined for completeness but is arbitrary with respect to the integrals presented here.

Once the coordinate system is defined, a solid angle ($\Omega$) can be defined by the surface integral of the surface S, subtended at the origin (0,0,0). When placed on a hemisphere, the solid angle creates an acceptance cone as seen in Figure 9.7 (right). Beneath the hemisphere is a square-based cuboid, representing a micropore, which can be used to illustrate the link between the acceptance cone generated and the transmission rate through a single micropore.

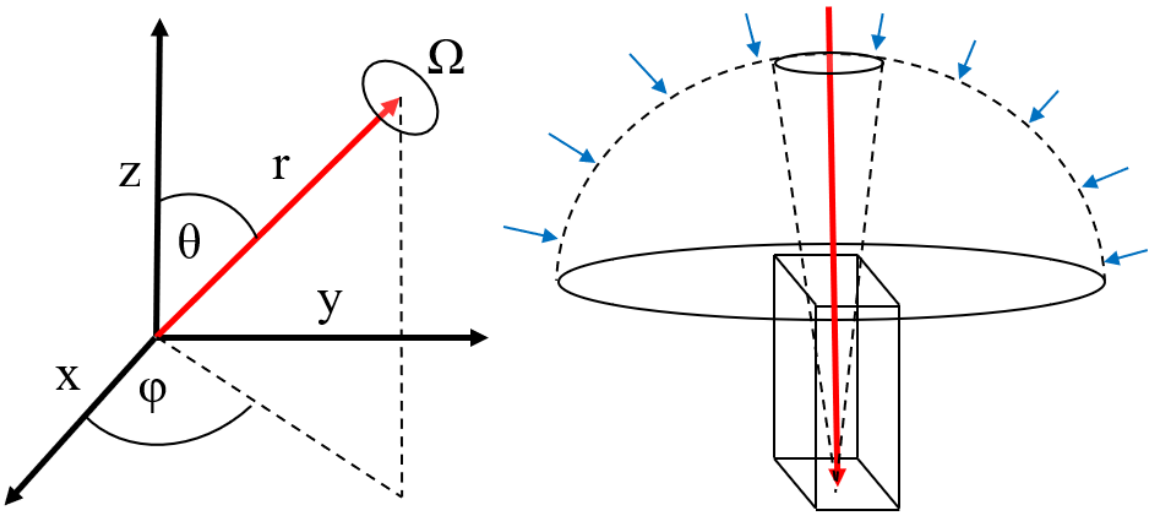


**Figure 9.7**: Coordinate geometry for the analytical solution. Left – Cartesian axis with spherical polar coordinates overlaid. Right – Solid angle acceptance cone combined with micropore geometry to highlight the methodology.

### 9.3.1.2. Solid angle integrals

The general solid angle surface integral is given by Eq. 9.1, with the following Eq. 9.2 showing the same integral but with defined limits. The limits of φ provide a full rotation, generating the acceptance cone shape, mimicking the flux of particles originating from all directions. The limits of θ are defined by the critical angle of scattering ($\alpha_{critical}$), that can be altered accordingly. Evaluating Eq. 9.2 at the defined limits provides the solid angle shown in Figure 9.7 (right).

$$\Omega = \iint_{s} \sin\theta \, d\theta \, d\varphi \qquad \text{Eq. 9.1}$$

$$\Omega = \int_{0}^{2\pi} . \int_{0}^{\frac{\alpha_{critical}\,\pi}{180}} \sin\theta \, d\theta \, d\varphi \qquad \text{Eq. 9.2}$$

To be able to use the result from Eq. 9.2 to attain the TR analytically, another integral must be computed which, mathematically, provides the solid angle of a single hemisphere. Physically, however, the hemisphere integral represents the flux of particles incident on the entrance of a

single micropore from a 180-degree viewing angle (depicted by the blue arrows in Figure 9.7 – right). Eq. 9.3 below shows the two integrals.

$$\text{Hemisphere factor} = \frac{\int_0^{2\pi} . \int_0^{\frac{\alpha_{critical}\,\pi}{180}} \sin\theta \, d\theta \, d\varphi}{\int_0^{2\pi} . \int_0^{\pi/2} \sin\theta \, d\theta \, d\varphi} \qquad \text{Eq. 9.3}$$

#### 9.3.1.3. Incorporating particle diameter

The second part of the analytical solution is associated with the reduction of micropore area as a function of particle diameter. This can be calculated by the following equation:

$$\text{Pore area scaling factor (PASF)} = \left(1 - \frac{D}{W}\right)^2 \qquad \text{Eq. 9.4}$$

where D is the diameter of the particulate in metres and W is the width of the micropore in metres.

#### 9.3.1.4. Modifications for cosine distribution

Once the integrals in Eq. 9.3 are evaluated and then modified dependent upon particle diameter, one modification is still needed to ensure a physically accurate answer. As mentioned in section 4.2, the angular distribution of particulates incident upon a randomly tumbling surface follows a cosine (and not isotropic) distribution. This means that the denominator in Eq. 9.3 is incorrect, as the integral assumes and represents an isotropic distribution, leading to an underestimate of flux that enters the acceptance cone. Figure 9.8 below shows a graphical illustration of the effect of a cosine distribution, compared to that of an isotropic distribution. Physically, a cosine distribution is more appropriate as the proportion of a surface that is "seen" by particles with random velocities in space is maximised when the surface is orthogonal to the velocity of the particle (for a more detailed explanation see Zhao et al., 2013).

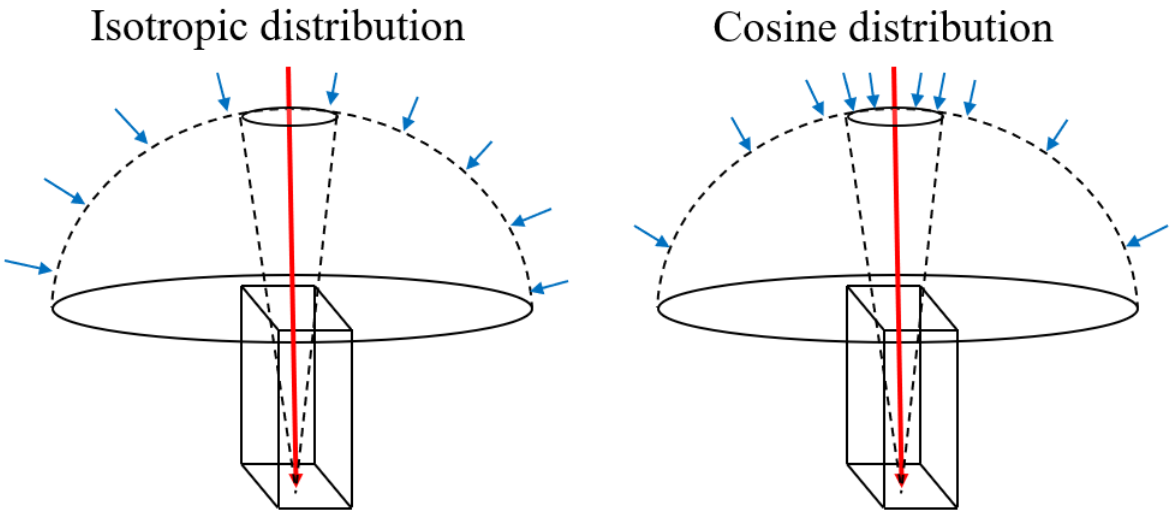


**Figure 9.8**: Comparison of the physical representation of the integral solution for an isotropic and cosine angular distribution.

The cosine distribution effectively increases the particle flux which enters the micropore with low angles (as measured from the normal to the plane of the pore entrance), as a larger number of particles occupy a smaller solid angle. This is shown explicitly by the proximity of blue arrows (representing incident particles), in Figure 9.8 (right) versus Figure 9.8 (left). Therefore, for a physically accurate analytical solution, the cosine distribution must be implemented in the final solution.

Due to the nature of the integral in Eq. 9.3, incorporating a cosine distribution with respect to θ is simple, leading to the final expression for the analytical solution for the transmission rate as a function of incident particle diameter (d) and the critical scattering angle (α):

$$\text{Transmission factor } (d,\alpha) = \frac{\int_0^{\frac{\alpha_{critical}\,\pi}{180}} \cos\theta \sin\theta \, d\theta}{\int_0^{\pi/2} \cos\theta \sin\theta \, d\theta} * \text{PASF}(d) \qquad \text{Eq. 9.5}$$

#### 9.3.1.5. Limitations

Although the analytical solution is neatly evaluated using solid angle integrals and additional scaling factors, it underestimates the transmission rate of particulates due to the nature of solid angle integrals. The first, and most obvious incorrect approximation is regarding the shape that

is projected onto the hemisphere, which is subtended by the surface integral at the origin (an explicit illustration is provided below in Figure 9.9).

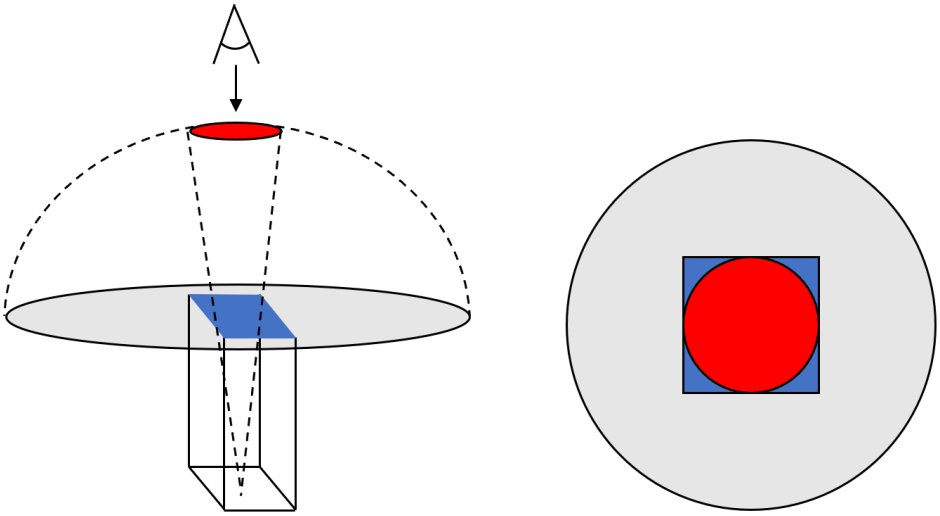

**Figure 9.9**: Solid angle geometry from two different viewpoints with areas of interest highlighted. Left – Solid angle acceptance cone area in red, with the micropore entrance area in blue. Right – Birds eye view, showing the underestimate of the solid angle integral methodology.

Figure 9.9 (left) shows the previous arrangement of solid angle acceptance cone and hemisphere accompanied by an example micropore. Three areas are highlighted, the entrance to the micropore in blue, the solid angle defined by the surface integral, red, and finally the base of the hemisphere, for clarity, in grey. Viewing this arrangement from directly above the red solid angle is shown by the 2D representation given in Figure 9.9 (right). Although the solid angle integral provides an acceptance cone, the true acceptance area is defined by the micropore entrance shape, in this case a square projected onto the surface of a hemisphere. This means that the area given by the solid angle integral (red circle) is an underestimate of the true area/acceptance cone area (blue square). As a result, the expected transmission factor given by Eq. 9.5 should be higher, although the exact factor higher is difficult to determine exactly.

Although this analytical solution is computationally quick and simple to evaluate, the limitations outlined above, and the subsequent underestimate of transmission rates, motivated the development of a Monte-Carlo based method to provide a more accurate and physical transmission rate.

### 9.3.2. Monte Carlo ray tracing simulation

The simulation proposed has several stages to accurately represent the total particulate flux that traverses a micropore. A qualitative description is given below of each stage:

1. Generate initial particle coordinates in spherical coordinates considering the cosine distribution above.
2. Generate secondary particle coordinates on an area equal to the dimensions of the open area of a micropore.
3. Using both sets of coordinates, trace the trajectories of each particulate through a distance equal to the length of one micropore length.
4. Take the final coordinates and calculate the number of particles that exit an area which aligns with the exit to the simulated micropore, while also incorporating particulate diameter.
5. For the particles that do not fall into the designated area, using trigonometry to calculate the angle that each particle strikes the inner wall of the micropore.
6. The final transmission rate is equal to the ratio of incident particles over the sum of the particles which exit the micropore directly plus the particles which strike the inner walls with an angle less than the critical angle of deflection.

#### 9.3.2.1. Coordinate system

Before running the simulation, the coordinate geometry must be generated correctly to ensure a physical simulation. Figure 9.10 shows a reconstructed cubic structure representing a micropore of 4×4×4 units. The centre of the pore aligns with (0,0) in the XY plane, indicated by the black dashed line. The entrance to the pore is represented by a 4×4 square mesh grid, in the Z = 0 plane. The exit of the pore is in identical XY coordinates, but with a Z coordinate below 0, in the case of Figure 9.10 the identical 4×4 mesh grid is in the plane Z = -4. The azimuth coordinate is defined as the plane between dashed red and blue line rotated around the black dashed line. The elevation angle is defined as the angle measured between the red dashed line and the black dashed line. Finally, the radial component is defined as the distance of the vector originating from (0,0,0).

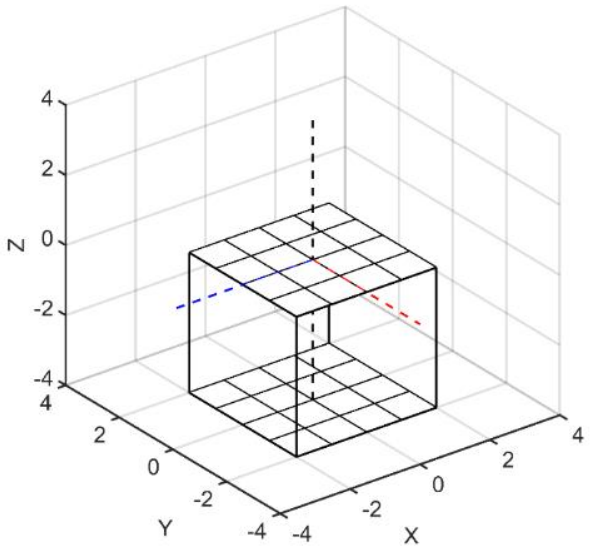


**Figure 9.10**: Representation of a single micropore. Additional vectors connecting the entrance mesh and exit mesh have been shown for clarity although they do not affect the result of the simulation. Arbitrary units are also used as the only key dimension in the simulation is the length of the micropore relative to the pore opening dimension (known as ratio, R).

#### 9.3.2.2. Generating initial coordinates

For initial particle coordinate generation, spherical polar coordinates are used as this geometry is more suitable for the angular cosine distribution. Once generated, the spherical polar coordinates can be translated into cartesian coordinates for the ray tracing part of the simulation. Figure 9.11 shows the initial distributions of particle coordinates in both spherical polar and cartesian coordinates.

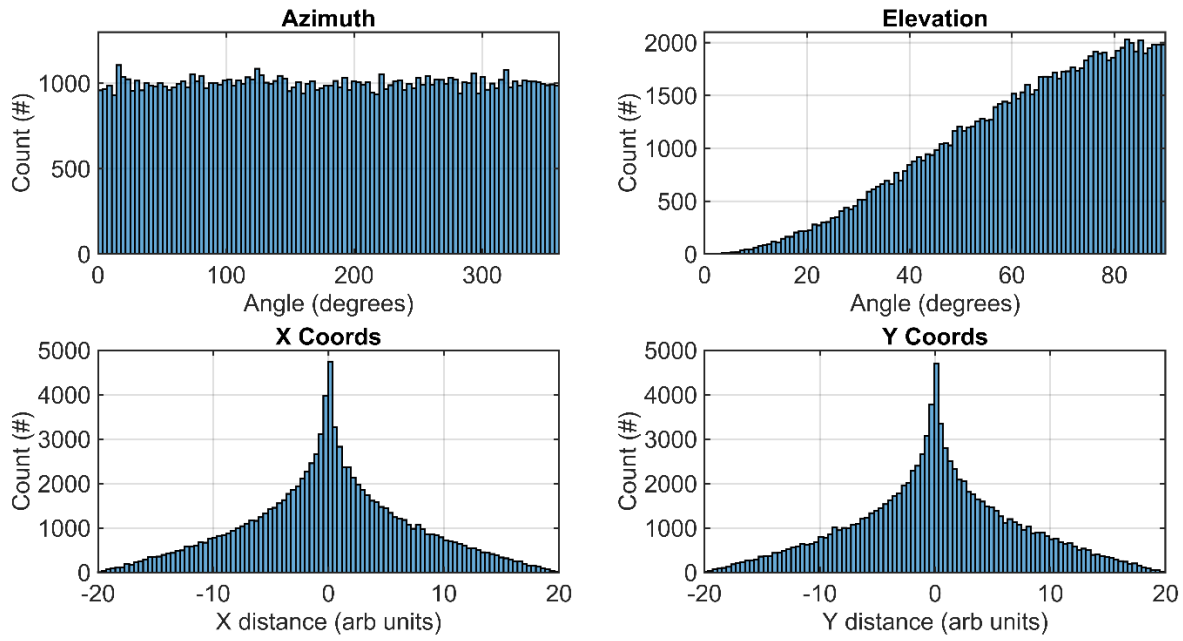


**Figure 9.11**: Distributions of initial particle coordinates in both cartesian and spherical polar coordinates. In the elevation, the angle of 90 degrees is normal to the sMPO surface plane.

Particle coordinates in the azimuth and elevation direction are generated by a pseudo-random number generator. The azimuth direction is scaled between 0 – 360 degrees as particulates can strike the optics from any direction, shown by a flat distribution in Figure 9.11 (top-left). The elevation angle is scaled between 0 – 90 degrees to ensure particles can only strike one side of the optics and to avoid double counting when using an azimuth angle between 0 – 360 degrees. The flat elevation angle is then scaled by a cosine distribution, which appears as a sine distribution as generally the cosine distribution angle is measured by the normal to the surface. The radial direction is taken as constant as this does not affect the results of the simulation.

Spherical polar coordinates are then converted to cartesian and are shown in the lower half of Figure 9.11. Both X and Y coordinates show a weighting towards 0, respectively. A coordinate of (0,0) represents the centre of a square micropore (also seen in Figure 9.10), meaning that initial particle coordinates are preferentially directly above the centre of the pore (as expected).

#### 9.3.2.3. Pore entrance distributions and ray tracing

Once initial spherical polar coordinates are generated and transformed to cartesian coordinates, the next stage is to generate entrance coordinates where particles will enter the open micropore area. Figure 9.12 (left) shows the random distribution of points in X and Y in a 4×4 grid. Once

micropore entrance coordinates are generated, the vector from the initial coordinate to the micropore entrance coordinates is used to create particle tracks as seen by the blue lines in Figure 9.12 (right).

After the tracks are created, the vectors can be extrapolated following the same trajectory until the designated Z plane is reached for the exit of the pore (Z = - 4 in this case), as seen by the red lines in Figure 9.12 (right). The depth of extrapolation represents the length of micropore, specific to that simulation. Once extrapolation is complete, the combination of each blue and red track represents a particle trajectory originating from space, entering the pore at random locations, and travelling until an equivalent micropore length is reached.

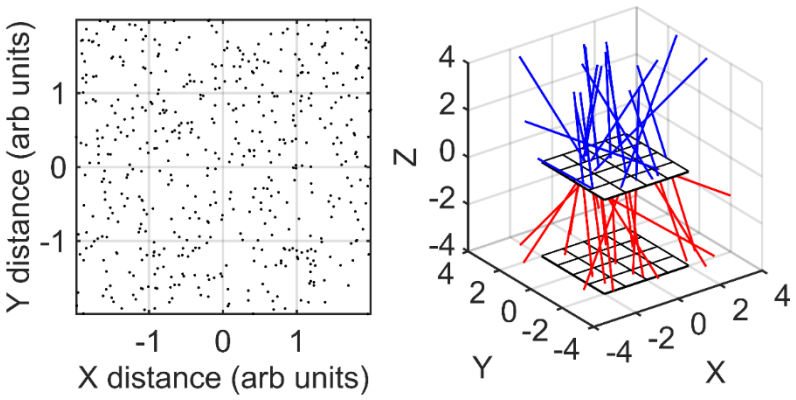


**Figure 9.12**: Left – Uniform distribution of particle entry points over a single micropore. Right - 3D representation of full particle tracks through an example micropore of dimensions 4×4×4 arbitrary units. Note that the number of points and tracks on the right plot is significantly less than the left for clarity. The pore length chosen is also unrealistic, as most micropore are significantly longer in the Z dimension than the XY plane dimensions. The cubic pore dimensions were only chosen for illustrative purposes.

#### 9.3.2.4. Pore entrance and exit distributions for differing pore ratios

Once ray tracing is complete, the entry and exit coordinates of each particulate can be interrogated for the necessary information regarding direct, non-direct or no transmission. Before this stage however, it is necessary to check the coordinate distributions to ensure they are as expected. Figure 9.13 shows the distributions of both entrance and exit coordinates for four different sizes of micropore. Each micropore is described by the R value – the ratio of the length to the width. A high R value suggests a long and thin micropore, whereas an R value of

1 represents a cubic micropore. By looking at the entry and exit coordinates relative to the pore ratio, it is possible to check whether the simulation is producing physical results.

Figure 9.13 (top-right) shows the distributions of entry and exit points for the four different micropore dimensions, with the X and Y dimensions matching those seen in Figure 9.10 and Figure 9.12. The micropore entry coordinates (black dots) show a sharp square distribution also seen in the XY histograms. This is as expected as any black dot outside the ranges between -2 and 2 in both X and Y would suggest that the incident particulate has not entered the micropore. The distribution is also flat in X and Y due to the uniform random distribution used for the generation of particle entry point.

The remaining points represent exit coordinates for differing pore ratios. As the pore ratio is decreased from 30 to 1 the distribution of exit coordinates changes, with a higher number of points distributed around the 2×2 grid, seen most clearly via the pink dots. This suggests that for longer pores (with a higher R), particles are spreading over a narrower XY range when reaching the designated Z plane, which is physically expected and intuitive.

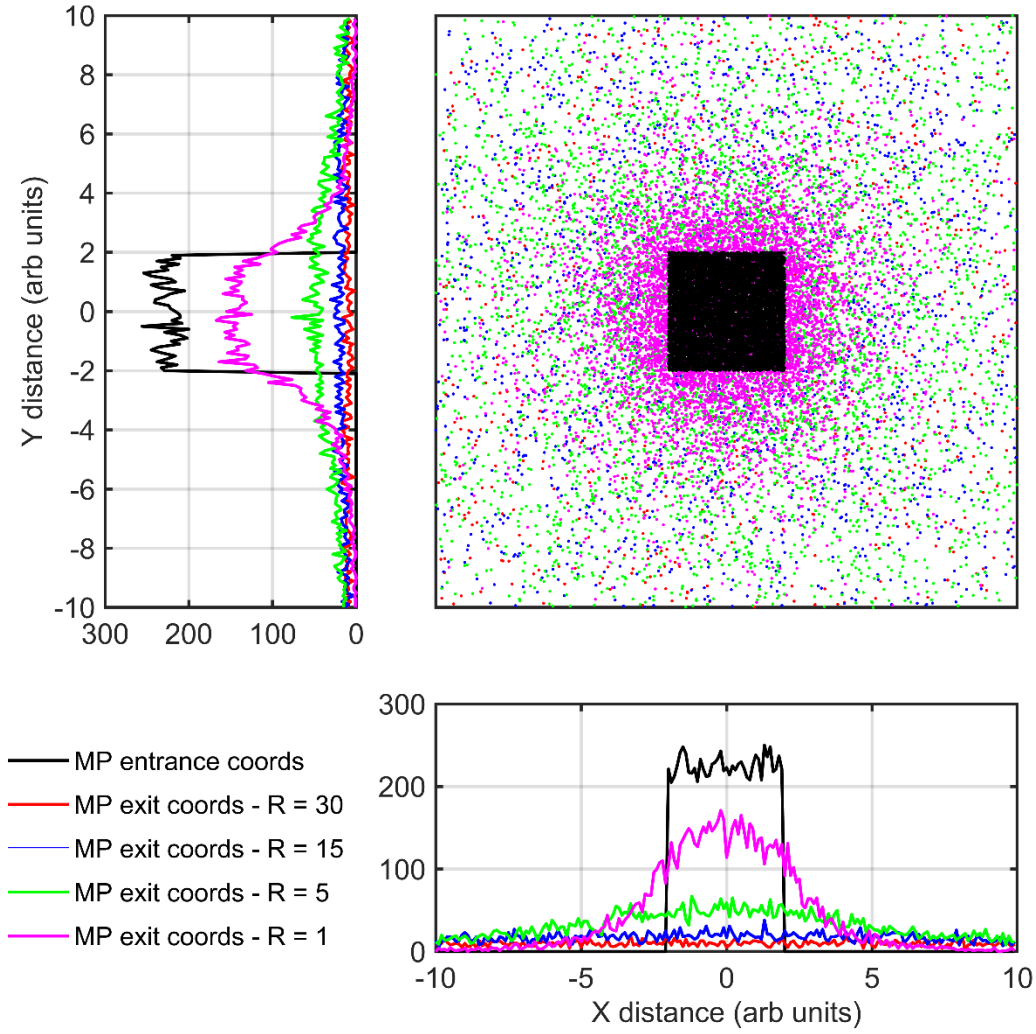


**Figure 9.13**: Spatial distributions of both entry and exit coordinates for different simulated micropore ratios. Note that only the black points represent entrance coordinates, as the generation of entrance coordinates is independent of micropore ratio. 10,000 particles were used to simulate these distributions.

#### 9.3.2.5. Incorporating particle diameter

The analysis until this stage has assumed that the simulated particulates are point sources and can be modelled as such. However, physically, each particulate has a set diameter that will alter the mechanics of interactions with the micropore. The main effect of particle diameter is to reduce the effective open area of each micropore, by an amount proportional to the diameter of the incident particulate.

Figure 9.14 (left) shows a schematic of a birds-eye view of the entrance to a 4×4 unit micropore centred on the origin (0,0). The micropore has a width and depth defined by the solid black line. Also shown are four particulates in black, pink, blue and red with different coordinates, indicating the XY coordinate in which they potentially enter the micropore. The pink and black particulate have an entrance coordinate such that the particle collides with the edge of the micropore. It is assumed that if this occurs, the particle cannot enter the micropore and thus cannot be transmitted (0% chance of transmission through the micropore). On the other hand, the red and blue particulate have coordinates which means that the particulate does not collide with the spacers between the pores and can successfully enter the micropore.

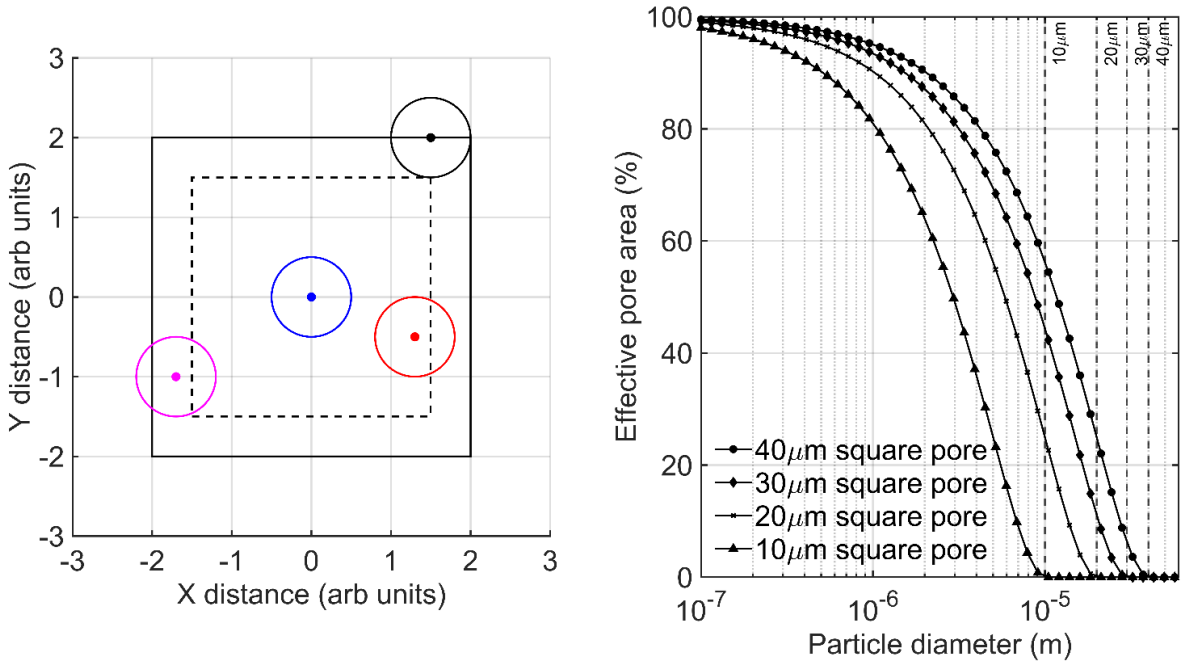


**Figure 9.14**: Effect of particle diameter on pore area. Left – Schematic illustrating the change in effective pore area due to particle diameter for four different particle entrance coordinates. Right – Variation in effective pore area for different size pores.

To quantify this effect, the pore area can be reduced, leading to an "effective" pore area (indicated by black dashed line in Figure 9.14 – left), based upon the radius of the particulate. To validate this stage of the simulation, the effective pore area (EPA) can be plotted vs particle diameter for different sizes of pores, as seen in Figure 9.14 (right). As expected, the effective area of each pore decreases as particle diameter increases. For smaller pore sizes, the effective area decreases at a faster rate, as each particle diameter takes up a larger proportion of the initial

micropore size. The effective pore area for each pore size also reduces to zero as soon as the particle diameter is equal to the size of the pore. Physically, this makes sense as the micropore opening is not large enough for the particle to enter the micropore.

#### 9.3.2.6. Calculating particle transmission rates

Once ray tracing is complete, the number of particles that traverse a single micropore can be calculated. The total transmission rate is given by the following equation:

$$\text{Transmission rate} = \frac{N_{P_d} + N_{P_n}}{N_{P_t}} \qquad \text{Eq. 9.6}$$

where $N_{Pd}$ is the total number of particles that are transmitted directly through the micropore, $N_{Pn}$ is the total number of particles that are transmitted indirectly through the micropore, and $N_{Pt}$ is the total number of particles incident on the micropore. The following section will outline explicitly how the simulation calculates the number of particles that are both directly and non-directly transmitted through a single micropore.

#### 9.3.2.7. Calculating the number of directly transmitted particulates

A particle that is transmitted directly through a single micropore is defined as a particle that traverses a single micropore without scattering from an inner pore surface. For a particle track to be classified as a directly transmitted particle, it must meet two simple criteria:

- The XY coordinate of the particle track entering the micropore must fall within the effective pore area.
- The XY coordinate of the particle track exiting the micropore must fall within the effective pore area.

Figure 9.15 illustrates the selection process for five particle tracks, showing both the XY coordinates for the entrance and exit from the micropore, along with the particle tracks themselves. In the example of Figure 9.15 (left), a birds-eye view of the entrance (grey square) and EPA (effective pore area) due to particle size are shown (black square). Each point with a dashed outline represents the entrance coordinate, with the solid outline of the same colour representing the exit coordinate of the same particle. To complement, the 3D tracks of the same five particle tracks are shown in the right half of Figure 9.15 also. In the example below, the black, blue, and red particle would successfully traverse the micropore and be included in the

total number of directly transmitted particles. The green and pink particle, however, do not meet the two requirements above, so will need further analysis to determine whether the particle is treated as a non-directly transmitted particle.

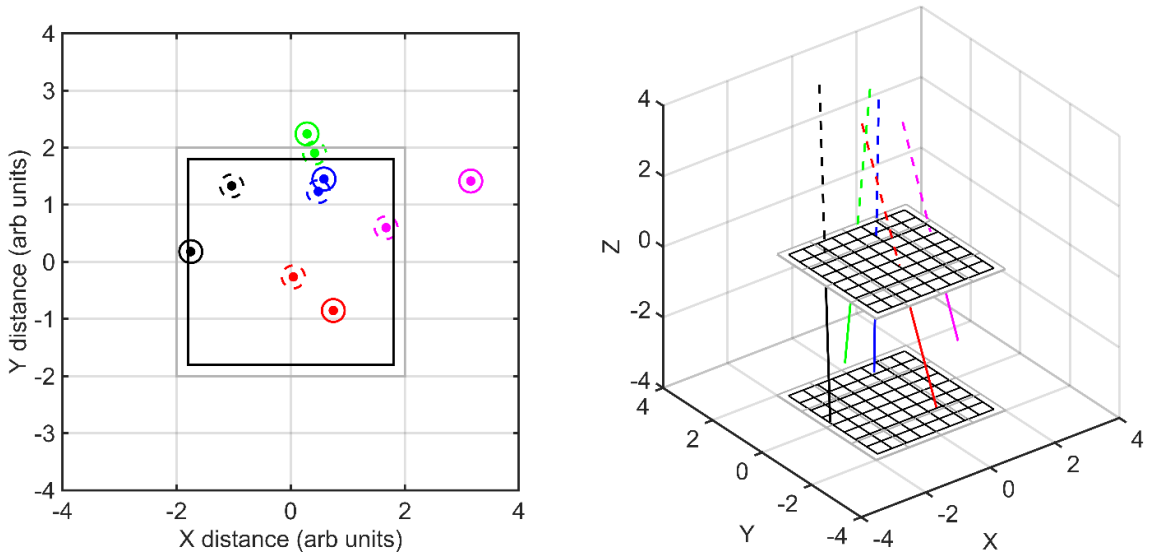


**Figure 9.15**: Illustration of the down-selection process of particle tracks. Left – Birds eye view of the micropore entrance and exit. Right – Complete particle tracks showing expected trajectories in relation to the entrance and exit of a micropore. The colour of each track is coordinated with the same points in the left section of the figure.

#### 9.3.2.8. Calculating the number of non-directly transmitted particulates

A non-directly transmitted particle is defined as a particle (or particle track) that successfully traverses a single micropore by scattering off the inner walls (see section 9.3.4 for what occurs post-scattering). For a particle to be considered a non-directly transmitted particle it must therefore meet two criteria:

- The XY coordinate of the particle track entering the micropore must fall within the effective pore area.
- The incident angle of the particle track must be less than or equal to the critical scattering angle.

The first criterion is calculated in the same way as directly transmitted particles. The second criterion, however, requires use of the known particle coordinates, along with basic geometry and subsequent calculations. Figure 9.16 shows the particle track geometry, (red), associated

micropore (blue) and the three coordinates used in the simulation. $P_1$ represents the initial particle coordinates, $P_2$ and $P_3$ represent the XY coordinates in the Z plane of the micropore entrance and exit, respectively.

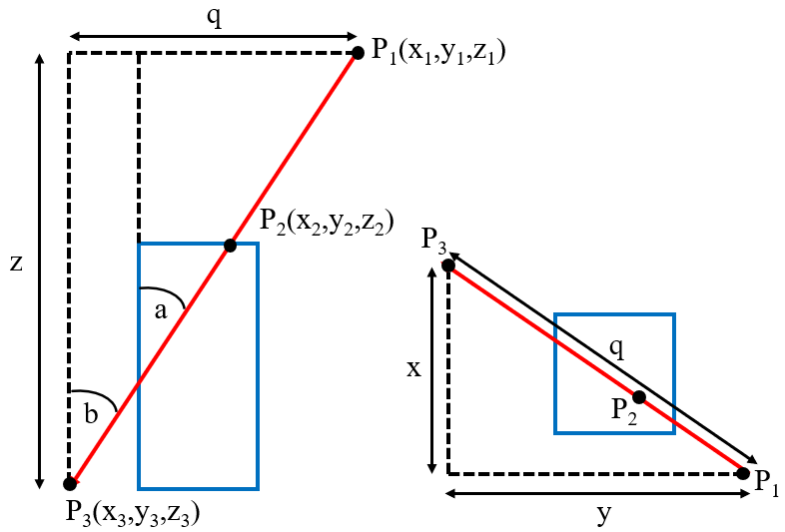


**Figure 9.16**: Schematic of the geometry of a single particle track and associated scattering angles. Left – A side profile is shown of the particle track entering the micropore. Right – A birds-eye view of the same schematic, highlighting key dimensions in calculating the scattering angle b. Note that the micropore is the blue rectangle viewed from the side (left) or above (right).

The incident angle is shown as angle a in Figure 9.16 (left), and calculation of this angle via trigonometry would require additional knowledge of the coordinate where the particle strikes the wall of the simulated micropore. However, due to geometry, angle b is equal to a, and is given by the equation:

$$\tan(b) = \frac{q}{z} \qquad \text{Eq. 9.7}$$

To calculate distance q, Pythagoras' theorem is used, by utilising knowledge of the coordinates already known (shown by Figure 9.16 – right):

$$q = \sqrt{x^2 + y^2} \qquad \text{Eq. 9.8}$$

Substituting Eq. 9.7 into Eq. 9.8 leads to the following expression which describes the incident angle in which a particle strikes the inner wall of the micropore:

$$b = \tan^{-1}\left[\frac{\sqrt{(x^2 + y^2)}}{z}\right] \qquad \text{Eq. 9.9}$$

Using Eq. 9.9 it is possible to calculate the crucial incident particle angle, which when evaluated against the critical angle of scattering, provides the information as to whether a particle scatters off the inner surface of the micropore and exits successfully. Figure 9.17 below shows the distribution of calculated incident angles for differing pore ratios.

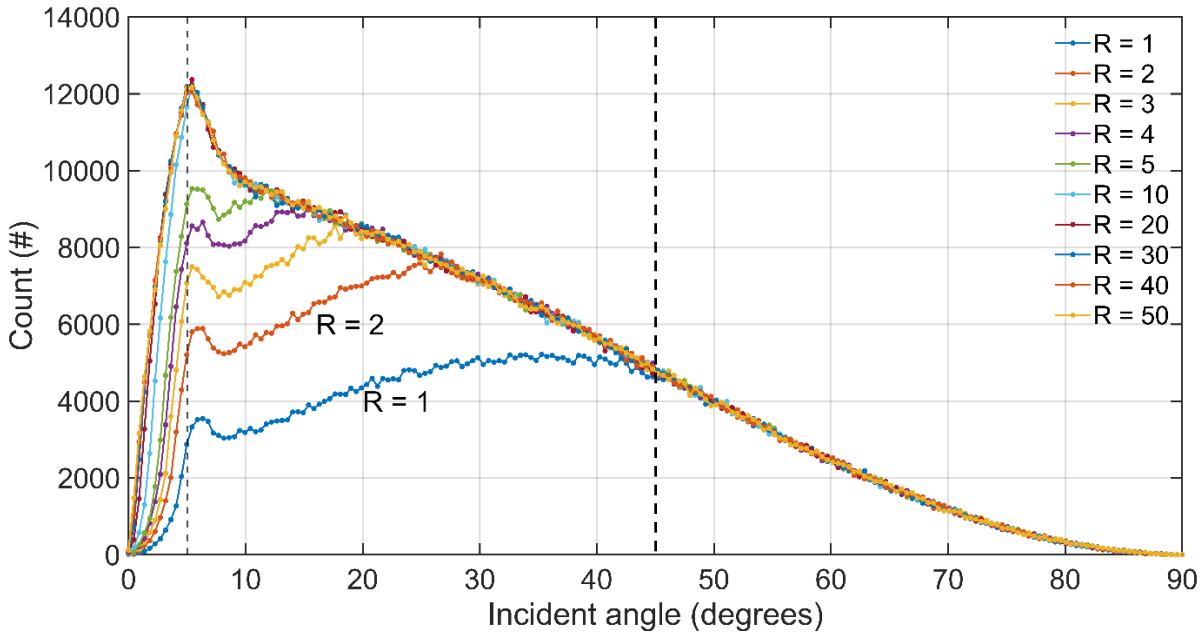


**Figure 9.17**: Angular distribution for differing pore ratios (R), where the incident angle is measured from the normal to the plane of the entrance of the micropore. These data were simulated using particulates with a diameter of $1\times10^{-6}$ m only.

For angles above 45 degrees, regardless of pore ratio, the relationship between count and scattering angle is identical, with a gradual decrease in count with respect to increasing incident angle. Considering the initial generation of points followed an angular cosine distribution, the gradual decrease in count after 45 degrees is consistent with the tail of a cosine distribution.

Below 45 degrees however, the angular distribution is not consistent across different pore ratios. A distinct cut-off point exists for each pore ratio, where below this angular cut-off, the

distribution changes, showing considerably different behaviour compared to above 45 degrees. As pore ratio increases, this cut-off point decreases until the pore ratio approaches the values of ~ 5-10. At this point, and for pore ratios above, the angular distribution is almost identical.

For pore ratios above 10, a sharp peak in seen at approximately 5 degrees followed by a sharp decrease in count for the next 5 degrees. After 10 degrees however, the gradient is still negative but decreases at a slower rate. The exact reason for this peak location is unknown at this stage, however smaller peaks are also seen in lower pore ratios.

For pore ratios below 10, the overall count decreases, especially at lower angles (below 45 degrees). The physical explanation for this may be due to the combination of low pore ratio and low incident angle increasing the number of directly transmitted particles, although it is hard to explicitly confirm this with Figure 9.16 above. However, in real sMPO applications pore ratios tend to be greater than 20, so these features are not explored further.

Note that for this section of the analysis, the particulate diameter is not used. Once the particulate enters the optic (where the diameter is assessed accordingly), it is assumed that the scattering mechanics and potential exit of the micropore is independent of particulate diameter. Once exiting/not exiting the optic, the particulate diameter is used as input to the damage equations in section 9.4.

#### 9.3.2.9. Ratio of direct and non-direct transmission versus pore ratio

Once the number of directly and non-directly transmitted particles are calculated, the total transmission rate can be calculated for different pore ratios. Figure 9.18 shows the number of transmitted particles plotted as a function of both pore ratio and percentage of total incident particles. Also shown is the overall transmission rate for comparison.

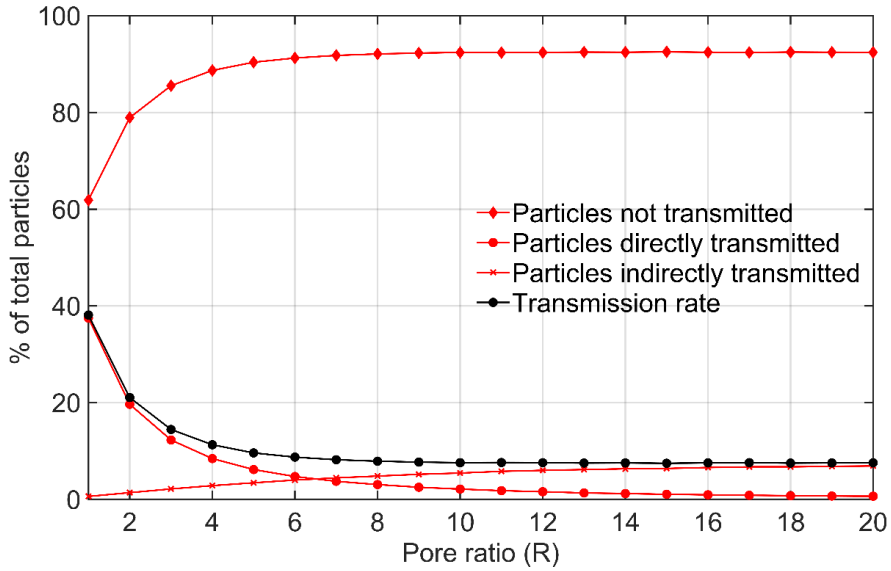


**Figure 9.18**: Proportion of total particles that are either not transmitted, transmitted indirectly, or transmitted directly through a single micropore as a function of pore ratio. The particle diameter used for these simulations was $1\times10^{-6}$ m, with a square pore diameter of $40\times10^{-6}$ m.

At low pore ratios, the transmission rate is at a maximum, which is dominated by particles which are directly transmitted through the pore. As pore ratio increases, both the percentage of particles directly transmitted decreases along with overall transmission rate. This suggests that for low pore ratios, the transmission rate is dominated by directly transmitted particles. Above a pore ratio of ~10, a steady state is reached, with transmission rate now dominated by scattered particles and the number of particles directly transmitted is negligible. Physically, this is intuitive as the micropores are now significantly longer than the entrance dimensions, so the chance of a particle traversing the entire length of a micropore without scattering is small.

The result seen in Figure 9.18 is also consistent with the result in Figure 9.17, as after the pore ratio goes above ~10, a steady state is seen, with regards to both transmission rate and the angular distributions.

### 9.3.3. Comparison of transmission rate results

Once the Monte Carlo (MC) simulation is complete, the transmission results of both the MC and analytical can be compared for differing pore ratios as a function of particle diameter. Figure 9.19 shows the transmission rate of the MC solution in red, accompanied by the analytical solution in blue. The MC solution shows that for micropores of increasing R value,

the TR decreases as expected, due to the lower chance of particulates being directly transmitted in longer pores. TR results for the MC solution also drastically reduce as the particle diameter approaches that of the micropore entrance dimensions, showing that the EPA reduction as a function of particle diameter is working correctly.

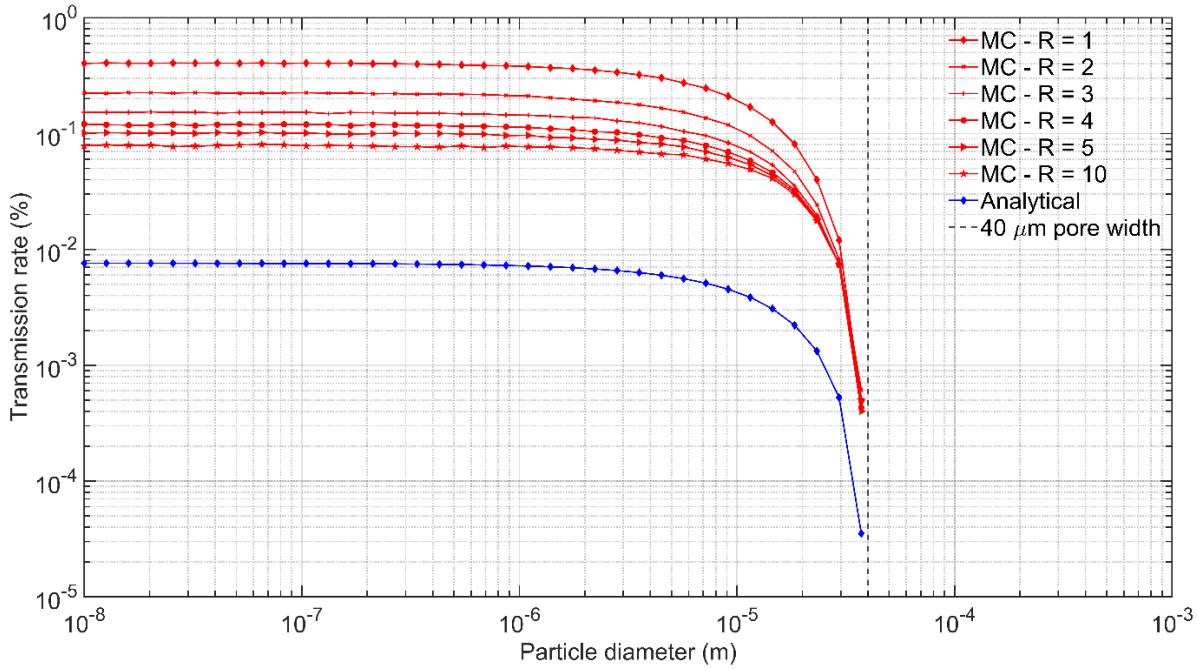


**Figure 9.19**: Transmission rate values produced by the MC and analytical solution in red and blue, respectively. The MC simulation was run for pore ratios of 20, 30 and 40 also, however the transmission rate was identical to that of R = 10, so the additional results were omitted for clarity.

As mentioned in section 9.3.1.5, the analytical solution is most likely to be an underestimate due to approximations in the solid angle integrals. However, the difference in TR magnitudes between the MC and analytical solution is significant (~factor 15), even when comparing the analytical solution to the MC solution with the highest TR (R = 10). It is difficult to comment on whether all the discrepancy between the MC and analytical solution can be attributed to the approximations in the solid angle integrals. One other additional effect not seen in the analytical solution is the effect of changing pore ratio on the TR. Currently the TR of the analytical solution is not a function of pore ratio, whereas the TR of the MC is a function of pore ratio.

Another difference between the MC and analytical solution, which could also contribute to the difference between the two solutions, arises due to the method in which the total particle

transmission rate is calculated. In the MC solution, the total transmission rate is given by Eq. 9.6 with the total particles transmitted (directly and non-directly) being calculated separately. Both the non-directly and directly transmitted particles interact with the micropore in different ways, so separate calculations mean that the methodology can also be checked for consistency. However, in the analytical solution, the integral in Eq. 9.5 calculates both the non-directly and directly transmitted particles in a single stage. This means that it is impossible to gain extra insight into the answer output by the integral. Furthermore, and more specifically, large pore ratios should intuitively lead to a narrower acceptance cone, which in turn will change the transmission rate as a function of pore ratio. It is unclear at this stage how to incorporate the calculation of directly and non-directly transmitted particles separately in Eq. 9.5.

To summarise, the work contained in this chapter has so far calculated the total number of particulates that will enter the optics of SMILE SXI over the course of its 3-year science mission. Two separate solutions have then been implemented and tested to estimate the transmission rate of a range of particle diameters through micropores of varying sizes. The solutions provide different transmission rates; however, the MC solution is considerably more physical given the scenario, providing a range of results that are intuitive. In the following section, the flux results will be combined with the MC transmission rates to calculate the total number of micrometeoroids that will successfully exit the optics of SMILE SXI and potentially impact the focal plane.

### 9.3.4. Particle flux transmitting through SMILE SXI optics and onto the focal plane

To calculate the total number of micrometeoroids that enter and transmit through the optics over the course of SXI's 3-year science mission, the flux results from Figure 9.6 are combined with the MC solution developed above, using a 40 µm square pore with a length of 1.2 mm (R = 30) as well as a critical scattering angle of 5 degrees measured experimentally and simulated with hydrocode models (Ambrosi, R. M., et al., 2006; Meidinger et al., 2003; Palmieri, D., 2004). Note that the scattering angle was specifically found in Wolter Type 1 optics only, and it is assumed (until experimental verification), that this effect is also present in sMPO. The results are shown in Figure 9.20 with the cumulative flux exiting optics plotted versus particle diameter.

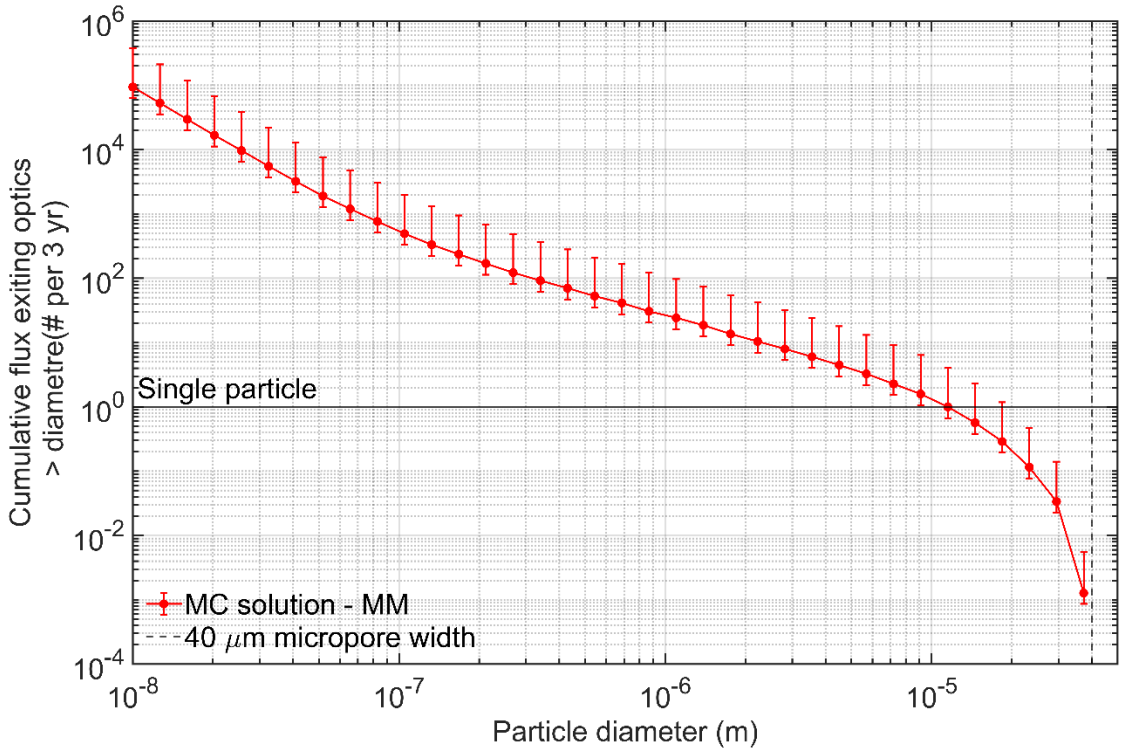


**Figure 9.20**: Variation of cumulative flux exiting the optics of SMILE SXI versus particle diameter.

The distribution is similar to that seen in Figure 9.6 (as expected), with every value scaled down due to the transmission rate of a R = 30 micropore. The values shown in Figure 9.20 predict that between approximately 20 and 100 micrometeoroids of at least $10^{-6}$ m diameter will exit the optics of SMILE SXI, with the flux increasing sharply when considering smaller particulates.

However, micrometeoroids that exit the optics still must travel to the focal plane before causing damage. For the subsequent analysis presented here it is assumed that all micrometeoroids that exit the optics will hit the focal plane. The reason for this assumption is that most particulates that exit the optics for the pore ratio considered here (R = 30), traverse after scattering from the inner surface of a single micropore. Due to the current understanding of scattering in soft X-ray optics, the velocity vector of a scattered particulate after scattering is directly parallel to the surface of the micropore (Ambrosi, R. M., et al., 2006; Meidinger et al., 2003). The orientation of the optics, designed specifically to point towards the critical focal plane, means that the scattered trajectories of particles are also preferentially focused on the detectors.

Once the total quantity of micrometeoroids hitting the focal plane are calculated, attention now turns to the damage caused by each individual impact. To be able to quantify this affect, additional equations are required, as mentioned in section 4.2.

## 9.4. Implications of flux incident on the focal plane of SXI

To fully quantify the effect of micrometeoroid impacts on the focal plane of SXI, the damage caused by individual impacts must first be assessed. The main mechanism through which detector performance is degraded is via the creation of craters within the silicon of the CCD. By quantifying the crater morphology, including the crater diameter, for a single micrometeoroid impact, the total number of pixels cratered can be estimated via the flux measurements calculated and shown in Figure 9.20. Before this however, additional damage equations must be utilised to estimate the size of craters caused via single impacts for a given set of parameters.

The equation below was introduced in section 4.2.4.1 and can be used to calculate the diameter of a crater for a given set of input parameters (summarised in Table 4.2)

$$D_c = K_1 K_c d_p^{\lambda} \rho_p^{\beta} v_p^{\gamma} \cos(\alpha)^x \rho_t^{\kappa} \qquad \text{Eq 4.13}$$

By using Eq 4.13, it is possible to calculate the estimated diameter of craters from particulate impacts for the four most relevant damage equations (Cour-Palais, B. G., 1969; Fechtig, H. et al., n.d.; Gault, 1973; McHugh, A. H. and Richardson, A. J., 1974). Figure 9.21 below shows the depth of craters created for four separate models, utilising the assumed parameters in Table 4.2.

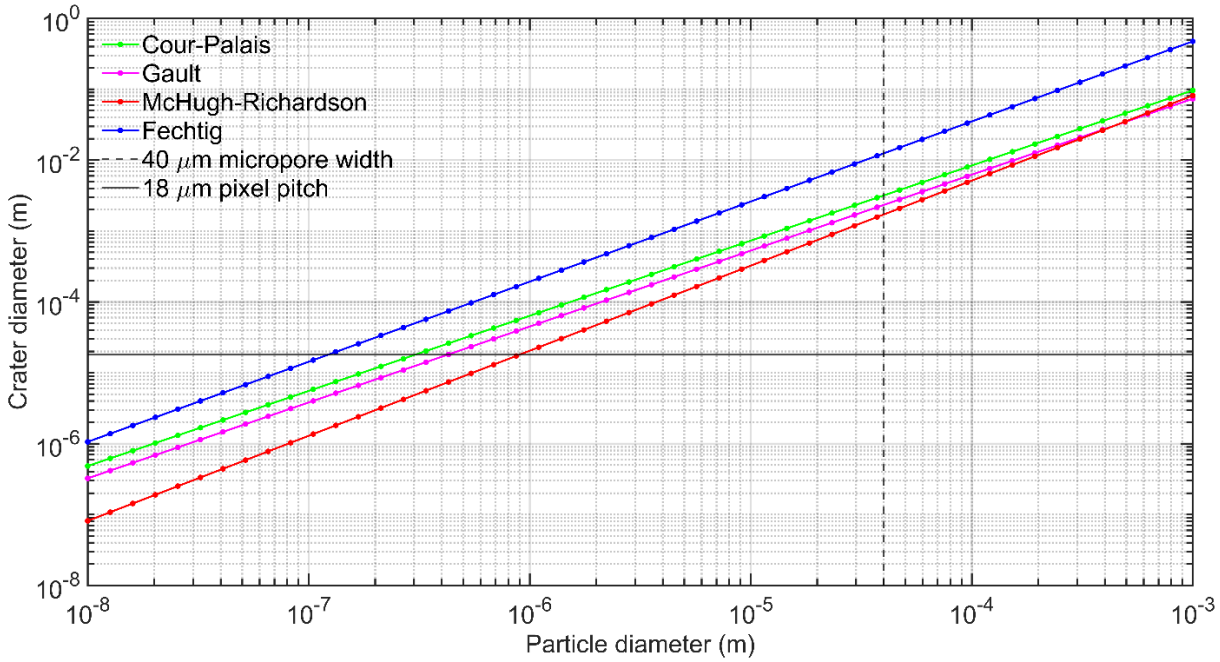


**Figure 9.21**: Variation of incident particle diameter with the size of crater caused for four separate models. The 18 µm pixel pitch of the CCD370s is also included for reference.

All models show similar trends of increasing crater depth with diameter as expected, due to a higher imparted kinetic energy per particulate. The difference in crater diameters between the four empirical models is due to slight differences in the values K1, λ, β, γ, x and κ. For all four models however, the value of $K_c$, which quantifies the brittleness/ductileness of the target material can range between 1-10. Due to the brittleness of silicon, a value of 10 was assumed for all four models shown in Figure 9.21. However, there is little literature on the source of these values, especially for silicon, so assuming a value of 10 will potentially overestimate the crater size. Due to the difference in model values already seen in Figure 9.21, without including potential differences in $K_c$, analysis from here will only include the Fechtig and McHugh-Richardson model in combination with a value of $K_c = 10$ and $K_c = 1$ applied respectively. This creates an upper and lower limit for the size of crater diameters caused as a function of incident particle diameter. The author notes that including an additional factor of 1 – 10 creates significant disparity between the upper and lower limit but this is unavoidable considering the lack of literature knowledge and experimental work.

Using the crater diameters shown in Figure 9.21, these values can then be scaled to a quantity that is more representative of the direct effect on a SMILE SXI detector. If the craters formed

are circular, the predicted crater diameters can be represented in terms of the number of effective pixels (based on area) cratered per impact. The results are shown in Figure 9.22, along with the two models (McHugh Richardson and Fechtig) which are used as lower and upper limits, respectively.

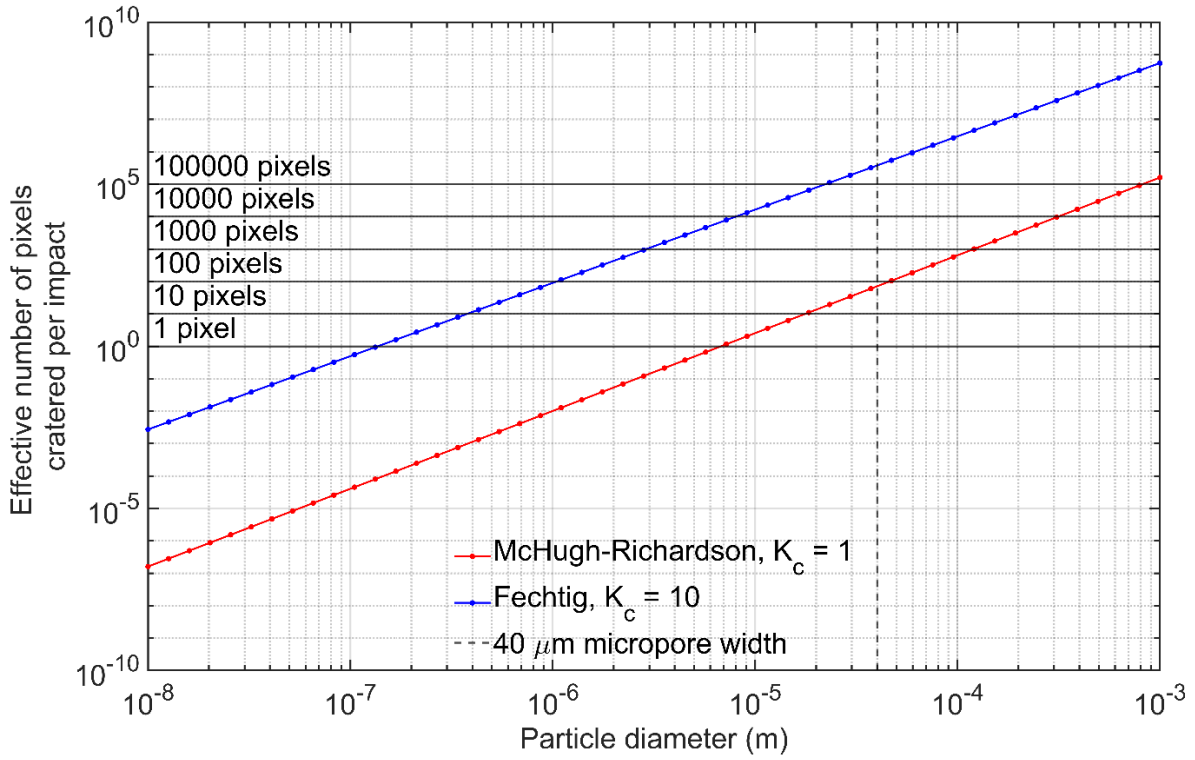


**Figure 9.22**: Effective number of pixels created per impact as a function of particle diameter, assuming that craters are circular. Also highlighted for clarity are 1-100000 pixels cratered to be able to compare each model.

Once the effective number of pixels cratered have been calculated per impact as a function of particle diameter, the flux values shown in Figure 9.20 can be combined to predict the total number of effective pixels cratered (as a function of crater diameter) in the focal plane of SXI over the course of its 3-year science mission (seen in Figure 9.23).

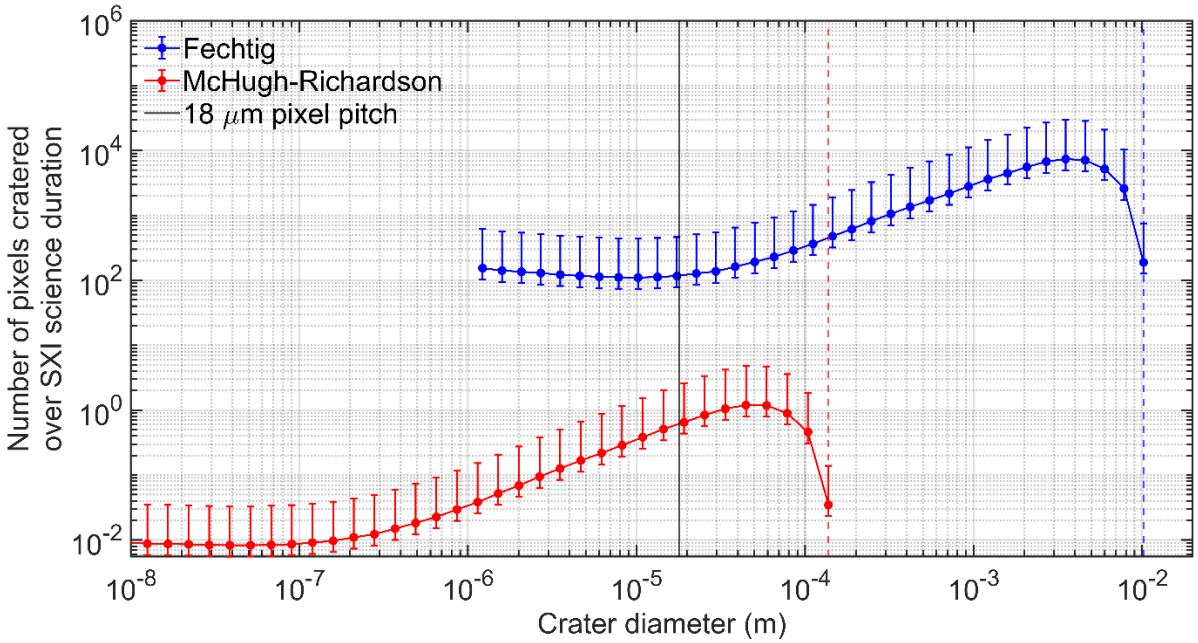


**Figure 9.23**: Total pixels cratered as a function of crater diameter, including both the Fechtig and McHugh-Richardson models.

## 9.5. Discussion and implications for SMILE SXI

The upper limit of crater diameter for both the Fechtig and McHugh-Richardson (MR) model (shown as the blue and red dashed line respectively) arise from the 40 µm micropore size placing a limit on the maximum diameter particle that can reach the focal plane of SXI. Although particles larger than 40 µm exist and are predicted to strike the optics of SMILE SXI over the course of the mission (Figure 9.6), these particles are unable to enter a micropore, and instead will strike the mechanical spacing between each micropore. It is currently assumed that after a particle strikes the spacing between a micropore, it cannot cause damage to the focal plane of SXI. It is also assumed that even if the particle damages a micropore wall/spacing, the total number of undamaged micropores (approximately $10^7$ total pores) is significantly higher and thus the number of damaged micropore is irrelevant.

The lower limit is more difficult to define as any particulates smaller than 40 µm can enter a micropore and subsequently impact the detector. The lower limit is easier to define in terms of device performance, as the overall aim of the work presented here is to quantify the extent of detector degradation that occurs because of hyper-velocity particulate impacts over the course of SMILE SXI's 3-year science lifetime. Previous work has shown that the device metric that

is degraded due to particulate impacts is detector noise, specifically an increase in dark current, in and around the initially impacted pixel. Previous work completed (Meidinger et al., 2003) showed that pixels which were impacted by hyper-velocity particulates showed significantly higher dark current post-impact. The adjacent pixels also showed increased dark current in an approximate radial direction (Figure 9.24 – left).

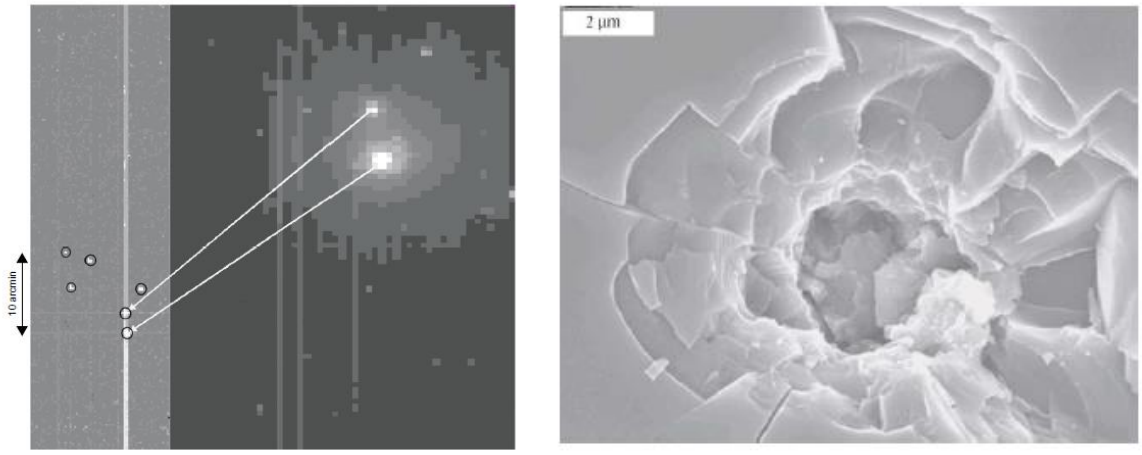


**Figure 9.24**: Dark current generation and pixel (Meidinger et al., 2003). Left – Left hand of the figure shows the increase in dark current affecting the entire column of a pn-CCD. The right-hand part shows a zoomed-in version of a single frame where a particle struck a single pixel. Right – SEM image of a crater within the silicon after a particle impact.

If the magnitude of dark current generation also scales with crater size, then it follows that there will be a lower crater diameter where the excess dark current generated is insignificant compared to that of the other noise sources. This means that although a crater exists within a pixel, it is effectively invisible to the detector in terms of device performance. Establishing where this soft limit is, however, is not possible without additional-experimental work.

The analysis method presented here also adds additional complication to the interpretation of the results. For example, crater diameters smaller than a single pixel, that only occupy a small % of a pixel (say 5%) will be analysed such that it would take 20 craters each covering 5% of a pixel to constitute a single pixel worth of damage. However, as alluded to above, each of those 20 craters may in fact lead to a single bright pixel, leading to a total of 20 bright pixels as opposed to one in the scenario above. This means that summing the curves in Figure 9.23 may also underestimate the number of pixels affected by particulate craters.

Another physical effect that also means the values presented in Figure 9.23 could potentially be an underestimate is also shown in Figure 9.24. Craters of a certain size will produce a level of dark current such that the excess noise generated leaks into the entire column that the pixel is situated within. This means that instead of the dark current affecting the main cratered pixel along with some number of adjacent pixels, an additional number of pixels (up to a maximum of 3700 rows) could potentially also see an increase in noise. Again, it is not clear at this stage without experimental verification, where this limit lies.

Using the number of pixels cratered as a function of diameter (Figure 9.23), and then summing values across particle diameters for both the Fechtig and MR models, it is possible to calculate the percentage of image area that will be cratered and potentially seen an increase in dark current. The results are summarised in Table 9.4 below:

**Table 9.4**: Summary of total number of pixels crater across SXIs 3 year observing period with errors.

| **Model** | **Summed pixels cratered** | **Summed pixels cratered error (upper and lower)** | **Total pixels cratered as a percentage of image area** | **Total pixels cratered as a percentage of image area error (upper and lower)** |
|---|---|---|---|---|
| Fechtig, $K_c$ = 10 | $5.67 \times 10^4$ | Upper - $4.92 \times 10^4$<br>Lower- $5.4 \times 10^3$ | 0.16 % | Upper - 0.14%<br>Lower - 0.095% |
| McHugh-Richardson, $K_c$ = 1 | 8.44 | Upper - 7.74<br>Lower - 0.85 | $2.47 \times 10^{-5}$ % | Upper - $2.26 \times 10^{-5}$<br>Lower - $2.49 \times 10^{-6}$ |

The upper and lower limit for the percentage of focal plane pixels (including both CCD370s) that are cratered during the 3-year science period of SXI is 0.16% and $2.47 \times 10^{-5}$ % respectively, with accompanying errors seen in Table 9.4. These cratered pixels are likely to see an increase in dark current, with the true value closer to the Fechtig model due to the reasons highlighted throughout the chapter

One final issue to consider is the difference between the streaming and sporadic component of micrometeoroids in space with regards to the Grün model. The Grün model utilises averages which includes the cumulative sporadic component plus stream flux component averaged over

one year. This means that highly sporadic stream components have most certainly been underestimated within the Grün model. Intermittent sporadic components are classified between moderate events (micrometeoroid streams (Jenniskens, P., 1994; SPENVIS, 2019)) and extreme events (micrometeoroid *storms* (Beech et al., 1997)), both of which can increase the fluxes by large factors. Individual micrometeoroid stream events can potentially increase fluxes by up to a factor of 5 for multiple days, with < 5 events occurring per year. Micrometeoroid storms, while significantly less frequent (storm duration ~ few hours, with one event every few years), increase the flux significantly higher, with quotes values > $10^4$ factor increase above the background flux level. The increase in flux presents a serious risk to detector performance if the RSM is open during a micrometeoroid storm.

## 9.6. Conclusions and future work

This work presented in this chapter has aimed to answer the initial questions posed:

- How many hyper-velocity particulates are expected to be incident on the SMILE spacecraft during the mission's lifetime?
- For the particles that strike the sMPO, what are the mechanisms that control the passage of these particulates?
- Once understood, how many particulates can pass through the optics and hence impact the detector for the specific case of SMILE SXI?
- For the impacting particles, how can the damage caused be quantified and translated to a change in detector performance?

Initially, micrometeoroid flux estimates were generated using the Grün model in combination with orbit-specific parameters as well as the optical geometry of SMILE SXI. Once attained, the transmission rate of micrometeoroids through individual micropores was calculated using both an analytical solution and a bespoke MC solution. The MC solution was deemed to be far more physical, producing intuitive results for different micropore ratios as a function of varying incident particle diameter. The MC solution predicted that between approximately 20 and 100 micrometeoroids (with a diameter of at least $1 \times 10^{-6}$ m) will exit the sMPO of SMILE SXI over the 3-year science duration.

Known damage equations were then applied to the scenario of a hyper-velocity particulate impact in a CCD for the first time, estimating the crater sizes seen in silicon for a range of particle diameters. These crater sizes were combined with the flux estimates incident upon the optics of SXI along with the calculated transmission rate to estimate the number of pixels that would be subject to craters during SMILE SXI's 3-year mission. The damage equations predicted that between 8 and approximately $1 \times 10^4$ pixels will be cratered, with the considerable range arising from the different damage equation sub-models and associated variables (most notably the value of $K_c$, the brittleness of silicon).

The work presented here would benefit significantly from a hyper-velocity particulate impact campaign, using both SMILE-like CCDs and sMPOs. An experimental campaign would be able to answer the following questions fully or partly:

- What is the critical scattering angle for sMPO? How does the flux of transmitted particles change with incident angle?
- What is the quantity of dark current generated for hyper-velocity particle impacts in SMILE-like CCDs? How does this generation of dark current change with incident particle velocity? How does the generation of dark current vary around the centrally impacted pixel?
- How does the quantity of dark current generated change over time?
- What is the crater limit that dictates the lowest detectable hot pixel due to a particulate impact?
- What is the limit whereby any particle larger than a certain diameter generates enough dark current to affect the whole CCD column?
- What are the failure modes associated with micrometeoroid impacts in CCDs?

### 9.6.1. Experimental setup

To complete the micrometeoroid dust impact experimental campaign, the author has assembled and tested a vacuum chamber and associated electronics (seen in Figure 9.25). Four SMILE-like CCD270s are available for testing and are currently stored at the OU, awaiting testing. A detailed test plan was also written by the author (Buggey, T. and Soman, M., 2018) that will guide the experimental activities.

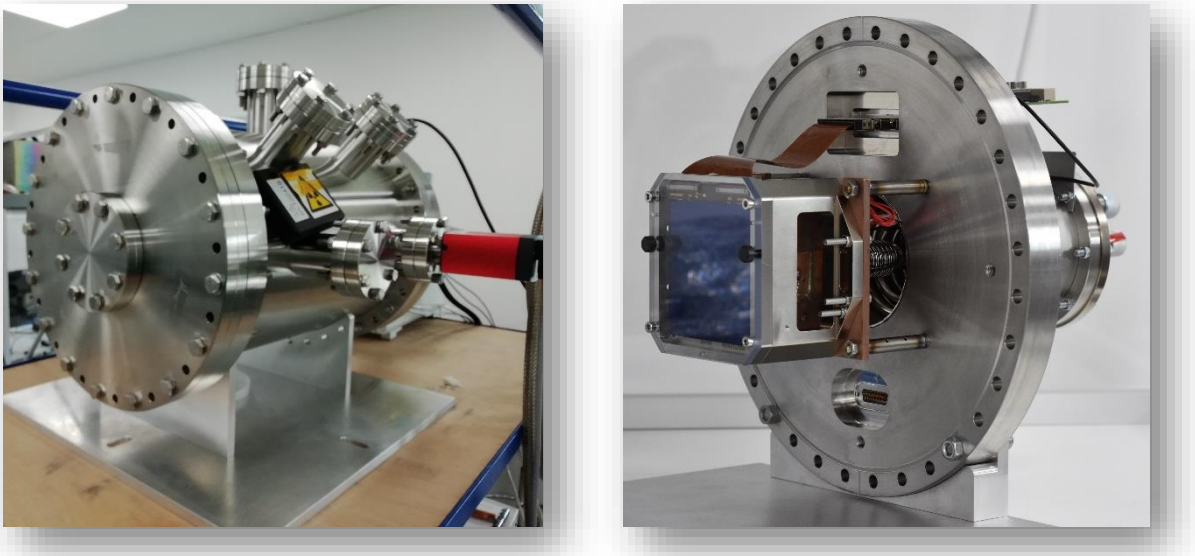

**Figure 9.25**: Micrometeoroid CCD impact experimental equipment. Left – Chamber assembled by the author. Right – CCD270 (one of four) mounted on the inside of a vacuum flange.

# 10. Conclusions and future work

This thesis has investigated the effects of the space environment on the CCDs of SMILE SXI, with the work broadly split into two streams; micrometeoroid and radiation damage. Initially, science goals of the SMILE mission were described (chapter 2), complemented by a broad overview of the Earth's magnetosphere and associated process contained within. The suite of four instruments within the spacecraft were then outlined, with focus placed on the key features of SXI that enabled the instrument to meet its science requirements of soft X-ray observations in the 0.2 – 2 keV band. Description of the SMILE CCDs followed, with a summary of the operating modes and the rationale behind each.

Chapter 3 described the basic operation of the CCD, including the processes of charge generation, collection, storage, transfer, and conversion. CCDs available to the OU for radiation testing (PLATO and SMILE) activities were then described, with key modifications between the PLATO and SMILE CCDs highlighted. Chapter 4 followed, by placing the operation of CCDs in the context of the hazardous space environment, namely the effects of radiation and micrometeoroid damage. The underlying mechanisms of radiation damage in

CCDs were described, focusing on the role of displacement damage and the defects of most interest with regards to SMILE SXI CCD performance. A literary review of the previous suspected hyper-velocity particulate impacts effects on space-based soft X-ray telescopes followed, accompanied by publications outlining the relevant scattering and damage mechanisms in soft X-ray optics and CCDs, respectively. Key equations and models were described (flux models and damage equations) that would be necessary to develop the damage-quantifying framework for hyper-velocity impacts in space-based soft X-ray telescopes (chapter 9).

Chapter 5 described radiation-based testing activities, including a description of the main experimental technique used in this thesis (trap pumping). An experiment planned and executed by the author was described (probing key defects in a room-temperature irradiated CCD280), with preliminary results presented.

Chapter 6 was the first original results chapter, focusing on development and use of an analytical technique (Active Trap Model) to guide experimental CCD charge transfer optimisation activities using knowledge of the defects within an irradiated CCD. **The analytical model was found to accurately predict changes in CTI as a function of temperature when an appropriate trap landscape was used**. The work contained in this chapter laid the foundation for adapting the model further, to model more intricate CCD readout modes (CCD370) and help to guide both experimental optimisation activities and inform in-orbit CCD operation modes.

Chapter 7 presented results from a trap pumping experiment, planned and executed by the author, focusing on post-irradiation defect behaviour in a cryogenically irradiated CCD280. **The first key result was analysis of an unstable defect species, calculated to have a half-life of approximately 4 hours (4.12 hours ±0.643 hours and 3.51 hours ±0.674 hours for each irradiation)**. Implications of this dynamic behaviour mean that for one orbit (approximately 48 hours), SMILE SXI CCDs will see variable CTI, potentially affecting X-ray resolution of the detector, with the author recommending a flag mechanism to highlight the affected orbit. Future work could investigate the severity of this dynamic defect behaviour as a function of CCD temperature, as each CCD-based space mission most likely operates at a different instrument temperature, which in turn could change the decay of this defect species. The second experiment focused on temperature annealing cycles, mimicking the orbital

temperature fluctuations of the SMILE SXI spacecraft (and CCDs). **It was found that (in the emission time constant window probed), the number of defects decreased by approximately 6%, with the true value most likely being below this.** For the purposes of CTI (and X-ray resolvability), this is promising as the decrease in defects is relatively low. Future work however is key, as SMILE SXI will experience many orbital temperature fluctuations, and the decrease in defects as a function of the *number* of temperature cycles (at the same temperature) must be investigated.

Chapter 8 focused on adapting the ATM to predict CCD370 charge transfer performance for different operating modes. The difference between the simple FF readout mode, and the more complex CCD370 FT readout mode was discussed, with implementation of the changes in the ATM described. **The ATM predicted that slower serial clocking frequencies would provide the lowest number of effective traps** (and hence CTI), with the number of effective traps also being a weak function of the image and store clocking frequencies. A key caveat (and future work that must be investigated), is that the effect of the store region titanium shield (11 mm) on the number of defects present in the store region of the CCDs. The store shield will reduce the number of defects, improving the benefit of optimising the image clocks, as the defect contributions from transfers in the store region of the device will naturally decrease.

The CCD operation mode of TLC was then described within the context of SMILE SXI CCDs. Implementation of TLC within the ATM was outlined, with the adapted model then used to accurately predict previous experimental performance of TLC in both EUCLID (Murray et al., 2013b) and PLATO CCDs (Peter Verhoeve – Private Communication). **The charge transfer benefit of TLC was then simulated by the ATM in a CCD370 readout mode, showing a performance benefit of approximately 7-8%. This result was presented to the SMILE SXI CCD working group, and the decision was made to remove TLC from the SMILE drive electronics due to the overall low performance benefit predicted, when compared to the work to implement the operational mode in the drive electronics.**

Chapter 9 presented development of an end-to-end framework for quantifying the effects of hyper-velocity particulate impacts in space-based CCD soft X-ray telescopes, although specifically tailored to the example of SMILE SXI. Using the Grün flux model, the number of micrometeoroids incident on the optics of SMILE SXI over the nominal 3-year science window was calculated. Using two methods (an analytical and Monte-Carlo method), the transmission

rate of particulates through the optics was calculated. The Monte-Carlo method was deemed more reliable, as it could produce many more physically intuitive results as a function different particulate and micropore sizes. **The bespoke Monte-Carlo particulate tracing method estimated that between approximately 20 – 100 micrometeoroids of minimum diameter 1 × $10^{-6}$ m will successfully traverse the sMPO and be incident on the focal plane.** Known damage equations were then applied to the micrometeoroid flux exiting the optics, predicting that **between 8 and 1 × $10^{4}$ pixels within SMILE SXI's CCD focal plane will suffer cratering** (and most likely increased dark current) during the 3-year science observation time. The considerable range arises from different empirical damage equation sub-models and associated variables (most notably the brittleness of silicon, $K_c$). A significant amount of future work could follow from the simulation work presented in this chapter, focusing on the critical scattering angle present in sMPO and the quantity and distribution of dark current generated in cratered pixels. Finally, an experimental vacuum chamber setup constructed and tested by the author was shown, with the CCD270s baselined for the hyper-velocity impacts campaign shown mounted onto the inside of the vacuum chamber.

# 11. References


Abbey, A., Carpenter, J., Read, A., Wells, A., Centre, X., Center, S., 2005. Micrometeroid Damage to CCDs in XMM-Newton and Swift and its Significance for Future X-ray Missions 604, 943.

Ambrosi, R. M., Green, S. F.,, Carpenter, J. D, 2006. ESA contract 18512/14/NL/LvH/gm.

Anderson, B., Smith, Robert., n.d. Natural orbital environment definition guidelines for use in aerospace vehicle development.

Anderson, P.C., Rich, F.J., Borisov, S., 2018. Mapping the South Atlantic Anomaly continuously over 27 years. Journal of Atmospheric and Solar-Terrestrial Physics 177, 237–246. https://doi.org/10.1016/j.jastp.2018.03.015

Bavdaz, M., Collon, M., Beijersbergen, M., Wallace, K., Wille, E., 2010. X-Ray Pore Optics Technologies and Their Application in Space Telescopes. X-Ray Optics and Instrumentation 2010, 1–15. https://doi.org/10.1155/2010/295095

Bavdaz, M., Wille, E., Wallace, K., Shortt, B., Collon, M., Ackermann, M., Olde Riekerink, M., Haneveld, J., van Baren, C., Erhard, M., Christensen, F., Krumrey, M., Burwitz, V., 2012. Silicon pore optics developments and status, in: Takahashi, T., Murray, S.S., den Herder, J.-W.A. (Eds.), . Presented at the SPIE Astronomical Telescopes + Instrumentation, Amsterdam, Netherlands, p. 844329. https://doi.org/10.1117/12.926111

Beech, M., Brown, P., Jones, J., Webster, A.R., 1997. The danger to satellites from meteor storms. Advances in Space Research 20, 1509–1512. https://doi.org/10.1016/S0273-1177(97)00427-4

Blanc, M., Bolton, S., Bradley, J., Burton, M., Cravens, T.E., Dandouras, I., Dougherty, M.K., Festou, M.C., Feynman, J., Johnson, R.E., Gombosi, T.G., Kurth, W.S., Liewer, P.C., Mauk, B.H., Maurice, S., Mitchell, D., Neubauer, F.M., Richardson, J.D., Shemansky, D.E., Sittler, E.C., Tsurutani, B.T., Zarka, Ph., Esposito, L.W., Grün, E., Gurnett, D.A., Kliore, A.J., Krimigis, S.M., Southwood, D., Waite, J.H., Young, D.T., 2002. Magnetospheric and Plasma Science with Cassini-Huygens. Space Science Reviews 104, 253–346. https://doi.org/10.1023/A:1023605110711

Bochsler, P., 2007. Minor ions in the solar wind. Astron Astrophys Rev 14, 1–40. https://doi.org/10.1007/s00159-006-0002-x

Boteler, D.H., 2019. A 21st Century View of the March 1989 Magnetic Storm. Space Weather 17, 1427–1441. https://doi.org/10.1029/2019SW002278

Buggey, T., Soman, M., 2018. SMILE SXI Testing and Calibration Micrometeoroid Test Plan.

Buggey, T., Soman, S., Keelan, J., 2018. SMILE SXI CCD Micrometeoroid Modelling Report.

Bush, N., Dryer, B., Lindley-DeCaire, A., 2018. P-Channel CCD performance characterisation and radiation testing final report. OU-PCHAN-FP-1-Iss-Rev0.

Bush, N, Hall, D., Buggey, T., Holland, A., 2020. Optimisation of charge transfer in electron multiplying CCDs through the use of an Active Trap Model, in: [In Prep].

Bush, Nathan L., 2018. The Impact of Radiation Damage on Electron Multiplying CCD Technology for the WFIRST Coronagraph. https://doi.org/10.21954/OU.RO.0000D70D

Bush, N.L., Hall, D., Burgon, R., Holland, A.D., Jordan, D., 2018. Improving charge transfer performance within irradiated EMCCDs (Conference Presentation), in: Holland, A.D.,

Beletic, J. (Eds.), High Energy, Optical, and Infrared Detectors for Astronomy VIII. Presented at the High Energy, Optical, and Infrared Detectors for Astronomy VIII, SPIE, Austin, United States, p. 39. https://doi.org/10.1117/12.2313574
Carpenter, J.D., Abbey, A.F., Ambrosi, R.M., Wells, A., 2006. Effects of micrometeoroid and space debris impacts in grazing incidence telescopes, in: Turner, M.J.L., Hasinger, G. (Eds.), . Presented at the SPIE Astronomical Telescopes + Instrumentation, Orlando, Florida , USA, p. 62663K. https://doi.org/10.1117/12.677410
Carrington, R.C., 1859. Description of a Singular Appearance seen in the Sun on September 1, 1859. Monthly Notices of the Royal Astronomical Society 20, 13–15. https://doi.org/10.1093/mnras/20.1.13
Cour-Palais, B. G., 1969. Meteoroid Environment Model.
Cravens, T.E., 1997. Comet Hyakutake x-ray source: Charge transfer of solar wind heavy ions. Geophysical Research Letters 24, 105–108. https://doi.org/10.1029/96GL03780
Crowley, C., Kohley, R., Hambly, N.C., Davidson, M., Abreu, A., van Leeuwen, F., Fabricius, C., Seabroke, G., de Bruijne, J.H.J., Short, A., Lindegren, L., Brown, A.G.A., Sarri, G., Gare, P., Prusti, T., Prod'homme, T., Mora, A., Martín-Fleitas, J., Raison, F., Lammers, U., O'Mullane, W., Jansen, F., 2016. *Gaia* Data Release 1: On-orbit performance of the *Gaia* CCDs at L2. A&A 595, A6. https://doi.org/10.1051/0004-6361/201628990
Dessler, A.J., 1968. Solar Wind Interactions and the Magnetosphere, in: Carovillano, R.L., McClay, J.F., Radoski, H.R. (Eds.), Physics of the Magnetosphere, Astrophysics and Space Science Library. Springer Netherlands, Dordrecht, pp. 65–105. https://doi.org/10.1007/978-94-010-3467-8_2
Dungey, J.W., 1961. Interplanetary Magnetic Field and the Auroral Zones. Phys. Rev. Lett. 6, 47–48. https://doi.org/10.1103/PhysRevLett.6.47
Eastwood, J.P., Hietala, H., Toth, G., Phan, T.D., Fujimoto, M., 2015. What Controls the Structure and Dynamics of Earth's Magnetosphere? Space Science Reviews 188, 251–286. https://doi.org/10.1007/s11214-014-0050-x
Einstein, A., 1905. Über einen die Erzeugung und Verwandlung des Lichtes betreffenden heuristischen Gesichtspunkt. Ann. Phys. 322, 132–148. https://doi.org/10.1002/andp.19053220607
Endicott, J., Walker, A., Bowring, S., Turner, P., Allen, D., Piersanti, O., Short, A., Walton, D., 2012. Charge-coupled devices for the ESA PLATO M-class Mission, in: Holland, A.D., Beletic, J.W. (Eds.), . Presented at the SPIE Astronomical Telescopes + Instrumentation, Amsterdam, Netherlands, p. 84531J. https://doi.org/10.1117/12.926299
ESA, 2018. SMILE: Solar Magnetosphere Ionosphere Link Explorer Definition Study Report.
ESA-ESTEC, 2008. ECSS-E-ST-10-04C.
Fechtig, H., Gentner, W., Hartung, J. B., Nagel, K., Neukum, G., Schneider, E., Storzer, D., n.d. Microcraters of lunar samples, in: Proceedings of the Soviet American Conference on Cosmochem. Presented at the Moon Planets, NASA-SP-370, pp. 585–603.
Forbes, T.G., 2000. A review on the genesis of coronal mass ejections. J. Geophys. Res. 105, 23153–23165. https://doi.org/10.1029/2000JA000005
Frey, H.U., Han, D., Kataoka, R., Lessard, M.R., Milan, S.E., Nishimura, Y., Strangeway, R.J., Zou, Y., 2019. Dayside Aurora. Space Sci Rev 215, 51. https://doi.org/10.1007/s11214-019-0617-7

Gailhanou, M., Walter, P., Schyns, E., Sarrazin, P., Blake, D.F., Marchis, F., Thompson, K., Bristow, T., 2017. Full field x-ray fluorescence imaging using micro pore optics for planetary surface exploration, in: Karafolas, N., Cugny, B., Sodnik, Z. (Eds.), International Conference on Space Optics — ICSO 2016. Presented at the International Conference on Space Optics 2016, SPIE, Biarritz, France, p. 180. https://doi.org/10.1117/12.2296170

Gault, D.E., 1973. Displaced mass, depth, diameter, and effects of oblique trajectories for impact craters formed in dense crystalline rocks. The Moon 6, 32–44. https://doi.org/10.1007/BF02630651

Geomagnetic Storms Can Threaten Electric Power Grid Earth in Space, 1997. . American Geophysical Union 9, 9–11.

Ginet, G.P., O'Brien, T.P., Huston, S.L., Johnston, W.R., Guild, T.B., Friedel, R., Lindstrom, C.D., Roth, C.J., Whelan, P., Quinn, R.A., Madden, D., Morley, S., Su, Y.-J., 2013. AE9, AP9 and SPM: New Models for Specifying the Trapped Energetic Particle and Space Plasma Environment. Space Science Reviews 179, 579–615. https://doi.org/10.1007/s11214-013-9964-y

Godet, O., Beardmore, A.P., Abbey, A.F., Osborne, J.P., Cusumano, G., Pagani, C., Capalbi, M., Perri, M., Page, K.L., Burrows, D.N., Campana, S., Hill, J.E., Kennea, J.A., Moretti, A., 2009. Modelling the spectral response of the *Swift* -XRT CCD camera: experience learnt from in-flight calibration. A&A 494, 775–797. https://doi.org/10.1051/0004-6361:200811157

Grün, E., Zook, H. A., 1979. Dynamics of Micrometeoroids. Solid particles in the solar system 293–298.

Grün, E., Zook, H.A., Fechtig, H., Giese, R.H., 1985. Collisional balance of the meteoritic complex. Icarus 62, 244–272. https://doi.org/10.1016/0019-1035(85)90121-6

Guo, K., Aquino, M., Vadakke Veettil, S., 2019. Ionospheric scintillation intensity fading characteristics and GPS receiver tracking performance at low latitudes. GPS Solutions 23. https://doi.org/10.1007/s10291-019-0835-1

Gusev, A.A., Pugacheva, G.I., Jayanthi, U.B., Schuch, N., 2003. Modeling of low-altitude quasi-trapped proton fluxes at the equatorial inner magnetosphere. Braz. J. Phys. 33, 767–774. https://doi.org/10.1590/S0103-97332003000400029

Hall, D.J., Murray, N.J., Holland, A.D., Gow, J., Clarke, A., Burt, D., 2014. Determination of In Situ Trap Properties in CCDs Using a "Single-Trap Pumping" Technique. IEEE Trans. Nucl. Sci. 61, 1826–1833. https://doi.org/10.1109/TNS.2013.2295941

Hall, R.N., 1952. Electron-Hole Recombination in Germanium. Phys. Rev. 87, 387–387. https://doi.org/10.1103/PhysRev.87.387

Hathaway, D.H., 2015. The Solar Cycle. Living Rev. Sol. Phys. 12, 4. https://doi.org/10.1007/lrsp-2015-4

Holland, S.E., Groom, D.E., Palaio, N.P., Stover, R.J., Mingzhi Wei, 2003. Fully depleted, back-illuminated charge-coupled devices fabricated on high-resistivity silicon. IEEE Trans. Electron Devices 50, 225–238. https://doi.org/10.1109/TED.2002.806476

Hopkinson, G.R., Dale, C.J., Marshall, P.W., 1996. Proton effects in charge-coupled devices. IEEE Trans. Nucl. Sci. 43, 614–627. https://doi.org/10.1109/23.490905

Hubert, B., Blockx, C., Milan, S.E., Cowley, S.W.H., 2009. Statistical properties of flux closure induced by solar wind dynamic pressure fronts: PROPERTIES OF SHOCK-INDUCED FLUX CLOSURE. J. Geophys. Res. 114, n/a-n/a. https://doi.org/10.1029/2008JA013813

J. R. Srour, C. J. Marshall, P. W. Marshall, 2003. Review of displacement damage effects in silicon devices. IEEE Transactions on Nuclear Science 50, 653–670. https://doi.org/10.1109/TNS.2003.813197

Janesick, J.R., 2001. Scientific charge-coupled devices. SPIE Press, Bellingham, Wash.

Jenniskens, P., 1994. Jenniskens, P., Meteor Stream Activity I, The annual streams, J. Astron. Astrophys., 287, 990-1013, 1994. Astronomy and Astrophysics, 990 287.

Katsuda, S., Tsunemi, H., Mori, K., Uchida, H., Petre, R., Yamada, S., Akamatsu, H., Konami, S., Tamagawa, T., 2012. HIGH-RESOLUTION X-RAY SPECTROSCOPY OF THE GALACTIC SUPERNOVA REMNANT PUPPIS A WITH *XMM-NEWTON* /RGS. ApJ 756, 49. https://doi.org/10.1088/0004-637X/756/1/49

Kendziorra, E., Colli, M., Kuster, M., Staubert, R., Meidinger, N., Pfeffermann, E., 1999. Operational aspects of the pn-CCD camera for XMM and ABRIXAS, in: Siegmund, O.H.W., Flanagan, K.A. (Eds.), . Presented at the SPIE's International Symposium on Optical Science, Engineering, and Instrumentation, Denver, CO, pp. 204–214. https://doi.org/10.1117/12.366502

Koyama, K., Tsunemi, H., Dotani, T., Bautz, M.W., Hayashida, K., Tsuru, T.G., Matsumoto, H., Ogawara, Y., Ricker, G.R., Doty, J., Kissel, S.E., Foster, R., Nakajima, H., Yamaguchi, H., Mori, H., Sakano, M., Hamaguchi, K., Nishiuchi, M., Miyata, E., Torii, K., Namiki, M., Katsuda, S., Matsuura, D., Miyauchi, T., Anabuki, N., Tawa, N., Ozaki, M., Murakami, H., Maeda, Y., Ichikawa, Y., Prigozhin, G.Y., Boughan, E.A., LaMarr, B., Miller, E.D., Burke, B.E., Gregory, J.A., Pillsbury, A., Bamba, A., Hiraga, J.S., Senda, A., Katayama, H., Kitamoto, S., Tsujimoto, M., Kohmura, T., Tsuboi, Y., Awaki, H., 2007. X-Ray Imaging Spectrometer (XIS) on Board Suzaku. Publ Astron Soc Jpn 59, S23–S33. https://doi.org/10.1093/pasj/59.sp1.S23

Lee-Payne, Z., Skottfelt, J., Dryer, B., n.d. EM1A Post-Irradiation Test Report.

Lindley-DeCaire, A., Hall, D., Bush, N., Dryer, B., Holland, A., 2019. The silicon lattice defects in proton and gamma irradiated n-channel CCDs, in: Breckinridge, J.B., Stahl, H.P., Barto, A.A. (Eds.), UV/Optical/IR Space Telescopes and Instruments: Innovative Technologies and Concepts IX. Presented at the UV/Optical/IR Space Telescopes and Instruments: Innovative Technologies and Concepts IX, SPIE, San Diego, United States, p. 11. https://doi.org/10.1117/12.2530639

Lisse, C.M., Dennerl, K., Englhauser, J., Harden, M., Marshall, F.E., Mumma, M.J., Petre, R., Pye, J.P., Ricketts, M.J., Schmitt, J., Trumper, J., West, R.G., 1996. Discovery of X-ray and Extreme Ultraviolet Emission from Comet C/Hyakutake 1996 B2. Science 274, 205–209. https://doi.org/10.1126/science.274.5285.205

Lobzin, V., Krasnoselskikh, V., Bosqued, J.-M., Pinçon, J.-L., Schwartz, S., Dunlop, M., 2007. Nonstationary and reformation of high-Mach-number quasiperpendicular shocks: Cluster observations. Geophys. Res. Lett 34. https://doi.org/10.1029/2006GL029095

Lumb, D., 2004. Radiation Damage Effects in XMM-Newton Epic Mos CCDs, in: Amico, P., Beletic, J.W., Beletic, J.E. (Eds.), Scientific Detectors for Astronomy. Springer Netherlands, Dordrecht, pp. 577–580. https://doi.org/10.1007/1-4020-2527-0_79

Mark Millinger, 2018. SMILE Environment Specification Document.

Marklund, G.T., Blomberg, L.G., Fälthammar, C.-G., Erlandson, R.E., Potemra, T.A., 1990. Signatures of the high-altitude polar cusp and dayside auroral regions as seen by the Viking Electric Field Experiment. J. Geophys. Res. 95, 5767. https://doi.org/10.1029/JA095iA05p05767

Massey, R., Stoughton, C., Leauthaud, A., Rhodes, J., Koekemoer, A., Ellis, R., Shaghoulian, E., 2010. Pixel-based correction for Charge Transfer Inefficiency in the *Hubble Space Telescope* Advanced Camera for Surveys. Monthly Notices of the Royal Astronomical Society 401, 371–384. https://doi.org/10.1111/j.1365-2966.2009.15638.x

McHugh, A. H., Richardson, A. J., 1974. Hypervelocity impact damage to glass.

Meidinger, N., Aschenbach, B., Braeuninger, H.W., Drolshagen, G., Englhauser, J., Hartmann, R., Hartner, G.D., Srama, R., Strueder, L., Stuebig, M., Truemper, J.E., 2003. Experimental verification of a micrometeoroid damage in the pn-CCD camera system aboard XMM-Newton, in: Truemper, J.E., Tananbaum, H.D. (Eds.), . Presented at the Astronomical Telescopes and Instrumentation, Waikoloa, Hawai'i, United States, p. 243. https://doi.org/10.1117/12.461154

Micro Pore Optics [WWW Document], n.d. . Photonis. URL https://www.photonis.com/products/micro-pore-optics (accessed 1.7.21).

Milan, S.E., 2004. Response of the magnetotail to changes in the open flux content of the magnetosphere. J. Geophys. Res. 109, A04220. https://doi.org/10.1029/2003JA010350

Morley, S.K., Freeman, M.P., 2007. On the association between northward turnings of the interplanetary magnetic field and substorm onsets: ON THE TRIGGERING OF SUBSTORMS. Geophys. Res. Lett. 34. https://doi.org/10.1029/2006GL028891

Murray, N.J., Burt, D.J., Hall, D., Holland, A.D., 2013a. The relationship between pumped traps and signal loss in buried channel CCDs, in: MacEwen, H.A., Breckinridge, J.B. (Eds.), . Presented at the SPIE Optical Engineering + Applications, San Diego, California, United States, p. 88600H. https://doi.org/10.1117/12.2024826

Murray, N.J., Burt, D.J., Holland, A.D., Stefanov, K.D., Gow, J.P.D., MacCormick, C., Dryer, B.J., Allanwood, E.A.H., 2013b. Multi-level parallel clocking of CCDs for: improving charge transfer efficiency, clearing persistence, clocked anti-blooming, and generating low-noise backgrounds for pumping, in: MacEwen, H.A., Breckinridge, J.B. (Eds.), . Presented at the SPIE Optical Engineering + Applications, San Diego, California, United States, p. 88600K. https://doi.org/10.1117/12.2024839

Murray, N.J., Holland, A. D., Gow, J.P.D., Hall, D.J., Tutt, J.H., Burt, D., Endicott, J., 2012. Mitigating radiation-induced charge transfer inefficiency in full-frame CCD applications by "pumping" traps, in: Holland, Andrew D., Beletic, J.W. (Eds.), . Presented at the SPIE Astronomical Telescopes + Instrumentation, Amsterdam, Netherlands, p. 845317. https://doi.org/10.1117/12.926804

Oliveira, D.M., Zesta, E., 2019. Satellite Orbital Drag During Magnetic Storms. Space Weather 17, 1510–1533. https://doi.org/10.1029/2019SW002287

Palmieri, D., 2004. ESA report EWP-2167.

Parsons, S., 2019. SMILE SXI CCD Testing and Calibration CCD Radiation Test Plan.

Perinati, E., Rott, M., Santangelo, A., Tenzer, C., 2017. Hyper-velocity impact risk assessment and mitigation strategies in the context of future X-ray astronomy missions. Exp Astron 44, 337–357. https://doi.org/10.1007/s10686-017-9546-1

Pichler, P., 2004. Intrinsic Point Defects, Impurities, and Their Diffusion in Silicon, Computational Microelectronics. Springer Vienna, Vienna. https://doi.org/10.1007/978-3-7091-0597-9

Raab, W., Branduardi-Raymont, G., Wang, C., Dai, L., Donovan, E., Enno, G., Escoubet, P., Holland, A., Jing, L., Kataria, D., Li, L., Read, A., Rebuffat, D., Romstedt, J., Runciman, C., Sembay, S., Spanswick, E., Sykes, J., Thornhill, J., Wielders, A.,

Zhang, A., Zheng, J., 2016. SMILE: a joint ESA/CAS mission to investigate the interaction between the solar wind and Earth's magnetosphere, in: den Herder, J.-W.A., Takahashi, T., Bautz, M. (Eds.), . Presented at the SPIE Astronomical Telescopes + Instrumentation, Edinburgh, United Kingdom, p. 990502. https://doi.org/10.1117/12.2231984
Ranalli, P., Comastri, A., Origlia, L., Maiolino, R., 2008. A deep X-ray observation of M82 with XMM–Newton. Monthly Notices RAS 386, 1464–1480. https://doi.org/10.1111/j.1365-2966.2008.13128.x
Reiff, P.H., Hill, T.W., Burch, J.L., 1977. Solar wind plasma injection at the dayside magnetospheric cusp. J. Geophys. Res. 82, 479–491. https://doi.org/10.1029/JA082i004p00479
Richardson, I.G., Cliver, E.W., Cane, H.V., 2001. Sources of geomagnetic storms for solar minimum and maximum conditions during 1972-2000. Geophys. Res. Lett. 28, 2569–2572. https://doi.org/10.1029/2001GL013052
Schroder, D.K., Thomas, R.N., Swartz, J.C., 1978. Free Carrier Absorption in Silicon. IEEE J. Solid-State Circuits 13, 180–187. https://doi.org/10.1109/JSSC.1978.1051012
Schubert, G., Soderlund, K.M., 2011. Planetary magnetic fields: Observations and models. Physics of the Earth and Planetary Interiors 187, 92–108. https://doi.org/10.1016/j.pepi.2011.05.013
Seabroke, G.M., Prod'homme, T., Murray, N.J., Crowley, C., Hopkinson, G., Brown, A.G.A., Kohley, R., Holland, A., 2013. Digging supplementary buried channels: investigating the notch architecture within the CCD pixels on ESA's Gaia satellite. Monthly Notices of the Royal Astronomical Society 430, 3155–3170. https://doi.org/10.1093/mnras/stt121
Shindo, S., Kawai, R., 1986. Quantum theory of charge exchange scattering of atoms at solid surfaces. Surface Science 165, 477–487. https://doi.org/10.1016/0039-6028(86)90821-6
Shockley, W., Read, W.T., 1952. Statistics of the Recombinations of Holes and Electrons. Phys. Rev. 87, 835–842. https://doi.org/10.1103/PhysRev.87.835
Shprits, Y.Y., Subbotin, D., Drozdov, A., Usanova, M.E., Kellerman, A., Orlova, K., Baker, D.N., Turner, D.L., Kim, K.-C., 2013. Unusual stable trapping of the ultrarelativistic electrons in the Van Allen radiation belts. Nature Phys 9, 699–703. https://doi.org/10.1038/nphys2760
Sibeck, D.G., Lin, R.-Q., 2014. Size and shape of the distant magnetotail. Journal of Geophysical Research: Space Physics 119, 1028–1043. https://doi.org/10.1002/2013JA019471
SILSO | World Data Center for the production, preservation and dissemination of the international sunspot number [WWW Document], n.d. URL https://wwwbis.sidc.be/silso/ (accessed 10.19.21).
Skottfelt, J., Hall, D.J., Dryer, B., Bush, N., Gow, J.P.D., Holland, A.D., 2018. Importance of charge capture in interphase regions during readout of charge-coupled devices. J. Astron. Telesc. Instrum. Syst. 4, 1. https://doi.org/10.1117/1.JATIS.4.1.018005
Southwood, D.J., Farrugia, C.J., Saunders, M.A., 1988. What are flux transfer events? Planetary and Space Science 36, 503–508. https://doi.org/10.1016/0032-0633(88)90109-2
SPENVIS - Space Environment, Effects, and Education System., 2019. . ESA.
Strüder, L., Briel, U., Dennerl, K., Hartmann, R., Kendziorra, E., Meidinger, N., Pfeffermann, E., Reppin, C., Aschenbach, B., Bornemann, W., Bräuninger, H.,

Burkert, W., Elender, M., Freyberg, M., Haberl, F., Hartner, G., Heuschmann, F., Hippmann, H., Kastelic, E., Kemmer, S., Kettenring, G., Kink, W., Krause, N., Müller, S., Oppitz, A., Pietsch, W., Popp, M., Predehl, P., Read, A., Stephan, K.H., Stötter, D., Trümper, J., Holl, P., Kemmer, J., Soltau, H., Stötter, R., Weber, U., Weichert, U., von Zanthier, C., Carathanassis, D., Lutz, G., Richter, R.H., Solc, P., Böttcher, H., Kuster, M., Staubert, R., Abbey, A., Holland, A., Turner, M., Balasini, M., Bignami, G.F., La Palombara, N., Villa, G., Buttler, W., Gianini, F., Lainé, R., Lumb, D., Dhez, P., 2001. The European Photon Imaging Camera on XMM-Newton: The pn-CCD camera. A&A 365, L18–L26. https://doi.org/10.1051/0004-6361:20000066

Sze, S.M., Ng, K.K., 2006. Physics of Semiconductor Devices: Sze/Physics. John Wiley & Sons, Inc., Hoboken, NJ, USA. https://doi.org/10.1002/0470068329

Tremblin, P., Chiang, E., 2013. Colliding planetary and stellar winds: charge exchange and transit spectroscopy in neutral hydrogen. Monthly Notices of the Royal Astronomical Society 428, 2565–2576. https://doi.org/10.1093/mnras/sts212

Tsujimoto, M., 2012. XIS status report. Presented at the SUZAKU 2011: Exploring the X-ray Universe: Suzaku and Beyond, Palo Alto, California, USA, pp. 107–110. https://doi.org/10.1063/1.3696158

Van Allen, J.A., 1959. Radiation Belts around the Earth. Scientific American 200, 39–47.

Weiss, N., 2002. Dynamos in planets, stars and galaxies. Astronomy & Geophysics 43, 3.9-3.14. https://doi.org/10.1046/j.1468-4004.2002.43309.x

Wild, J.A., Woodfield, E.E., Morley, S.K., 2009. On the triggering of auroral substorms by northward turnings of the interplanetary magnetic field. Ann. Geophys. 27, 3559–3570. https://doi.org/10.5194/angeo-27-3559-2009

Windhorst, R.A., Cohen, S.H., Hathi, N.P., McCarthy, P.J., Ryan, R.E., Yan, H., Baldry, I.K., Driver, S.P., Frogel, J.A., Hill, D.T., Kelvin, L.S., Koekemoer, A.M., Mechtley, M., O'Connell, R.W., Robotham, A.S.G., Rutkowski, M.J., Seibert, M., Straughn, A.N., Tuffs, R.J., Balick, B., Bond, H.E., Bushouse, H., Calzetti, D., Crockett, M., Disney, M.J., Dopita, M.A., Hall, D.N.B., Holtzman, J.A., Kaviraj, S., Kimble, R.A., MacKenty, J.W., Mutchler, M., Paresce, F., Saha, A., Silk, J.I., Trauger, J.T., Walker, A.R., Whitmore, B.C., Young, E.T., 2011. THE *HUBBLE SPACE TELESCOPE* WIDE FIELD CAMERA 3 EARLY RELEASE SCIENCE DATA: PANCHROMATIC FAINT OBJECT COUNTS FOR 0.2-2 μm WAVELENGTH. ApJS 193, 27. https://doi.org/10.1088/0067-0049/193/2/27

Wood, Daniel, 2018. Radiation-induced Deep-level Defects in CCD Imaging and Spectroscopy Sensors. https://doi.org/10.21954/OU.RO.0000D8BB

Yamauchi, M., Lundin, R., 1997. The wave-assisted cusp model: Comparison to low-altitude observations. Physics and Chemistry of the Earth 22, 729–734. https://doi.org/10.1016/S0079-1946(97)00203-6

Zhao, X.-Y., Wang, H.-Y., Wu, F., Meng, X.-C., Ma, Y.-Q., Lu, H., Wang, H., Wang, P., Li, X.-Q., Xu, Y.-B., Shi, F., Jiang, W.-Q., An, Z.-H., Yu, X.-X., Liu, H.-Y., 2013. A geometric factor calculation method based on the isotropic flux assumption. Chinese Phys. C 37, 126201. https://doi.org/10.1088/1674-1137/37/12/126201